



**HAL**  
open science

# In situ analysis of an organic redox flow battery using magnetic resonance and additive manufacturing

Borja Caja Muñoz

► **To cite this version:**

Borja Caja Muñoz. In situ analysis of an organic redox flow battery using magnetic resonance and additive manufacturing. Analytical chemistry. Université Paris-Saclay, 2023. English. NNT : 2023UP-AST061 . tel-04426883

**HAL Id: tel-04426883**

**<https://theses.hal.science/tel-04426883>**

Submitted on 30 Jan 2024

**HAL** is a multi-disciplinary open access archive for the deposit and dissemination of scientific research documents, whether they are published or not. The documents may come from teaching and research institutions in France or abroad, or from public or private research centers.

L'archive ouverte pluridisciplinaire **HAL**, est destinée au dépôt et à la diffusion de documents scientifiques de niveau recherche, publiés ou non, émanant des établissements d'enseignement et de recherche français ou étrangers, des laboratoires publics ou privés.

# In situ analysis of an organic redox flow battery using magnetic resonance and additive manufacturing

*Analyse in situ d'une batterie à flux redox organique par  
résonance magnétique et fabrication additive*

## Thèse de doctorat de l'université Paris-Saclay

École doctorale n° 573, Interfaces : matériaux, systèmes, usages

Spécialité de doctorat: Chimie

Graduate School : Sciences de l'ingénierie et des systèmes

Référent : Université de Versailles-Saint-Quentin-en-Yvelines

Thèse préparée dans l'unité de recherche **NIMBE** (Université Paris-Saclay, CEA, CNRS),  
sous la direction de **Patrick BERTHAULT**, directeur de recherche, et la co-direction de  
**Lionel DUBOIS**, directeur de recherche.

Thèse soutenue à Gif-sur-Yvette, le 14 avril 2023, par

**Borja CAJA-MUNOZ**

### Composition du jury

Membres du jury avec voix délibérative

**Saïd SADKI**

PR, Université Grenoble Alpes, CEA

**Emmanuel BAUDRIN**

PR, Université de Picardie, LRCS

**Michael DESCHAMPS**

PR, Université d'Orléans, CNRS, CEMHTI

**Michel BARDET**

DR émérite, Université Grenoble Alpes, CEA, CNRS

**Charlotte MARTINEAU-CORCOS**

Dr., Cortecnet

Président

Rapporteur & Examineur

Rapporteur & Examineur

Examineur

Examinatrice

**Title:** In situ analysis of an organic redox flow battery using magnetic resonance and additive manufacturing.....

**Keywords:** Battery, Redox-flow, NMR, MRI, Electrochemistry, Operando

**Abstract:** This thesis project aims at studying the operation of electrochemical cells using integrated nuclear magnetic resonance systems combined with additive manufacturing technologies. Recent advances allow the development of a real time monitoring tool for the identification of the different molecular species and migrations generated during the operation of an organic redox flow battery. To this end, several 3D printed mini-battery prototypes have been designed by optimizing parameters such as size, geometry, the volume of the compartments and the material of the electrodes. A wide bore vertical magnet allows for imaging of the batteries during operation as well as obtaining real-time localized spectra over the region corresponding to the molecules of interest during cycling. The main challenge to make

this system work was to overcome operational constraints such as size limitations of the volumes of interest, radio frequency interference or magnetic field inhomogeneities.

On the other hand, fluidic devices for NMR microdetection connected on a standard microimaging NMR probe base were designed with different radio frequency coil geometries. The 3D printed insert is coupled to a bubble pump where an inert carrier gas establishes a closed-loop fluid flow circuit. This high-sensitivity system allows in situ and operando monitoring of liquid electrolytes by studying the dynamic mechanisms and structure of molecular species (high-resolution homonuclear and heteronuclear spatially localized 1D and 2D spectra) during the redox reaction.

**Titre :** Analyse in situ d'une batterie à flux redox organique par résonance magnétique et fabrication additive.....

**Mots clés :** Batterie, Flux Redox, RMN, IRM, Électrochimie, Operando

**Résumé :** Le présent projet de thèse vise à étudier le fonctionnement de cellules électrochimiques mettant à profit des systèmes intégrés de résonance magnétique nucléaire combinés avec des technologies de fabrication additive. Les avancées récentes permettent le développement d'un outil de suivi en temps réel pour l'identification des différentes espèces moléculaires et les migrations générées lors du fonctionnement d'une batterie à flux redox organique. À cet effet, plusieurs prototypes de mini-batteries imprimés en 3D ont été conçus en optimisant des paramètres tels que la taille, la géométrie, le volume des compartiments et le matériau des électrodes. Un aimant vertical de grande cavité permet l'obtention d'images des batteries en fonctionnement ainsi que l'obtention en temps réel de spectres localisés sur la région correspondant aux molécules d'intérêt au cours du cyclage. Le principal défi pour faire fonction-

ner ce système a consisté à surmonter les contraintes opérationnelles telles que les limitations de taille des volumes d'intérêt, les interférences radiofréquences ou les inhomogénéités de champ magnétique.

D'autre part, des dispositifs fluidiques pour la micro-détection RMN connectés sur une base de sonde RMN de micro-imagerie standard ont été conçus avec différentes géométries de bobine radiofréquence. L'insert imprimé en 3D est couplé à une pompe à bulle où un gaz porteur inerte établit un circuit d'écoulement de fluide à boucle fermée. Ce système à haute sensibilité permet le suivi in situ et operando d'électrolytes liquides par l'étude des mécanismes dynamiques et de la structure des espèces moléculaires (spectres 1D et 2D à haute résolution homonucléaires et hétéronucléaires localisés dans l'espace) pendant la réaction redox.

## Résumé Substantiel

La production anthropogénique d'énergie a provoqué une augmentation des émissions de gaz à effet de serre au cours des cent cinquante dernières années, étant donné que les combustibles à base de carbone dominent le bouquet énergétique mondial. Par conséquent, décarboniser le secteur des transports et le réseau électrique mondial sont les deux principaux leviers pour relever le défi global de réduction de ces émissions. Ainsi, la fission nucléaire et les énergies renouvelables, comme le solaire et l'éolien, se présentent comme les alternatives les plus intéressantes pour atteindre cet objectif. Parmi les systèmes de stockage du surplus d'énergie, les dispositifs de stockage d'énergie électrochimiques peuvent être adaptés pour fournir des services très divers en termes de puissance nominale et temps de décharge. A ce stade, les batteries à flux redox se distinguent comme l'une des voies les plus prometteuses pour aborder l'intermittence des sources d'énergies renouvelables, permettant non seulement une sauvegarde et alimentation d'énergie sans interruption, mais également sa distribution sur le réseau électrique et la gestion énergétique à grande échelle. Le plus grand avantage par rapport aux batteries lithium-ion est la possibilité de dissocier énergie et puissance car le dimensionnement de la cellule de conversion et les réservoirs est indépendant, en offrant une configuration flexible qui peut être modifiée en fonction des disponibilités et besoins énergétiques.

Le défi actuel des batteries à flux redox réside dans la transition énergétique des principales technologies industrialisées vers une technologie d'avenir. À titre d'illustration, la technologie commerciale basée sur le vanadium est coûteuse, corrosive et soumise à une disponibilité limitée en fonction de la situation économique et géopolitique. Dans ce contexte, l'état de l'art des batteries à flux redox vise une technologie à faible toxicité et peu onéreuse avec une durabilité modérée. Les systèmes organiques se présentent comme de véritables alternatives aux batteries au vanadium car ils utilisent des molécules redox durables qui peuvent être adaptées pour obtenir des propriétés électrochimiques optimales. À cet égard, la résonance magnétique nucléaire est proposée comme l'une des techniques les plus adaptées pour la caractérisation des molécules organiques présentes dans ce type de dispositifs, car elle fournit des informations sur l'environnement des atomes étudiés, la structure des molécules et les processus dynamiques. Cependant, plusieurs contraintes sont associées à l'environnement difficile à l'intérieur des champs magnétiques. De plus, l'idée de coupler l'électrochimie et la spectroscopie de résonance magnétique en phase liquide semble étrange pour la majorité des cercles de recherche. La plupart des approches menées dans ce domaine jusqu'à présent sont basées (i) soit sur des batteries à flux redox organique surveillées en temps différé, faisant sortir la cellule de conversion du champ de franges de l'aimant, (ii) soit le suivi en temps réel de cellules électrochimiques autres que les batteries à flux redox.

Ainsi, la nouveauté exploitée dans le cadre de ce doctorat consiste à développer des dispositifs de micro-détection RMN fluide nous permettant le suivi sensible à haute résolution spatiale et spectrale d'électrolytes liquides en milieu aqueux. Grâce à cette approche, il est devenu possible de monitorer en temps réel l'état de charge des batteries organiques en étudiant les mécanismes de déplacement et la structure des espèces moléculaires au fil des cycles de charge et de décharge. Pour parvenir à cet objectif, nous nous sommes servis d'un spectromètre imageur vertical à très large cavité ('super wide bore' de diamètre utile 65 mm et 7 Tesla) et de différents spectromètres à haute résolution ('narrow bore' de diamètre utile 18 mm et 11,7 Tesla) pour caractériser les molécules organiques, tandis que les mesures électrochimiques ont

été accomplies par plusieurs potentiostats monovoies. Nous avons pu avoir accès aussi à d'imprimantes 3D pour la conception des différents modèles de batteries en nous libérant des contraintes liées à la fabrication traditionnelle, que ce soit par jet d'encre ou par stéréolithographie à faible force.

En ce qui concerne les expériences réalisées avec le spectromètre imageur, nous avons étudié les problèmes associés au couplage des techniques électrochimiques et de résonance magnétique, y compris les effets de susceptibilité magnétique ou les perturbations de champ à travers la cellule, la définition de la position et de la taille des voxels, et l'effet magnétohydrodynamique entre autres. Pour ce faire, différents paramètres ont été optimisés pour faciliter à la fois le suivi des produits par RMN (*i.e.* pH de la solution) et maximiser sa durée de vie (*i.e.* composition des électrolytes) en fonction des contraintes liées aux champs magnétiques. Nous avons élaboré deux modèles définitifs en variant la nature de la cellule électrochimique. D'une part, nous avons conçu un système contenant un double réservoir et une cellule de conversion imprimés en 3D, dont les électrodes sont des feutres de carbone. Le suivi par RMN des électrolytes liquides peut être réalisé (i) soit en temps différé dans le double réservoir avec de performances analytiques optimales (online), (ii) soit en temps réel dans la cellule électrochimique si elle est placée de manière optimale par rapport aux champs magnétiques  $B_0$  et  $B_1$  (*operando*), malgré certains problèmes d'homogénéité et de sensibilité lors du cyclage. De plus, il est possible d'empiler plusieurs feutres de carbone afin d'augmenter la surface développée de contact avec les électrolytes et ainsi accélérer la réaction électrochimique, ce qui a néanmoins un impact sur la perte ohmique de la batterie pouvant entraîner des réactions secondaires non désirées. En revanche, nous avons développé une cellule à base de graphite offrant une perte ohmique minimale due à la proximité entre les électrodes à travers la membrane, mais l'analyse à l'intérieur est entravée à cause de l'écrantage de la radiofréquence généré par le graphite massif (online).

Par ailleurs, nous avons optimisé la miniaturisation d'une cellule complète afin d'effectuer pour la première fois l'analyse *in situ* et *operando* de l'électrolyte organique d'une batterie à flux redox en fonctionnement par résonance magnétique du  $^1\text{H}$  et du  $^{13}\text{C}$ . L'insert imprimé en 3D est couplé à une pompe à bulle où un gaz porteur inerte établit un circuit d'écoulement de fluide à boucle fermée. Nous avons donc mis en œuvre des séquences RMN innovantes pour faciliter le suivi même en présence d'une électrode de carbone vitreux dans la zone de détection. Il s'agit notamment de séquences qui permettent l'acquisition de spectres 1D et 2D à haute résolution, homonucléaires et hétéronucléaires, localisés dans l'espace. De plus, lors des cycles d'oxydoréduction nous avons pu conforter nos hypothèses sur la dimérisation des produits intermédiaires du sel disodique utilisé (2,7-AQDS) par des expériences de mesure de leur coefficient de diffusion, confirmée par des calculs *ab initio* dans le cadre de la théorie de la fonctionnelle de la densité. Les petits volumes requis, de l'ordre de quelques millilitres, permettent l'étude de composés coûteux avec un outil bon marché sur mesure.



## Remerciements

Je voudrais commencer par remercier mes deux directeurs de thèse pour m'avoir tout d'abord considéré et ensuite retenu comme candidat au doctorat à l'Université Paris-Saclay. Ça ne devait pas être une décision facile de choisir un ingénieur espagnol spécialisé en photoémission pour développer un travail de thèse sur la résonance magnétique de batteries. Lors de notre première rencontre, j'ai réussi à vous transmettre que j'étais la personne idéale malgré mon parcours non linéaire, et vous avez placé votre confiance en moi les yeux fermés. Merci spécialement à Patrick d'avoir consacré des heures et des heures à m'apprendre les fondements de la RMN, et surtout d'avoir cru en mes capacités même quand je n'étais pas loin de baisser les bras. La route a été différente de celle que nous attendions, y compris la crise de la Covid-19 en jeu, mais il me semble que nous devons être fiers du travail qui a été accompli. Merci aux professeurs Emmanuel Baudrin et Michael Deschamps d'avoir accepté d'être rapporteurs de mon manuscrit de thèse, ainsi qu'aux Pr. Saïd Sadki, Dr. Charlotte Martineau-Corcus et Dr. Michel Bardet de faire partie de mon jury de thèse - et plus particulièrement à ce dernier de m'avoir si gentiment conseillé et encouragé à mi-parcours. Je n'oublierai jamais le jour ma soutenance ni les riches et intéressants échanges avec chacun d'entre vous, encore merci.

Merci du fond du cœur à chaque membre du Laboratoire de Structure et Dynamique par Résonance Magnétique (LSDRM), que ce soit sous forme liquide ou solide. Je ne voudrais oublier personne d'entre vous : ceux avec qui j'ai commencé (Guillaume Carret, Covadonga Lucas-Torres, Ziyad Chaker), ceux avec qui j'ai partagé une partie du parcours (Hicham Jabraoui, Alexianne Schenberg, Mosbah Al Hayek, Marco Bertani, Yohan Clément, Chenqin Cao), ceux avec qui j'ai achevé (Corentin Coutellier, Konstantin Romanenko, Arthur Listwan, François Nghiem, Jing Li) et, surtout, ceux avec qui j'ai parcouru tout - ou presque tout - ce chemin. Estelle Léonce pour ton sens de l'humour, mes premières expériences au laboratoire, les renseignements sur le centre et m'avoir prêté d'innombrables fois ton vélo. Thierry Bernard pour me rendre service avant tout le monde, ton rire contagieux et tes histoires interminables. Céline Boutin d'avoir partagé ton bureau et de penser toujours à immortaliser mes moments les plus gênants. Gaspard Huber pour ton sourire, ta gentillesse et ton aide chaque fois que c'était nécessaire. Mélanie Moskura pour ton énergie positive et me procurer cette électrode en platine qui m'a accompagné durant tant d'expériences. Jean-Pierre Dognon pour ton aide pendant les derniers mois, sans ta contribution les résultats ne seraient pas aussi précieux. Alan Wong pour m'apporter un autre point de vue lorsque je me sentais quelque peu perdu scientifiquement. Rodolphe Pollet pour ton calme contagieux et ces discussions si intéressantes sur les arts martiaux. Thibault Charpentier de m'avoir déposé à Paris plusieurs fois et surtout ne pas me confiner au laboratoire lorsqu'il y avait juste nous deux à 20h43.

Mais tout éloge est insuffisant si je commence à parler de mes acolytes Kévin Chighine et Mahmoud Attia. Kévin était arrivé seulement quelques mois avant moi, mais son désir d'apprendre et sa bonne volonté le positionnaient déjà comme une pierre angulaire au sein du groupe. Mon fidèle écuyer durant plus de trois ans, celui qui vivait à l'autre bout de Paris mais qui n'hésitait pas à partir avec le dernier bus si j'avais besoin d'un coup de main pour lancer une nouvelle expérience (manifestement ratée). J'hésite à savoir si tu me manques plus pour tes bricolages à deux sous – je rigole – ou tes blagues de goût douteux. Il est aussi difficile de décrire avec des mots tout ce que Mahmoud m'a démontré depuis son arrivée en région

parisienne. Il est pratiquement impossible de rencontrer quelqu'un qui donne autant en échange de si peu, je suis persuadé qu'un jour ta bienveillance sera récompensée comme tu le mérites. Merci d'avoir été le long de la dernière ligne droite, en journée en soirée et même le week-end. Je n'exagère pas en disant que je ne pense pas mériter tout le soutien reçu de la part des deux.

Impossible d'oublier ceux qui ont dû supporter dans les coulisses mes frustrations, mes quelques heures de sommeil, mes sautes d'humeur et ainsi de suite. Je dois commencer, bien sûr, par ma copine, que j'ai rencontrée peu de temps après le début du doctorat et que je ne sais pas comment elle fait encore pour être ici. Merci d'avoir été mon plus grand soutien et d'avoir si bien prétendu comprendre ce que je faisais dans la vie, je me doute que ce n'est pas du tout évident. Merci de comprendre que c'était une période de fatigue passagère et de me permettre d'arriver tant de nuits à table mise, maintenant c'est à moi de cuisiner pour les deux prochaines années. Je remercie aussi tes – désormais également mes – amies pour les repas multitudinaux dans ton studio de cinquante mètres carrés, ainsi que l'amitié solide forgée avec notre couple de *guancho* Tino & Gema. Un énorme merci à toute ma famille et à mes ami(e)s qui m'ont beaucoup aidé à travers ces années, en particulier à mes parents pour ces conversations pratiquement quotidiennes sur tout et rien. Merci d'avoir été un soutien sans faille et toujours si attentifs et disponibles, même à distance.

En parlant de famille, je ne peux m'empêcher de parler de la mienne tout au long des sept années que j'ai eu la chance de vivre à Palaiseau, le CA Orsay Rugby Club. Un grand merci à sept ans de matchs sous la pluie, de feintes de passes, de capitans en touche rocambolesques et de folles troisièmes mi-temps au clubhouse. Je remercie tout particulièrement les différents colocataires avec lesquels j'ai cohabité aux *Lucioles* tout au long des deux dernières années de thèse : Alexis, Louis, Killian, Yohan, Baptiste, Dimitri et Guillaume. J'apprécie vraiment que vous m'ayez permis d'effectuer des horaires de travail délirants et un régime alimentaire hasardeux, ainsi que de respecter un certain nombre de décibels pendant les derniers mois de rédaction - à l'exception de quelques soirées inattendues courtoises de mes très chers *enfers*. Enfin, ce n'est pas facile de résumer en quelques mots le chemin le plus exigeant que j'ai parcouru, mais tout ce dont je suis sûr c'est que je n'aurais jamais atteint l'objectif tout seul : Merci beaucoup à vous tous / Many thanks to all of you / Muchas gracias a todos vosotros / Muito obrigado a todos vocês.





# List of Abbreviations

- AC** Alternative Current
- ADC** Analog-to-Digital Converter
- ADS** Anthranol-2,7-disulfonic acid
- AORFB** Aqueous Organic Redox Flow Battery
- AQ** Anthraquinone
- AQDS** 9,10-Anthraquinone-2,7-disulfonic acid disodium salt
- AQDSH<sub>2</sub>** Hydroanthraquinone
- BASING** BAnd Selective Inversion with gradient dephasiNG
- BW** Bandwidth
- CA** Chronoamperometry
- CAD** Computer Aided Design
- CE** Counter Electrode
- COLOC** COrrrelation via LOng range Coupling
- COSY** COrrrelated SpectroscopY
- CP** Chronopotentiometry
- CPMG** Carr-Purcell-Meiboom-Gill
- CSI** Chemical Shift Imaging
- CV** Cyclic Voltammetry
- DC** Direct Current
- DE** pre-acquisition DElay
- DEPT** Distortionless Enhancement by Polarization Transfer
- DFT** Density Functional Theory
- DL** electrical Double Layer
- DNP** Dynamic Nuclear Polarization

**DoD** Depth-of-Discharge

**DOSY** Diffusion Ordered Spectroscopy

**DPSCA** Double Potential Step Chronoamperometry

**DQS** Double Quantum Spectroscopy

**EC-NMR** in situ Electrochemical Nuclear Magnetic Resonance

**EE** Energy Efficiency

**EES** Electrochemical Energy Storage

**EIS** Electrochemical Impedance Spectroscopy

**EPR** Electron Paramagnetic Resonance

**ESS** Energy Storage Systems

**EXSY** EXchange Spectroscopy

**FE** Faradaic Efficiency

**FID** Free Induction Decay

**FLASH** Fast Low Angle SHot

**FOV** Field-Of-View

**FT** Fourier Transform

**FWHM** Full Width Half Maximum

**GCPL** Galvanostatic Cycling with Potential Limitations

**HER** Hydrogen Evolution Reaction

**HETCOR** HETeronuclear CORrelation

**HMBC** Heteronuclear Multiple Bond Correlation

**HMQC** Heteronuclear Multiple Quantum Coherence

**HSQC** Heteronuclear Single Quantum Coherence

**ID** Inner Diameter

**INEPT** Insensitive Nuclei Enhancement by Polarization Transfer

**IS** Image Size

**ISIS** Image-Selected In vivo Spectroscopy

**JRES** J-RESolved spectroscopy

**LCOS** Levelized Costs Of Storage

**LIB** Lithium-Ion Battery

**LSV** Linear Sweep Voltammetry

**MAFB** Metal-Air Flow Battery

**MHD** Magnetohydrodynamic

**MRI** Magnetic Resonance Imaging

**MRSI** Magnetic Resonance Spectroscopic Imaging

**MSME** Multi-Slice Multi-Echo

**NAORFB** Non-Aqueous Organic Redox Flow Battery

**NMR** Nuclear Magnetic Resonance

**NOESY** Nuclear Overhauser Effect Spectroscopy

**NS** Number of Scans

**OCP** Open Circuit Potential

**OD** Outer Diameter

**OER** Oxygen Evolution Reaction

**OP** Optical Pumping

**ORFB** Organic Redox Flow Battery

**OSIRIS** Outer volume Suppressed Image Related In vivo Spectroscopy

**OVS** Outer Volume Suppression

**PCB** Printed Circuit Board

**PGSE** Pulsed Gradient Spin Echo

**PGSTE** Pulsed Gradient STimulated Echo

**PMMA** Polymethyl Methacrylate

**PRESS** Point RESolved Spectroscopy

**RARE** Rapid Acquisition with Relaxation Enhancement

**RAREVTR** Rapid Acquisition with Relaxation Enhancement with Variable Repetition Time

**RE** Reference Electrode

**RF** Radio-Frequency

**RFB** Redox Flow Battery

**ROESY** Rotating frame Overhauser Effect Spectroscopy

**RT** Room Temperature

**SAR** Specific Absorption Rate

**SCE** Saturated Calomel Electrode

**SE** Spin Echo

**SMFB** Solid redox-Mediated Flow Battery

**SNR** Signal-to-Noise Ratio

**SoC** State-of-Charge

**SPI** Selective Population Inversion

**SSFB** Semi-Solid Flow Battery

**ST** Slice Thickness

**STE** STimulated Echo

**STEAM** STimulated Echo Acquisition Mode

**SVS** Single-Voxel Spectroscopy

**SW** Spectral Width

**SWB** Super Wide Bore

**TE** Echo Time

**TET** Total Experiment Time

**TM** Mixing Time

**TOCSY** Total Correlation Spectroscopy

**TR** Repetition Time

**UTE** Ultrashort Echo Time

**VAPOR** VAriable Power radio-frequency pulses with Optimized Relaxation delays

**VE** Voltage Efficiency

**VOI** Volume Of Interest

**WE** Working Electrode

**WS** Water Suppression

**ZBFB** Zinc-Bromine Flow Battery

**ZTE** Zero Echo Time

# Contents

<b>I</b>	<b>Outlook of the Thesis</b>	<b>18</b>
<b>1</b>	<b>Interest of Redox Flow Batteries</b>	<b>19</b>
1.1	Renewables to tackle the Climate Problem . . . . .	19
1.2	Energy Storage Systems . . . . .	19
1.2.1	Electrochemical Energy Storage Devices . . . . .	20
1.2.2	Redox Flow Batteries for long-term Stationary Storage of Intermittent Energies . . . . .	21
<b>2</b>	<b>Scope of the Project</b>	<b>23</b>
<b>II</b>	<b>Introduction to Nuclear Magnetic Resonance</b>	<b>25</b>
<b>3</b>	<b>Overview</b>	<b>26</b>
3.1	Key concepts about NMR . . . . .	26
3.1.1	Nuclear Spin . . . . .	26
3.1.2	Magnetic Susceptibility . . . . .	27
3.2	Instrumentation . . . . .	27
3.2.1	NMR Magnets . . . . .	28
3.2.2	Transmission and Reception of the NMR Signal . . . . .	28
3.2.3	Magnetic Field Gradients . . . . .	30
3.3	Spin Interactions . . . . .	31
3.3.1	Zeeman Effect . . . . .	31
3.3.2	Internal Interactions experienced by the Spins . . . . .	32
<b>4</b>	<b>Basic Methods in NMR Spectroscopy</b>	<b>36</b>
4.1	Principle of Multidimensional NMR . . . . .	36
4.2	Magnetization Transfer Experiments . . . . .	36
4.2.1	Using the Scalar Coupling . . . . .	36
4.2.2	Using Dipolar Cross-Relaxation . . . . .	40
4.2.3	Using Chemical Exchange . . . . .	41
4.3	Self-Diffusion and Velocimetry Measurements . . . . .	41
<b>5</b>	<b>Magnetic Resonance Imaging</b>	<b>44</b>
5.1	Introduction to MRI . . . . .	44
5.1.1	Slice Selection . . . . .	46
5.1.2	Frequency Encoding . . . . .	47
5.1.3	Phase Encoding . . . . .	48

5.2	Cartesian and Non-Cartesian Techniques . . . . .	48
5.3	MRI Contrast and Artifacts . . . . .	49
5.3.1	Contrast . . . . .	49
5.3.2	Artifacts . . . . .	50
<b>6</b>	<b>Localized Spectroscopy</b>	<b>52</b>
6.1	Single-Voxel Spectroscopy . . . . .	52
6.1.1	Localization based on Alternate RF Pulses . . . . .	53
6.1.2	Localization based on Echo Formation . . . . .	54
6.2	Multi-voxel Chemical Shift Imaging . . . . .	57
6.2.1	Conventional CSI Techniques . . . . .	57
6.3	Comparison of SVS and CSI Techniques . . . . .	58
<b>III</b>	<b>Insights into Redox Flow Batteries</b>	<b>61</b>
<b>7</b>	<b>Introduction to Electrochemistry</b>	<b>62</b>
7.1	Primary Concepts . . . . .	62
7.1.1	Electrochemical Systems . . . . .	62
7.1.2	Basic Thermodynamics and Kinetics . . . . .	63
7.2	Overview of Electrochemical Methods . . . . .	65
7.2.1	Open Circuit Potential . . . . .	65
7.2.2	Potential Techniques . . . . .	66
7.2.3	Galvanic Techniques . . . . .	68
7.2.4	Application for Batteries Characterization . . . . .	69
<b>8</b>	<b>State-of-the-art of RFB</b>	<b>71</b>
8.1	Generalities . . . . .	71
8.2	Industrialized Technologies . . . . .	73
8.3	Organic-based Alternatives . . . . .	76
8.3.1	Non-Aqueous ORFB . . . . .	76
8.3.2	Aqueous ORFB . . . . .	77
<b>IV</b>	<b>In Situ Analysis of a Redox Flow Mini-Battery using MRI</b>	<b>80</b>
<b>9</b>	<b>Conversion Cell in the NMR Detection Area</b>	<b>81</b>
9.1	Coupling Electrochemistry and Liquid State NMR . . . . .	81
9.1.1	Magnetohydrodynamic Effect . . . . .	82
9.2	Model System - Materials and Methods . . . . .	82
9.3	Mini-Battery Prototypes and Problematics . . . . .	84
9.3.1	Silicone Model . . . . .	84
9.3.2	Cylindrical Model . . . . .	89
9.3.3	Spherical Model . . . . .	91



9.3.4	Square Model . . . . .	94
9.4	Model Optimization according to Magnetic Field Constraints . . . . .	94
9.4.1	Electrodes and Current Collectors' Choice . . . . .	94
9.4.2	Orientation of the Mini-Battery . . . . .	97
9.4.3	Electrolytes pH Management . . . . .	98
<b>10</b>	<b>Complete Redox Flow Battery</b>	<b>102</b>
10.1	Single Tank RFB . . . . .	102
10.2	Double Tank RFB and Conversion Cell Types . . . . .	105
10.3	Complete RFB Operation . . . . .	106
10.3.1	3D-printed Toric Model . . . . .	106
10.3.2	Full Graphite-based Model . . . . .	109
10.3.3	3D-printed Double Sense Model . . . . .	114
<b>V</b>	<b>Conception of a Fluidic NMR Micro-Detection Device</b>	<b>118</b>
<b>11</b>	<b>Miniaturization in a Microimaging Probe</b>	<b>119</b>
11.1	Specifications . . . . .	119
11.2	Choice of the Working Electrode . . . . .	121
11.2.1	Real-Time Monitoring with a Non-Commercial WE . . . . .	123
11.2.2	Operando Monitoring with a Commercial WE . . . . .	126
<b>12</b>	<b>A 3D-printed Device for In Situ Monitoring of an ORFB via NMR/MRI</b>	<b>128</b>
<b>VI</b>	<b>Conclusions and Outlooks</b>	<b>161</b>
<b>13</b>	<b>Concluding Remarks</b>	<b>162</b>
13.1	Key Findings . . . . .	162
13.2	Perspectives and Future Developments . . . . .	163



**Part I**

**Outlook of the Thesis**

# 1 - Interest of Redox Flow Batteries

## 1.1 Renewables to tackle the Climate Problem

Throughout the last hundred fifty years, there has been a rapid increase of global greenhouse gases emissions as a result of anthropogenic energy production. Since the first commercialized internal combustion engine (*Etienne Lenoir, 1860*) until today, fossil fuels-based technologies (oil, coal, and natural gas) are regarded as the backbone driving the energy economy. Global primary energy consumption, corresponding to the sum of the total energy used in heating, transport, and electricity, increases from year to year since the energy efficiency improvements do not offset the amount of people who have access to such resources due to the constant world population growth. In this regard, carbon-based fuels still clearly dominate the global energy mix (around 83.1% in 2021 [1]), releasing into the atmosphere over 35 gigatons of carbon dioxide every year.[2]

Decarbonizing the transportation sector and the worldwide electrical grid are the two main levers to address the CO<sub>2</sub> challenge. Notwithstanding the fact that the share of efficient low-carbon sources of energy (nuclear power and renewable technologies) have more than double over the last half century, their growth rate is insufficient to combat climate change and their geographical distribution portrays a mixed picture (disparities between wealthy and poor countries) that must be harmonized. Nuclear fission broke into the energy market in the 1960s as a zero-CO<sub>2</sub> emitting technology, but it has been increasingly rolled back due to the complex challenges it entails.[3] Against this background, solar and wind renewable energies have shown a huge growth in the past decade thanks to their vital role in mitigating greenhouse gases emissions together with their low cost, accessibility and non-depletive character. Nevertheless, deploying large amounts of these modern renewable energies requires the incorporation of energy storage systems in the power grid which compensates their intermittent nature.

## 1.2 Energy Storage Systems

Energy storage systems (ESS) emerge as a long-term solution to store surplus energy, offering operational flexibility and a wide array of power and discharge durations. The most popular method to categorize the different technologies is based on the form of energy stored, as shown in Figure 1.1. The global ESS power capacity in operation reached 186.1 GW by 2020, with a year-on-year growth of 2.2%. [4] Conventional pumped hydropower storage is currently the most matured ESS, with a worldwide share of 91.9%. [4] Despite its outstanding technical parameters (high power rating with a full load in 20–30 seconds, long discharge duration and lifetime, or low energy cost and self-discharging rate), traditional pumped hydropower storage technology has high capital costs and is geographically and resource constrained. [5] These mechanical systems

are mainly used for electric supply capacity, energy time-shift and frequency regulation, while electrochemical systems can be adapted to provide all the ESS services, including managing renewables or transportation.[6] As a result, the United States National Renewable Energy Laboratory predicts that the grid-scale storage capacity of electrochemical devices will surpass that of mechanical ones in less than ten years.[7]

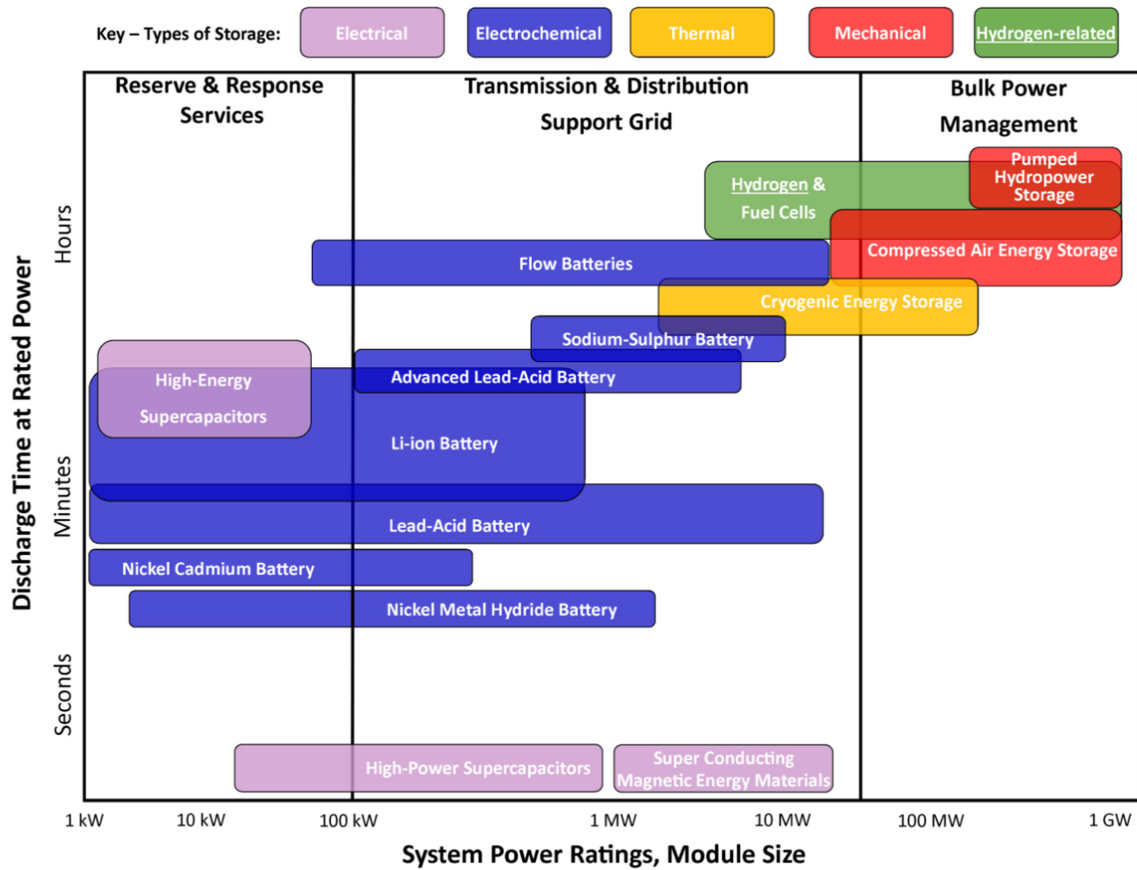


Figure 1.1: Comparison of power rating and discharge timescale of key-type ESS. Reprinted from [8], Copyright 2017, with permission from Elsevier.

### 1.2.1 Electrochemical Energy Storage Devices

Due to fact of the high importance of the electrochemical energy storage (EES) devices, and despite of their ancient nature, it is still being a hot topic of research. By way of example, advanced lead-acid batteries are still in growing demand for large-scale energy storage, microgrids or hybrid and internal combustion vehicles because of its high specific power density ( $150\text{--}180\text{ W}\cdot\text{kg}^{-1}$ ), low initial cost and high rate of recycling (over 90%). Nonetheless, lithium-ion batteries (LIB, first commercialized by Sony Corp. in 1991 [9]) clearly dominate the EES market due to their outstanding energy densities ( $75\text{--}250\text{ W}\cdot\text{h}\cdot\text{kg}^{-1}$ ). The continuous incorporation of

innovative performing cathode materials is essential to power electronics, electric transportations and stationary storage. Other key technical features of LIBs include a specific power density of 150–315 W·kg<sup>-1</sup>, from 5 to 15 years of service life (~10,000 cycles), a round-trip efficiency of 85–95%, and a self-discharge rate of 0.1–0.3% (characteristics defined in Chapter 7.2.4).[10] However, LIBs are approaching their capacity limit given the high degree of maturity of the technology and their maximum discharge duration at rated power only allows short-term storage of up to 4–6 hours (see Fig. 1.1). Therefore, alternative low-cost EES systems must be proposed for long-duration renewable energy storage (> 8 h) during night and adverse harsh weather and environmental conditions.[11]

Power-to-gas technology could fulfill the above-mentioned premise by converting electricity into an energy carrier, such as hydrogen by means of water electrolysis. Alkaline and polymer electrolyte membrane electrolyzers produce hydrogen that can be stored, used as a chemical, or react with CO<sub>2</sub> to produce synthetic natural gas.[5] The stored hydrogen can be easily reconverted to electricity using a fuel cell, which usually have high specific energy (200–1000 W·h·kg<sup>-1</sup>) and low specific power (10–200 W·kg<sup>-1</sup>) densities.[4] Nevertheless, the sluggish kinetics of the O<sub>2</sub> and H<sub>2</sub> reactions limit the round trip efficiency of the full cycle (electrolyzer + storage + fuel cell) to about 25% and require the use of high cost precious metal catalysts in an effort to mitigate it.[12] In this regard, redox flow batteries (RFB) stand as one of the most promising choice to address the intermittent nature of renewable energy sources thanks to its ability to separate power and energy, increasing the storage capacity with relatively ease and minimal cost compared to the expensive cell stack.

## 1.2.2 Redox Flow Batteries for long-term Stationary Storage of Intermittent Energies

Redox flow batteries are EES devices able to reversibly convert chemical energy into electrical energy through a redox reaction. Since their initial development fifty years back by NASA in response to the energy crisis (L. H. Taller, 1974 [13]), the technology has grown with the same general running principles depicted in Figure 1.2. RFB main components are (i) the electrochemical conversion cells, (ii) the storage tanks and (iii) the hydraulic pumps. A unit cell usually contains a separator, two electrodes, two current collectors and in most cases two bipolar/contact plates, resembling the stacking method used in fuel cells. Two redox-active materials are dissolved each in a different electrolyte: the one with higher redox potential is named posolyte (or catholyte), and the other negolyte (or anolyte). The separator, which is an ion-exchange membrane, allows the electrolytes to be chemically and electrically separated in two compartments (half-cells) to avoid cross-contamination; nonetheless, it enables the diffusion of the ions of a salt (supporting electrolyte) that ensure the system electroneutrality. Both electrolytes are pumped from the tanks into the respective half-cell of the reactor stack (eventually comprised of various unit cells) and are distributed through bipolar plate flow fields in contact with porous electrodes. In discharge mode, the oxidation takes place at the negolyte and the released electrons flow into an external electric circuit toward the posolyte, where re-

duction takes place. At the same time, the membrane allows ion transfer from one half-cell to the other.

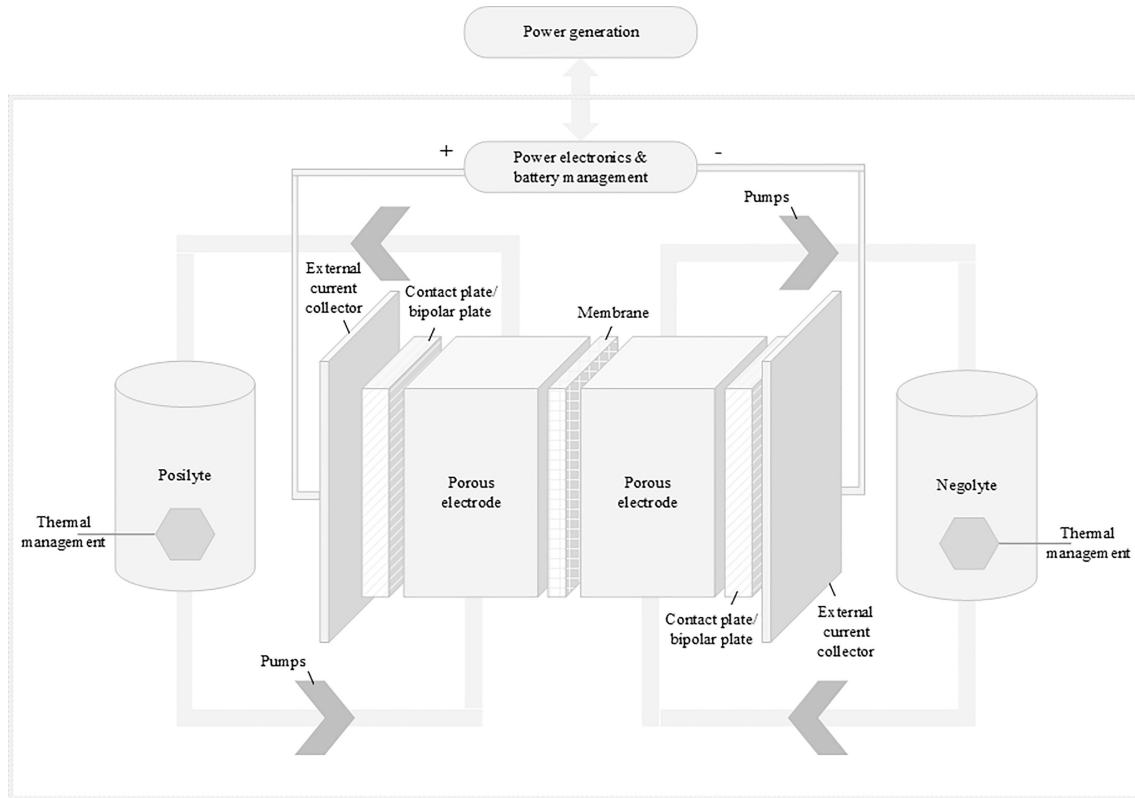


**Figure 1.2:** Generic scheme of a redox flow battery. Reprinted from [14], Copyright 2022, with permission from Elsevier.

The flexible configuration of RFB, where the cell stack and the tanks are physically separated, enables decoupling the quantity of energy stored in a total volume of tanks, so-called energy capacity (expressed in W·h), and the power generated by a total active electrode surface area or power capacity (in W). Taking into account the grid, this unmatched capability provides renewables integration possibilities unachievable with conventional sealed EES devices, such as LIB or (super)capacitors. Among its many unique advantages, they have (i) a precise adaptation to the intermittent generator unit that enables peak shaving (leveling out peaks in electricity) with a quick change between charging and discharging; (ii) a mobile modular system that offers power supply in decentralized regions; [15] and (iii) the possibility of replacing individual components of the electrochemical cell to experiment with innovative chemistries and materials. [5] In general, the industrialized technologies (all-vanadium and zinc-bromine RFB) offer high specific power (100-150 W·kg<sup>-1</sup>) and moderate specific energy (20-85 W·h·kg<sup>-1</sup>) densities, long lifetime (10-20 years), a round trip efficiency of 65–90% and small self-discharge rate. [10] However, achieving optimal performance entails very specific operating conditions in terms of thermal stability (0-40 °C) and corrosivity, as well as high operating costs.

## 2 - Scope of the Project

The current challenge in redox flow batteries lies in the energy turnaround from the main industrialized technologies towards a forward-looking approach. By way of illustration, vanadium-based technology is expensive ( $0.16 \text{ €}\cdot\text{kW}^{-1}\cdot\text{h}^{-1}\cdot\text{cycle}^{-1}$  in 2021), corrosive and has limited availability subject to the economic and geopolitical situations. In this context, the RFB state-of-the-art aims a low-toxicity and low-cost technology ( $0.05 \text{ €}\cdot\text{kW}^{-1}\cdot\text{h}^{-1}\cdot\text{cycle}^{-1}$ ) with moderate durability. Organic-based systems show up as real alternatives to vanadium batteries as they employ sustainable redox active molecules that can be tailored for achieving optimal electrochemical properties.

In this regard, Nuclear Magnetic Resonance (NMR) appears to be a suitable technique to control the stability of organic molecules present in these energy storage devices and to analyze the intermediate products. NMR spectroscopy and NMR imaging can provide informative images of the different electrolytes when they are diamagnetic as well as quantitative information about structures at the atomic level and dynamic processes (*e.g.* molecule diffusion in solution). The main goal of this project is the development of a real-time monitoring device for the identification of different molecular species and migrations generated during the operation of an organic redox flow battery. There are however several constraints related to the above-mentioned NMR techniques and associated instrumentation. Hence, it is important to:

- Verify the compatibility of conductive materials with the magnetic fields, avoiding large magnetic susceptibility differences inside the magnet (*e.g.* no ferromagnetic electrodes);
- Correctly choose a chemical system that minimizes the presence of free radicals, as NMR is not adapted for the study of paramagnetic species;
- Maintain spatial homogeneity of the system to keep a sufficient spectral resolution;
- Handle the space limitation linked to the magnet bore size;
- Maximize the filling factor in order to offset the inherent low sensitivity of the technique, by tailoring the radio-frequency coil geometry to the sample or vice-versa.





**Part II**

**Introduction to Nuclear Magnetic  
Resonance**

## 3 - Overview

Nuclear Magnetic Resonance was first discovered in 1946 by Felix Bloch and Edward Mills Purcell research groups at Stanford University and Massachusetts Institute of Technology respectively and independently from each other. NMR physical phenomenon allows the observation of an ensemble of atoms possessing nuclear spins. It has been employed for the characterization of processes and mechanisms in various disciplines, including chemical analysis, medical imaging, chemical engineering, geophysics and quality control. Emerging analytical techniques such as NMR spectroscopy, NMR imaging (MRI) and Electron Paramagnetic Resonance (EPR) spectroscopy, are of great interest to the scientific community since they are non-destructive (radio-frequency range), element specific and sensitive to dynamics while not requiring crystallinity. By way of example, NMR has become the main technique to gain insight on macromolecules structural information at atomic resolution.

### 3.1 Key concepts about NMR

#### 3.1.1 Nuclear Spin

Spin is an intrinsic property of all elementary particles describing a rotational motion (angular momentum) which generates local magnetic fields. The total spin of an atomic nucleus, known as nuclear spin  $I$ , depends upon the combination of protons and neutrons making it up, which both have  $I = \frac{1}{2}$ . This spin angular momentum leads to a magnetic dipole moment  $\mu$  (expressed in  $\text{A}\cdot\text{m}^2$ ), defined by:

$$\mu = I\hbar\gamma \quad (3.1)$$

Here  $\hbar$  (in  $\text{J}\cdot\text{s}$ ) is the Planck's constant divided by  $2\pi$  and  $\gamma$  (in  $\text{Hz}\cdot\text{T}^{-1}$ ) the gyromagnetic ratio, a constant depending on the observed isotope which is positive or negative on the basis of whether  $\mu$  is parallel or antiparallel to the spin  $I$ .

With this in mind, NMR can be observed on nuclei which exhibit a non-zero spin angular momentum ( $I \neq 0$ ), while those with even atomic and mass number ( $I = 0$ ) do not possess nuclear spin and are consequently termed *NMR silent*. Most elements have at least one NMR active isotope and therefore almost all the periodic table is accessible by this technique. Although we are constrained by the natural abundance of the active isotopes, they are likely to be artificially (and expensively) enriched to facilitate the task.

### 3.1.2 Magnetic Susceptibility

Considering ideal isotropic magnetic properties, the net bulk magnetization  $M$  (in  $\text{A}\cdot\text{m}^{-1}$ ) corresponds to the total magnetic moment per unit volume and, for the so-called linear materials, is proportional to the applied magnetic field  $H$  (in  $\text{A}\cdot\text{m}^{-1}$ ), the magnetic flux density  $B$  (in T) and the vacuum permeability  $\mu_0$  (in  $\text{H}\cdot\text{m}^{-1}$ ):

$$M = \frac{\mu}{V} = \chi_V H \quad (3.2)$$

$$B = \mu_0(H + M) = \mu_0(1 + \chi_V)H = \mu H \quad (3.3)$$

The magnetic susceptibility per unit volume ( $\chi_V$ ) is the degree of induced magnetism a material experiences under the influence of an applied magnetic field. It is a dimensionless property that facilitates the classification of materials on the basis of their magnetism, as shown in Table 3.1. Furthermore, for materials with interacting magnetic moments, there is a magnetic ordering temperature at which the atoms start to vibrate and  $\chi_V$  takes the form of Curie's law reaching the paramagnetic regime ( $\text{T}^{-1}$  dependence). For ferromagnets it is named Curie temperature ( $T_C$ ).

**Table 3.1:** Summary of the main forms of magnetism and their features.  $T_C$ : Curie temperature. Own elaboration.

Material	Diamagnetic	Paramagnetic	Ferromagnetic
<b>Electron pairing</b>	No unpaired electrons	At least one unpaired electron	Unpaired electrons in the d- or f-orbitals
<b>Magnetic behavior (<math>H = 0</math>)</b>	No magnetic moments (T independent)	Randomly oriented magnetic moments ( $\text{T}^{-1}$ dependence)	Parallel aligned magnetic moments if $T < T_C$
<b>Alignm with field (<math>H \neq 0</math>)</b>	Antiparallel, repelled (linear materials)	Parallel, weakly attracted (linear materials)	Parallel, strong magnetization at $H \gg 0$ (non-linear materials)
<b>Magnetic susceptibility</b>	Small and negative ( $10^{-6} - 10^{-5}$ )	Small and positive ( $10^{-5} - 10^{-3}$ )	Large (generally $> 100$ ), maximum value at $T_C$
<b>Effect on field lines</b>	Field bends away from the material (reduced B inside)	Field bends slightly towards the material (increased B inside)	Field bends strongly towards the material (increased B inside)
<b>Examples</b>	$\text{H}_2\text{O}$ , Cu, Si, inert gases	Al, $\text{O}_2$ , $\text{Gd}^{3+}$	Fe, Ni, Co

## 3.2 Instrumentation

In short, a sample is subjected to a static magnetic field which orients its nuclear magnetic moments and places them onto energy levels according to the Boltzmann distribution. The axis of the static magnetic field, and thereby of the magnetization at thermal equilibrium, defines the longitudinal  $z$  axis, and consequently the  $xy$  transverse plane. A transient radio-frequency

(RF) field is able to modify these populations and provide the global magnetization a given orientation in space (keep in mind that NMR was the first coherent spectroscopy). If this magnetization has a component perpendicular to the static magnetic field axis, an oscillating signal is detected by a coil in the  $xy$  plane (Larmor precession). Thus, in addition to a static field to which the sample is subjected ( $B_0$ ), an NMR spectrometer needs an RF magnetic field to perturb the spin populations ( $B_1$ ), a detection system and a console to manage events (pulses, delays). Additionally, for modern high-resolution spectrometers as well as imagers, magnetic field gradients are added to the setup. All these elements are depicted in Figure 3.1 and reviewed below.

### 3.2.1 NMR Magnets

Most of today's market NMR magnets are made of Nb-Ti or Nb-Sn type-II superconductors, materials with a low critical temperature  $T_c$ , high critical magnetic field  $B_c$  (typically  $10\text{ K} < T_c < 20\text{ K}$  and  $B_c > 1\text{ T}$ , respectively), and a gradual loss of magnetization above the latter. These superconducting magnets can provide an extremely stable magnetic field over time if they are immersed in a liquid-He bath, which in turn is surrounded by an independent liquid  $N_2$  jacket. These cryogenic reservoirs are insulated from the external environment with a vacuum chamber to minimize thermal leakage. In the magnet central part, there is a separated large bore through which a cylindrical probe positions the sample at the spot of the maximum magnetic field.

In order to achieve an uniform field over the entire volume of the sample, the magnet is equipped with additional electrical windings called shims. A set of superconducting shims embedded within the cryostat offer a primary correction, while additional room-temperature (RT) shims located inside the magnet bore are employed to obtain high field homogeneity. The current in the latter is adjusted to optimize the NMR signal resolution and sensitivity in a process called shimming. A perfectly shimmed magnet provides extremely high field homogeneity ( $< 10^{-9}$ , in the order of 0.1 Hz for a  $^1\text{H}$  resonance frequency of 500 MHz), enabling observation of the scalar couplings or discrimination between nuclear spins with slightly different local chemical environment.

### 3.2.2 Transmission and Reception of the NMR Signal

NMR instruments include different subsystems to irradiate the sample and interpret the consequential radio signals emitted by the nuclei. The most common way to flip magnetization away from the  $z$  axis position is by pulsing an oscillating magnetic field at the nuclear Larmor frequency  $\omega_0$  (in  $\text{rad}\cdot\text{s}^{-1}$ ). The nutation or flip angle  $\theta$  is defined by the amplitude  $B_1$  (in T) and duration  $\tau_p$  (in s) of the radio-frequency pulses:

$$\theta = \gamma B_1 \tau_p \tag{3.4}$$

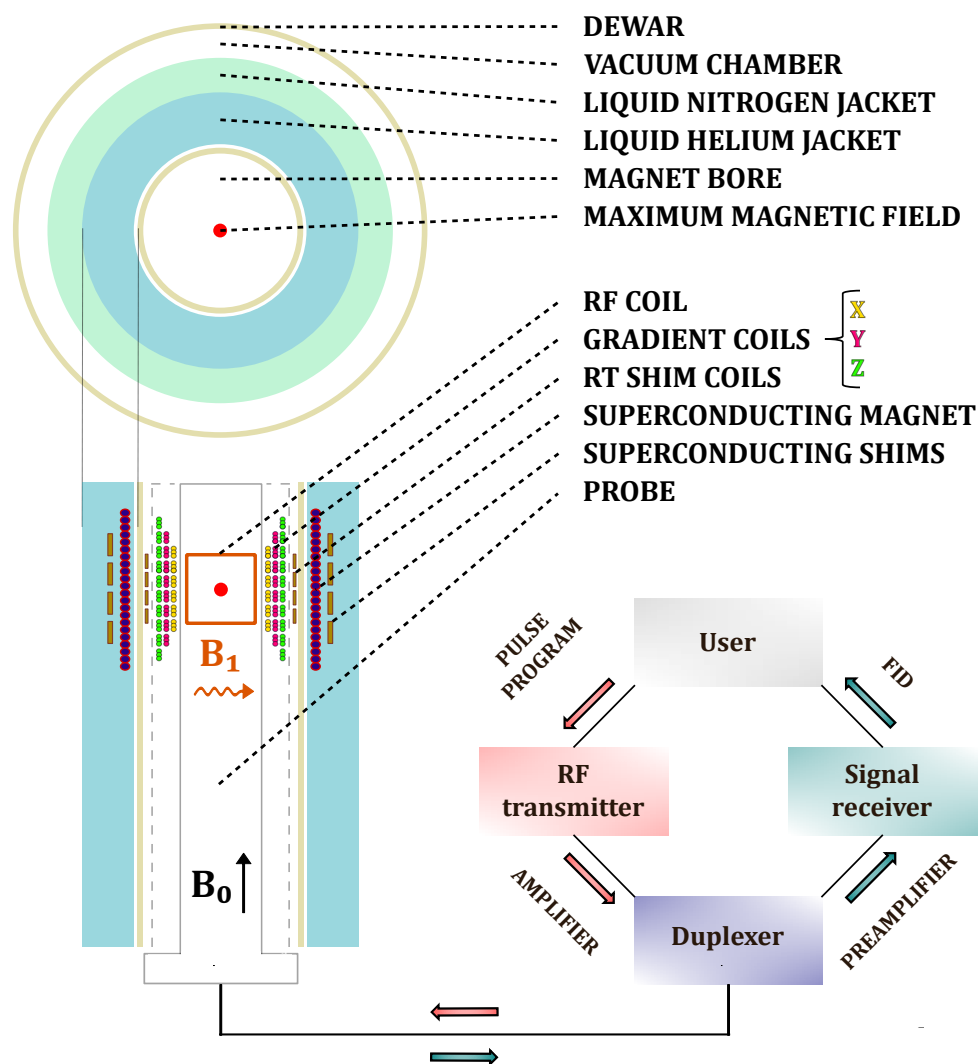


**Figure 3.1:** Simplified diagram of an NMR spectrometer and the circuitry required for an NMR experiment.

The RF transmitter generates a current flowing through a coil which induces the transient magnetic field (Biot-Savart law). Synthesizers generate oscillating electrical waves which are modulated into pulses and a power amplifier scales up their amplitude transmitted to the probe.

Being the most complex and specialized among the spectrometer elements, the probe contains electronic circuits to interact with the nuclear spins, as well as devices for rotating the sample and stabilizing its temperature. The probe heads are exchangeable depending on the analytical technique employed (*e.g.* spectroscopy, imaging), the condition of the sample (liquid-state, solid-state) or the nature and number of observable nuclei (*e.g.*  $^1\text{H}$ - $^{13}\text{C}$  double resonance). The most common RF circuit broadly consists of a copper transmission/detection coil and two ceramic variable capacitors, one wired in parallel with the coil (tuning) and the second in series with the resulting dipole (matching):

- The RF coil surrounds the sample and has the twofold purpose of generating a homoge-

neous excitation field within the detection region, as well as detecting the electrical nuclei response for subsequent processing. The most commonly used coil geometries are the solenoid, the saddle coil and the birdcage. The inductance  $L$  (in Henry) and resistance  $R_L$  (in ohm) of the full coil system (capacitors, wires and welding) determine the quality factor  $Q$  of the probe circuit.

$$Q = \frac{\omega_0 L}{R_L} \quad (3.5)$$

- The tuning capacitor  $C_T$  (in farads) allow the circuit to resonate at the nuclei Larmor frequency, thereby increasing the transmitted and detected signal.
- The matching capacitor  $C_M$  cancels out the inductive component of the probe, adjusting the circuit impedance to the purely resistive industry standard ( $50 \Omega$ ) and thus minimizing signal reflection.

$$\omega_0 = \frac{1}{\sqrt{L(C_T + C_M)}} \quad (3.6)$$

The duplexer couples the probe to the transmitter or receiver subsystems. This switch allows the high powered pulse sequences to reach the RF coil (transmit mode), as well as it transmits the nuclear spin signal to the detection circuitry (receive mode).

The signal receiver processes the oscillating electrical current generated by the excited sample, which is called free induction decay (FID). A preamplifier scales the voltage of the weak signal to a convenient level. Then, a quadrature receiver down-converts the Larmor frequency of the NMR signal into a relative one handled by the electronics (demodulation). The emerging complex signal distinguishes between positive and negative frequency offsets thanks to its real and imaginary components (quadrature detection). At this point, an analog-to-digital converter (ADC) turn the continuous current into an ordered set of consecutive values (digitalization). The time elapsed between the sampling of each ADC point is the sampling interval (dwell time), and its reciprocal is referred to as sampling bandwidth or maximum range of signal frequencies (spectral width). After Fourier transform (FT), an NMR spectrum is obtained with peaks corresponding to nuclear spins precessing at different frequencies.

### 3.2.3 Magnetic Field Gradients

Magnetic field gradients consist in a spatial linear variation of the static field along one ( $x$ ,  $y$  or  $z$ ), two ( $xy$ ,  $xz$ ,  $yz$ ), or three ( $xyz$ ) orthogonal directions through the use of additional coils. As a general rule, gradient coils are combined with RT shim ones in the case of NMR imagers whereas a gradient jacket is integrated into the probe for high resolution NMR spectrometers (dotted line in Fig. 3.1). They are usually applied during a limited period of time and thus are often called pulsed field gradients. In the presence of a gradient of amplitude  $G$  (in  $\text{T}\cdot\text{m}^{-1}$ ) a nucleus  $i$  at a spatial coordinate  $r_i$  from the magnetic center will experience a field  $B_i =$

$B_0 + Gr_i$  and thus will precess at a frequency  $\nu_i = \nu_0 + \gamma Gr_i$  (in Hz) according to Larmor equation.

Nowadays, magnetic field gradients are used in applications as diverse as spatial cartography (see Chapter 5), self-diffusion/velocimetry experiments (see Chapter 4) and coherence selection. Most of the modern pulse sequences contain pulsed field gradients for coherence selection, since this avoids (or completes) the use of complex and time-consuming phase cycling [16]. They are based on the principle that a coherence of order  $p$  has a sensitivity  $p$  times higher than a single coherence of order 1 to magnetic field variation (coherences of order 0, *e.g.* populations, are not sensitive to magnetic field inhomogeneity for instance). The coherence pathway that is kept at the end of the pulse sequence containing various gradients  $G_i$  at different steps of its execution is the one for which the final magnetization is refocused. It must obey:

$$\sum \gamma_i p_i G_i = 0 \quad (3.7)$$

All the other pathways being rejected. We will see later on that gradients for spatial encoding and coherence selection gradients can coexist in the same sequence.

## 3.3 Spin Interactions

The total energy of a nucleus encompasses not only the external but also the internal spin interactions. The external contribution comprises the interaction of the nuclear spins with the main magnetic field  $B_0$  and the RF field  $B_1$ , whereas the internal one includes different spin interactions with local environment.

### 3.3.1 Zeeman Effect

Nuclei placed in a magnetic field  $B_0$  possess  $2I+1$  spin states  $i \in \{-I, I+1, \dots, I-1, +I\}$  of energies  $E_i$  given by:

$$E_i = i h \nu_0 = i h \gamma B_0 \quad (3.8)$$

$\nu_0 = \frac{\omega_0}{2\pi} = \gamma B_0$  is known as the Larmor law. For a spin  $\frac{1}{2}$  system (two spin states  $|-\frac{1}{2}\rangle$  and  $|+\frac{1}{2}\rangle$ ), both discrete energy levels are thus splitted by  $\Delta E = h \gamma B_0$  with the application of a magnetic field (Zeeman effect). As nuclear spins are fermions, they obey the Boltzmann distribution law:

$$\frac{n_{\uparrow}}{n_{\downarrow}} = \exp\left(-\frac{\Delta E}{k_B T}\right) \quad (3.9)$$

Here  $T$  is the system temperature (in K) and  $k_B$  the Boltzmann constant ( $1.38 \cdot 10^{-23} \text{ J} \cdot \text{K}^{-1}$ ). Nuclear polarization ( $P$ ) derived in Equation 3.10 from the combination of Bohr [Eq. 3.8], Larmor and Boltzmann [Eq. 3.9] equations:

$$P = \frac{n_{\downarrow} - n_{\uparrow}}{n_{\downarrow} + n_{\uparrow}} = \tanh\left(\frac{\hbar \gamma B_0}{2k_B T}\right) \quad (3.10)$$



The energy difference between the eigenstates ( $\Delta E$ ) is small at common magnetic field and temperature values, and consequently the population difference and the nuclear polarization. The hyperbolic tangent term can be removed (high-temperature approximation). For instance, the  $^1\text{H}$  polarization at 10 T and room temperature is on the order of  $4 \cdot 10^{-5}$ . In order to compensate for the low sensitivity of the technique, several methods exist:

- Choosing a nucleus with high gyromagnetic ratio (*e.g.*  $^1\text{H}$ ) whenever possible;
- Increasing the static magnetic field (technically limited and expensive);
- Lowering the temperature (working at 77 K, the temperature of liquid nitrogen, affords a gain of ca. 4 in sensitivity);
- Transferring polarization for a more ordered system. For decades, this is the basis of heteronuclear experiments (transfer from protons to heteronuclei of lower gyromagnetic ratio), and more recently this has led to the advent of hyperpolarization. Electrons are the source for Dynamic Nuclear Polarization (DNP), while photons are for optical pumping (OP).

Precisely, the NMR signal is linked to the global magnetization, which is the only observable:

$$M = \frac{1}{2} \gamma \hbar P \mu (n_{\uparrow} + n_{\downarrow}) = \frac{1}{4} \frac{\hbar^2 \gamma^2 B_0}{k_B T} (n_{\downarrow} - n_{\uparrow}) \quad (3.11)$$

Here we can find the terms precedently evoked, including hyperpolarization that tends to maximize  $(n_{\downarrow} - n_{\uparrow})$ . In classical NMR, it is the magnetic induction which is detected, proportional to the time derivative of the magnetization component perpendicular to  $B_0$ :

$$\frac{dM_{\perp}}{dt} = \frac{1}{4} \frac{\gamma^3 \hbar^2 B_0^2}{k_B T} (n_{\downarrow} - n_{\uparrow}) \quad (3.12)$$

### 3.3.2 Internal Interactions experienced by the Spins

#### Order and Disorder

The majority (though not all) of the interactions experienced by the spins are anisotropic, *i.e.* their magnitude depends on the orientation of the considered spins with respect to the static magnetic field. According to the state of the sample in question, a large difference between liquid and solid-state NMR is seen herein. Each interaction experienced by the nucleus can be translated into an energy term, and thus by a modification of the precession frequency according to the Larmor relationship. However, the anisotropic internal interactions are averaged out in solution NMR due to fast random molecular motion and therefore only the time- and population-average of the signals is observed. In other words, the sum of the magnetic fields created by these individual interactions is averaged to zero ( $\sum \vec{B}_{loc} = 0$ ) but the sum of their squares is different from 0 ( $\sum B_{loc}^2 \neq 0$ ), meaning that only the second-order perturbation has to be considered (*i.e.* relaxation). So, in liquid-state NMR, the interactions described below can influence energy levels and/or relaxation.

## Chemical Shift

For a given isotope, spins in distinct sites or chemical functions have different chemical environments thus different local fields and precess at different frequencies, being shown up as separate peaks in the NMR spectrum. The electrons neighbouring the nucleus modify the effective magnetic field ( $B_{local}$ ) experienced by it:

$$B_{local} = B_0(1 - \sigma) \quad (3.13)$$

The shielding constant ( $\sigma$ ) depends on the charge in the nucleus, symmetry of the atomic orbitals, bonds anisotropy, ring current or solvent effect among others. The chemical shift ( $\delta$ ) has been introduced for the chemists who wanted a parameter independent of the static magnetic field. Expressed in parts per million (ppm), it represents the frequency of a spin population on the spectrum relative to a standard (*e.g.* tetramethylsilane for  $^1\text{H}$  in organic solvents):

$$\delta_i = \frac{\nu_i - \nu_{ref}}{\nu_{ref}} \times 10^6 \quad (3.14)$$

## Scalar Coupling

The nuclear spins can be coupled via their bonding (valence) electrons, involving electron-nucleus coupling (Fermi contact) and electron-electron coupling (Pauli principle). These indirect spin-spin interactions, also known as scalar or J-coupling, lead to lifting of frequency degeneracy and thus splitting of resonance lines. The magnitude of the splitting depends on not only the number of bonds separating the two nuclei but also on geometrical considerations (for instance the Karplus law expresses the vicinal or three-bond scalar coupling constant as a function of the torsion angle). The J-coupling constant between two nuclei A and B can be found on each signal and is independent on  $B_0$ . It can be homonuclear (*e.g.*  $^1\text{H}$ - $^1\text{H}$ , 0-20 Hz) or heteronuclear (*e.g.*  $^1\text{H}$ - $^{13}\text{C}$ , 100-200 Hz). For the homonuclear case, one distinguishes weak coupling ( $|\frac{\delta_A - \delta_B}{J_{AB}}| > 10$ ) where the line multiplicity is easy to interpret, and strong coupling ( $|\frac{\delta_A - \delta_B}{J_{AB}}| < 10$ ) giving rise to very complicate lines.

## Relaxation Phenomenon

Relaxation is the process by which the spins return to equilibrium. In NMR, this process is non-radiative, *i.e.* it does not involves either absorption or emission of photons, which, according to Einstein's law on black bodies, is of very low probability given the low energies involved. As previously stated, molecular motion and collisions in solution create local fluctuating fields limited in time which average is null. They cannot induce a global flip of the magnetization as would do an RF pulse, which keeps the coherence between spins. But if one of these fluctuations occurs at a frequency close to the frequency difference between nuclear spin energy levels, microscopically it can cause a - local - transition. Statistically there will be transitions favoring the return to Boltzmann equilibrium that will be dominant.

The longitudinal relaxation, characterized by  $T_1$  (in s), is sometimes called spin-lattice relaxation as it implies population changes and therefore energy exchange from and to the lattice, which is defined as the magnetic and thermal environment that contributes to local field variations. A particular case is that of transverse relaxation, characterized by  $T_2^*$  and systematically  $\leq T_1$ . Thinking in terms of magnetic field: in the same manner as the RF field  $B_1$  must be perpendicular to  $B_0$  to have an effect, only the field fluctuations along  $B_0$  can have an effect on  $T_2^*$  (e.g. gradients). Therefore, taking into account that the previously described local motions are responsible of this effect, the transverse relaxation component due to lattice is minimal. That being said,  $T_2^*$  directly depends on magnetic susceptibility effects ( $T_2^{MS}$ ), static magnetic field inhomogeneities ( $T_2^M$ ) and intrinsic spin-spin interactions ( $T_2$ ):

$$\frac{1}{T_2^*} = \frac{1}{T_2^{MS}} + \frac{1}{T_2^M} + \frac{1}{T_2} \quad (3.15)$$

The former term can be refocused by a spin echo sequence [17] while the two latter cannot.

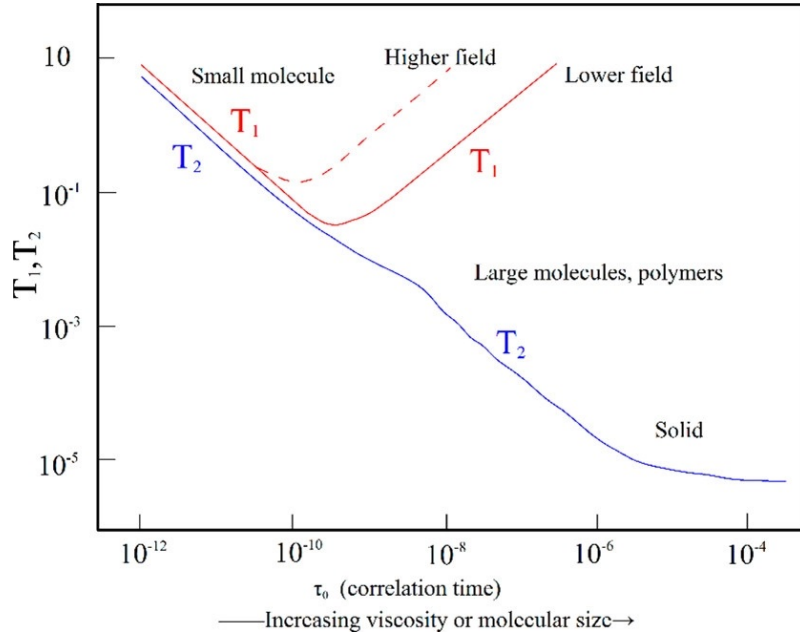


**Figure 3.2:** Plot of  $T_1$  and  $T_2$  relaxation times versus  $\tau_c$ .

Figure 3.2 shows the dependence of the longitudinal and transverse relaxation rates as a function of the molecular motion.  $\tau_c$  is the rotational correlation time, considered to be the delay for a rotation of 1 radian of an equivalent spherical molecule. This parameter is directly proportional to its size and the viscosity of the solution, and inversely proportional to the temperature. While  $T_1$  has a minimum at the inverse of the Larmor frequency,  $T_2$  displays a quasi-linear decrease with the rotational correlation time  $\tau_c$ . According to these general considerations it is easy to understand that (i) all motions are not useful to relaxation due to this need of frequency matching, (ii) isotopes do not have the same sensitivity to the fluctuating fields due to the difference of the influence of the interactions on them.

## Dipolar Relaxation

A nuclear spin interacts with the neighboring spins through space. The magnitude of this direct dipolar coupling contains radial and angular terms. For liquids the angular term is averaged to zero by fast molecular tumbling and for solids via magic angle spinning. In liquid state, only the second-order perturbation remains, leading to dipolar (or dipole-dipole) relaxation. For two nuclei  $i$  and  $j$  separated by a distance  $r$ , in the case of an isotropic motion and in the extreme narrowing limit ( $\omega_0\tau_c < 1$ ,  $T_2 = T_1$ ), the longitudinal relaxation is given by:

$$\frac{1}{T_{1DD}} = \frac{\gamma_i^2 \gamma_j^2 \hbar^4 \tau_c}{r^6} \quad (3.16)$$

Another remarkable dipolar interaction is the one between unpaired electrons and the nuclear species, encountered for paramagnetic species. The electron gyromagnetic ratio being *ca.* 660 times that of proton, the corresponding efficiency of the relaxation is multiplied by *ca.*  $4 \cdot 10^5$ ! This leads to an extra shift of the nucleus resonance frequency and/or a significant linewidth broadening. These complex interactions hinder the spectral analysis but in turn provide information on the presence of paramagnetic species, which is of great interest in energy applications.

## Quadrupolar Relaxation

On another front, seventy percent of the nuclei in the periodic table are quadrupolar ( $I > \frac{1}{2}$ ), which means that their electric charge distribution is not spherical and interacts with the surrounding nuclei and electrons (electric field gradient). This quadrupolar interaction is orientation dependent and in solid state tell us about structural symmetry, being the most important line broadening factor. As for the dipolar interaction, in liquid state this energy term is averaged to zero by fast molecular tumbling and only the second-order perturbation remains, leading to (efficient) quadrupolar relaxation.

## 4 - Basic Methods in NMR Spectroscopy

### 4.1 Principle of Multidimensional NMR

Conventional multidimensional NMR is based on four key points:

- The long coherence times ( $T_2$  of several tens of milliseconds) allow to exploit the conservation of the system memory.
- The signals are acquired according to a numerically incremental time. Each spectrum is therefore related to the previous one by a function depending on this time, thus generated by a phase equal to the product of the magnetic moment precession frequency by this time.
- Via a 2D Fourier transformation, one obtains in the first/indirect dimension (F1) the evolution frequency during the increment time, and in the second/direct dimension (F2) the precession frequency of the magnetization as in the 1D spectra.
- Any 2D sequence can be written in the form:

**Preparation | Evolution ( $t_1$ ) | Mixing ( $\tau_m$ ) | Detection ( $t_2$ )**

During the preparation period, firstly the excited nuclei return to their equilibrium state between two consecutive sequences. Then, a set of RF pulses creates a coherent transverse magnetization. Each nuclear spin evolves as a function of the internal interaction (chemical shift, scalar coupling) along the evolution time  $t_1$ . Facultative pulses may alter this coherence and the nuclear spins interact with each other (polarization transfer) over the mixing time  $\tau_m$ . Finally, the transverse one-quantum magnetization is detected (also spin-decoupling can occur) during the period  $t_2$ , giving rise to the FID.

### 4.2 Magnetization Transfer Experiments

#### 4.2.1 Using the Scalar Coupling

##### General Principles

When two spins  $I$  and  $S$  are coupled, there is degeneracy of the energy levels, with 4 states that can be denoted  $\alpha_I\alpha_S$ ,  $\alpha_I\beta_S$ ,  $\beta_I\alpha_S$  and  $\beta_I\beta_S$ . Thus, provided that  $|\frac{\nu_I - \nu_S}{J_{IS}}| \geq 10$  (see Chapter 3.3.2), the NMR signals will be 4, corresponding to the four transitions:  $\alpha_I\alpha_S \rightarrow \beta_I\alpha_S$  (1),  $\alpha_I\beta_S \rightarrow \beta_I\beta_S$  (2), both centered on the  $I$  frequency, and  $\alpha_I\alpha_S \rightarrow \alpha_I\beta_S$  (3),  $\beta_I\alpha_S \rightarrow \beta_I\beta_S$  (4), centered on the  $S$  frequency (see Figure 4.1).

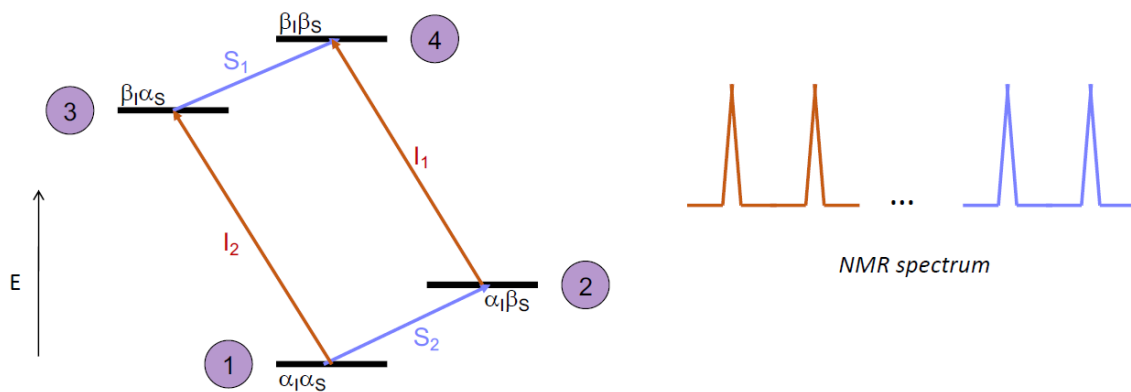


**Figure 4.1:** Energy levels of an AX spin system and corresponding NMR spectrum.

It is easy to understand that a modification of the populations of one spin affect the other transitions. This is the basis of the Selective Population Inversion (SPI) experiment [18], shown in Figure 4.2. If  $I$  stands for  $^1\text{H}$  spins and  $S$  for  $^{13}\text{C}$  spins, due to the factor 4 between the proton polarization and the carbon polarization, at equilibrium the relative populations of the levels are  $5p$ ,  $3p$ ,  $-3p$ ,  $-5p$  for the  $\alpha_I\alpha_S$ ,  $\alpha_I\beta_S$ ,  $\beta_I\alpha_S$  and  $\beta_I\beta_S$  levels, respectively. Thus the amplitudes of the proton transitions  $\alpha_I\alpha_S \rightarrow \beta_I\alpha_S$  (13) and  $\alpha_I\beta_S \rightarrow \beta_I\beta_S$  (24) are  $5p - (-3p) = 8p$  and  $3p - (-5p) = 8p$ , that of the carbon transitions are  $5p - 3p = 2p$  and  $-3p - (-5p) = 2p$ . We find here the factor 4 of the intensities of the proton lines compared to the carbon lines.

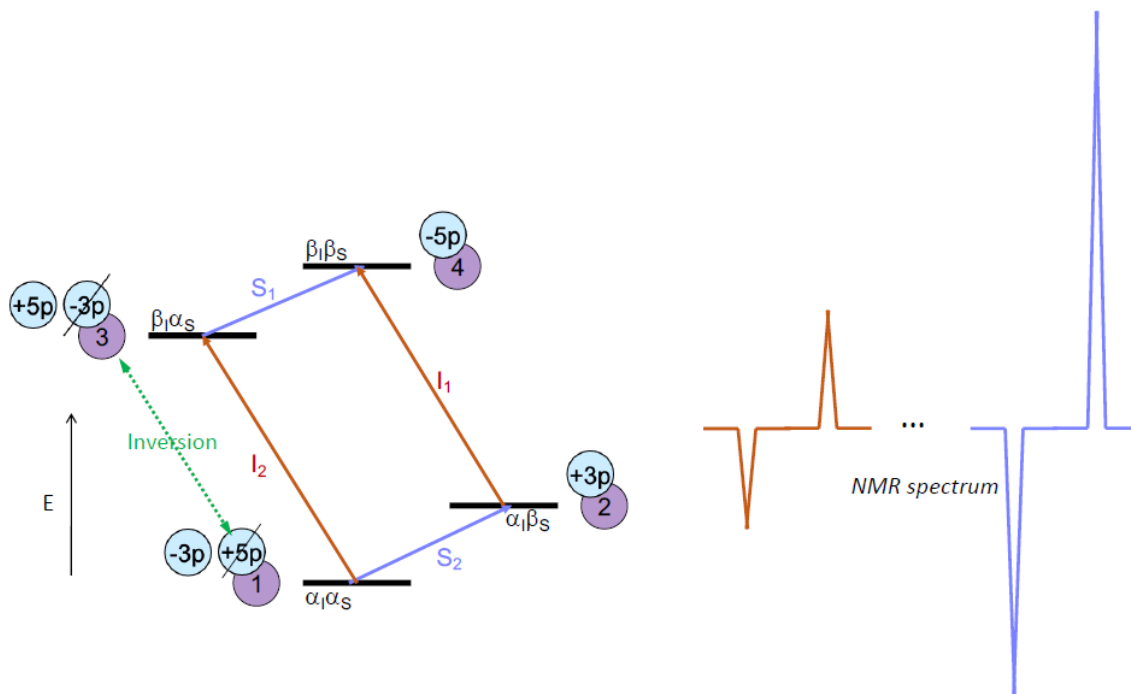


**Figure 4.2:** SPI experiment. Left: energy levels on which the relative spin populations for a C-H pair are indicated. In this virtual experiment the populations of the levels 1 and 3 are inverted; Right: corresponding NMR spectra.

Imagine that one is able to selectively invert the populations of the  $\alpha_I\alpha_S$  and  $\beta_I\alpha_S$  levels (see Fig. 4.2), it is immediate to see that the  $S$  transitions are impacted, as now the intensities of these transitions are  $-3p(-3p) = -6p$  and  $5p(-5p) = -10p$  for the  $\textcircled{2}$  and  $\textcircled{3}$  transitions, respectively. The concrete realization of such an experiment would require a soft pulse inverting selectively one of the two  $^{13}\text{C}$  lines (or satellites), leaving the second one unchanged. While this is conceivable for the C-H pairs as the  $^1J_{C-H}$  coupling is large, this is not practically feasible for smaller couplings. In this case, the soft inversion pulse can be replaced by a  $90^\circ$  hard pulse followed by a delay where the coupling acts and another  $90^\circ$  hard pulse to transform the phase difference into a population difference:

$$\text{Soft } 90^\circ \rightarrow 90^\circ - \text{Delay} - 90^\circ$$

This is the basis of the experiments involving through-bond magnetization transfer.

## Heteronuclear Experiments

### Direct detection

In these experiments, magnetization is transferred from the protons to the coupled heteronuclei X, which are detected. During the evolution period of a 2D sequence, the protons evolve according to their chemical shifts. Thus, while the direct dimension displays the X frequencies, the indirect dimension contains the  $^1\text{H}$  frequencies. The most common experiments are INEPT (Insensitive Nuclei Enhancement by Polarization Transfer) [19], DEPT (Distortionless Enhancement by Polarization Transfer) [20], HETCOR (HETeronuclear CORrelation) [21] and COLOC (CORrelation via LONG range COUpling) [22]. The first two are for spectral editing (separation of the XH, XH<sub>2</sub> and XH<sub>3</sub> groups), the third one is a  $^1J$  correlation, and the last one a long range - multiple bonds - correlation. While they all use the previously described magnetization transfer mechanism, DEPT is more difficult to describe with hands as it involves multi-quantum coherences of the type  $\alpha_I\alpha_S \leftrightarrow \beta_I\beta_S$ .

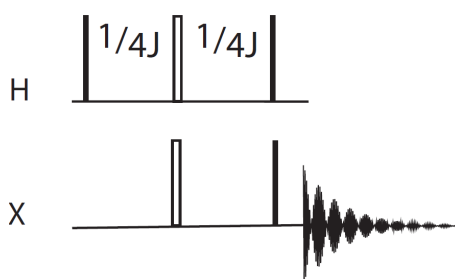


**Figure 4.3:** Simplified scheme of a non-decoupled INEPT experiment. Black rectangles represent  $90^\circ$  pulses, white rectangles  $180^\circ$  pulses.

The INEPT sequence (see Figure 4.3) is essentially the scheme previously described for magnetization transfer, with a spin-echo ( $\tau - 180^\circ_{H,X} - \tau$ ) in order to refocus the chemical shift

while preserving the evolution due to coupling. Note that the delay  $\tau$  for optimal magnetization transfer is equal to  $1/4J$ .

### Inverse detection

In these experiments protons are initially excited, then either heteronuclear multi-quantum coherences evolve during the evolution period in the indirect dimension, as in the case of HMQC (Heteronuclear Multiple Quantum Coherence) [23] and HMBC (Heteronuclear Multiple Bond Correlation) [24] experiments, or proton magnetization is transferred to the coupled heteronuclei before this period. In both scenarios, the magnetization is returned back to the protons before detection. Thus, while the indirect dimension contains the X frequencies the direct dimension displays the  $^1\text{H}$  frequencies, which leads to more sensitive experiments.

The HSQC (Heteronuclear Single Quantum Coherence) sequence [25] shown in Figure 4.4 - and used later in our work under the form of a spatially-localized experiment - commences with a first INEPT scheme. Then the spins X coupled to H evolve in the indirect dimension and the  $180^\circ$  proton pulse at the middle of the evolution period refocuses the heteronuclear coupling effect. At the end of this period, the magnetization is switched back to proton via a mirrored retro-INEPT scheme. After the two  $90^\circ$  pulses,  $^1\text{H}$  magnetization is antiphase, thus an additional  $\tau - 180^\circ_{\text{H,X}} - \tau$  spin-echo scheme is required to transform it into in-phase coherence, enabling X-decoupling during acquisition.

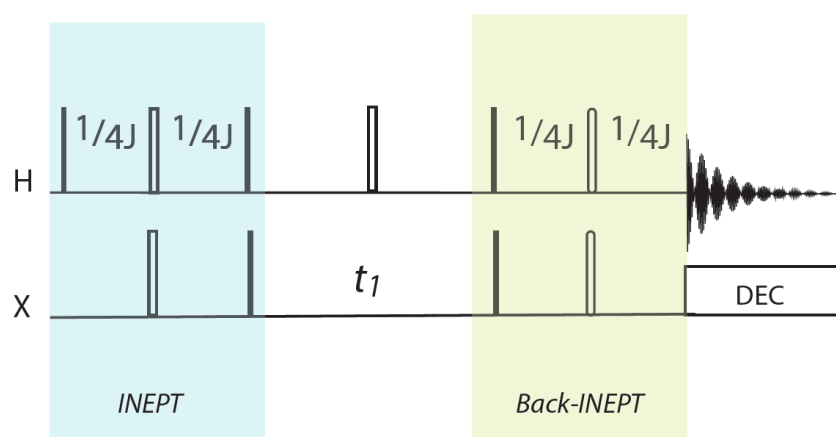


**Figure 4.4:** Simplified scheme of the HSQC sequence. Black rectangles represent  $90^\circ$  pulses, white rectangles  $180^\circ$  pulses.

### Homonuclear Experiments

The main sequences using the principle of through-bond magnetization transfer previously described are COSY (COrelated SpectroscopY, where correlations appear between protons coupled to each other) [26], DQS (Double Quantum Spectroscopy, where the indirect dimension contains the sum of the frequencies of the coupled protons) [27] and JRES (J-RESolved



spectroscopy, where the indirect dimension contains only the scalar couplings) [28].

Another method to efficiently transfer magnetization through bonds is to use a spin-lock field, in order to reach the Hartmann-Hahn condition ( $\gamma_I B_{1I} = \gamma_S B_{1S}$ ). In this case, the system can be considered as similar to this of strongly coupled spins ( $|\frac{\nu_I - \nu_S}{J_{IS}}| \sim 1$ ), and the transfer is favored. In a nutshell, the interaction term is no more negligible toward the Zeeman term, and the transfer is now an in-phase transfer. This is the basis of the TOCSY (Total Correlation Spectroscopy) experiment [29].

## 4.2.2 Using Dipolar Cross-Relaxation

Among the interactions previously described, only two - the scalar coupling and the dipolar relaxation - involve two spins. In 1955, Solomon showed that for two spins  $I_1$  and  $I_2$  in dipolar interaction, the time evolution of their magnetization can be written:

$$\frac{dI_{1z}}{dt} = \rho_1(I_{1z} - I_{1z}^0) - \sigma(I_{2z} - I_{2z}^0) \quad (4.1)$$

$$\frac{dI_{2z}}{dt} = \rho_2(I_{2z} - I_{2z}^0) - \sigma(I_{1z} - I_{1z}^0) \quad (4.2)$$

$I_{1z}^0$  and  $I_{2z}^0$  are the thermal equilibrium magnetizations,  $\rho_1$  and  $\rho_2$  the longitudinal self-relaxation rates and  $\sigma$  the rate of cross-relaxation between spins  $I_1$  and  $I_2$ .

From these equations, it is easy to understand that the two spins  $I_1$  and  $I_2$  are dependent on each other through the  $\sigma$  term, so any departure of spin from equilibrium has an effect on the other one. This is the basis of the NOESY (Nuclear Overhauser Effect Spectroscopy) experiment [30], which 2D sequence is described in Figure 4.5. The first  $90^\circ$  pulse flips the spins in the transverse plane, where they precess under the effects of chemical shift and scalar coupling, thereby creating the indirect dimension. Then the second  $90^\circ$  pulse flips a part of the magnetization along  $-z$ . This out-of-equilibrium longitudinal magnetization experiences self-relaxation (leading to the diagonal peaks) but also cross-relaxation with neighboring spins, which leads to cross-peaks.

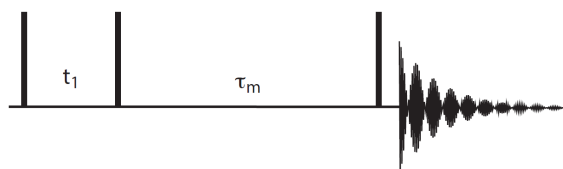


**Figure 4.5:** Simplified scheme of the NOESY sequence. Black rectangles represent  $90^\circ$  pulses.  $t_1$ : evolution time;  $\tau_m$ : mixing time.

In the region  $\omega\tau_c \simeq 1$ ,  $\sigma$  vanishes and even if two nuclei are in close proximity, no cross-peak is observed. In this case, the ROESY (Rotating frame Overhauser Effect Spectroscopy) sequence [31], using relaxation in the presence of a spin-lock field, will be preferred.

### 4.2.3 Using Chemical Exchange

It is frequent that a nucleus experiences a change of magnetic environment linked to a change of chemical environment. This is the case of protons in exchange with the solvent, or belonging to a molecule exchanging between conformers. An exchange phenomenon will be characterized by its rate relative to the NMR parameter that we observe. For instance, we speak in a simplified way of slow exchange when its rate is (largely) lower than the frequency difference of the signals in the two magnetic environments. It could also be rephrased as 'slow exchange in relation to the frequency difference'. Two signals appear on the NMR spectrum, and a 2D experiment similar to NOESY, so-called EXSY (EXchange Spectroscopy) [32], indicates as cross-peaks the environments connected through exchange. As the idea both in NOESY and EXSY is to detect and identify a stochastic phenomenon, it is logical to use the same sequence.

And thus conversely a fast exchange situation is when its rate is higher than the frequency difference. In fast exchange, the NMR observable is the average of the two signals. For instance, the chemical shift observed for a nucleus exchanging between two sites  $a$  and  $b$  is:

$$\delta_{obs} = f\delta_a + (1 - f)\delta_b \quad (4.3)$$

Here  $f$  is the fraction of molecules in the  $a$  state;  $f = \frac{[a]}{[a]+[b]}$ .

## 4.3 Self-Diffusion and Velocimetry Measurements

Molecules in solution move in a random time dependent process known as translational diffusion or self-diffusion. This motion is described by a coefficient according to the Debye–Einstein theory.[33] The Stokes-Einstein equation is obtained assuming spherical shaped molecules:

$$D = \frac{Tk_B}{f_T} = \frac{Tk_B}{6\pi\eta r_s} \quad (4.4)$$

Here  $D$  is the diffusion coefficient (in  $\text{m}^2 \cdot \text{s}^{-1}$ ),  $T$  is the system temperature (in K),  $k_B$  the Boltzmann constant ( $1.38 \cdot 10^{-23} \text{ m}^2 \cdot \text{kg} \cdot \text{s}^{-2} \cdot \text{K}^{-1}$ ),  $f_T$  the friction factor (in  $\text{kg} \cdot \text{s}^{-1}$ ),  $\eta$  the viscosity of the solvent (in  $\text{kg} \cdot \text{m}^{-1} \cdot \text{s}^{-1}$ ) and  $r_s$  the hydrodynamic radius of the molecule (in m).

In addition to the self-diffusion, it is possible to detect flow velocity ( $v$ ) if the solution is circulating. In order to evidence these phenomena and measure their amplitude, two types of pulse sequences shown in Figure 4.6 can be performed: PGSE (Pulsed Gradient Spin Echo) [34] and PGSTE (Pulsed Gradient STimulated Echo) [35], while all others are subsequent modifications. Both are more robust against susceptibility artifacts than sequences based on gradient echos (generally used with a short echo time for fast imaging), but stimulated echo experiments are useful to measure a wider range of substances (see Chapter 6). Magnetic field gradients alter the Larmor precession of the spins in a spatially defined manner (see Chapter 3.2.3). The initial position of the molecules is encoded by a first gradient whereas

their final position is decoded by a second; if both positions are different, the measured spins are defocused and the NMR signal amplitude is attenuated. A series of experiments varying either the amplitude of the gradient pulses  $g$  (gradient strength) or the delay between their centers  $\Delta$  (diffusion time) can be performed. Nonetheless, in most experiments the delays are kept constant to avoid signal attenuation coming from spin relaxation.

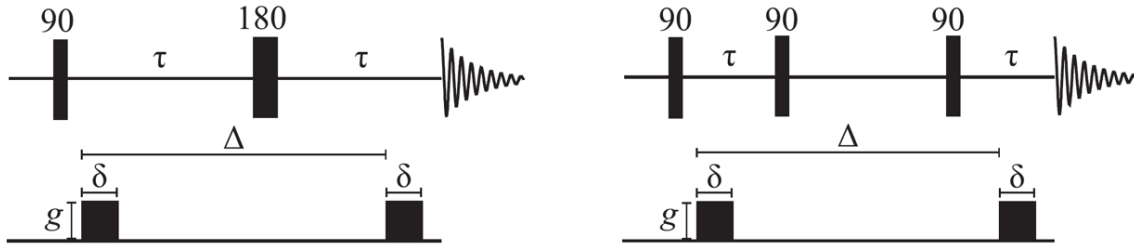


**Figure 4.6:** Simplified scheme of the pulsed field gradient diffusion sequences. Left: Pulsed gradient Spin Echo (PGSE); Right: Pulsed gradient Stimulated Echo (PGSTE).  $\Delta$ : diffusion time;  $\delta$ : gradient length;  $g$ : gradient strength;  $\tau$ : echo time.

In the case of non-equilibrated motion flows ( $v \neq 0$ ), self-diffusion and velocimetry measurements are usually performed under the form of 2D PGSTE experiments [36]. The gradient strength is thus varied in the indirect dimension, and the signal is modulated according to:

$$S(\vec{q}) = \exp(-4\pi^2 \vec{q} D \vec{q} \Delta + i2\pi \vec{q} v \Delta) \quad (4.5)$$

$S(\vec{q})$  is the observed signal intensity,  $\vec{q} = \gamma \vec{G} \delta$  the wavenumber (in  $\text{m}^{-1}$ ) and  $\delta$  the effective length of the gradient pulses (in s). In this equation, the first term represents the effect of self-diffusion, which leads to the linewidth in the indirect dimension after FT, and the second one the effect of the group flow velocity, leading to a shift from the zero frequency in the same dimension. The average liquid speed can be weighted by the arithmetic mean of the signal intensity in the indirect coordinate. It can be written for the maximal encoded velocity:

$$v_{max} = \frac{1}{dq\Delta} = \frac{1}{\gamma(dg)\delta\Delta} = \frac{N}{2\gamma G^{max}\delta\Delta} \quad (4.6)$$

Here  $dg$  is the gradient strength increment varied between two FIDs,  $N$  the number of points and the factor 2 at the denominator comes from the fact that one samples from  $-G^{max}$  to  $+G^{max}$  in the indirect dimension.

If the group flow velocity is equilibrated ( $v = 0$ ), only the real part of Equation 4.5 remains and the self-diffusion appears as a signal attenuation according to the equation:

$$\ln \frac{S(q)}{S(0)} = -q^2 D = -\gamma^2 G^2 \delta^2 D \quad (4.7)$$

In general, a DOSY (Diffusion Ordered SpectroscopY) experiment [37] consists of a 2D matrix showing the chemical shift in the direct dimension after Fourier transformation and the diffusion coefficient in the indirect one after inverse Laplace transformation.

The following sequence modifications are among the most widely-used in stimulated echo self-diffusion and velocimetry measurements:

- Spoil gradients [38] during the delay  $\Delta$  can be employed to destroy all remaining coherence and speed up the acquisition of multiple scans;
- The use of bipolar gradients [39] results in a flow-induced phase shift independent of the spin position, self-compensating at the same time the eddy currents and the chemical shift effects;
- A double STE sequence [40] refocuses the effects of constant flow avoiding convection effects.

# 5 - Magnetic Resonance Imaging

## 5.1 Introduction to MRI

MRI is neither more nor less than an optical instrument, intended to complete the range of other imaging techniques and sometimes allow the understanding of the nature and structure of the observed matter. It is well known that the spatial resolution of an optical instrument is limited by the wavelength of the radiation used. It is the wavelength that imposes the maximum magnification of a microscope for example. Also, the Blue Ray technology of DVD players is an example that shows that with blue light, we can have smaller engravings of the DVD than with red light and therefore have more information.

In the introduction of his seminal article in Nature in 1973 [41], Paul Lauterbur wrote *"Image formation usually requires that the object interact with a matter or radiation field characterized by a wavelength comparable or smaller than the smallest features to be distinguished"*. With NMR, for which the energies involved are very low and therefore the wavelengths very high (of the order of a meter at 7 Tesla), the problem is easily understood. But in the same article, Lauterbur also stated *"In the presence of a second field that restricts the interaction of the object with the first field to a limited region, the resolution becomes independent of wavelength, and is instead a function of the ratio of the normal width of the interaction to the shift produced by a gradient in the second field"*. By this method, he invented zeugmatography, which later became MRI, and together with Peter Mansfield received the Nobel Prize in Medicine in 2003.

Thus, compared to an NMR spectrometer, an imager has additional coils allowing to encode the static field in three orthogonal dimensions (see Figure 5.1), and it is immediate to understand that the resolution of the image is directly related to the strength of this additional field ( $G$ ). The intrinsic spatial resolution ( $r_1 - r_2$ ) is the ability to discriminate two separated spins of the same chemical species by their respective Larmor frequencies:

$$\nu_1 - \nu_2 = (\gamma B_0 + \gamma G r_1) - (\gamma B_0 + \gamma G r_2) = \gamma G (r_1 - r_2) \quad (5.1)$$

The effective spatial resolution is lower as it depends on parameters such as relaxation time or diffusion rate. Also, the presence of the  $\gamma$  term indicates that the highest spatial resolution is obtained with the proton nucleus (the case of tritium is ignored in here).

As in spectroscopy, the passage from time domain for the acquired signal to - more descriptive - frequency domain is carried out via Fourier transformation. The main difference with MRI is that the frequency also depends on the spatial coordinates of the spins considered. It is, therefore, useful to use the reciprocal space, as in other imaging techniques such as SAXS or SANS, and define the wavenumber  $k = \gamma G \delta$  (analogous to  $q$  used in diffusion, *cf.* Chapter 4.3). With this notation, the FT of the signal in time domain ( $s(k)$ ) is written:

$$S(r) = \int_{-\infty}^{+\infty} s(t) e^{-i\nu(r)t} dt = \int_{-\infty}^{+\infty} s(t) e^{-i\gamma G r t} dt = \int_{-\infty}^{+\infty} s(k) e^{-ikr} dk \quad (5.2)$$

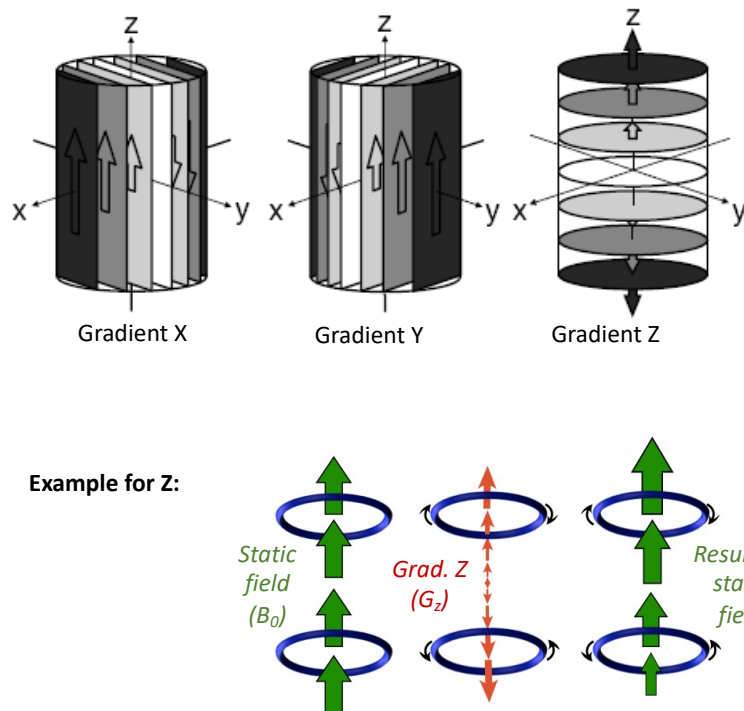


**Figure 5.1:** Schematics of magnetic field gradients in three orthogonal directions of an imager, typically via three pairs of Maxwell ( $z$ ) and saddle ( $x, y$ ) coils.

Low values of  $k$  (low gradient strengths) describe the global shape of the object, while high  $k$  values correspond to the object details. It could be observed as an analogy with the FID acquired in spectroscopy, where the first points represent the envelope of the peaks on the spectrum, but where it is necessary to acquire on a longer delay and wait for the following points to increase the spectral discrimination between two signals. In spectroscopy, being able to record long FID means increasing the intrinsic spectral resolution, whereas in imaging acquiring high  $k$  values means increasing the intrinsic spatial resolution.

Therefore to get an image, the  $k$  space is to be covered to a certain extent. It is worth considering that the symmetry properties of the FT make unnecessary to sample the whole  $k$  space. The MRI pulse sequences can be classified according to the trajectory they give rise in this reciprocal space. They can be Cartesian, where a 2D image is obtained after double FT, as well as radial or spiral, which requires more complex processing (*i.e.* interpolation on a grid or projection-reconstruction as in computerized tomography). Similarly to classical 2D spectroscopy experiments (see Chapter 4.1), a basic Cartesian 2D imaging sequence contains three steps, cited here in chronological order:

### Preparation | Evolution ( $\Delta G$ ) | Detection

1. A preparation step, in which a delay enables the spin system to reach a certain level of longitudinal magnetization. This delay is followed by one or several radio-frequency pulses

designed to excite the spins. There are two main differences between 2D spectroscopy and imaging sequences. In MRI, the interscan delay is shorter and it is rather uncommon to wait for delays of several times the  $T_1$  value as in spectroscopy (*e.g.*  $5 \times T_1$ ). Also, most of the time the excitation pulse is frequency-selective and accompanied by a simultaneous pulsed field gradient, which enables selecting a slice in the sample.

2. An evolution step, which gives rise to the second (indirect) dimension. While in spectroscopy an incremented delay constitutes this step, in imaging it is the strength of a pulsed field gradient which is incremented.
3. A detection step, where generally an echo is recorded and during which a field gradient is applied in the case of frequency-encoded MRI sequences (see below).

As an example, a basic gradient echo 2D sequence known as FLASH (Fast Low Angle SHot) [42] with one slice selection is depicted in Figure 5.2.

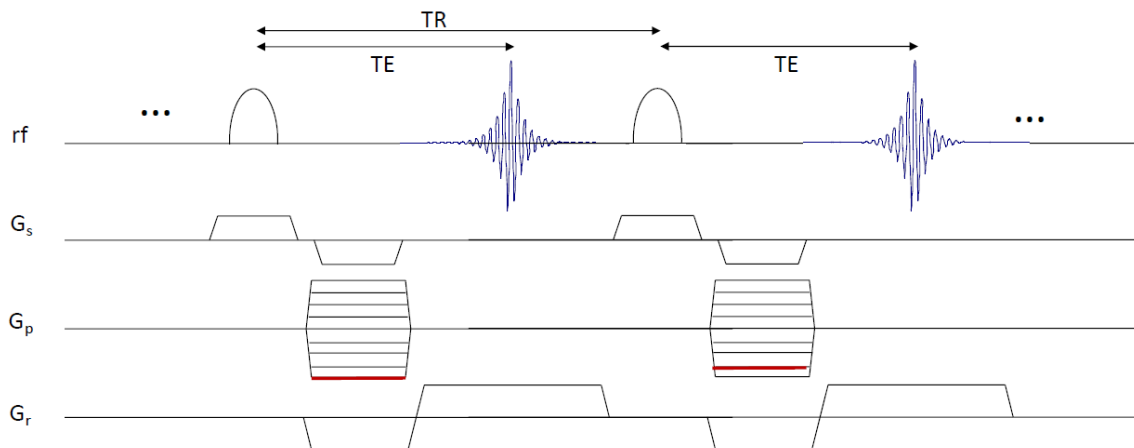


**Figure 5.2:** Simplified scheme of a 2D FLASH sequence with an  $x$  axis slice selection. Semi-ellipses represent the excitation pulse of low flip angle.  $G_s$ : slice gradient;  $G_p$ : phase gradient;  $G_r$ : read gradient.

In the analogous spin echo experiment, sometimes called spin-warp [43] and derived to RARE (Rapid Acquisition with Relaxation Enhancement) [44] or MSME (Multi-Slice Multi-Echo) [45], the sequence 'Pulse - TE' is replaced by 'Pulse - TE/2 - 180° pulse - TE/2'. The phase gradient is placed during the first or the second TE/2 delay. As already stated for INEPT, the latter sequence enables the refocusing (annihilation) of chemical shift and magnetic susceptibility variation effects.

### 5.1.1 Slice Selection

The principle of the slice selection is to simultaneously use a frequency-selective RF pulse (so-called soft pulse) and a field gradient. While the gradient broadens the frequency response of the spins according to the spreading of their spatial coordinates, the soft pulse acts only on

a well-defined spectral region instead of exciting all the spins that are resonating at different Larmor frequencies as with non-selective square pulses (hard pulses). A soft pulse has to be defined by its shape, amplitude, duration and phase. The most widely used shapes are gauss, sinc, hyperbolic secant (sech), asymmetric and adiabatic. For a given amplitude, the angle by which a frequency-selective pulse flips the magnetization depends on its duration  $\tau_p$  [Eq.3.4].

The excited or inverted spectral bandwidth ( $BW$ ) depends on the magnetization trajectories during the pulse. Additionally,  $R = BW \times \tau_p$  is a unitless factor defined for each flip angle and shape. According to Equations 3.4 and 5.1, the slice thickness  $\Delta r_s$  is given by:

$$\Delta r_s = \frac{BW}{\gamma G_s} = \frac{R}{\tau_p \gamma G_s} = \frac{B_1 R}{\theta G_s} \quad (5.3)$$

Selecting a thinner slice means using a stronger slice gradient and/or lengthening the duration of the pulse.

## 5.1.2 Frequency Encoding

In a frequency encoded sequence the signal is detected in the presence of a pulsed field gradient. This so-called read gradient modifies the main magnetic field in a predictable pattern, causing spins resonance frequencies to vary linearly with their position. It is therefore impossible to recover the spectrum during the acquisition as the NMR fingerprint is lost. The chosen field-of-view ( $FOV_r$ ) has to be greater than the object size in the considered dimension in order to avoid aliasing artifacts. Besides, the Nyquist theorem specifies that to accurately reproduce a sinusoidal function, the sampling rate has to be greater than twice the maximum frequency of the signal being sampled. According to this theorem and Equation 5.1, the minimal spectral width  $SW$  is given by:

$$SW = \frac{1}{\Delta t} = \gamma G_r FOV_r \quad (5.4)$$

Here  $\Delta t$  is the dwell time, *i.e.* the delay between two consecutive points in the FID. Thus it is immediate to derive the intrinsic spatial resolution  $\Delta r_r$  from the field-of-view and the number of data points acquired ( $N_r$ ) in the read dimension:

$$FOV_r = \frac{1}{\gamma G_r \Delta t} = \frac{1}{\Delta k_r} \quad (5.5)$$

$$\Delta r_r = \frac{FOV_r}{N_r} = \frac{1}{\gamma G_r t} = \frac{1}{k_r^{max}} \quad (5.6)$$

It is worth noting that, even if the Nyquist theorem is not respected, in the direct dimension there is usually a digital filter that avoids any signal folding. Normally, the detection which is accompanied by a gradient  $G_r$  is preceded by an antigradient (gradient of opposite sign), so as to create a signal echo at the middle of the acquisition.



### 5.1.3 Phase Encoding

A pulsed field gradient induces spin-phase effects (dephasing) that persists even once it is switched off prior to the acquisition of the signal. The net phase shift  $\phi_i$  experienced by a spin population is defined by:

$$\phi_i = 2\pi(\nu_i - \nu_0)\delta_p = \gamma G_p \delta_p r_i = k_i r_i \quad (5.7)$$

The experiment is repeated  $N_p$  times with increment of the phase gradient by a value of  $\Delta G_p$  (see red lines in Fig. 5.2), thereby creating the indirect dimension of the  $k$  space. Similarly to Equations 5.5 and 5.6, the field-of-view ( $FOV_p$ ) and resolution ( $\Delta r_p$ ) in the indirect dimension are given by:

$$FOV_p = \frac{1}{\gamma \Delta G_p \delta_p} = \frac{1}{\Delta k_p} \quad (5.8)$$

$$\Delta r_p = \frac{FOV_p}{N_p} = \frac{1}{2\gamma G_p^{\max} \delta_p} = \frac{1}{k_p^{\max}} \quad (5.9)$$

Here  $\delta_p$  is the time during which the phase gradient  $G_p$  is applied and  $N_p$  the number of points in the indirect dimension (analogous to Equation 4.6). Note that factor 2 comes from the fact that one usually samples from  $-G_p^{\max}$  to  $+G_p^{\max}$ . Also, the order with which the  $k$  rows are sampled can also be different, for instance, the phase gradient amplitude follows  $0, +G_p, -G_p, +2G_p, -2G_p, \dots$  in the centric encoding.

## 5.2 Cartesian and Non-Cartesian Techniques

Although some sequences only use phase encoding for obtaining an image (pure phase encoding methods), most of the 2D MRI experiments include phase and frequency encoding steps (see Fig. 5.2), corresponding to indirect and direct dimensions respectively. Note that they are less time-consuming than the pure phase encoding methods as a  $k$  line is recorded per acquisition instead of one  $k$  point. The previous section describes frequency and phase encoding, but the imaging techniques can also be sorted according to the way they sample the  $k$  space (trajectories). Regardless of the order of coverage of the reciprocal space, an image will be obtained as long as enough points are recorded. The Cartesian sampling, which is the basis of most of the sequences (FLASH, RARE, etc.), provides a grid of  $k$  value data and a double Fourier transformation in both dimensions gives the 2D image.

But radial imaging techniques also exist, and belong also to frequency-encoded methods as gradients are applied during acquisition. The acquisitions cover  $k$  lines (called 'spokes') that pass across the center of the  $k$  space and are rotated with respect to each others. For achieving this trajectory, they are based on a combination of gradients that obey:

$$\frac{G_y}{G_x} = \tan \Phi \quad (5.10)$$

These sequences (*e.g.* 2D imaging in Figure 5.3) are less sensitive to motion than Cartesian ones as the center of  $k$ -space is oversampled and continuously updated due to the overlapping spokes that repeatedly pass through this region. This redundancy can be exploited to detect and correct for movement if the signal from the  $k$ -space center changes between views. Additionally, all radial spokes make equal contributions to the image, so motion on just one or a few radial views is not likely to severely degrade image quality. Obviously, radial methods generate data points that do not fall into a rectangular matrix. To efficiently process such non-uniformly acquired data, these points must be either interpolated into a Cartesian grid, or procedures of projection-reconstruction such as in X-Computerized Tomography can be used.

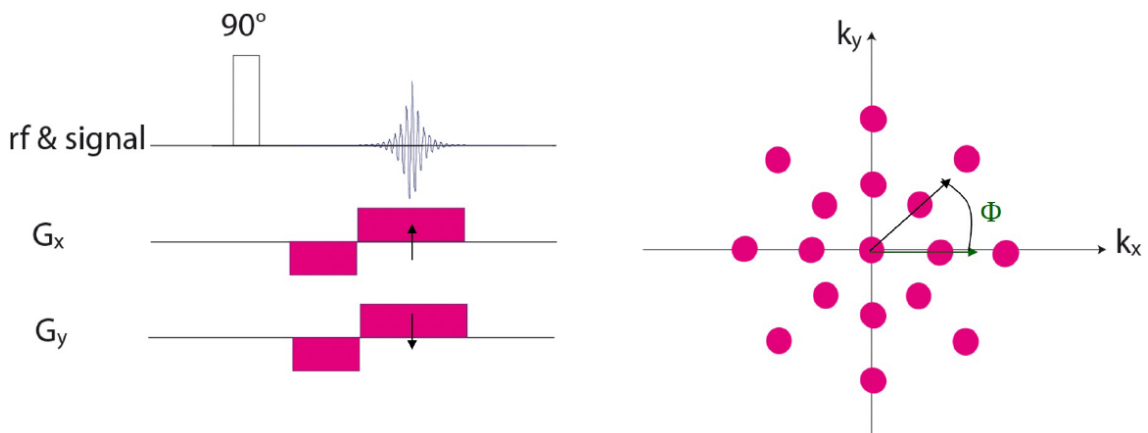


**Figure 5.3:** Simplified scheme of a standard 2D radial imaging experiment.

Among these methods, those employing short or null echo time (TE) have a particular interest for the study of very short  $T_2$  samples. While in UTE (Ultrashort TE) sequence [46], the acquisition starts in the presence of gradients just after the excitation pulse, for ZTE (Zero TE) [47] the pulses are simultaneous to the gradients (see Fig. 5.4). This is only possible with modern electronics in the imager: (i) the pulse has to have sufficient broadband to cover the whole spectral range in the presence of gradients that can be strong; (ii) the dead time  $\tau_d$  between the pulse and the opening of the receiver has to be small (otherwise too many central points of the  $k$  space are going to be missing). Other trajectories are also possible, such as spiral imaging, but this falls outside the scope of this thesis.

## 5.3 MRI Contrast and Artifacts

### 5.3.1 Contrast

An important notion in MRI is also the contrast. It obviously depends on the sample, but also on the type of MRI sequence used as well as of the choice of some acquisition parameters by the operator. In the case of a gradient echo experiment (see Fig. 5.2), the detectable

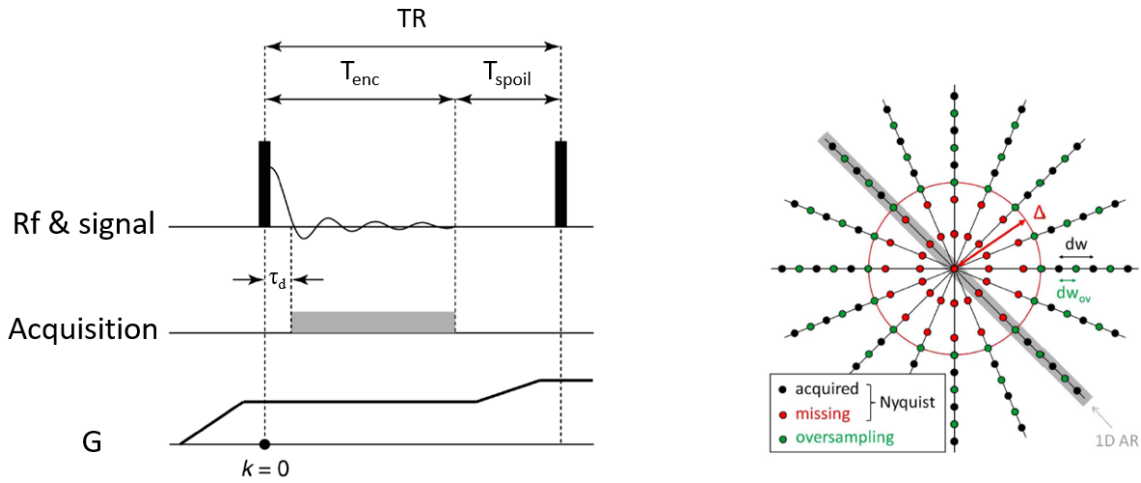


**Figure 5.4:** Simplified scheme of the ZTE sequence. TR: repetition time;  $T_{enc}$ : encoding time;  $T_{spoil}$ : time for spoil gradient;  $\tau_d$ : dead time. Adapted from [48], Copyright © 2012 John Wiley & Sons, Ltd. All rights reserved.

magnetization obeys:

$$M_{xy}(TR, TE) = M_0 \left(1 - e^{-\frac{TR}{T_1}}\right) e^{-\frac{TE}{T_2^*}} \quad (5.11)$$

While for a spin echo experiment,  $T_2^*$  has to be replaced by  $T_2$  due to the cancellation of the field inhomogeneity effects. Thus, for two different sample regions that one wants to distinguish, the contrast can be either a density contrast (through the  $M_0$  term, for what short TE and long TR are chosen) a  $T_1$  contrast (in this case TE and TR will be chosen short) or also a  $T_2$  contrast (emphasized by choosing TE and TR long).

Employing these principles, in order to measure  $T_1$  and  $T_2$  with the same pulse sequence, it is possible to apply the RARE sequence with Variable Repetition Time (RAREVTR), which generates multiple spin echoes using a Carr-Purcell-Meiboom-Gill (CPMG) echo train [49] with slice selective RF pulses. Each echo is separately phase encoded, and the phase encoding is incremented within one echo train to accelerate the acquisition. It is possible to obtain two or more echo-images with different effective TE values. Multiple acquisitions may be made with TR varied for  $T_1$  measurement through saturation recovery.

### 5.3.2 Artifacts

Due to the low intensity of the recorded MRI signals, any disturbance in them could become problematic. It is thus necessary for the operator to be able to identify the sources of artifacts and how to remedy them. The following effects are among the most important MRI artifacts:

**Table 5.1:** Summary of the most important causes and potential solutions of MRI artifacts. Own elaboration.

Nature	Expression	Remedy
<b>Motion artifact</b>	Ghosting in the phase-encoding direction if the patient or object explored moves during scan	Switch phase and frequency directions; fast imaging; radial sampling
<b>Gibbs (or truncation) artifact</b>	Series of lines parallel to regions where there are abrupt intensity changes	Increase the matrix size ( $SW$ for read, $N_p$ for phase); smoothing filters; fat suppression
<b>Aliasing (or wrap-around) artifact</b>	A part of the object beyond the edge of the $FOV$ projected onto the image due to a non-compliance with the sampling conditions	Enlarge the $FOV$ ; Outer Volume Suppression surface coils; anti-aliasing software switch phase and frequency directions
<b>Zipper (or RF noise) artifact</b>	Spurious bands of electronic noise across the frequency-encoding direction related to a RF shielding failure	Check if the scanner room-door is shut and if the cables are shielded
<b>Chemical shift artifact</b>	Spatial misregistration in the frequency-encoding direction due to two abundant nuclei with different resonance frequencies	Increase $G_r$ , $SW$ ; decrease $B_0$ , $FOV_r$ $r_1 - r_2 = \frac{\nu_1 - \nu_2}{\gamma G_r} = \frac{(\nu_1 - \nu_2) FOV_r}{SW} \quad (5.12)$
<b>Magnetic susceptibility artifact</b>	Distortions due to local $B_0$ inhomogeneities (read dimension)	Spin echo sequences; Pure-phase Imaging

## 6 - Localized Spectroscopy

Hereafter, Single-Voxel Spectroscopy (SVS) and multi-voxel Chemical Shift Imaging (CSI) are introduced. SVS sequences provide high-resolution spectra from a single well-defined region inside a given sample, while CSI sequences cover multiple volumes of interest (VOI) via phase-encoding gradients in combination with a signal generation method.

### 6.1 Single-Voxel Spectroscopy

SVS techniques are the most commonly used because they are straightforward and provide high signal-to-noise ratio (SNR) in short time experiments. Commonly, coil arrangements are either a surface receiver/transmitter coil that offers high transmit efficiency and sensitivity over a very restricted region of interest, or a volume transmit coil coupled with a surface receive coil to provide homogeneous excitation and high SNR respectively. The first step is to identify a VOI from previously recorded NMR images (pilot images). Then, a combination of frequency-selective pulses simultaneous to magnetic field gradients (following the principle of the already described slice selection) defines the position, size and orientation of a volumetric pixel (*voxel*). By way of example, a selective  $90^\circ$  pulse could be utilized to generate transverse magnetization or to convert transverse magnetization to longitudinal one, whilst  $180^\circ$  ones must be added either to invert longitudinal magnetization or to refocus transverse magnetization (spin echoes). In case of an imperfect flip angle, the generated spurious signals can be canceled out using phase cycling [16] along with spoil/crusher gradients [38].

On the other hand, paramagnetic species in the vicinity of the VOI, such as oxygen at the tissue-air interface, have an impact on the local  $B_0$  field homogeneity affecting the signal linewidth. These nonlinear  $B_0$  inhomogeneities are significant at increased field strengths and can be compensated by static field shimming over the selected region (so-called local shim) once a  $B_0$  distribution mapping is performed. A high-order shim coil system becomes therefore indispensable to linewidth improvement, that determines spectral resolution, signal-to-noise ratio and, consequently, the precision and accuracy of molecule quantification.

Some size limitations have been found in our systems with regard to the voxel definition:

- If the VOI is too small for a desired flip angle and a given maximal gradient strength, a rather long pulse length will be tailored exciting a limited spectral region [Eq. 5.3]. Such a pulse leads to low SNR due to transverse relaxation during its execution. One alternative solution would be to use stronger gradients, which is risky for the hardware. Most of the softwares (*e.g.* ParaVision) include a minimal voxel size to avoid hardware damage. Consider also that the NMR signal increases with the number of spins in the VOI, which obviously depends on its size.

- Conversely, if one dimension of the voxel is too big, the pulse must be completed in a very short time because the software avoids to reduce too much the gradient strength in order to avoid potential chemical shift artefacts. Thus the  $B_1$  peak power can be a limitation [Eq. 3.4] and if the desired flip angle is not achieved this can become problematic for sequences such as PRESS (see below).

SVS methods can be broadly classified into echo formation based on alternate radio-frequency pulses and/or gradients.

### 6.1.1 Localization based on Alternate RF Pulses

Developed in the mid-1980s, the ISIS (Image-Selected In vivo Spectroscopy) method [50] is based on volume selection by post-acquisition combination of NMR signals. The FID signals from a set of eight RF-pulse cycles are added and subtracted in a specific way (see Table 6.1) that cancels out unwanted signals from outside the target volume, thus defining the 3D selection. As shown in Figure 6.1, each acquisition consists of a preparation period, a suitable waiting stabilization delay and a non-selective  $90^\circ$ -pulse before signal acquisition. During the preparation period, the longitudinal magnetization is shaped by applying different combinations of  $180^\circ$  inversion pulses in the presence of slice-selective gradients. The pre-acquisition delay (DE) between the selective pulses and the read out one must be a trade-off between minimal eddy current losses and maximal signal intensity. The recorded FIDs are processed in order to obtain optimal SNR performance from the selected VOI.

**Table 6.1:** Add-subtract scheme of the selective pulses application during the ISIS sequence preparation period.

Experiment number	X-selective pulse	Y-selective pulse	Z-selective pulse	Receiver phase
1	OFF	OFF	OFF	$0^\circ$
2	OFF	OFF	ON	$180^\circ$
3	OFF	ON	OFF	$180^\circ$
4	ON	OFF	OFF	$180^\circ$
5	OFF	ON	ON	$0^\circ$
6	ON	OFF	ON	$0^\circ$
7	ON	ON	OFF	$0^\circ$
8	ON	ON	ON	$180^\circ$

The advantage of this method is the absence of any  $T_2$  weighting and J-evolution since the magnetization remains in the transversal plan only for the signal acquisition period, enabling thus for instance the analysis of metabolites of interest in  $^{31}\text{P}$  and  $^{15}\text{N}$  spectroscopy with short  $T_2$  values. Being based on a subtraction of FIDs or spectra, ISIS is more subject to imperfections. This subtraction-derived noise can be minimized by adding saturation of the outer volume bands in a sequence called OSIRIS (Outer volume Suppressed Image Related In vivo Spectroscopy) [51].

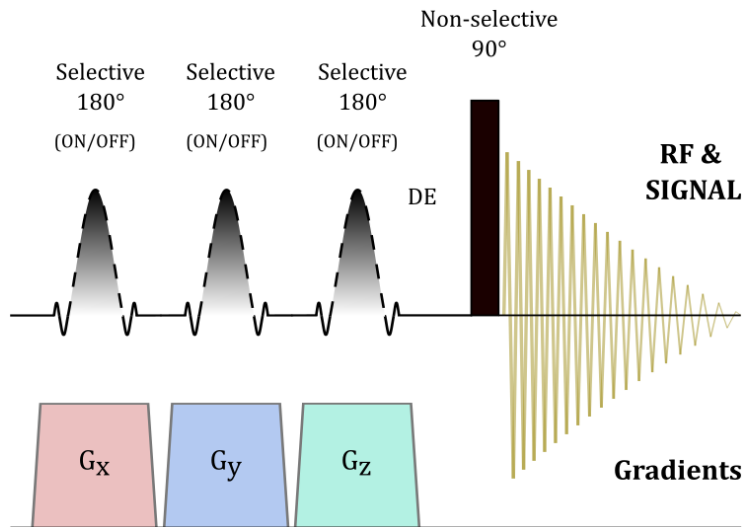


Figure 6.1: Simplified scheme of the ISIS sequence. DE: pre-acquisition delay.

## 6.1.2 Localization based on Echo Formation

Echo methods achieve the localization in one scan by refocusing only the spins that underwent all the excitation pulses, while the rest of spins in the surroundings of the VOI are either not excited or dephased. At present, PRESS (Point RESolved Spectroscopy) and STEAM (STimulated Echo Acquisition Mode) are the most widespread echo methods, exploiting Carr-Purcell and stimulated echoes, respectively.

### Point RESolved Spectroscopy

This double spin-echo sequence developed in 1984 [52] is built on three orthogonal slice selections (see Figure 6.2). An initial soft  $90^\circ$  RF pulse in the presence of a field gradient ( $G_x$ ) generates transverse magnetization for spins in a given  $x$  slice. After a delay of  $\frac{TE}{4}$ , a soft  $180^\circ$  refocusing pulse is applied simultaneously to a  $G_y$  gradient in order to invert the spin population in the selected orthogonal slice. After a delay  $\frac{TE}{2}$ , a final  $180^\circ$ -pulse in combination with a gradient along the remaining orthogonal direction inverts the spin population along a  $z$  slice. Finally, the selected voxel corresponds to the intersection of the three slices.

The real values of the pulse flip angles is often deviated from the nominal ones as a result of  $B_1$  spatial inhomogeneities, causing a continuum of angles at the voxel edges, from zero to a maximum value located in its center. Therefore, spoil gradients and phase cycling are employed to dephase all unwanted coherences from both outside and inside the voxel and get rid of spurious signals owing to RF pulses imperfections. On the other hand, a BASING (BAND Selective Inversion with gradient dephasing) module [53] can be placed between the two inversion pulses of PRESS to invert water, lipid (or both) spins.

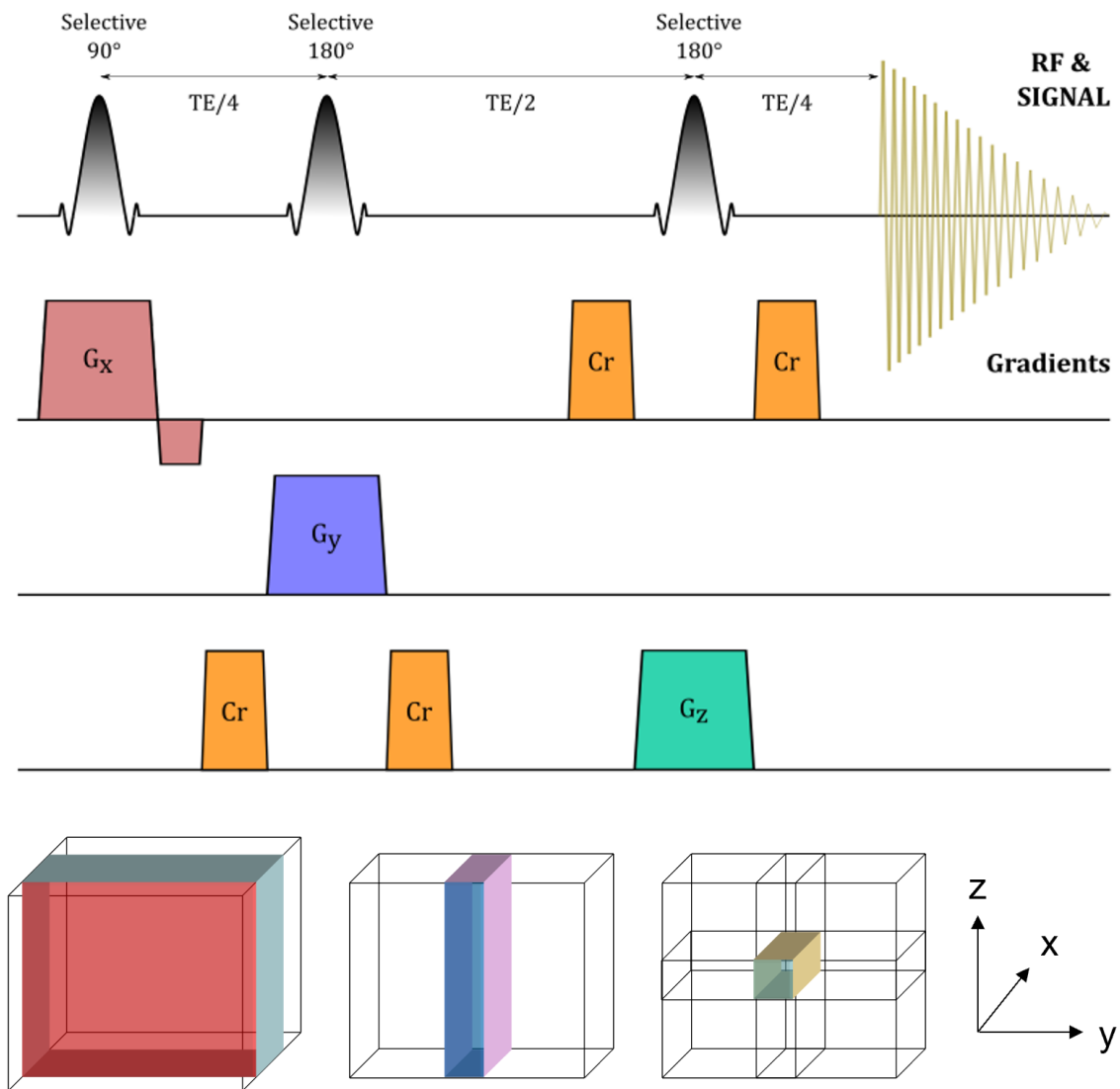


**Figure 6.2:** Simplified scheme of the PRESS sequence. TE: echo time; Cr: crusher gradients.

### STimulated Echo Acquisition Mode

This stimulated echo method was first proposed in 1986 [54] and consists of three 90°-pulses in combination with magnetic field gradients along orthogonal directions (see Figure 6.3). During the mixing time (TM), usually of few milliseconds, the spins experience  $T_1$  relaxation, higher than transverse relaxation. The echo time (TE) is optimized to ensure a magnetization vector where all the spins are in the same phase, at the same time as it is reduced rearranging the rephasing lobes and crusher gradients.



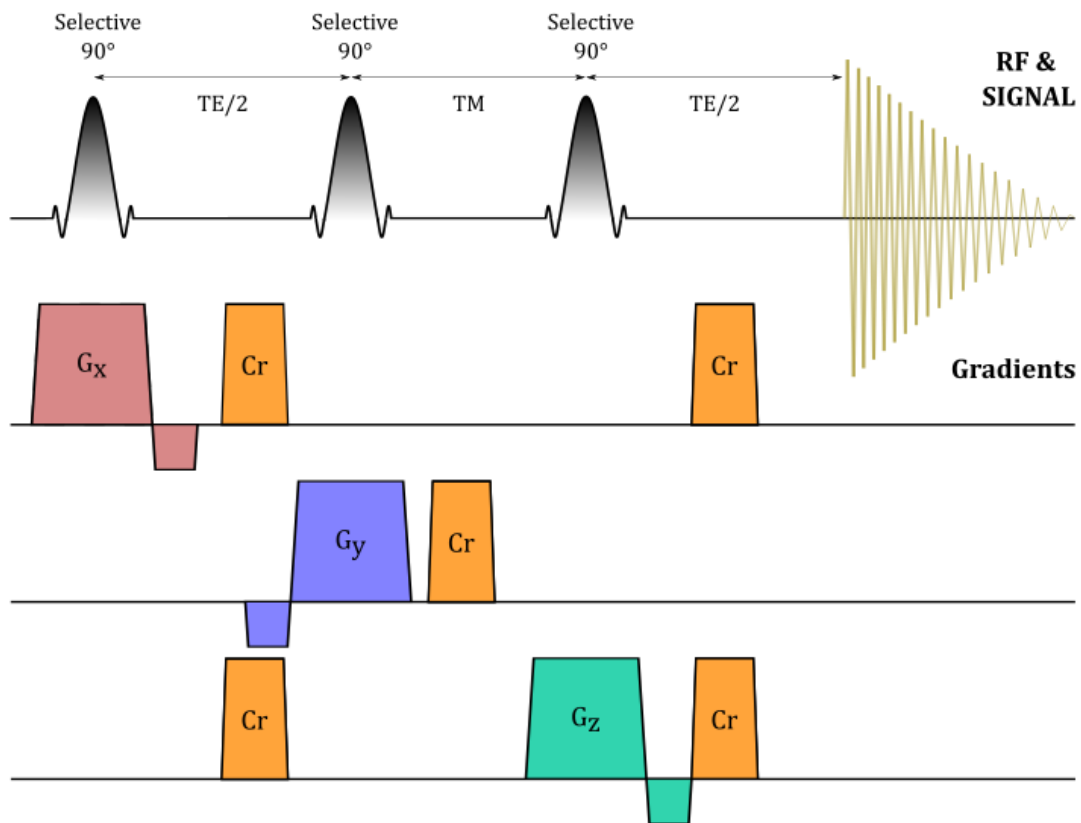


**Figure 6.3:** Simplified scheme of the STEAM sequence. TE: echo time; TM: mixing time; Cr: crusher gradients.

### Comparison between PRESS and STEAM

Both stimulated and spin echo methods have been compared for the purpose of elucidating each of which is to be performed. The first difference lies in the fact that PRESS is a Hahn echo method (where the spins are subjected to transverse relaxation during its execution) while STEAM is a stimulated echo method (with longitudinal relaxation occurring during TM). Accordingly, STEAM is preferred for fast-relaxing nuclei analysis. On the other hand, STEAM is less sensitive than PRESS to flip angle misadjustments and at the same time, 90° pulses allow increased *BW* at a given RF power, minimizing chemical shift artifacts [Eq. 5.12]. It is implementable in small-bore and whole-body systems since the applied RF loads and, consequently, the specific absorption rate (SAR) are low. Finally, STEAM allows the insertion of superior water suppression (WS) pulses during the TM, which can be lengthened as spins are only subjected to longitudinal relaxation.

On the other hand, the signal intensity in PRESS sequence is about twice that of STEAM (50% dephased in TM) and it is best suited to <sup>1</sup>H spectroscopy, as the spin-echo delays can be tailored to reach a compromise solution between fat or water suppression and SNR. Table 6.2 offers an in-depth comparison of both echo highly effective localization methods.

**Table 6.2:** Comparison of the main sequences based on direct excitation of the spins. Own elaboration.[55-57]

SVS sequence	RF pulses	Echo technique	Echo time	Mixing time	Water suppression	Displacement effects
<b>STEAM</b>	90° provide better voxel definition + small SAR	STE ( $\geq 3$ RF-pulses); signal $T_1+T_2$ weighted	$\downarrow TE$ ( $\geq 9$ ms) maximizes signal for $\downarrow T_2$ and for homonuclear effects	WS or crushers; minimize to avoid $\phi$ dephasing	Potentially optimized during $TM$	Diffusion and motion sensitivity for long $TM$
<b>PRESS</b>	180° require more power + chem. shift artif. + $B_1$ inhomog.	Double SE (1+2 RF-pulses); signal $T_1$ weighted and J-modulated	$\uparrow TE$ ( $\geq 15$ ms) offers a gain in $SNR \geq 2$ at the same conditions	-	Improvement by including a BASING module	Barely sensitive to diffusion and motion

## 6.2 Multi-voxel Chemical Shift Imaging

Multi-voxel CSI, also called multivoxel spectroscopy and latterly MR Spectroscopic Imaging (MRSI), refers to a family of methods developed in the 1980s [58] after the formulation of Fourier transform MRI. MRSI employs phase-encoding for spatial localization to collect spectra from a one-, two- or three-dimensional array of voxels. The multi-voxel sequences utilizes mapping techniques drawn from conventional MRI but usually avoiding frequency-encoding, therefore the resultant MR signal merely depends on the referenced chemical shift.

### 6.2.1 Conventional CSI Techniques

The sequence of standard 3D CSI [59] is depicted in Fig. 6.4. It consists of a phase-encoding method where the whole FID is kept. A non-selective RF-pulse excites the whole sample before the action of three phase-encoding gradients. The spatial resolution along each phase-encoded dimension is determined by the number of gradient steps, while the spectral resolution is dependent on the number of points of the FID.

MRSI can operate in combination with any type of excitation and signal generation sequences. The most common modification is based on spatially selective RF-pulses and gradients similar to ISIS, STEAM or PRESS (see Fig. 6.5) in combination with phase-encoding along two axes. The slice-selective pulses define the VOI and avoid the excitation of outer signals, allowing good field homogeneity and limiting the phase-encoding steps. Conventional CSI methods are time-intensive, with pulse sequence lengths for each slice in the order of 0.5-1.5 s. Minimizing the  $FOV$  is a valid option to reduce the scan time while maintaining the desired spatial resolution. Moreover, a highly-effective strategy is to speed data acquisition drawing on the wealth of fast MR imaging.[60]

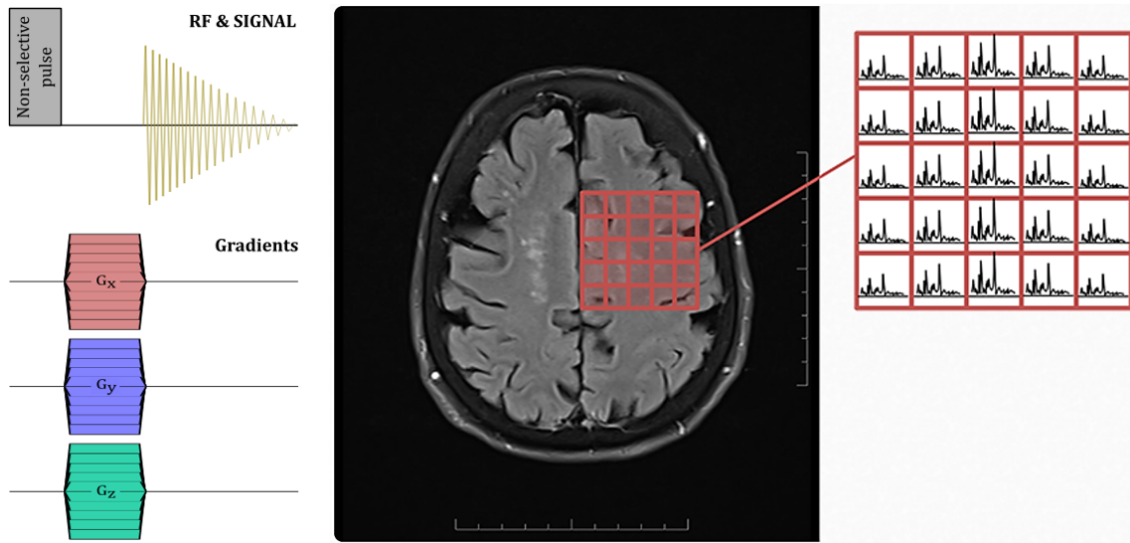


**Figure 6.4:** Simplified scheme of a 3D CSI sequence using a non-selective RF-pulse and three phase-encoding gradients.

## 6.3 Comparison of SVS and CSI Techniques

It is essential to highlight the nature of the study in order to make the right choice between SVS and CSI methods. For instance, human scanners have strict limits regarding the RF pulses (number, power and duration) and field gradients (amplitude and rise time) in comparison to animal or lifeless systems such as batteries.

From an operational point of view, single-voxel techniques are the most straightforward, quick and widely used, whereas multi-voxel have longer set-up and scanning times. Regarding the signal-to-noise ratio, the number of averages in SVS is equivalent to that of CSI phase-encoding steps. Nonetheless, SVS provide high SNR in a relatively short scan time, while CSI has lower SNR and individual spectral quality. Moreover, putting aside imperfect pulse profiles, the comparison is limited by MRSI voxel 'bleeding' phenomenon insofar as multi-voxels are affected by spectral contamination from adjacent ones and single-voxels are generally well-defined. Furthermore, small single voxel regions enable excellent local shimming and therefore high-quality spectra relatively free from contamination, whilst it is not obvious to obtain an homogeneous shim over the whole MRSI area in the presence of susceptibility inhomogeneities.

On the other hand, CSI techniques cover bigger regions with higher spatial resolution and do not require prior knowledge of the region of interest. It is also noteworthy that phase-encoding gradients are free from spatial offsets due to chemical shift artifacts and that the truncation artifacts and quantization problems can be minimized by a weighting k-space function. The smaller size of MRSI individual voxels permit the study of tiny, irregularly shaped structures. To sum up, multi-voxel sequences are preferred when spatial distribution is necessary and when the number of scans in single-voxel ones is comparable to the phase-encoding steps for the same

SNR. On the contrary, SVS techniques are preferable if a small number of averages provides an acceptable SNR and if metabolites quantification is necessary. In fact, a combination of methods can be advantageous, as shown in Figure 6.5.

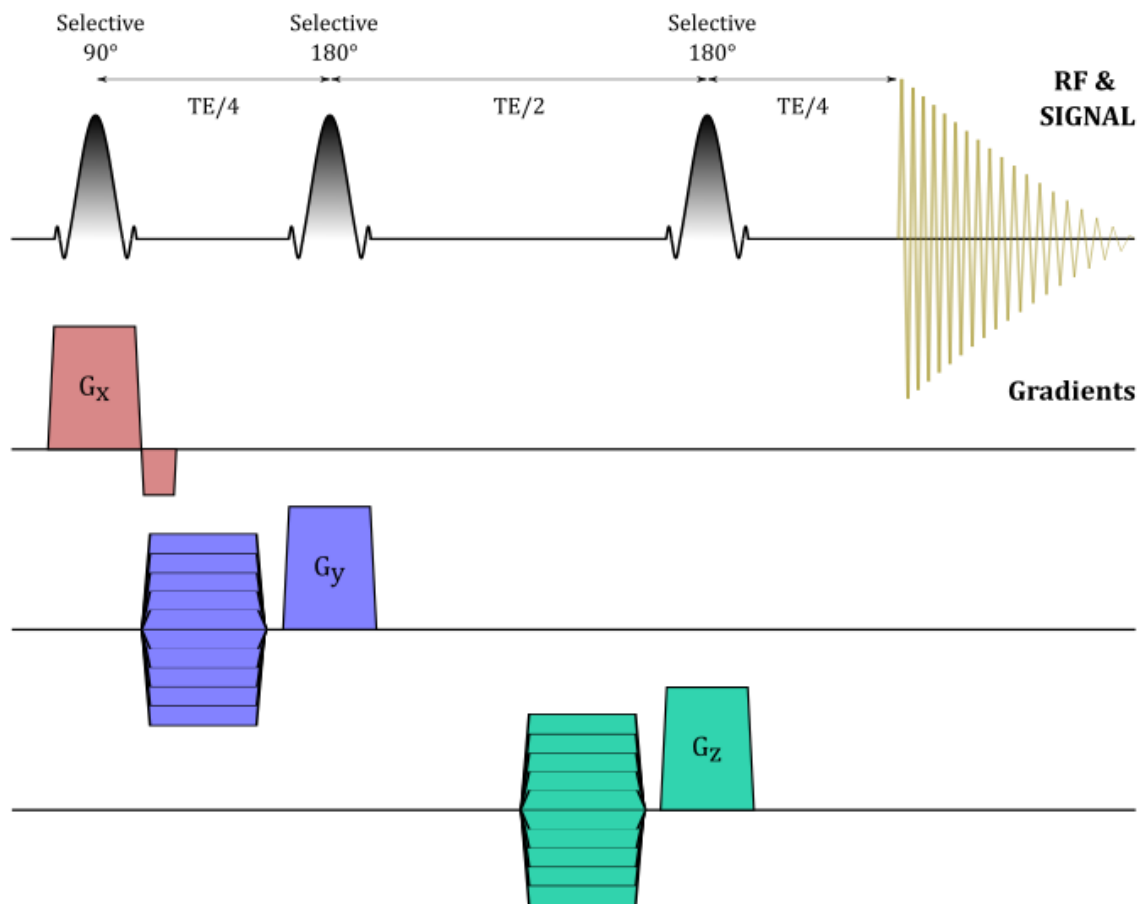


**Figure 6.5:** Simplified scheme of a 2D PRESS-CSI sequence using three slice-selective RF-pulses with stepped phase-encoding gradients along two axes.



## **Part III**

# **Insights into Redox Flow Batteries**

# 7 - Introduction to Electrochemistry

## 7.1 Primary Concepts

### 7.1.1 Electrochemical Systems

Electrochemistry is a physical chemistry branch that entails the study of electron transfer between an electrochemical and a chemical species. At its most basic, an electrochemical cell consists of two electron conductors (electrodes) separated by an ionic conductor (electrolyte) and linked by an external conductive pathway. Thus, a potential difference between the electrodes (voltage) can be applied to modulate the energy of the electrons from their interaction with atomic nuclei. The electrochemical cells are either composed of two or three electrodes systems:

- A three-electrode setup is composed of a working electrode (WE), a counter electrode (CE) and a reference electrode (RE). The process of interest is the half redox reaction at the WE, which works as an electron donor or acceptor to the analyte with the suitable potential in the electrolyte. An inert CE balances the current observed at the WE, thus avoiding current passing through the RE. Therefore, the current flows between the WE and CE and the RE is used to accurately measure the applied potential relative to a stable reference reaction. The use of three electrode systems is highly recommended for accurate analytical purposes (electrochemical analytical cells).
- A two-electrode system includes a working electrode and a counter/reference electrode to measure the potential across the complete cell. A consistent current flows in the external circuit from the anode, where oxidation takes place, to the cathode, where reduction occurs.

The invention of the voltaic cell (*Alessandro Volta, 1800*) was a breakthrough in electrochemistry and is considered the forerunner of present-day galvanic cells, where a spontaneous reaction occurs converting the chemical energy into electrical energy. Conversely, electrolytic cells (*Michael Faraday, 1830*) require an external electron source like a direct electrical current (DC) potentiostat or an alternative current (AC) generator to drive non-spontaneous reactions. A primary cell (pile) is a non-rechargeable device that produces DC through a single spontaneous reaction, while a secondary one can have its chemical reaction reversed and be reused multiple times. For these rechargeable cells, during discharge (galvanic cell reaction) the reduction takes place at the positive highest potential electrode  $E(+)$ , whereas during charge (electrolysis cell reaction) the polarity is reversed and it is the oxidation reaction which happens at the positive terminal (see Figure 7.1). Properly speaking, two or more electrochemical cells connected in series or parallel make up a battery, although these two terms are used here interchangeably.

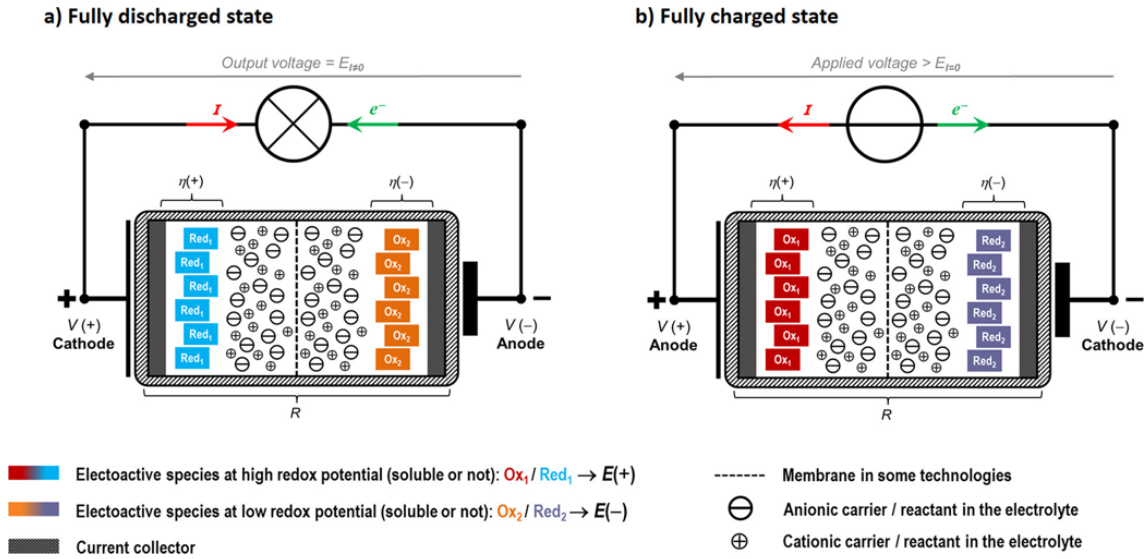


**Figure 7.1:** General architecture of an electrochemical cell (a) under discharge at 100% depth-of-discharge (DoD) and (b) under charge at 100% state-of-charge (SoC). Reprinted with permission from [12]. Copyright 2020 American Chemical Society.

## 7.1.2 Basic Thermodynamics and Kinetics

Each electron conductor has an internal potential that depends on its Fermi level, defined as the thermodynamic work required to add one electron to its structure. In a typical electrochemical cell, the electrolyte solutions have a large distribution of charge (ions, dipoles) that will interact electrostatically together creating an average internal potential. When an electrode is dipped in an electrolyte (heterogeneous electron transfer), there is a momentary interface potential until charges in both sides redistribute to get a continuous potential variation. At this stage, the formation of a space-charge layer so-called electrical double layer (DL) occurs, which is defined by a large interfacial voltage and capacity behavior using the Helmholtz, Gouy-Chapman or Stern models [61].

By driving a considered WE to a potential over a critical cell voltage value, the electrons reach an energy level high enough to transfer from electrode into vacant electronic states on species in the electrolyte (reduction current). Analogously, at a sufficiently low potential the electrons flow from the solution occupied molecular orbitals to the electrode unoccupied one (oxidation current) [62]. The number of electrons  $n$  that cross the conductor-solution interface is measured in terms of the total charge  $Q$ , expressed in coulombs ( $1\text{ C} \ll 1\text{ A}\cdot\text{s} \ll 6.24\cdot 10^{18}\text{ e}^-$ ). The Faraday's law states the relationship between charge and moles of product electrolyzed/formed ( $N$ ):

$$Q = nFN \quad (7.1)$$

Here  $F$  is the Faraday constant ( $96485.4\text{ C}\cdot\text{mol}^{-1}$ ). For the electrical description across the interface there are two possible cases:

- Faradaic or charge-transfer processes: the transfer of charges in an electrochemical re-



action between the electrode and the electrolyte is governed by Faraday's law. It states that the reaction kinetic becomes so fast that the oxidized and reduced electroactive species cannot coexist at the electrode surface.

- Nonfaradaic or capacitive processes: charge-transfer reactions are thermodynamically or kinetically unfavorable. Adsorption or desorption processes can occur at the electrode–electrolyte interface generating transient external currents.

Mass transfer in solution occurs by diffusion, migration and convection. The first is the movement of charged species down a concentration gradient because of chemical changes in the electrode surface. Migration results from a gradient in electrochemical potential due to an externally applied electric field, therefore negative ions are attracted to positive electrodes and vice versa. Finally, convection movement arises from a velocity gradient due to an imbalance of mechanical forces (*e.g.* stirring or vibrations). The current in the vicinity of an active electrode can be separated into diffusion and migration contributions. It is possible to restrict mass transfer to the diffusive mode near the electrode by using a so-called supporting electrolyte. Its (electro)chemically inert ions migrate to balance the charge as electron transfers occur and complete the electrical circuit. The use of large dissolved salts concentrations not only limits analyte migration but also increase solution conductivity.

In the case of a complete electrochemical cell, the potential difference between electrodes with antagonist redox couples is determined by the Gibbs free energy change between reactants and products ( $\Delta G$ ), which is defined as the maximum net work obtainable from the cell. In the Nernst-diffusion layer model [63], the concentrations of the reduced and oxidized species are uniform and constant in the bulk solution, while concentration gradients occur on the electrode surface. Furthermore, all actual processes take place at finite rates and therefore cannot proceed with strict thermodynamic reversibility. Nonetheless, they can be termed as practically reversible as they can be described accurately enough by thermodynamic equations. For the diffusion-controlled systems where the electrode reaction is reversible, the Nernst equation relates the cell potential ( $E$ ) to the standard one ( $E^0$ ) and the chemical activities of the oxidized and reduced analyte forms (frequently replaced by the experimentally accessible concentrations):

$$E = E^0 + \frac{RT}{nF} \ln \frac{c_{ox}}{c_{red}} = -\frac{\Delta G}{nF} \quad (7.2)$$

Here  $R$  the Universal Gas Constant ( $8.314 \text{ J}\cdot\text{mol}^{-1}\cdot\text{K}^{-1}$ ),  $T$  the temperature of the system (in K) and  $c_{ox}$  and  $c_{red}$  the molar concentration (in  $\text{mol}\cdot\text{cm}^{-3}$ ) of oxidized and reduced species, respectively.

However, the operating voltage value ( $E_{i \neq 0}$ ) is subject to deviations from equilibrium due to ohmic and polarization losses when a current  $i$  flows through the cell:

$$E_{i \neq 0} = E \pm (iR + \eta) = E \pm \left( i \frac{l}{\rho A} + \eta \right) \quad (7.3)$$

The ohmic drop ( $iR$ ) often refers to the overall internal resistance (electrolyte, electrodes and connectors) and can be minimized by reducing the distance between electrodes ( $l$ ) and raising

the electrode surface area ( $S$ ) and the solution specific conductance ( $\rho$ ). The overpotentials or polarization losses ( $\eta$ ) can be categorized as the sum of activation and concentration losses. The activation polarization takes into account kinetic retarding factors, such as undesired side reactions or the work function to overcome at the electrode-electrolyte interface, while the concentration polarization refers to the mass transfer resistance (defined earlier).

## 7.2 Overview of Electrochemical Methods

Electrochemical processes relied exclusively on the application of a constant current (galvanostatic conditions) until the apparition of the potentiostat in 1942. This Hicking invention operates with two different setups based on the use of an operational amplifier that boosts the input voltage signal by an order of magnitude without leak of current. Taking as reference a three-electrode system, in the potentiostatic setup the applied potential is controlled by a voltage follower in the RE and the DC response is monitored by a current follower in the WE. The internal circuit is defined as a high-impedance voltage controller loop that links the input (RE) to the output (WE-CE pair). Potential techniques, such as chronoamperometry (CA) and cyclic voltammetry (CV), are mainly used to study kinetics and thermodynamics of electron transfer reactions. As regards the galvanostatic setup, a current is imposed through the WE-CE interface (current follower) and the potential difference between the WE and the RE is measured (voltage follower). Galvanic techniques represent a practical way to study electrode materials and assess the response of EES devices during charge-discharge measurements (so-called cycling). On the other hand, Electrochemical Impedance Spectroscopy (EIS) enables decoupling the different contributions to the global resistance of a battery (out of scope).

### 7.2.1 Open Circuit Potential

Open circuit potential (OCP) is a passive method also known as open circuit voltage or zero-current potential. The potential difference between the WE and CE is measured by placing a very high impedance resistor in its path or by disconnecting the CE. A constant value over long periods of time (*i.e.*  $\leq 5$  mV for several minutes) indicates that the electrode potential is stable enough to withstand a perturbation-based experiment, either because of kinetically slow electron transfer or a thermodynamically stable system. Under ideal conditions, the ratio of the oxidized and reduced species can be determined by measuring the OCP [Eq. 7.2].

### 7.2.2 Potential Techniques

## Basic Potential Step Methods

In basic potential step techniques, the current is recorded as a function of a constant or varied in a pre-established manner potential. Chronoamperometry is a step method in which a potential is applied to the WE and the current is monitored over time. Two phenomena could be at the origin of the measured current:

- A capacitive behaviour of the electrode (nonfaradaic process). The current charge or discharge the electrode's capacity until it reaches the new potential. Its initial value could be high due to the potential step but drops very quickly (*e.g.* few seconds).
- A charge transfer at the electrode surface (faradaic process) due to a mismatch between the imposed potential and that of redox couples in solution. The faradaic current ( $i(t)$ ) is in a general way lower but decays very slowly over time [Eq. 7.4].

In the event that the potential step is high enough to reach very fast electron transfer kinetics in diffusion-limited reactions, it is possible to obtain easily the diffusion coefficient of the electroactive species in solution (Cottrell equation):

$$i(t) = nFAc_0\sqrt{\frac{D}{\pi t}} \quad (7.4)$$

Here  $A$  is the area of a planar WE (in  $\text{m}^2$ ),  $D$  the diffusion coefficient (in  $\text{m}^2\cdot\text{s}^{-1}$ ) and  $c_0$  the initial concentration of the electroactive starting species (in  $\text{mol}\cdot\text{m}^{-3}$ ). The concentration of electrolyzed species decreases with distance from electrode.

Other step experiments include sampled-current voltammetry, where the current is sampled at some fixed time with increasing potential steps, and double potential step chronoamperometry (DPSCA), reversal technique analogous to CA with consecutive transitions between potentials.

## Potential Sweep Methods

In potential sweep techniques, the potential is varied linearly with time and the current is monitored. In linear potential sweep chronoamperometry, also known as linear sweep voltammetry (LSV), the potential is varied between two preset values. The technique is referred as cyclic voltammetry if the scan is reversed at the vertex potential, which a powerful method that can provide both qualitative and quantitative information.

In most electrochemical systems, it is possible to establish three differentiated regions governed by faradaic processes (see Figure 7.2a):

- Electron transfer region: current intensity is usually low and exponentially increases when the applied voltage approaches the operating value. Electron transfer is limited by the kinetics of the reaction (not by transport properties) and governed by the Tafel law, where  $\alpha$  is the charge transfer coefficient (between 0 and 1):

$$\ln\left(\frac{i}{i_0}\right) \cong \frac{\alpha n F \eta}{RT} \quad (7.5)$$

- Electron transfer and diffusion region: the concentration gradient leads to an increased flux of mass transfer to the surface of the electrode. Then the mass transfer reaches its maximum and the concentration of the oxidized (if cathodic current  $i_c$ ) or reduced (anodic  $i_a$ ) species becomes nearly zero at the surface of the electrode (peak).
- Diffusion region: the current decreases after the peak and reaches a plateau, which corresponds to stationary conditions limited by diffusion [Eq. 7.4]. This region is not appreciable for rotating disk electrodes (forced convection) or other spatially well-distributed systems since they are not diffusion-controlled systems.

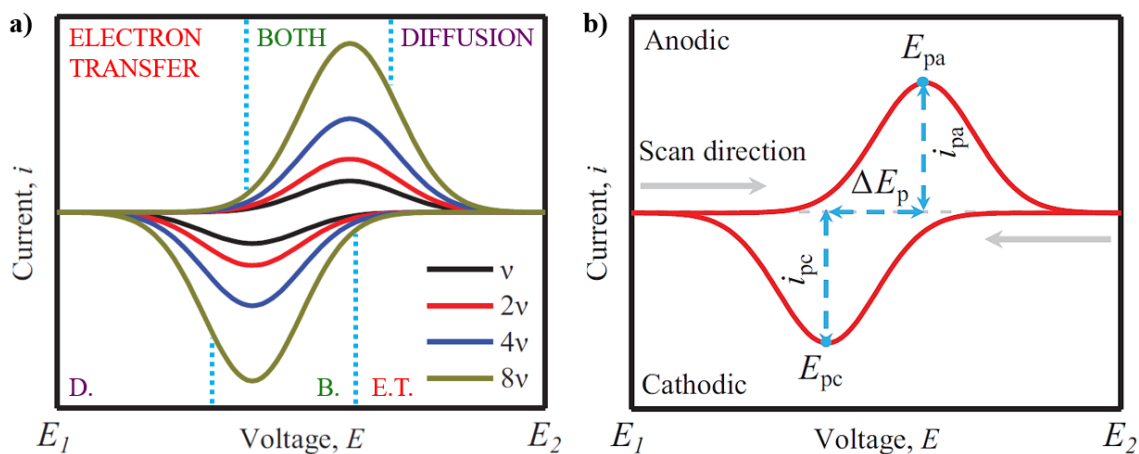


**Figure 7.2:** Standard cyclic voltammetry method. (a) Regions profile at different scan rates; (b) Typical anodic and cathodic current response versus voltage. Adapted from [64], Copyright © 2019 WILEY-VCH Verlag GmbH & Co. KGaA, Weinheim. All rights reserved.

A typical current response for a single electrode reaction is a 'duck shape curve', from which the anodic and cathodic peak voltages ( $E_{Pa}$  and  $E_{Pc}$ , respectively) are easily identified as shown in Figure 7.2b. The IUPAC convention is used to report CV data, where anodic currents correspond to positive values. The reversibility of the system can be evaluated according to the peak currents ratio ( $i_{Pa}/i_{Pc}$ ) and the difference of peak voltage in cathodic and anodic segments ( $\Delta E_p$ ). Ideally, the peak-to-peak separation for the reduction and oxidation waves is 59 mV for a one-electron electrochemically reversible process and 28.5 mV for a two-electron one. However, these values are higher in practical systems and the peak voltage shifts with scan rate ( $\nu$ ) due to increased polarization [Eq. 7.3].

The scan rate (expressed in  $V \cdot s^{-1}$ ) should be slow enough in order that the diffusion controls the process, ensuring practical thermodynamic reversibility. Likewise,  $\nu$  should be fast enough to prevent the diffusion of charge carriers from being the limiting step as well as to decrease the diffusion layer size maximizing current response, among other practical reasons. Matsuda and Ayabe [65] proposed a dimensionless parameter to determine the apparent reversibility of a

system according to the sweep rate and the kinetics of the redox reaction. A process is termed quasi-reversible (or electrochemically irreversible) when electron transfer at the electrode surface is slow compared to mass transport, thus  $\Delta E_P$  increases with  $\nu$  and necessitate greater applied potentials for appreciable current to flow.[66]

As for CA, the resulting current can be separated into capacitive and faradaic current:

$$i = k_1\nu + k_2\nu^{\frac{1}{2}} \quad (7.6)$$

- The capacitive current ( $k_1\nu$ ) is linked to the potential change of the electrode's capacity. As the potential is swept linearly, this term is constant during the whole process and makes the current differ from zero. This background current is not negligible for certain systems (*e.g.* batteries with large developed area) and can be removed by subtracting the CV of the blank.
- The faradaic current ( $k_2\nu^{\frac{1}{2}}$ ) occurs when the sweeping potential is close enough to the redox potential of an electroactive species in solution.

The peak height ( $i_P$ ) is described by the Randles-Ševčík equation for fast reversible systems:

$$i_P = 0.45nFAc\sqrt{\frac{nF\nu D}{RT}} \quad (7.7)$$

Therefore,  $D$  can be easily calculated in those cases where the current peak intensity is barely influenced by increased polarization.

### 7.2.3 Galvanic Techniques

In controlled-current techniques the potential is recorded with a data acquisition device (oscilloscope) as a function of time. In constant-current chronopotentiometry (CP), a steady current superior to the limited diffusion one is applied (Sand condition) causing the active species diffusion and electrolysis at the electrode surface. In the case liquid batteries, the concentrations change at a constant rate while the potential moves in a time-based Nernstian fashion, shown in Equations 7.8 and 7.9, to values characteristic of the redox couple. The time needed for reaching this potential is called the transition or Sand time ( $\tau$ ) and decreases with increasing current [Eq. 7.10].

$$E = E_{\frac{\tau}{4}} + \frac{RT}{nF} \cdot \ln\left(\frac{\tau^{\frac{1}{2}} - t^{\frac{1}{2}}}{t^{\frac{1}{2}}}\right) \quad (7.8)$$

$$E_{\frac{\tau}{4}} = E_0 - \frac{RT}{2nF} \cdot \ln\left(\frac{D_{ox}}{D_{red}}\right) \cong E_0 \quad (7.9)$$

$$\sqrt{\tau} = \frac{nFAc_0\sqrt{\pi D}}{2i} \quad (7.10)$$

Once the diffusion-limited concentration reaches zero, the potential changes to the redox value of the next species in solution (*e.g.* degradation products, impurities or solvent).

Furthermore, it is possible to apply a current that varies with time in a predetermined manner (programmed current CP) or that is reversed after a known time (current reversal CP). In an extension of the latter method, the current can be continuously reversed between two potential values corresponding to the oxidation and reduction reactions, respectively. This technique, so-called cyclic voltammetry or galvanostatic cycling with potential limitations (GCPL), records the time-resolved voltage evolution under a certain applied current (see Figure 7.3a) and can be followed by a potentiostatic step until the current reaches a stated value.

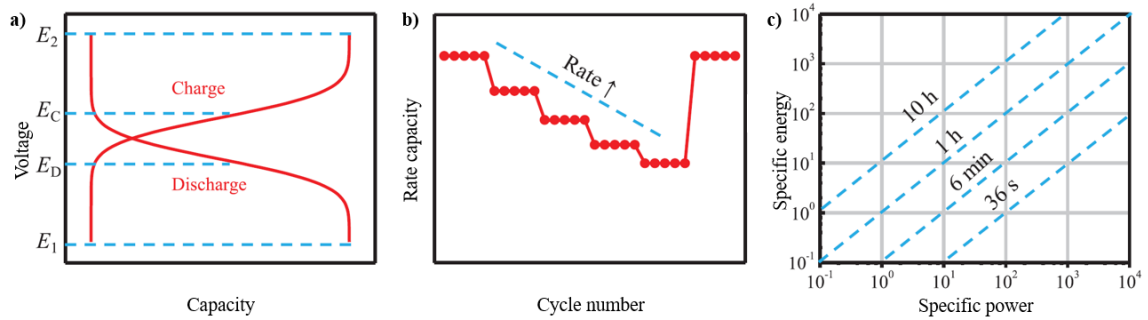


**Figure 7.3:** Standard galvanostatic cycling with potential limitations method. (a) Typical voltage response versus battery capacity; (b) Rate capability performance at different C-rates versus cycle number; (c) Ragone plot at different C-rates (dotted blue lines). Adapted from [64], Copyright © 2019 WILEY-VCH Verlag GmbH & Co. KGaA, Weinheim. All rights reserved.

## 7.2.4 Application for Batteries Characterization

Battery cycling can be performed in a potentiostatic (*i.e.* DPSCA) or a galvanostatic-potentiostatic (*i.e.* GCPL) way. In the latter method, the constant voltage phase enables accessing total available cell capacity, which is defined as the quantity of electric charge accumulated, stored and released in a reversible manner. Mathematically, it is described as follows:

$$Q_F = \int idt \quad (7.11)$$

$$Q_E = \int EdQ_F \quad (7.12)$$

$Q_F$  ( $Q$ ) is the faradaic capacity (expressed in A·s or coulombs) and  $Q_E$  the energy capacity (in W·s or J). During GCPL experiments the capacity is often expressed as a function of the C-rate (see Fig. 7.3b), which is a measure of the cycling rate (in mA) with regard to the battery maximum capacity (in mAh). Thus 1 C means a complete charge or discharge in one hour, whereas 0.1 C corresponds to ten hours.

High C-rate values involve high current densities ( $j$ ) that maximize battery polarization and therefore modify charge ( $E_{charge}$ ) and discharge ( $E_{discharge}$ ) voltages, since they result from adding or subtracting the above-mentioned operating cell losses respectively [Eq. 7.3]. Polarization curves ( $E_{discharge}$  vs  $j$ ) are a useful tool to identify practical capacity values in

moderate cycling times. Specific energy (in  $\text{W}\cdot\text{h}\cdot\text{kg}^{-1}$ ) and specific power (in  $\text{W}\cdot\text{kg}^{-1}$ ) densities can be determined at different C-rates, and the graph of one versus the other (Ragone plot) is of great use to compare various power devices (see Fig. 7.3c). This comparison should be realized at the same current density (in  $\text{mA}\cdot\text{cm}^{-2}$ ), although volumetric densities are often of major importance (*cf.* Chapter 8.1).

The degradation of a battery with ageing is usually quantified by the faradaic or coulombic efficiency ( $FE$ ), the voltage efficiency ( $VE$ ) and the round-trip or energy efficiency ( $EE$ ):

$$EE = FE \times VE \quad (7.13)$$

$$\frac{Q_{E,discharge}}{Q_{E,charge}} = \frac{Q_{F,discharge}}{Q_{F,charge}} \times \frac{\overline{E}_{discharge}}{\overline{E}_{charge}} \quad (7.14)$$

The most used one is the faradaic efficiency, defined as the ratio of the outflowing charge from the battery divided by the amount employed to recharge it over a full cycle. This parameter assess the efficiency of charge carriers transfer and depends on multiple factors including side reactions, polarization, temperature or state-of-charge. Current interruptions at various SoC (in %) and adding a rest time between charge and discharge steps (OCP step) can provide insights on the degradation mechanisms. Battery self-discharge is caused by internal reactions and leads to a reduction of the state-of-charge, which in turn leads to a reduction of the provided OCP. The battery lifespan can be determined by the number of charge/discharge cycles that can be performed before its capacity fades beyond acceptable limits (around 70-80% of its initial value). In short, high reversibility of the redox reaction, high  $FE$  and low self-discharge are needed for long-lasting cycling of secondary batteries.

# 8 - State-of-the-art of RFB

## 8.1 Generalities

Redox flow batteries are considered the most suitable devices for long-term stationary storage (> 8 h) of intermittent energies as their power and energy capacities (expressed in W and W·h, respectively) can be scaled independently from each other and offer low self-discharge rate. Despite the apparent simplicity of the device (see Chapter 1), several factors must be taken into account to ensure optimal performance of redox flow batteries. The liquid electrolytes typically consist of active species, solvent and supporting electrolyte. The nature of the solvent along with the presence of supporting salts determine the accessible potential window and the maximum concentration of the redox-active materials. Overpotentials [Eq. 7.3] can lead to low discharge voltage and undesirable side reactions, such as hydrogen and oxygen evolution reactions (HER, OER) in aqueous solvents due to water electrolysis. To avoid this phenomenon, kinetics of electron-transfer reactions must be fast and reversible, as well as the supporting electrolyte conductivity and concentration must be maximized (related to the viscosity and the relative permittivity of the solvent, respectively). The solubility of each redox state must be controlled (pH adjustment, temperature monitoring) with the aim of optimizing this concentration. The theoretical capacity of an electrolyte  $C_{th}$  (expressed in A·h·L<sup>-1</sup>) is defined as the amount of charge stored in a given volume, and depends on the concentration of the electroactive starting species ( $c_0$ ) and the number of electrons involved in the redox reaction ( $n$ ) [Eq. 8.1].[67] Thus, the volumetric energy density of a RFB (in W·h·L<sup>-1</sup>) stands for energy stored per unit volume and is determined by the smaller capacity of either the negolyte or posolyte and the total average discharge voltage [Eq 8.1]. On the other hand, the surface power density (in mW·cm<sup>-2</sup>) is the one supplied by the battery per unit of effective membrane surface area [Eq 8.2]. The normal operating current density  $j$  (in mA·cm<sup>-2</sup>) must offer a good compromise between power and energy densities.

$$\text{Volumetric energy density} = C_{th}\bar{E}_{discharge} = nFc_0\bar{E}_{discharge} \quad (8.1)$$

$$\text{Surface power density} = \frac{i\bar{E}_{discharge}}{S} = j\bar{E}_{discharge} \quad (8.2)$$

It is of paramount importance to optimize the main parameters from a performance standpoint as well as in terms of capital expenditures (capex) and operating expenses (opex).[68] By way of illustration, a high concentration of the redox-active materials contributes in increasing not just the specific energy but also the viscosity of the electrolytes, which hinders mass-transport processes increasing pump losses and balance of plant costs. In order to facilitate the inclusion of RFB in the market, the long-term cost of the overall system shall not exceed USD 100 per kW·h (not including installation costs). However, the cost of a commercialized all-vanadium RFB is estimated above USD 300 per kW·h.[69] The search for a stable (electro)chemical system that allows minimizing the costs of active energy electrolytes (at



present above 30% of the total share) while maintaining good performances and long lifetime (correlation shown in Figure 8.1) remains a big challenge addressed hereunder.

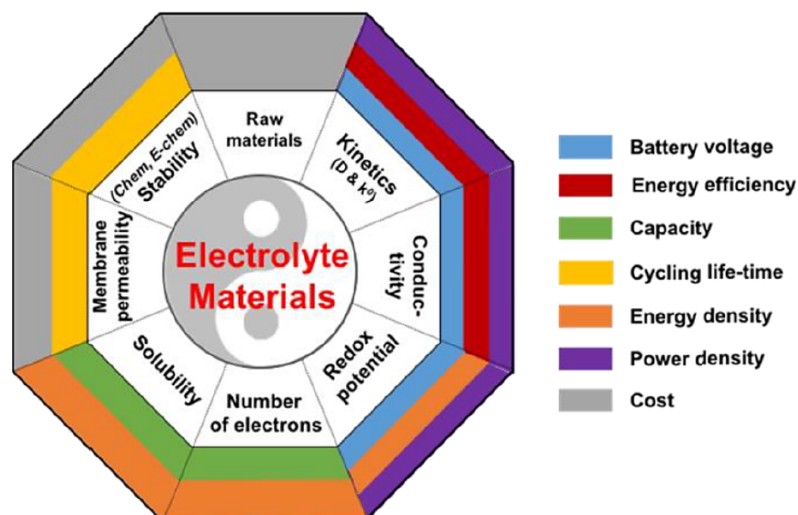


**Figure 8.1:** Correlation between physicochemical properties of the electrolytes and performance metrics of the battery. Reprinted with permission from [67]. Copyright 2019 American Chemical Society.

The choice of the separator also plays an important role in the final cost (between 10 and 25%) and directly depends on the chemical nature of the RFB, *i.e.* the electrolyte solvent or pH.[70, 71] A suitable ion-conducting membrane must have excellent ionic conductivity, chemical selectivity and stability, mechanical strength and solvent resistance, as well as prevent cross-mixing and the short-circuit of the two half cells. They are classified into cation and anion exchange membranes depending on the nature of the ions they allow to pass. Perfluorinated ionomers have been the most widely researched membranes since they possess good conductive, mechanical and stability properties. More specifically, Nafion is the benchmark membrane for aqueous RFB and fuel cells owing to its outstanding proton conductivity.[72] Nevertheless, among its drawbacks are the high cost (from 500 to 700 USD per m<sup>3</sup> [73]), large transport channels (likely cross-contamination) and excessive swelling (poor selectivity). Future high performance and low-cost alternatives under study include hydrocarbon-based membranes (*i.e.* sulfonated [74, 75] or ionic [76, 77] and non-ionic [78, 79] porous) as well as membrane-less batteries with immiscible redox electrolytes (aqueous/nonaqueous [80, 81] or aqueous biphasic [82, 83] ones).

With regard to the RFB electrodes (around 3% of the total cost), they must provide not only an active site for redox reactions but also a pathway for mass, ion and charge transport. The key features they must have are high electrical conductivity and specific surface area, good electrolyte wettability, chemical inertness and electrochemical stability. Currently, graphite felt [84] and carbon felt [85] are selected as the most suitable materials for both positive and negative electrodes, the former having generally higher carbon content and thermal conductivity and therefore higher current and power densities.[86] Nonetheless, other electrodes made up of metal meshes or foams (Pt, Au, Pb, IrO<sub>2</sub> or platinumized Ti) have been reported.[87–89] Recent

papers have studied the application of nanomaterials [90] such as metal-based nanoparticles, carbon nanotubes and graphene-based nanomaterials, the effect of O<sub>2</sub> and N<sub>2</sub> plasma [91] or electrospun carbon fibers [92] in the preparation of advanced electrodes with enhanced specific surface area and reactions kinetics for high-performance flow batteries.

The nature of the electrolyte solvent is the main classification criterion for redox flow batteries, which can be firstly divided into aqueous and non-aqueous systems as shown in Figure 8.2.[93] Water-based RFB offer a higher range of applicable current densities owing to the high ionic conductivity of their supporting electrolytes. In addition, they are low cost, non-volatile and non-explosive, while their performance depends on the pH conditions. On the contrary, organic solvents can operate at a wider working temperature and potential ranges, as well as they have the capability of dissolving a broad variety of organic molecules (*like dissolves like* law). Besides, metal ions are the most extended redox active materials owing to their fast kinetics and high stability at different oxidation states. With that in mind, certain aqueous systems based on transition metals have been able to carve a niche in the industry thanks to their established practical range of power and energy capacities with relatively low leveled costs of storage (LCOS, expressed in €/USD per kW·h·cycle).

## 8.2 Industrialized Technologies

Since its market inclusion in the 1980s [98], all-vanadium redox flow batteries (VRFB) have emerged as one of the most promising electrochemical devices for renewables stationary storage. Vanadium is the active material of both compartments thanks to its ability to exist in solution in four different oxidation states (from bivalent to pentavalent). The electrochemical cell reaction do not require catalyst, starting with VO<sup>2+</sup> (to VO<sub>2</sub><sup>+</sup>) in the posolyte and V<sup>3+</sup> (to V<sup>2+</sup>) in the negolyte for the discharged state. The capacity loss due to vanadium ions diffusion across the membrane (cross-contamination) can be mitigated through rebalancing techniques, achieving lifespan about 15,000-20,000 cycles. These electrolytes are nonflammable and have a high heat capacity to limit the temperature rise, avoiding therefore ignition or explosion. However, they are rather expensive (20-30 USD·kg<sup>-1</sup>), need for electrode pretreatment and have a temperature stability range rather limited (10-40 °C). The standard OCP of VRFB is 1.26 V (at 25 °C and 50% SoC), but the usual unequal proton concentrations in both electrolytes increase this value to around 1.4 V.[99] Depending on the state of charge, the actual operating cell voltage ranges between 1.7 and 1.0 V during charge and discharge, respectively [Eq. 7.3].

Electrochemical performance is optimal in acidic medium, with typical ions concentrations of 1.6-1.7 M in sulfuric acid, reaching up to 3 M using proper mixes and inhibitors.[100] The response time during the charge/discharge cycles are in the order of a millisecond given the fast kinetics. Normal operating current densities are in the order of 50-100 mA·cm<sup>-2</sup>, even if certain prototypes have been stably cycled at 600 mA·cm<sup>-2</sup>. [101] Therefore, power density barely exceeds 100 mW·cm<sup>-2</sup>, although a stack of unit cells can deliver a high total voltage (*e.g.* 10 V). The specific power density oscillates between 80 and 166 W·kg<sup>-1</sup>, while the specific

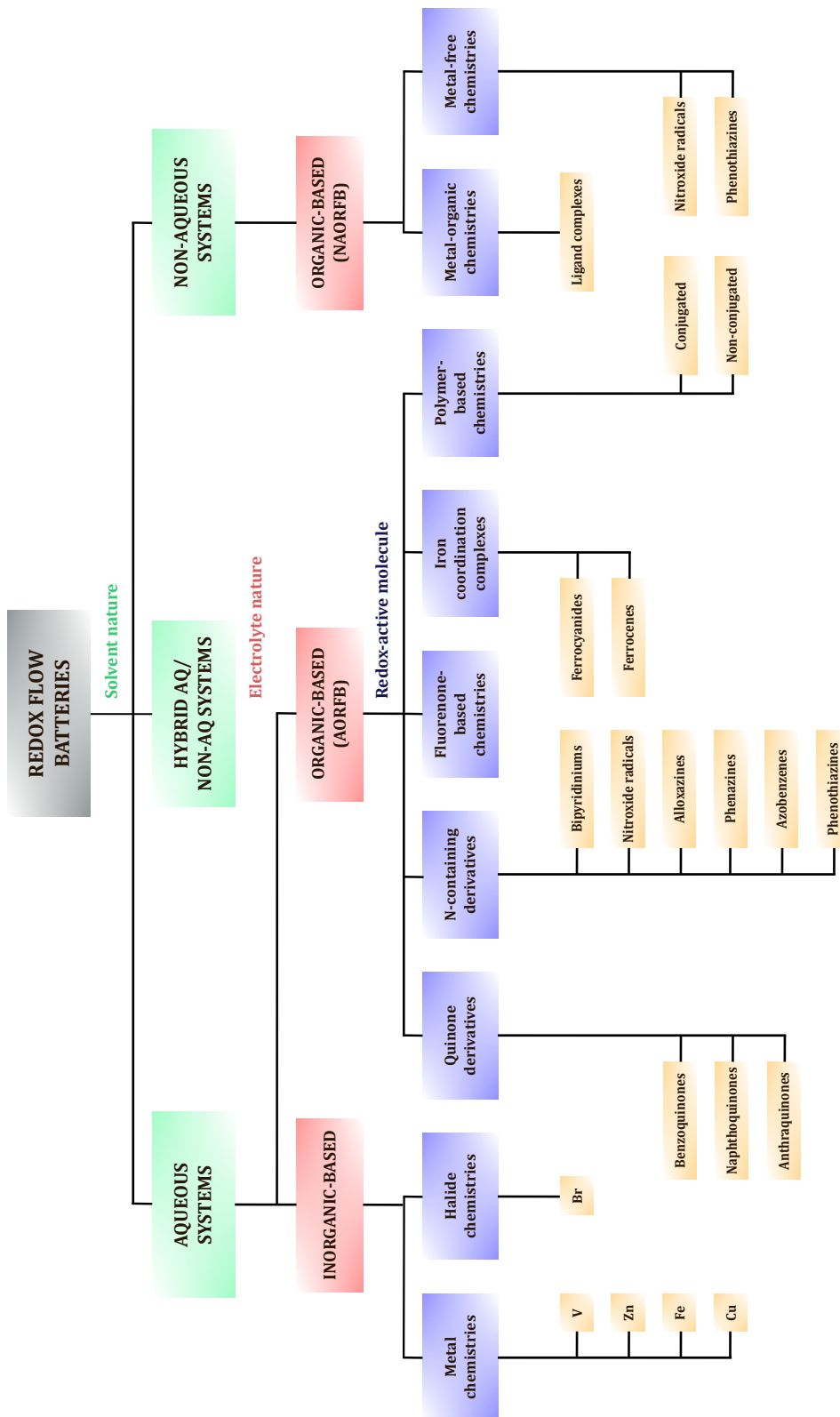


**Figure 8.2:** Classification of most relevant RFB systems sorted by the nature of the electrolyte solvent and the redox-active material. Own elaboration.[67, 94-97]

and volumetric energy ones are usually in the range of  $20\text{-}32 \text{ W}\cdot\text{h}\cdot\text{kg}^{-1}$  and  $25\text{-}35 \text{ W}\cdot\text{h}\cdot\text{L}^{-1}$ , respectively.[102, 103]

On the other hand, hybrid flow batteries typically combine a redox couple dispersed in a flowing fluid (gas or liquid) with a solid electroactive material deposited/stripped within the cell stack.[102, 104] Even though many metal-based systems have been designed in the last forty years (Pb [105], Fe [106] or Cu [107] based ones), to date only zinc-bromine flow batteries (ZBFB) [108] have carved out a sizeable gap in the market. In comparison to commercial VRFB, they offer higher specific ( $60\text{-}85 \text{ W}\cdot\text{h}\cdot\text{kg}^{-1}$ ) and volumetric ( $60\text{-}70 \text{ W}\cdot\text{h}\cdot\text{L}^{-1}$ ) energy densities, lower current densities ( $20 \text{ mA}\cdot\text{cm}^{-2}$ ) and a specific power ( $90\text{-}110 \text{ W}\cdot\text{kg}^{-1}$ ) of the same order of magnitude.[109] Alternative hybrid setups of growing interest include aqueous and non-aqueous metal-air flow batteries (MAFB) [110], gas-liquid hybrid systems [111–113] and membrane-free semiliquid batteries [114, 115].

Figure 8.3 illustrates the timeline of RFB state-of-the-art, with a clear target in terms of durability (10,000 cycles and 20 years lifetime) linked to LCOS ( $0.05 \text{ €}\cdot\text{kW}^{-1}\cdot\text{h}^{-1}\cdot\text{cycle}^{-1}$ ) for 2030.[94, 116] A new bunch of innovative technologies show up as real alternatives to standard pure flow vanadium batteries, some based on organic species (see section 8.3) and others on inorganic ones. By focusing on the aqueous inorganic-based systems, hydrogen-bromine [117], iron-based [118], vanadium-oxygen [119], vanadium-bromine [120, 121] and polyoxometalates-based [122] RFB comprise some of the most prominent technologies that aim to oust all-vanadium's supremacy. Alternatively, the use of solid active materials in a flowing system opens up the possibility of a high base energy density (due to their extremely high solubility) as well as decoupled energy and power scalability. The two main proposed technologies are the aqueous redox-mediated, also known as solid targeted/mediated/boosted flow batteries (SMFB), and the non-aqueous semi-solid flow batteries (SSFB).[123]

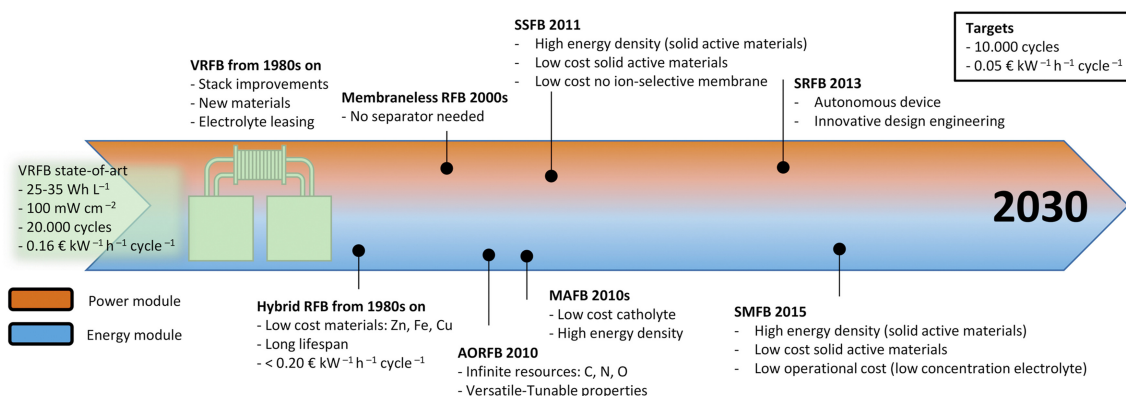


**Figure 8.3:** Timeline of redox flow battery state-of-the-art including technologies and strategies to achieve low cost batteries. Reprinted from [102], Copyright 2021, with permission from Elsevier.

Among all the technologies mentioned above, the ones that have been commercialized on a large scale up to 2022 are VRFB (by CellCube, Invinity, Largo, Schmid Energy Systems, Sumitomo, UniEnergy, VFlowTech, VionX Energy, VoltStorage or VRB Energy among others), ZBFB (Primus Power, Redflow and ZBB), the hydrogen-bromine (Elestor and EnStorage),

zinc-iron (ViZn Energy Systems), iron chromium (EnerVault), iron-chloride (ESS Tech), all-iron (ESS Tech) and certain organic RFB (Kemiwatt and Jena Batteries).

## 8.3 Organic-based Alternatives

Organic redox flow batteries (ORFB) present bright prospects for low-cost commercialization as they employ sustainable redox active molecules synthesizable from Earth-abundant elements such as carbon, hydrogen, oxygen, nitrogen or sulfur.[101, 124] These electroactive materials can be tailored based on molecular engineering for achieving optimal electrochemical properties in terms of solubility, stability, redox potential, kinetics or ion crossover. The organic-based systems are broadly classified into aqueous and non-aqueous according to the solvent used for dissolving the electroactive species (see Fig. 8.2).

### 8.3.1 Non-Aqueous ORFB

Many flow batteries using non-aqueous solvents have been proposed since the first metal-based concept was developed almost forty years ago [125], about all of them powered by organic compounds. As stated earlier in this document, organic systems have several advantages over aqueous ones thanks to the nature of their solvents. The low freezing and appropriate boiling points of certain organic electrolytes, such as ethanol and 1-propanol, allow deployment of RFB in places where traditional aqueous devices cannot operate. In addition, organic solvents offer a wide range of stable electrochemical windows (such as butyrolactone and valerolactone), enabling a wide array of redox pairs for achieving high cell voltages.[68] This can be coupled with a high active compounds concentration to get outstanding energy densities [126], but the voltage seldom exceeds 2 V and the (typically low) solubility remains the largest hurdle to overcome, eventually through different innovative strategies (*e.g.* eutectic electrolytes [127] or semi-solid suspensions [128]).[129] However, other major challenges associated with non-aqueous ORFB (NAORFB) should be addressed:

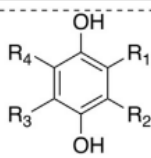
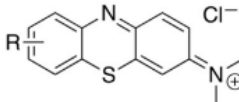
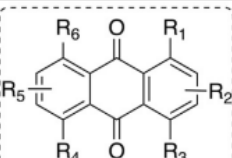
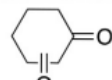
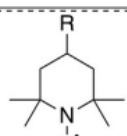
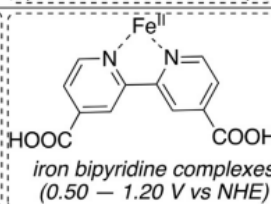
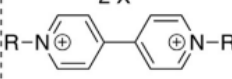
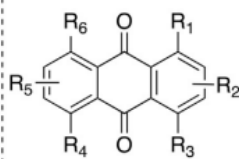
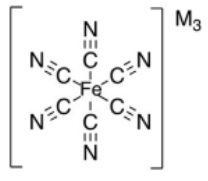
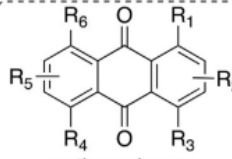
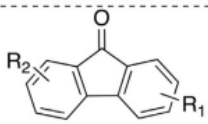
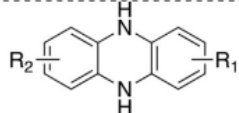
- The high internal cell resistance, arising from low ionic conductivity of both the electrolyte and the membrane, limits the discharge current density and consequently the discharge power density (see section 8.1) up to two to three orders of magnitude lower than those of aqueous RFB;[97]
- The present state-of-the-art membranes also show a lack of ionic selectivity (cross diffusion) and swells in organic solutions even though much progress has been made in that regard;[130]
- Safety concerns about toxicity and flammability should be considered in selecting the proper organic solvent.

NAORFB can be further classified into metal-organic and metal-free redox pairs.[95, 97] Metal-organic ligand complexes were firstly reported for this purpose in 1988 [131] owing to their facile kinetics and higher solubility with regard to metal ion-based compounds in aqueous and non-aqueous systems. The coordination compounds are based on a range of metals like copper, iron, nickel or vanadium, the latter being the most suitable in terms of redox reversibility and raw material cost trade-off.[132] On the other hand, two well-established metal-free posolytes can be distinguished since the development of the first all-organic NAORFB: nitroxide radical-based (TEMPO) and phenothiazine-based ones.[133] TEMPO is mainly employed due to its stability, high redox potential and high solubility in organic solvents [125, 134], while phenothiazine derivatives gained importance in the last decade since they provide noteworthy deep-cycling performance [135, 136]. Other promising all-organic compounds include dialkoxybenzene [137] or arylamines [138] as posolytes, as well as viologen [139, 140], benzothiadiazole [141], 4-benzoylpyridinium [142], N-methylphthalimide [143] or phenazine [144] as negolytes. Likewise, quinones serve as posolytes in hybrid metal-organic RFB [145–147] and as negolytes in pure flow ones [148–150].

### 8.3.2 Aqueous ORFB

Figure 8.4 summarizes the main organic redox couples employed in aqueous ORFB (AORFB) as a function of the pH and their presence in the posolyte (positive redox materials) or the negolyte (negative redox materials). Among them, the following five groups evoke greater interest:[124]

- Quinone-based negolyte and hydroquinone-based posolyte: well-known molecules with high electrochemical reversibility and fast reaction rates with a two-electron transfer that generally occurs in a proton-coupled single step.
- Anthraquinone-based negolyte: conjugated structure with high chemical stability and fast electron transfer kinetics. The Aziz group (MIT) was pioneer in the development of metal-free RFB [151] and mainly focuses their research in anthraquinone (AQ) derivatives both in acidic [152, 153] and alkaline [154, 155] medium, as well as in other quinones at neutral pH [156, 157]. AQ have also been studied at neutral pH [158] and differential pH as a method for increasing cell potential [159, 160].
- Viologen-based negolytes (bipyridines): redox-mediators and indicators owing to its electrochemical reversibility along with color change at neutral pH.[161, 162]
- Alloxazine-based negolyte: simple synthetic method and reversible one-electron electrochemical reaction used in alkaline conditions.[163, 164]
- TEMPO-based posolyte: well-known redox mediator and radical marker with recent interest at neutral pH.[165, 166]

	Positive Redox Materials	Negative Redox Materials
Acidic	<div style="border: 1px dashed black; padding: 5px; margin-bottom: 5px;">  <p><i>benzoquinones</i> (0.67 – 1.10 V vs NHE)</p> </div> <div style="border: 1px dashed black; padding: 5px; margin-bottom: 5px;"> <p>FeSO<sub>4</sub> (iron salts) 0.77 vs NHE</p> </div> <div style="border: 1px dashed black; padding: 5px;">  <p><i>phenothiazines</i> (0.65 – 0.71 V vs NHE)</p> </div>	<div style="border: 1px dashed black; padding: 5px; margin-bottom: 5px;">  <p><i>anthraquinones</i> (0.10 – 0.20 V vs NHE)</p> </div> <div style="border: 1px dashed black; padding: 5px;"> <p>Pb(OAc)<sub>2</sub> -0.13 V vs NHE</p> <div style="border: 1px dashed black; padding: 5px; margin-top: 5px;">  <p><i>cyclohexadiones</i> (-0.3 – -0.15 V vs NHE)</p> </div> </div>
Neutral	<div style="border: 1px dashed black; padding: 5px; margin-bottom: 5px;">  <p><i>TEMPO derivatives</i> (0.90 – 0.99 V vs NHE)</p> </div> <div style="border: 1px dashed black; padding: 5px;">  <p><i>iron bipyridine complexes</i> (0.50 – 1.20 V vs NHE)</p> </div>	<div style="border: 1px dashed black; padding: 5px; margin-bottom: 5px;">  <p><i>viologens</i> (-0.4 – -0.3 V vs NHE)</p> </div> <div style="border: 1px dashed black; padding: 5px;">  <p><i>anthraquinones</i> (-0.30 – -0.20 V vs NHE)</p> </div>
Alkaline	<div style="border: 1px dashed black; padding: 5px;">  <p><i>ferricyanides</i> (0.5 V vs NHE)</p> </div>	<div style="border: 1px dashed black; padding: 5px; margin-bottom: 5px;">  <p><i>anthraquinones</i> (-0.60 – -0.70 V vs NHE)</p> </div> <div style="border: 1px dashed black; padding: 5px; margin-bottom: 5px;">  <p><i>fluorenones</i> (-0.60 – -0.70V vs NHE)</p> </div> <div style="border: 1px dashed black; padding: 5px;">  <p><i>phenazines</i> (-0.67 – -0.78 V vs NHE)</p> </div>

**Figure 8.4:** Redox-active molecules employed in aqueous organic redox flow batteries. Reprinted from [167], Copyright 2022, with permission from Elsevier.





## **Part IV**

# **In Situ Analysis of a Redox Flow Mini-Battery using MRI**

## 9 - Conversion Cell in the NMR Detection Area

In order to achieve the main goal of this project (see Chapter 2), we take advantage of integrated flow NMR systems combined with the recent progress in additive manufacturing technologies. In the next chapters the main problems associated to the NMR operando monitoring of redox reaction will be described, including the static field uniformity, the passage of radio-frequency current through the battery, the effect of pulsed field gradients with electrodes and current collectors, the presence of paramagnetic species hindering the spectral analysis or the magnetohydrodynamic (MHD) effect.

### 9.1 Coupling Electrochemistry and Liquid State NMR

In the past decades, the study of energy storage systems was mainly carried out through ex situ NMR investigations.[168] However, the measured electrodes were likely to undergo changes in their composition as well as fully relaxation to their equilibrium state during these processes, along with the fact that a new full battery had to be assembled and subsequently destroyed for each single experiment. In situ NMR emerged as an alternative method in which the spectra are recorded on the unperturbed battery components without setup modification, thereby avoiding the major disadvantages of the previous investigation. Since the first in situ spectroscopic study of an electrochemical cell in 1964 [169] until recently [170], several approaches have been developed in order to identifying species electrochemically generated in solution.

In the case of in situ electrochemical NMR (EC-NMR), two main setups can be distinguished: online and operando. In the first arrangement, the electrochemical reaction takes place outside of the radio frequency coils of the probe and the product is subsequently flowed into the detection area, providing suitable conditions for the NMR measurements and allowing the coupling with other spectroscopic methods such as EPR.[171] Nevertheless, they require large solution volumes and, above all, there is an inherent time delay between formation and detection of products and intermediates (non-real-time monitoring method). For the operando detection, the battery must be positioned inside the detection region of the NMR probe, simultaneously generating and detecting the electrochemical products (real-time monitoring method). Both issues are addressed throughout the following chapters, with the ambitious goal of developing high-resolution operando NMR setups for the study of complete redox flow batteries.

### 9.1.1 Magnetohydrodynamic Effect

Magnetochemistry is an interdisciplinary topic that studies the different puzzling effects observed when magnetic fields create convection in electrochemical cells.[172] The Kelvin force [173] is the result of magnetic field gradients on paramagnetic species, whereas the Lorentz force ( $F_L$ ) [174] arises from the interaction of a uniform magnetic field ( $B$ ) with the local current density ( $j$ ) of a conducting fluid:

$$F_L = j \times B \quad (9.1)$$

This turbulence-inducing phenomenon is the main driving force of the so-called magnetohydrodynamic effect. In short, the magnetic field acts on ions migrating between the electrodes reducing the diffusion layer thickness and increasing the limiting current during cathodic processes in diffusion-controlled systems. On the contrary, during anodic processes the open circuit potential is shifted together with a potential corrosion of the electrodes. Its magnitude is minimized when the charge transport is parallel to the magnetic field direction and maximized when both are orthogonal, magnetically inducing flow patterns on a scale unattainable by mechanical agitation.

All papers published until 2017 that performed EC-NMR did not consider the strong magnetic field effect and its influence on the reaction kinetics.[175] This information needs to be passed on to the scientific community not only to deal with it, but also to take advantage. By way of example, the superposition of a magnetic field during water electrolysis for hydrogen production plays important role desorbing bubbles from the electrode surface, saving energy and greatly improving the efficiency of the process.[176] Moreover, an external magnetic field can also be used to improve the electrochemical characteristics of lithium-ion batteries [177] and deep eutectic solvent-based redox flow batteries [178, 179] among others, by reducing the viscosity of the electrolyte and increasing the conductivity of the active ions.

## 9.2 Model System - Materials and Methods

All the experimental instrumentation that has been employed through the project is listed herein:

- A 7 T vertical NMR imager (300 MHz  $^1\text{H}$ ) with a super wide bore (SWB) diameter of 154 mm (samples up to 66 mm) and a gradient strength of up to 67 G/cm;
- Two 11.7 T high-resolution NMR spectrometers (500 MHz  $^1\text{H}$ ) with Narrow Bore diameters of 52 mm (samples up to 18 mm) and a gradient strength of up to 200 G/cm;
- Two 3D-printers: a Stratasys Objet30 Pro, which employs the patented PolyJet printing technology (layer resolution up to 16 microns) and using a transparent photopolymer resin named *VeroClear* that simulates polymethyl methacrylate (PMMA), and a Formlabs Form 3+, built on advanced low force stereolithography technology (25 microns) and using a transparent polymer resin so-called *Clear*;

- Two potentiostats: a Biologic SP-150 single channel potentiostat with a potential range between -20 V to 20 V and a current range from 10  $\mu$ A to 800 mA, and an Autolab PGSTAT101 single channel potentiostat with a potential range between -10 V to 10 V and a current range from 10 nA to 10 mA.

As already stated, the main redox flow battery (RFB) components are the storage tanks, the hydraulic pumps and the electrochemical conversion cells (see Figure 9.1). In turn, the latter usually consist of a separator, two bipolar plates, two electrodes and two current collectors. With respect to our electrochemical system, the conductive plates were generally replaced by 3D-printed compartments containing the electrolytes and separated by a Nafion 212 proton-exchange membrane. This substitution was performed in order to avoid radio-frequency shielding (in the case of aluminium-based materials) and large magnetic susceptibility differences (ferromagnetic materials) through the cell. The computer aided design (CAD) of the conversion cell models were made with SolidWorks (Dassault System) and were subsequently built by additive manufacturing using the Stratasys Objet30 Pro printer. *VeroClear* resin was the chosen material since its magnetic susceptibility, around  $-9.06 \cdot 10^{-6}$  using the International System of Units (SI) convention [180], is of the same order of magnitude as water ( $-9.04 \cdot 10^{-6}$  [181]).

With regard to the chemical system, all the operational batteries reported in Chapters 9 and 10 have the following features in common. Both so-called half-cells were prepared in distilled water. One of them contained the aqueous posolyte, a 50-50 mix of potassium hexacyanoferrate(III) ( $\geq 99.0\%$ , Sigma-Aldrich) and potassium hexacyanoferrate(II) trihydrate ( $\geq 99.5\%$ , Sigma-Aldrich), while the other contained the aqueous negolyte, 9,10-Anthraquinone-2,7-disulfonic acid disodium salt (2,7-AQDS) with purity ranging from 80% (Santa Cruz Biotechnology) to 95% (eNovation Chemicals LLC). In addition to these redox-active species, both half-cells included sodium nitrate ( $\geq 99.0\%$ , Sigma-Aldrich) as supporting electrolyte to minimize the effects of migration. From a certain point in time onwards, the negolyte systematically contained potassium nitrate ( $\geq 99.0\%$ , Sigma-Aldrich) at a concentration that compensates the difference of osmotic pressure generated by the potassium ions of the posolyte, thereby avoiding water to pass between compartments. In other developments, both carbon felts and platinum wires (Pt:Rh 87:13 wt%, Alfa Aesar) were tested as battery electrodes, as well as stainless steel screws (type 304 S15, RS Group plc) and high-purity graphite rods (purity  $> 99.9995\%$ , Alfa Aesar) as current collectors.

Anthraquinone sulfonate salts are renowned for their rapid charge transfer kinetics, low redox potentials and relatively high solubilities. The 2,7-AQDS and ferrocyanide redox couple was chosen since it is a system already studied under different conditions [182–184], in which one can monitor the state-of-charge (SoC) and state-of-health (SoH) of the battery through the anthraquinone NMR signal. During charge, the starting oxidized anthraquinone (AQ) is reduced to dianion ( $\text{AQ} + 2\text{e}^- \rightleftharpoons \text{AQ}^{2-}$ ), protonated monoanion ( $\text{AQ} + 2\text{e}^- + \text{H}^+ \rightleftharpoons \text{AQH}^-$ ) or hydroanthraquinone ( $\text{AQ} + 2\text{e}^- + 2\text{H}^+ \rightleftharpoons \text{AQH}_2$ ) depending upon the pH value (explained below), while the ferrocyanide is oxidized giving ferricyanide ( $\text{Fe}(\text{CN})_6^{4-} \rightleftharpoons \text{Fe}(\text{CN})_6^{3-} + \text{e}^-$ ). These redox reactions are reversed during discharge and yield a standard cell potential of 0.74 V

at unbuffered neutral pH. Thus, the AQ redox reaction was considered the process of interest and accordingly connected to working electrode circuit of the potentiostat (therefore the observed cell potential is -0.74 V). Complementary, the posolyte mixture was highly concentrated with the dual purpose of making the negolyte the capacity limiting side and providing a stable reference reaction, acting both as counter and reference electrode.

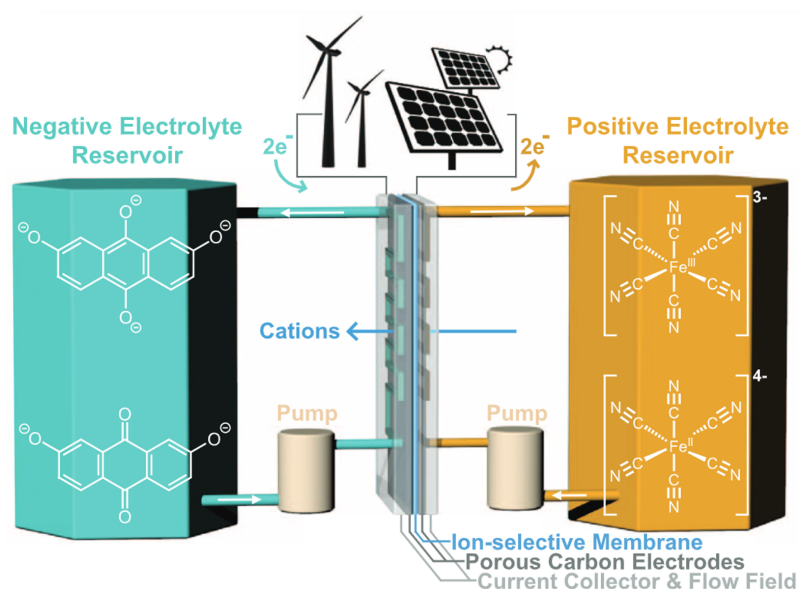


**Figure 9.1:** Schematic of a complete RFB in charge mode (SoC < 100%) built on a similar model system as the one used throughout this project. From [154]. Reprinted with permission from AAAS.

## 9.3 Mini-Battery Prototypes and Problematics

At first, it was decided to work solely on the electrochemical conversion cell (hereafter referred to as 'mini-battery') in order to optimize the battery components and better understand the main constraints related to magnetic fields. To this end, we made use of the vertical NMR imager, which enables us to break free from the space limitations. Several mini-battery models were conceptualized and analyzed through proton-based MRI techniques (spatially-resolved imaging and localized spectroscopy) in the search for a compromise between magnetic resonance and electrochemical approaches.

### 9.3.1 Silicone Model

In the first instance, a preliminary silicone-based model was built as shown in Figure 9.2a. A dozen silicone grommets of outside diameter (OD) = 31 mm, inside diameter (ID) = 31 mm and thickness = 1.5 mm were stacked to constitute the mini-battery compartments. A circular

Nafion membrane ( $\varnothing = 20$  mm, thickness = 100  $\mu\text{m}$ ) was placed in the middle of the stack to separate the two half-cells. Carbon felt electrodes ( $40 \times 40 \times 0.3$  mm) were fixed to both ends of the stack by means of a silicone sealant which cures at room temperature. Two polymer plates ( $45 \times 45 \times 5$  mm) hold the cell assembled with the help of nylon washers, nuts and screws ( $\varnothing = 5$  mm). A volume of 0.5 mL for each electrolyte was introduced in its corresponding compartment using syringes with a fine needle that slides between two silicone grommets. Like for each model, cell assembly was carried out both in inert and non-inert atmospheres, with no significant differences in terms of electrochemical performance (*i.e.* oxidative environment) since the electrolyte filling vents air from the system. Two additional nuts facilitated the contact between the electrodes and insulated copper wires with nonmagnetic brass washers welded at the end, which in turn were connected to the potentiostat.

### First in situ images and localized spectra of a mini-battery

The cell was built containing 2,7-AQDS 0.1 M 80% and  $\text{NaNO}_3$  1 M in the negolyte compartment, and trihydrated  $\text{K}_4\text{Fe}(\text{CN})_6$  0.3 M,  $\text{K}_3\text{Fe}(\text{CN})_6$  0.3 M and  $\text{NaNO}_3$  1 M in the posolyte compartment.

- UTE (Ultrashort TE) sequences were performed with a flip angle ( $\theta$ ) of  $15^\circ$ , a slice thickness (ST) of 2 mm and a total number of radii equal to 402 over a bandwidth (BW) of 100 kHz. The echo time (TE) was set at 0.379 ms and the repetition time (TR) at 30 ms for a total experiment time (TET) of about 13 s. The FID acquisition mode (gradient echo) was chosen taking into account the inhomogeneous distribution of the  $B_1$  field throughout the sample. Three axial images were obtained over a field-of-view (FOV) of  $50 \times 50$  mm ( $128 \times 128$  points) after selecting three slices at different mini-battery levels.
- FLASH (Fast Low Angle SHot) sequences were performed with a  $\theta$  of  $30^\circ$ , an ST of 2 mm, a BW of 50 kHz, an TE of 4 ms and a TR of 100 ms (TET = 13 s). Three images were obtained for each plane (axial, sagittal, coronal) over a FOV of  $50 \times 50$  mm ( $128 \times 128$  points). The set of pilot images was used systematically to identify a volume of interest in which single-voxel spectroscopy methods (*i.e.* PRESS, STEAM) can be applied.
- PRESS (Point RESolved Spectroscopy) sequences were performed with an acquisition BW of 6061 Hz and 4096 points for a total number of scans (NS) equal to 256. The TE was set at 20 ms and the TR at 2000 ms for a TET of 510 s. A voxel of  $2.2 \times 2.8 \times 1.6$  mm was selected and its water signal was reduced through an 8-pulse train VAPOR (VARIABLE Power radio-frequency pulses with Optimized Relaxation delays) module [185] operating at 4.7 ppm over a bandwidth of 210 Hz (0.7 ppm). Field homogeneity was systematically optimized prior to each SVS acquisition, in particular thanks to  $B_0$  field mapping followed by local shimming over the volume of interest.

Figures 9.2b-d show the UTE images corresponding to the ferro/ferricyanide compartment

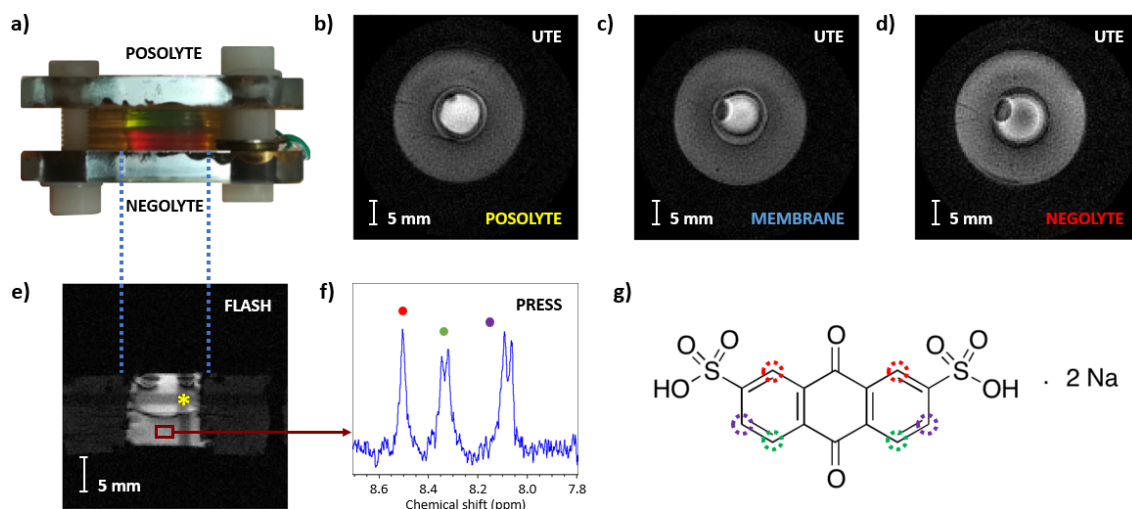


**Figure 9.2:** In situ analysis of a silicone model mini-battery. (a) Picture; (b-d) Axial UTE images of the (b) posolyte, (c) membrane and (d) negolyte; (e) Sagittal FLASH image of the whole conversion cell and voxel placement for (f); (f) Localized aromatic region of the PRESS voxel selected in (e); (g) Molecular structure of 9,10-Anthraquinone-2,7-disulfonic acid disodium salt.

(posolyte), the Nafion membrane and the quinone compartment (negolyte), respectively. This technique allows protons of the silicone grommets to be imaged despite their short transverse relaxation time. Conversely, the sagittal FLASH image depicted in Figure 9.2e does not show the silicone protons ( $T_E > T_{2,\text{silicone}}$ ) but provides a greater contrast between molecules with different relaxation time for the same acquisition time. Note that on this image, which is part of an experiment interleaving three orthogonal 2D images, the appearance of a cross of lower intensity (*i.e.* perpendicular bands converging at the yellow asterisk) is due to the partial saturation of the protons of these regions by the axial and coronal images (the excited spins have a non-complete return to equilibrium between each slice-selective RF pulse). Gas bubbles unintentionally introduced during the assembly of the battery can be distinguished in both types of images. They are characterized by absence of protons and appearance of magnetic susceptibility artifacts, being mainly present in the negolyte compartment (see Fig. 9.2d). Figure 9.2f shows a localized proton spectrum obtained through a PRESS sequence in the VOI denoted by the red rectangle on Figure 9.2e. The smaller the voxel, the higher the spatial homogeneity (and therefore the spectral resolution), but also the lower the number of spins (and therefore the signal-to-noise ratio). For the considered small voxel and quinone concentration ( $\approx 10 \text{ mm}^3$  and 0.1 M, respectively, thus approx.  $6 \cdot 10^{17}$  molecules), the SNR obtained in 510 seconds is 8.98, while nevertheless providing a high enough spectral resolution to discriminate a  $^1\text{H}$ - $^1\text{H}$  J-coupling of 8 Hz.

### First in situ and operando experiments coupling electrochemical and NMR techniques

A similar mini-battery to that of the previous experiment was prepared except that this time it was connected to the Biologic SP-150 potentiostat, in turn placed out of the fringe field of

the NMR magnet. This potentiostat model and disposition were the default ones for future experiments unless otherwise noted. FLASH and PRESS sequences were performed under the same conditions as in the previous experiments, except for the *FOV* ( $35 \times 35$  mm) and voxel size ( $2.3 \times 2.8 \times 1.4$  mm), respectively.

- CV (Cyclic Voltammetry) experiments were performed inside the magnet at different scan rates, always starting from the OCP value, in the absence of NMR radio-frequency emission.
- A CA (Chronoamperometry) experiment was performed inside the magnet at -1.2 V for an hour.

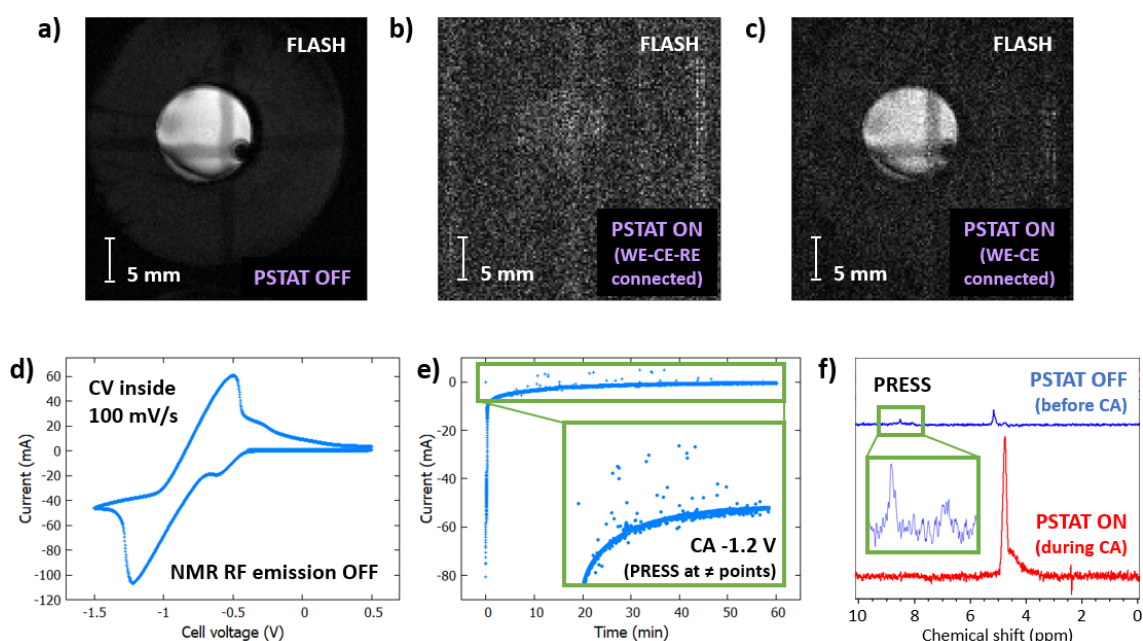


**Figure 9.3:** In situ and operando analysis of a silicone model mini-battery. (a-c) Axial FLASH images when (a) the potentiostat was switched off, (b) the negolyte was connected to WE, the posolyte to both CE and RE and the potentiostat was on, and (c) the negolyte connected to WE, the posolyte to the CE and the potentiostat on; (d) Cyclic voltammogram without performing NMR techniques; (e) Chronoamperogram performing simultaneous PRESS at different electrolysis times; (f) PRESS localized spectra after the CV depicted in (d) when the potentiostat was switched off and simultaneously during the first 8 minutes of CA.

Figures 9.3a-c correspond to axial FLASH images of the mini-battery at the negolyte level (compartment of interest) when the potentiostat was switched off (PSTAT OFF); the potentiostat was on but not in use (PSTAT ON), the negolyte connected to the working electrode (WE) circuit and the posolyte to both the counter (CE) and the reference electrode (RE) ones; and the PSTAT ON, the negolyte connected to the WE and the posolyte only to the CE, respectively. When the cell is electrically connected to the switched-on potentiostat, electromagnetic noise is injected into the NMR probe. This effect can be ascribed to the high-frequencies generated by the potentiostat close to the spectrometer working range of frequencies. A signal-to-noise ratio (SNR) degradation can be observed whether the RE wire is connected or not. Nevertheless,



there is a SNR difference between both images, which therefore can be attributed to the RE circuit. Significant radio-frequency degradation can also be caused by the copper wires towards the potentiostat acting as antenna leaks.

Besides, the cyclic voltammogram in Figure 9.3d shows the cathodic and anodic voltage peaks corresponding to the reduction and oxidation of the anthraquinone, respectively. The second electron-transfer step is thermodynamically more favorable than the first ( $AQ^{2-}$  is strongly stabilized in water relative to  $AQ^-$ ) and they overlap to produce a single CV wave. It can be considered a thermodynamically reversible process since the diffusion controls it even at a high scan rate (100 mV/s). According to the observed cathodic peak voltage, a quinone reduction was performed by applying this potential to the working electrode (-1.2 V) and the current was monitored over time (see Fig. 9.3e).

On the other hand, Figure 9.3f shows PRESS spectra localized in the negolyte compartment after the CV / before the CA with the potentiostat switched off, and simultaneously during the first 8 minutes of CA (obviously the potentiostat switched on). It can be observed that the resolution of the quinone aromatic peaks is much lower when compared with the one in Figure 9.2f, mainly because the flip angles of the PRESS do not reach the expected values ( $139^\circ$  instead of  $180^\circ$  for the second and the third soft pulses). For a given voxel size and maximal gradient value (provided by the ParaVision software but not displayed), the  $B_1$  peak power is a limiting factor to reach high flip angle values in very short time [Eq. 3.4]. Taking into account that the main difference between both measurements (given the analogous voxel size) was the performance of electrochemical techniques before the acquisition, it can be said that the electric current passage through the cell entails an induced perturbation. This phenomenon can be offset by lengthening the duration of the  $180^\circ$  pulses, affecting the excited bandwidth ( $R = BW \times \tau_p$ ), or by using sequences with smaller flip angles (*i.e.* STEAM).

When performing NMR and electrochemical techniques at the same time, they exert mutual effects on each other. Spikes can be observed on the chronoamperogram (see Figure 9.3e) as soon as the PRESS sequence is started. In parallel, Figure 9.3f shows a degradation of the aromatics signal coming from the molecule of interest as well as an intense water peak. Potentiostat operation generates static field inhomogeneities that broaden the spins frequency response, hindering proper slice selection and water signal suppression (WS). Bearing in mind the above-described findings, the unwanted frequencies and their associated noise generated by the potentiostat were henceforth minimized by integrating a low-pass filter (SLP-50 DC to 48 MHz pass-band, Mini-Circuits) and shielding the cables at the exit of the probe body as well as twisting the cables inside the magnet. It was also found that grounding the shield to (i) the potentiostat ground, (ii) the preamplifier ground or (iii) both of them, did not lead to improved results once the filter was integrated.

### 9.3.2 Cylindrical Model

We found empirically that the spectral resolution is improved if the voxel longest dimension is oriented in the  $z$  axis direction. This, together with the fact that the gradient non-linearity distortion can be exclusively corrected for this axis, spurred the development of a new cylindrical mini-battery to obtain well-resolved localized spectra in greater volumes of interest. Figure 9.4 shows the 3D rendering and actual images of the cylindrical cell, as well as its dimensions and relative size inside the SWB birdcage coil. This 3D-printed model was designed with two concentric compartments, the inner one with a cone-shaped ending. Two metal spirals were wound on the internal and external walls of the inner compartment to simulate the presence of a potential electrode. Initially, copper ( $\varnothing = 1$  mm) was the chosen material since its magnetic susceptibility ( $-1.08 \cdot 10^{-9}$  m<sup>3</sup>/kg) is of the same order of magnitude as water. A bottom cover was glued with silicone sealant, whereas the upper one is assembled with the help of nylon washers, nuts and screws ( $\varnothing = 3$  mm). Each electrolyte was introduced in its corresponding compartment thanks to a top opening in the upper cover by means of syringes with a fine needle inserted inside or outside the above-mentioned cone-shaped ending. The negolyte was housed in the inner compartment with the aim of minimizing magnetic susceptibility artifacts (*e.g.* air interface) if big voxels are selected.

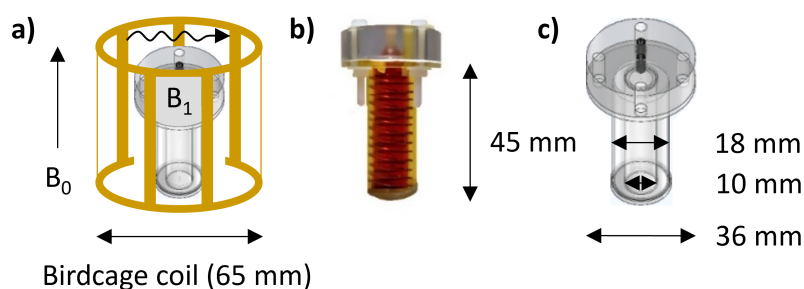


**Figure 9.4:** Cylindrical mini-battery model. (a) Depiction of the relative size of the cell inside the probehead coil; (b) Picture; and (c) 3D rendering and dimensions.

#### Optimization of localized spectroscopy parameters and Nafion integration challenge

The cell was built with the same negolyte and posolyte compositions as in the previous experiments. The FLASH sequences were performed under the same conditions, except for the *FOV* ( $65 \times 65$  mm). In turn, PRESS experiments varied the number of scans (8) and thereby the TET (16 s), the voxel size ( $4.5 \times 4.5 \times 20$  mm) and the WS bandwidth (300 MHz), as well as the occasional implementation of OVS (Outer Volume Suppression) bands [186] placed parallel to the surface of the voxel (gap of 2.5 mm, thickness = 5 mm) to eliminate contamination with signal from the surroundings.

- STEAM (STimulated Echo Acquisition Mode) sequences were performed with an acquisition bandwidth of 6061 Hz and 4096 points for a total NS = 8. The TE was set at 15 ms, the mixing time (TM) at 8 ms and TR at 2000 ms for a TET of 16 s. A voxel of

4.5 × 4.5 × 20 mm was selected and its water signal was minimized through a VAPOR suppression pulse train operating at 4.7 ppm. Different spectra were obtained varying the water suppression bandwidth (WS) from 210 Hz (0.7 ppm) to 500 Hz (1.67 ppm). Field homogeneity was systematically optimized as described above.

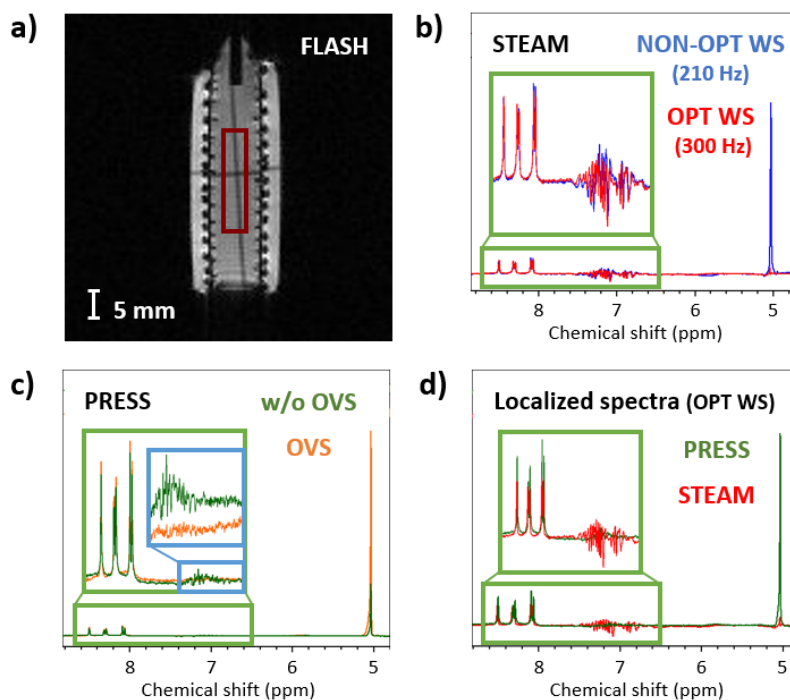


**Figure 9.5:** In situ analysis of a cylindrical model mini-battery. (a) Coronal FLASH image of the whole cell and voxel placement; (b) STEAM localized spectra over the selected voxel in (a) before and after optimizing the WS pulse train bandwidth; (c) PRESS localized spectra over the same voxel with and without the implementation of OVS bands; (d) Comparison of STEAM and PRESS localized spectra obtained under the same conditions.

Figure 9.5a depicts a coronal FLASH image of the mini-battery as well as the selected volume of interest over the negolyte compartment. The geometry of the cell allows the selection of bigger voxels, enabling decreasing the number of scans and therefore the experimental time (keep in mind that the SNR of the resulting spectra is proportional to the square root of the number of scans). STEAM localized spectra are shown in Figure 9.5b using different WS bandwidths centered at 4.7 ppm. The peak suppression is optimal when applying the frequency-selective pulses over a 300 Hz range. However, spurious signals in the surroundings of 7 ppm remain in both cases. On the other hand, PRESS experiments were performed keeping the improved WS selectivity and implementing or not an OVS in order to remove the aforementioned signals. Figure 9.5c demonstrates a complete deletion of these artifacts when implementing this spatial (but not frequency) specific suppression of peripheral regions (*e.g.* copper wires). Also, a slight increase in the aromatic peaks signal-to-noise ratio can be observed with respect to when it is not applied (1.12 times), as well as a less effective water peak suppression (4 times).

STEAM and PRESS spectra obtained under the same conditions were compared in Figure 9.5d. In both cases the spectra resolution is similar (2-3 Hz) and higher than the one obtained with the silicone model (6-8 Hz), even if the voxels are forty times bigger (from 10 to 405 mm<sup>3</sup>). It means that, at least in this instance, the spectral resolution is not directly linked to the spatial homogeneity, which seems high, but to the cell components and their disposition. Moreover, the spurious signal suppression and the SNR of the signals of interest are optimal in the PRESS sequence, while the water peak minimization is far more effective in the STEAM one.

Despite the many advantages of this model, there is a critical issue concerning the electrochemical approach. Multiple tests were carried out to replace the inner compartment by a cylindrical membrane without achieving the expected results, either by heat sealing or by a Nafion D2020CS solution deposition (20% weight, Ion Power GmbH) on diverse non-stick surfaces such as Teflon, quartz or pyrex. Besides, a thorough study of a suitable electrode to replace copper (susceptible to oxidation) was conducted in the hypothetical scenario where a cylindrically wound Nafion membrane would have been incorporated. Taking into account long-term stability, electrochemical performances and magnetic properties, carbon felt and platinum were postulated as the most interesting alternatives. Preliminary imaging tests with carbon felt cylinders in both compartments were conducted, revealing a perturbation of the magnetic field studied below.

### 9.3.3 Spherical Model

In order to bypass the above-mentioned challenge with the membrane, a new spherical model shown in Figure 9.6 was conceived. A circular Nafion membrane ( $\varnothing = 50$  mm) was placed between two semi-spherical 3D-printed pieces assembled with the help of nylon washers, nuts and screws ( $\varnothing = 4$  mm). Carbon felt circles ( $\varnothing = 33$  mm) were suspended in each compartment with the help of platinum wires ( $\varnothing = 0.127$  mm) before cell assembly. A dash of silicone sealant was applied in the junction point between carbon and platinum to ensure good electrical contact and positional stability (electrode surfaces parallel to the membrane). The platinum wires were subsequently fastened to previously pierced nylon screws ( $\varnothing = 5$  mm) with silicone sealant. Each compartment had threaded holes in opposite positions from where the electrolytes were introduced (and the electrodes fixed) one after another: once a compartment was filled (30-35 mL), its corresponding nylon screw ensured water tightness with the help of Teflon tape. The geometry of the mini-battery was chosen in order to maximize the voxel size between the electrodes, with its longest dimension in the  $z$  axis direction if the cell was correctly oriented. Moreover, its corner-free design helped to minimize dead or stagnant zones out of the area between the electrodes.

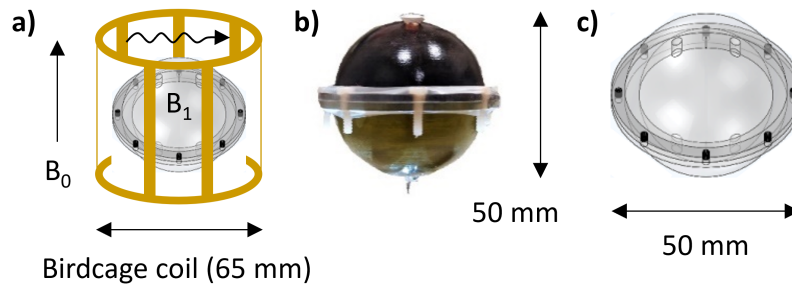


**Figure 9.6:** Spherical mini-battery model. (a) Depiction of the relative size of the cell inside the probehead coil; (b) Picture; and (c) 3D rendering and dimensions.

### Optimization of imaging parameters and challenge of the magnetic field perturbation

The cell was built with the same negolyte and posolyte compositions as in the previous experiments and was not initially connected to any potentiostat.

- FLASH sequences were performed as before except for a  $FOV$  of  $70 \times 70$  mm and varying the  $BW$  from 50 to 100 kHz and the TR from 100 to 400 ms (TET from 13 to 52 s, respectively).
- 3D ZTE (Zero TE) sequences were performed with a  $\theta$  of  $0.5^\circ$  and a total number of radii equal to 51896 over a  $BW$  of 100 kHz. TR was set at 2.5 ms for a TET of about 130 s. 3D images were obtained over a field-of-view of  $65 \times 65 \times 65$  mm ( $128 \times 128 \times 128$  points).
- MSME (Multi-Slice Multi-Echo) sequences were performed with an ST of 2 mm, a  $BW$  of 50 kHz, an TE of 8 ms (only one echo) and a TR of 100 ms (TET = 13 s). Different images were obtained for each plane (axial, sagittal, coronal) over a  $FOV$  of  $70 \times 70$  mm ( $128 \times 128$  points).

Figure 9.7a shows a ZTE image projection corresponding to the whole spherical mini-battery. A gradient shielding through the region between the electrodes is clearly observed. The phenomenon was initially attributed to a capacitive carbon felt effect, but the issue persisted after having connected the output platinum wires between them, short-circuiting the cell. This should rather come from power demanding RF pulses to reach the requested flip angle between the electrodes [Eq. 3.4] and therefore the occurrence of a gradient of flip angle values in different parts of the object.

Moreover, Figures 9.7b and 9.7c show spin echo (MSME) and gradient echo (FLASH) images taken under similar conditions. Both battery shapes are distorted due to magnetic susceptibility artifacts, even though this effect should theoretically be suppressed by spin echo sequences. However, the shielding between the electrodes creates  $B_1$  inhomogeneities and renders the artifact suppression less effective. These inhomogeneities are more pronounced in Figure 9.7b due the significant flip angle values of the sequence, and could possibly be

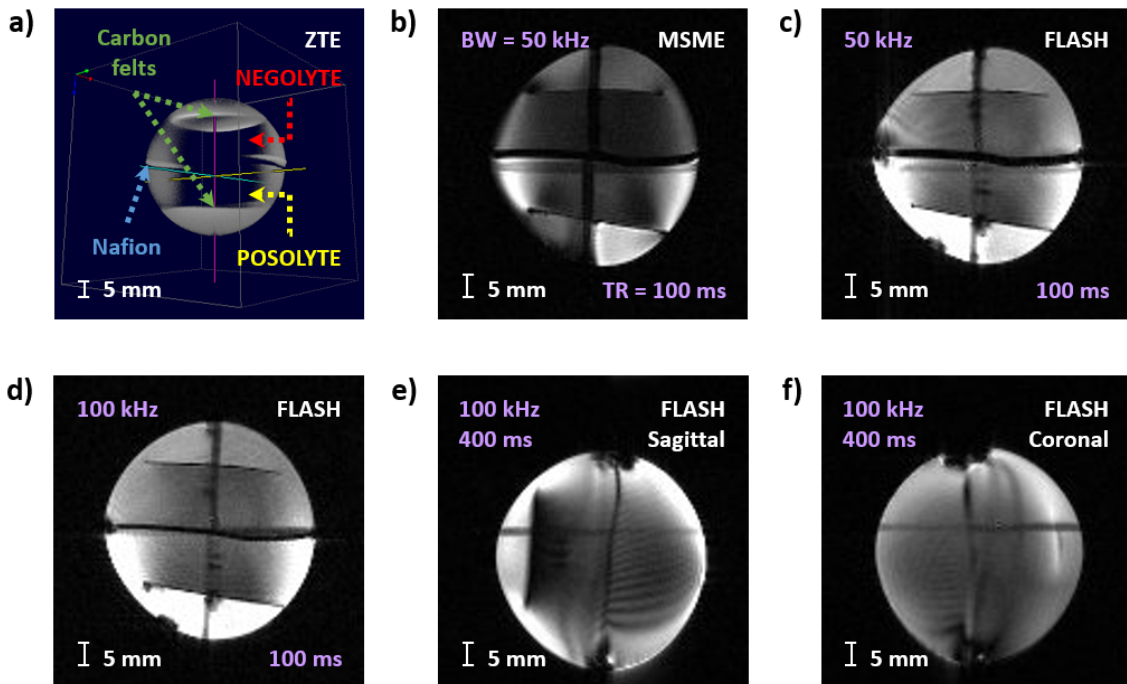


**Figure 9.7:** In situ analysis of a spherical model mini-battery. (a) Projection of a three-dimensional ZTE image of the whole cell where its different components are indicated, including the carbon felt electrodes oriented horizontally with respect to the  $z$  axis; (b-c) Sagittal (b) MSME and (c) FLASH images of the cell taken under the same conditions; (d) Sagittal FLASH image of the cell varying  $BW$  with respect to (c); (e) Sagittal and (f) coronal FLASH images of the cell with the carbon felts oriented vertically.

offset by composite or single adiabatic pulses. On the contrary, Figure 9.7d illustrates an efficient suppression of the magnetic susceptibility artifacts by increasing the excited bandwidth from 50 to 100 kHz and therefore increasing the gradient strength value for a given voxel size [Eq. 5.3]. It may also be pointed out that it is a  $T_1$ -weighted image since the contrast between both compartments is caused by their difference of longitudinal relaxation times, *i.e.* the paramagnetic character of the posolyte molecules (ferro/ferricyanide) in opposition to the diamagnetic ones in the negolyte (AQDS).

Finally, the mini-battery was axially rotated by  $90^\circ$  in order to study the shielding dependence with respect to the  $z$  axis orientation. Figures 9.7e and 9.7f show that this effect is not attenuated when the electrodes are oriented parallel to  $B_0$ . Nevertheless, the contrast between the different zones inside and outside the electrodes is not observed when the slice does not cross the carbon felt (see Fig. 9.7f). One potential solution to the persisting shielding issue is the full replacement of carbon felt sheets by platinum wires (see below), even though their low specific surface area would lead to low current densities and greatly increase the already long cycling time for realistic AQDS concentrations (*e.g.* 0.5 M).

### 9.3.4 Square Model

In the light of the above, a new all-around model depicted in Figure 9.8 was designed. A square-shaped membrane (side = 60 mm) was placed between two 3D-printed pieces assembled with the help of brass washers, nuts and screws ( $\varnothing = 4$  mm). The insertion of two silicone gaskets cut to size on both sides of the Nafion (outer side = 60 mm, inner side = 40 mm), together with a dash of inert vacuum grease (perfluoropolyether-based, Apiezon PFPE 501), ensured watertightness. Each compartment ( $40 \times 40 \times 8$  mm) had one threaded hole in its central area ( $\varnothing = 4$  mm) to drive a current collector (or a nylon screw), and another at the top ( $\varnothing = 3$  mm) to introduce the electrolyte (13 mL). The square mini-battery model was conceived considering the lessons already learned (straightforward Nafion integration, longest voxel dimension in the  $z$  axis, moderate volume for a reasonable cycling time) with the aim of optimizing its components and their arrangement within the limitations of the analytical techniques used.

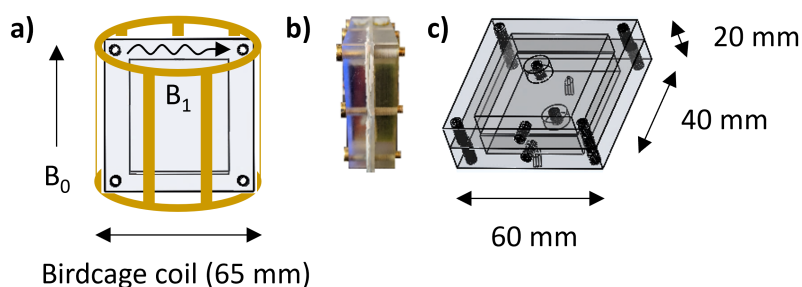


**Figure 9.8:** Square mini-battery model. (a) Depiction of the relative size of the cell inside the probehead coil; (b) Picture; and (c) 3D rendering and dimensions.

## 9.4 Model Optimization according to Magnetic Field Constraints

### 9.4.1 Electrodes and Current Collectors' Choice

#### Platinum electrodes with and without metallic screws as current collectors

A square model mini-battery was built with platinum wires ( $\varnothing = 0.127$  mm, total length = 95 cm) as electrodes in both compartments. The negolyte compartment contained AQDS 50 mM 80%, L-Phe 2.5 mM,  $\text{NaNO}_3$  0.5 M and  $\text{KNO}_3$  1 M, while the posolyte one was composed of trihydrated  $\text{K}_4\text{Fe}(\text{CN})_6$  0.5 M,  $\text{K}_3\text{Fe}(\text{CN})_6$  0.5 M and  $\text{NaNO}_3$  0.5 M. FLASH were performed under the same conditions as in the last experiments ( $BW = 100$  kHz), except for the the  $FOV$  ( $65 \times 65$  mm). Regarding PRESS experiments, all the parameters were similar except  $NS = 1024$  ( $TET = 34$  min 21 s), voxel size ( $2.5 \times 2.5 \times 5$  mm) and  $WS$  (operated at 4.8

ppm over 400 Hz). CV experiments were performed at two different scan rates (10 and 100 mV/s) with the cell (and the rest of the setup) out of the fringe field of the NMR magnet or vertically oriented inside the 7 T magnet in the absence of radio-frequency emission.

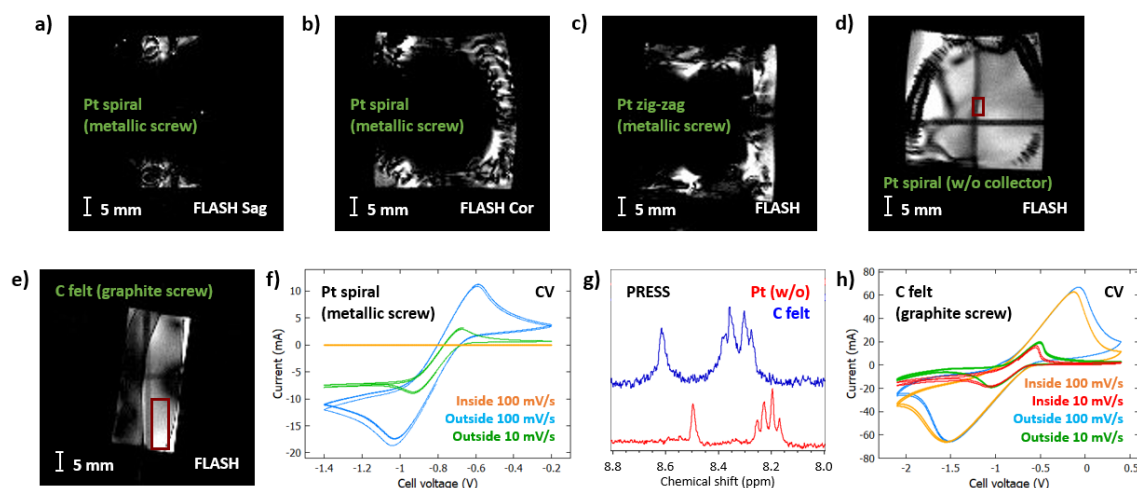


**Figure 9.9:** In situ analysis of a square model mini-battery. (a) Sagittal and (b) coronal FLASH images of the vertically oriented cell using torus-shaped platinum spirals as electrodes and stainless steel screws as current collectors; (c-d) Coronal FLASH images using (c) platinum in a zig-zag pattern and stainless steel screws, and (d) torus-shaped platinum spirals without current collectors; (e) Sagittal FLASH image using carbon felt and graphite screws; (f) Cyclic voltammograms of the cell in (a) and (b) inside and outside the magnet; (g) Localized quinone aromatics region of the PRESS voxels selected in (d) and (e) varying acquisition parameters; (h) Cyclic voltammograms of the cell in (e) inside and outside the magnet.

In a first experiment, stainless steel screws ( $\varnothing = 4$  mm) acted as current collectors and the wires were wound on the screw head to ensure good electrical contact. The screws were driven through the threaded holes with a dash of inert vacuum grease to ensure watertightness, and then isolated from the electrolytes inside the cell with epoxy bi-components glue to avoid side reactions. Additional nuts facilitated the contact between the screw and insulated copper wires outside the cell, which in turn were connected to the potentiostat. The platinum was laid out in torus-shaped spirals to adopt a spatially-distributed arrangement allowing the selection of a homogeneous voxel inside the electrolyte compartment. Figures 9.9a and 9.9b show a total radio-frequency shielding in the central zone of the vertically oriented cell image. Moreover, the cyclic voltammograms in Figure 9.9f display an interruption of the electrical current performance inside the magnet. Taking into account the presumed nonmagnetic nature of the current collectors, this issue was initially attributed to an eventual magnetic field generated inside the torus-shaped spirals. Hence, by arranging the platinum in a zig-zag pattern the electrical charges were supposed to be compensated. However, Figure 9.9c depicts an image of an analogous mini-battery with this specification where the problem persists.

At this point, the stainless steel screws were replaced by previously pierced nylon ones, where the platinum wires passed through and were fastened with silicone sealant. Outside the compartment, the electrodes were brought in direct electrical contact with the copper wires connected to the potentiostat by means of a dash of silicone sealant. Figure 9.9d depicts a



FLASH image of this modified mini-battery model, showing a complete disappearance of the RF shielding. Therefore, this issue was attributed to the use of metallic screws, even though they were made of a reportedly nonmagnetic alloy (*i.e.* austenitic stainless steel type 304). Once the problem was solved, localized spectra with high spectral resolution were obtained over homogeneous small voxels, as shown in Figure 9.9g. While these electrodes eventually provided a solution of the above-described RF shielding as well as better spatial distribution, the operating cell voltage was still subject to high overpotentials (see Chapter 7) at which the platinum has an immediate electrocatalytic effect on the formation of  $H_2$  in aqueous solutions. This phenomenon, so-called hydrogen evolution reaction (HER), was evidenced by the formation of bubbles at the electrode surface during CV. Having all included, carbon felts were henceforth again chosen as electrodes for both compartments and the quinone concentration was minimized to avoid high ohmic drops.

### Carbon felt electrodes with graphite screws as current collectors

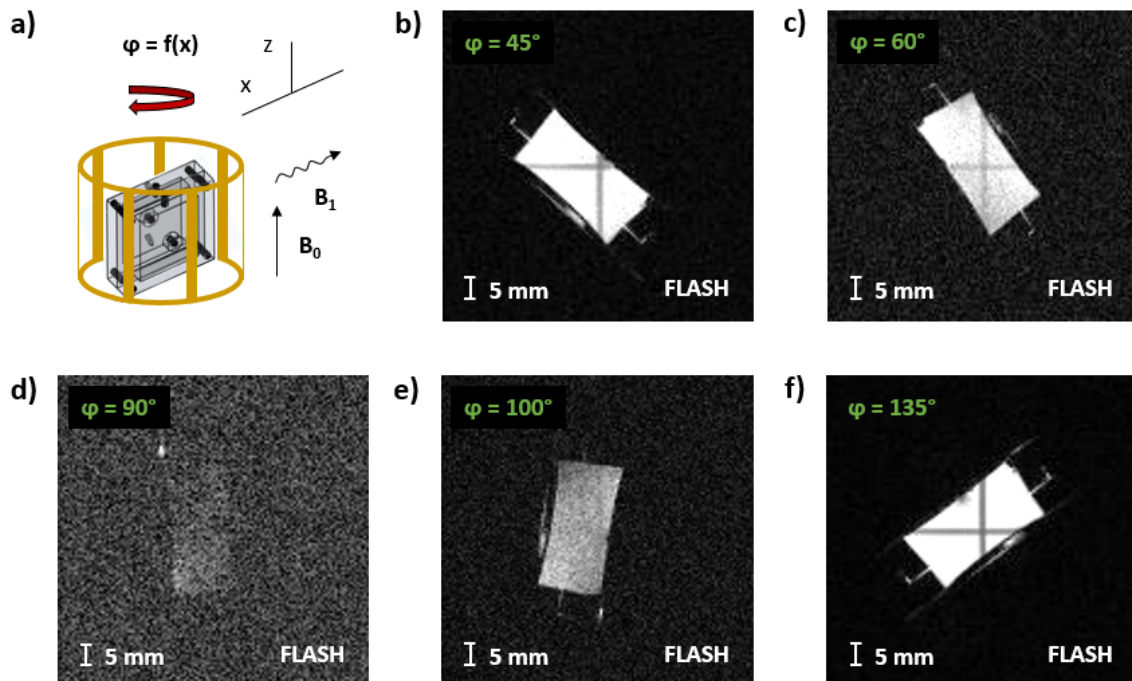
A similar square model mini-battery was assembled, replacing the platinum wires with carbon felts glued to the inner walls of the compartments with silicone sealant. Handcrafted graphite screws ( $\varnothing = 4$  mm) passed through the electrodes acting as chemically inert current collectors. In addition, the AQDS,  $KNO_3$ ,  $K_4Fe(CN)_6$  and  $K_3Fe(CN)_6$  concentrations were varied to 10 mM, 0.5 M, 75 mM and 75 mM, respectively. FLASH and CV experiments were performed under the same conditions (adapting the electrochemical window), while PRESS sequences varied the number of scans (256), the total experiment time (8 min 35 s), the water suppression  $BW$  (600 Hz) and the voxel size ( $5 \times 5 \times 15$  mm).

Figure 9.9e shows a sagittal FLASH image of the vertically oriented cell. It can be observed that the graphite screws partially obstructed the passage of the  $B_1$  field, probably due to the presence of ferromagnetic traces in the high-purity graphite composition (99.9995% purity but with metals basis). Despite this phenomenon and the already mentioned RF shielding between the electrodes, an in situ NMR and electrochemical analysis of the mini-battery is feasible unlike platinum model. PRESS spectra with high resolution were obtained by correctly placing the voxel and slightly lengthening the duration of the second and third pulses (1.05 ms for a  $BW$  of 3238 Hz instead of the standard 1 ms and 3400 Hz) to achieve the desired flip angle value (see paragraph in section 10.2.1). The frequency shift observed between the two curves represented in Figure 9.9g is caused by the difference in AQDS concentration used in each experiment (50 mM for the red wave and 10 mM for the blue one).<sup>[187]</sup>

Figure 9.9h displays the voltammograms inside and outside the magnet. There was a greater peak-to-peak separation with respect to the platinum model (see Fig. 9.9f) since the distance between the electrodes is higher and the concentration of  $KNO_3$  is lower (contributing to increase ohmic and polarization losses, respectively). At both sweep rates, the cathodic current is stronger for a CV inside the 7 T magnetic field than outside. Conversely, the anodic current is weaker and its peak voltage is also negatively shifted. This phenomenon is more pronounced for the lowest sweep rate and appears to match the outlined MHD effect.

## 9.4.2 Orientation of the Mini-Battery

It has been noted that the battery has to be not just aligned with respect to the external magnetic field ( $B_0$ ), but also with respect to the applied radio-frequency one ( $B_1$ ). In this context, a square model mini-battery was built with carbon felts glued to the inner walls of both compartments with silicone sealant. Nylon screws (with Teflon tape to ensure water tightness) substituted the current collectors in order to minimize components contributing to radio-frequency shielding. No membrane was included and the cell was filled with 25 mL of distilled water. FLASH sequences were performed under the same conditions as in the previous experiments, except for the ST (1.5 mm), the TR (250 ms), the TET (32 s) and the  $FOV$  ( $80 \times 80$  mm). The cell was axially rotated varying its orientation with respect to the direction of the applied  $B_1$  field ( $\phi$ ).



**Figure 9.10:** In situ analysis of the orientation of a square model mini-battery. (a) Depiction of the relative orientation of the battery inside the probehead coil ( $B_1$  field direction placed by convention in the  $x$  axis); (b-f) Axial FLASH images when the electrodes surface is rotated with respect to the applied RF field by  $\phi$  equal to (b)  $45^\circ$ , (c)  $60^\circ$ , (d)  $90^\circ$ , (e)  $100^\circ$  and (f)  $135^\circ$ .

Figure 9.10 shows an orientation-dependence study of the radio-frequency penetration into the carbon felt electrodes spacing. The angle  $\phi$  was calculated according to the minimal field propagation observed in Figure 9.10d. This phenomenon probably is caused by the induced eddy currents circulating perpendicular to the RF field direction and producing an opposing magnetic field (Lenz's law), which magnitude is greatly increased on the faces of the conductive electrode.[188, 189] Thus, the maximum penetration happens when the carbon felt surfaces are parallel to the  $B_1$  field propagation direction and therefore the mini-battery orientation at  $\phi = 0^\circ$  (not shown) was carefully considered for further in situ analysis.

### 9.4.3 Electrolytes pH Management

In order to facilitate the NMR real-time monitoring of the anthraquinone (AQ) of interest during the battery operation, a reversible two-electron transfer reaction in a single step process is desired. Various potential scenarios are possible depending on the nature of the solvent used:[190, 191]

- In aprotic solvents, the starting oxidized AQ undergoes two successive one-electron reductions without the participation of protons. The electrochemical steps appear as separate cathodic waves in a voltammogram, the first at lower potential corresponding to the semiquinone anion ( $AQ^{\cdot-}$ ) and the second to the quinone dianion ( $AQ^{2-}$ ). The cations of the supporting electrolyte form ion-pairs with both reduced forms that can potentially be adsorbed at the electrode surface, resulting in new set of peaks at more positive potential versus the free ligand wave.
- In buffered aqueous solvents, the AQ undergoes theoretically a reversible single step two-electron reduction (one wave) as the second electron transfer is thermodynamically more favorable than the first one. In general terms, it can be stated that: (i) under very alkaline conditions (pH greater than  $pK_{a6}$  shown in Figure 9.11), the reduction does not involve protons; (ii) at neutral or near-neutral pH, the reduction is either one proton two-electron ( $pK_{a6} > pH > pK_{a3}$ ) or two-electron without the participation of protons ( $pH > pK_{a6}$ ), and their concentrations depend upon the  $pK_a$ 's values of the hydroquinone phenolic groups; (iii) in acidic conditions ( $pH < pK_{a3}$ ), the reduction is a proton-coupled process. The latter is also observed in the case of unbuffered aqueous solvent with  $[H^+] > [AQ]$ .
- In unbuffered aqueous solvents with  $[H^+] < [AQ]$ , the AQ undergoes an overall two-electron reduction to give a mixture of dianion, protonated monoanion ( $AQH^-$ ) and hydroanthraquinone ( $AQH_2$ ) species depending upon the pH and  $pK_a$ 's values. The mono and dianions are initially stabilized by hydrogen bonding involving water molecules, which consumes solvent protons and creates an effective pH near the electrode greater than the one in the bulk. Therefore, since the redox potential is pH dependent (Pourbaix diagram), it moves to more negative values as the pH increases.

Thus far, no pH buffer was added to the aqueous solutions ( $pH_{ini} = 7$ ) and therefore their pH was prone to change, especially during electrochemical experiments. As already stated, once the available  $H^+$  of the solvent are consumed the remainder AQ is reduced to its deprotonated form at a more negative potential.[192] Thereby, working at the previous reduction potential is probably insufficient to complete the two-electron reaction and the semiquinone anion is potentially generated. This species contains paramagnetic free radicals that drastically broaden the signals hindering the spectral analysis (see Chapter 3.3.2). For this reason, it seems mandatory to buffer the pH value or to be in excess acid condition for future experiments.

AQDS displays a complex behavior in aqueous solutions at concentrations higher than 10 mM due to the emergence of intermolecular reactions, either with another pristine molecule

or with AQDSH<sub>2</sub> to form quinhydrones.[187, 193, 194] These - stacked or oblique - dimers arise from hydrogen bonding and cause the quinone activity to decrease in a process dependent on the AQDS pretreatment and the solution pH. Most of the RFB systems are operated in acidic or alkaline solutions due to faster reaction kinetics. Nevertheless, this has inevitable drawbacks including parasitic oxygen (in alkaline) and hydrogen (in acidic) evolution reactions, the need of corrosion resistant materials (which is not the case of PMMA at basic pH) and potential degradation pathways. Under highly alkaline (pH = 14) [195] and extremely acidic (pH = -1.49) [196] conditions, AQDS undergoes homogeneous disproportionation generating anthrone, which in turn irreversibly dimerizes (unless quick system aeration [197]). Both type of dimers (high concentration and chemical degradation ones) directly impact the energy storage capacity of the electrochemical system. It was believed that the maximum proven capacity of 2,7-AQDS, which is close to 1.5 electrons per molecule (instead of the theoretical 2 e<sup>-</sup>), was reversibly accessible under acidic conditions, whereas only 1 e<sup>-</sup> was accessible under buffered mild-alkaline conditions. However, recent research suggests that 1.5 electrons are also accessed at near-neutral pH, as well as that fully protonated hydroanthraquinone is more prone to dimer formation via hydrogen bonding.[184]

Regarding the polysolte, the chemical stability of the aqueous potassium ferro/ferricyanide solution depends on a wide variety of parameters. In acidic conditions, ferrocyanide is decomposed into aquopentacyanide and hydrogen cyanide (dangerous for humans) in a process favored by ferricyanide traces, diluted solutions, high temperatures (> 50 °C) and sunlight exposure ( $\lambda < 500$  nm).[198] The latter also leads to photo-induced reactions generating electrochemically inactive pentacyanide/iron hydroxide in alkaline [199], near-neutral [200] and unbuffered neutral solutions [201]. Under strong basic condition (pH = 14), an important capacity decay in symmetric cells was observed for different reasons, including a fluctuating membrane resistance during galvanostatic cycling [202] or cell unbalancing due to electroless reduction of ferricyanide via oxygen evolution reaction [203], which is exacerbated as the ratio of the total number of ferricyanide ions to the surface area of high porous carbon electrodes decreases. In summary, K<sub>4</sub>Fe(CN)<sub>6</sub>/K<sub>3</sub>Fe(CN)<sub>6</sub> solution is best used at neutral or near-neutral pH instead of strong acidic or alkaline conditions.

For all these reasons, it seems obvious that there is an interest in operating our battery in a buffered neutral or near-neutral environment. The scheme of the nine-membered square shown in Figure 9.11 summarizes the possible electrode and proton-transfer reactions (listed horizontal and vertically, respectively) as a function of the redox potentials (vs SCE) and pK<sub>a</sub> values. In the absence of large applied cell overpotentials to minimize side reactions, the chosen pH must ensure reversible oxidation-reduction reactions in a single step process. This allows one to avoid the formation of free radical intermediates and thereby the rapid loss of proton signals due to intermolecular electron-transfer interactions between the diamagnetic and paramagnetic ions.[204] Although we do not have the possibility of coupling our system to EPR techniques [171], we might actually be able to detect paramagnetic species through monitoring of T<sub>1</sub> and T<sub>2</sub> water signal in each compartment (*i.e.* RAREVTR sequences).

In the light of the above, a sodium acetate buffer (pH = 4.7) was chosen for the subsequent

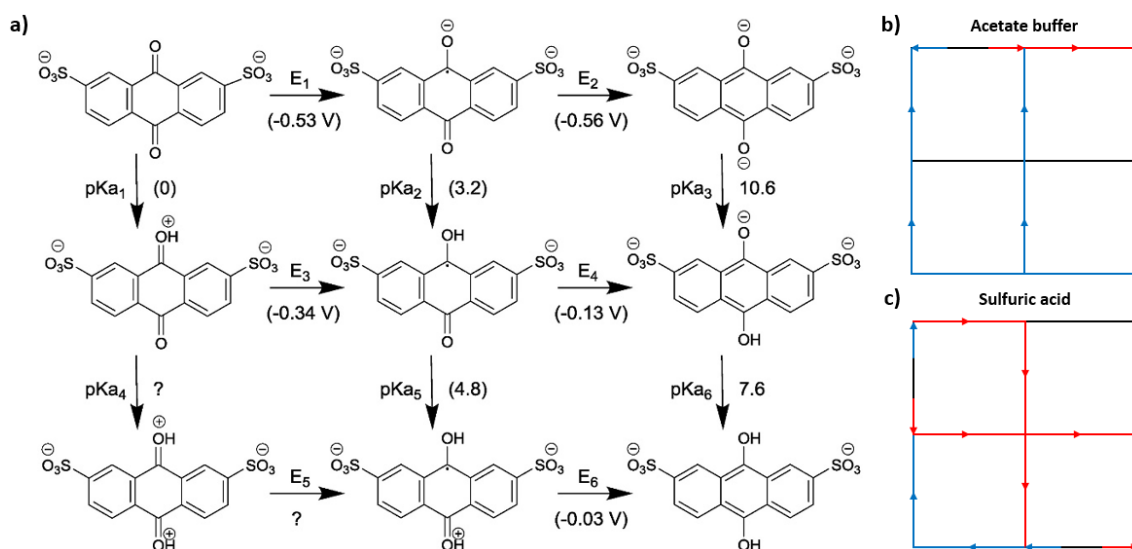


**Figure 9.11:** Framework for the reduction and oxidation of 2,7-AQDS. (a) Scheme of squares where the potentials referenced against the saturated calomel electrode (SCE); (b) Assumed scenario for the reduction (red lines) and the oxidation (blue) pathways in acetate buffer; (c) Assumed scenario for the reduction (red lines) and the oxidation (blue) pathways in sulfuric acid. It is worth noting that some reported reduction potentials and  $pK_a$  values are taken from 2,6-AQDS and assumed to be very close. Adapted from [194], Copyright 2019, with permission from Elsevier.

experiments. A square model mini-battery was built with carbon felt glued to the inner walls as electrodes and graphite screws as current collectors. The negolyte compartment contained AQDS 25 mM 80%,  $KNO_3$  1.7 M,  $CH_3COOH$  0.3 M and  $CH_3COONa$  0.3 M, while the posolyte one was composed of trihydrated  $K_4Fe(CN)_6$  0.1 M,  $K_3Fe(CN)_6$  0.1 M,  $KNO_3$  1 M,  $CH_3COOH$  0.3 M and  $CH_3COONa$  0.3 M. To simplify the cell design,  $KNO_3$  was used as supporting electrolyte in both compartments. To test the correct operation of the proposed chemical system, a quick electrochemical reduction was carried out outside the magnet. A cyclic voltammetry was used at 5 mV/s to identify the cathodic and anodic peaks. At this point, a chronoamperometry (0 V) was performed in order to reoxidize the potentially reduced molecules during the CV and regain a battery state-of-charge value equal to 0%. Then, a CA was conducted at -1.2 V with agitation (*i.e.* attaching the battery to a vortex mixer) with the goal of inducing turbulence that accelerates the electrolysis process. A LSV (Linear Sweep Voltammetry) was performed at the same scan rate of the previous CV (5 mV/s) so as to confirm the battery SoC, and it was stopped as soon as possible in order to avoid altering it. Finally, an ex situ analysis of the product was carried out by withdrawing a 600  $\mu$ L negolyte sample with a syringe under an inert atmosphere, introducing in a borosilicate glass J Young NMR tube (OD = 5 mm) and measuring at room temperature on a narrow-bore 11.7 T spectrometer (NS = 8, TET = 23 s).

In aqueous media, the potential varies with pH in a Nernstian manner commonly displayed in Pourbaix diagrams. The CV in Figure 9.12a depicts a shift to more positive potential values with respect to the unbuffered solution, which indicates that the redox reaction is easier thermodynamically. However, the slight increase in peak-to-peak separation ( $\Delta E_P$ ) suggests

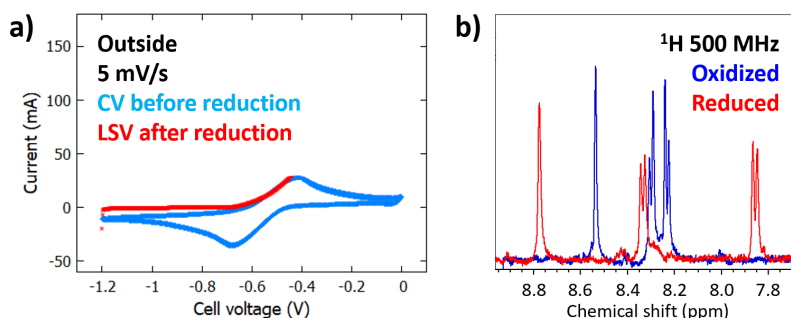


**Figure 9.12:** Ex situ analysis of a square model mini-battery with sodium acetate buffer (pH = 4.6). (a) Cyclic voltammogram and linear sweep voltammogram before and after performing a turbulence-induced chronoamperometry at -1.2 V during 35 minutes, respectively; (b) Aromatic region of the 2,7-AQDS proton spectra measured at 500 MHz before (oxidized) and after (reduced) the CA.

that the system is subject to more polarization losses (see Chapter 7.1.2), necessitating a high enough potential step to reach fast electron transfer kinetics. It can also be considered a chemically reversible process as the ratio of anodic and cathodic peak current is close to one ( $i_{Pa}/i_{Pc} \approx 1$ ). With this in mind, the potentiostatic reduction was performed at -1.2 V for 35 minutes (*i.e.* complete electrolysis). A rather high potential value was chosen in order to accelerate reaction kinetics under the risk of favouring HER. A total charge of 50 coulombs passed through the battery ( $Q_{exp}$ ), which differ from the theoretical calculated value ( $Q_{th} = nFN = 2 \times 96485 \times 0.025 \times 0.013 = 63C$ ) certainly because the AQDS impurities (20%) are electrochemically inactive. Both the LSV and the proton NMR spectra (see Fig. 9.12b) confirm that the reduction was accomplished, thereby validating sodium acetate as a suitable pH buffer for further experiments.

Having all included, it has been decided to delocalize the conversion cell with the dual purpose of minimizing persistent homogeneity problems when performing in-situ and operando analysis, as well as designing an actual flow battery storage system (see Chapter 10).

# 10 - Complete Redox Flow Battery

## 10.1 Single Tank RFB

In a first approach, a single tank was placed in the NMR detection zone (see Figures 10.1a and 10.1b) in order to optimize measurement performance and implement a genuine hybrid flow battery. The tank (ID = 27 mm, height = 38 mm; V = 22 mL) was connected by luer lock connectors and silicone tubing (ID = 2 mm, length = 150 mm) to the conversion cell. The latter consisted of a square model mini-battery with carbon felt as electrodes and graphite screws as current collectors, which was modified in order to couple the circulation system. The solution was put into circulation via a bubble pump where an inert carrier gas (N<sub>2</sub>) established a closed-loop fluid flow circuit from the bottom to the top of the cell. The gas outlet in the tank was far enough from the inlet, enabling high-speed bubbling. Moreover, a one-way luer lock check valve was placed in the gas outlet ensuring an inert atmosphere inside the tank, which becomes even more necessary with the reduced AQDS as it is an oxygen scavenger extremely sensitive to its content in solution.[205]

A syringe pump (Harvard Apparatus PHD 2000) was initially used to put in motion the solution, accurately controlling the infusion rate of the carrier gas. With the aim of checking the correct operation of the bubble pump, the appearance of a witness molecule in the tank (20 mL) was monitored while bubbling at 2 mL/min, which means one train of bubbles each 7-8 s. An aqueous solution of L-phenylalanine at 10 mM was used for this purpose, at the start only present in a conversion cell (13 mL). Consecutive PRESS<sup>1</sup> spectra represented in Figure 10.1c confirmed that the molecule appeared after 7 minutes (*i.e.* 14 mL N<sub>2</sub> injected) and its concentration in the tank was stabilized after 30-40 minutes. On the other hand, a flow-compensated gradient echo method so-called FLOWMAP<sup>2</sup> enables the mapping of flow velocity components through the use of bipolar gradient pulses during the encoding period. An analogous flow battery (33 mL) containing low quantities of L-phenylalanine (2.5 mM) and 2,7-AQDS 80% (2.5 mM) was set into motion and the above-mentioned sequence showed the bubble trajectories at 2 mL/min (see Fig. 10.1d). In addition, it was possible to obtain localized spectra (PRESS<sup>3</sup>) not only in static condition but also in dynamic condition far from the bubble trajectories, as shown in Figure 10.1e (voxel in Fig. 10.1f).

However, the kinetics of the planned redox reaction would be rather slow at such limited circulation rates. Hence, it was decided to connect the system to the nitrogen line of the laboratory instead of the syringe pump and regulate the bubbling rate with a flowmeter. In doing so,

---

<sup>1</sup>Voxel = 5 × 5 × 10 mm, TE = 15 ms, TR = 1327 ms, NS = 128, TET = 2 min 50 s, BW = 6061 Hz, 4096 points, WS = 400 Hz at 4.7 ppm

<sup>2</sup> $\theta = 30^\circ$ , TE = 5 ms, TR = 100 ms, NS = 1, TET = 51 s, FOV = 45 × 45 mm, image size = 128 × 128, ST = 1 mm

<sup>3</sup>Voxel = 5 × 5 × 10 mm, TE = 15 ms, TR = 1327 ms, NS = 2048, TET = 45 min 15 s, BW = 6061 Hz, 4096 points, WS = 400 Hz at 4.7 ppm

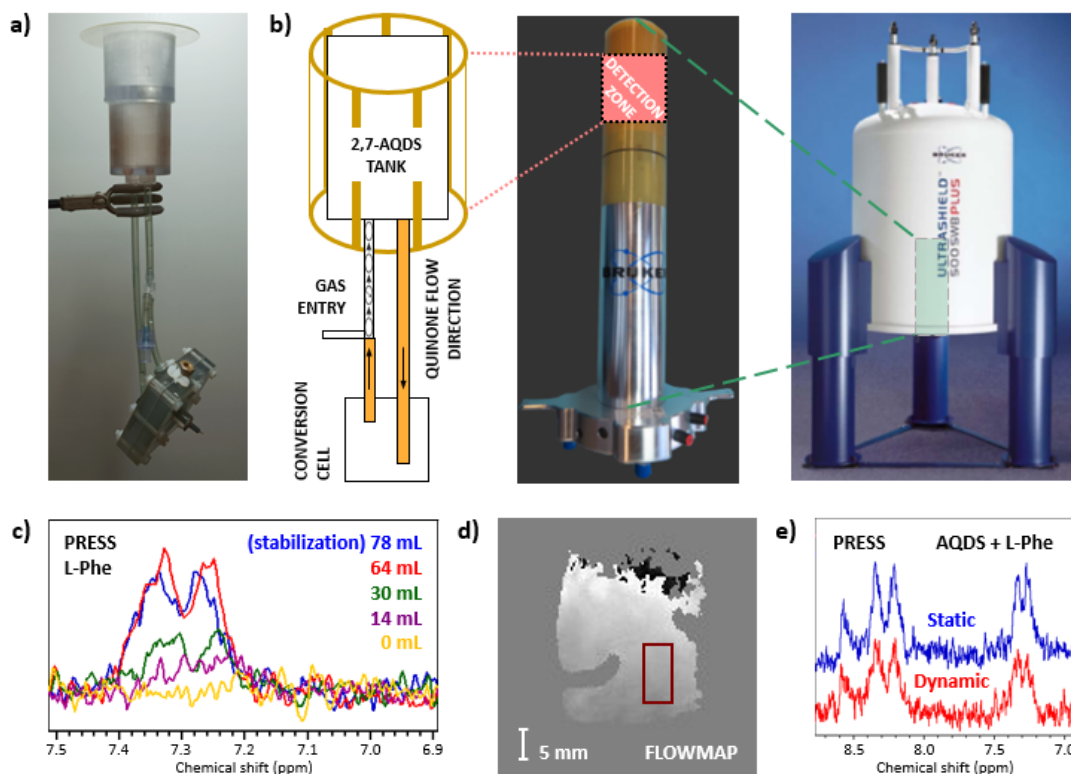


**Figure 10.1:** Operating principle of a single tank RFB. (a) Picture; (b) Relative size of the tank inside the probehead coil and system setup; (c) Localized aromatic region of a PRESS previously selected voxel during the bubble pump test; (d) Coronal FLOWMAP image of the tank while bubbling at 2 mL/min and voxel placement for (e); (e) Localized aromatic region of the PRESS voxel selected in (d) in dynamic (bubbling at 2 mL/min) and static conditions.

the negolyte could be subject to a flow circuit that increased the number of molecules reacting at the electrodes per second minimizing cycling time, even though it was not straightforward anymore to obtain localized spectra. In order to ensure a complete electrolysis of the total volume of quinone (capacity limiting side), the concentration of potassium ferro/ferricyanide was increased with respect to the previous experiments. The potassium nitrate concentration was accordingly increased in the negolyte to compensate the difference of osmotic pressure between compartments. Then, a new battery was prepared in which the negolyte compartment contained AQDS 25 mM 80%,  $\text{KNO}_3$  2.4 M,  $\text{CH}_3\text{COOH}$  0.3 M and  $\text{CH}_3\text{COONa}$  0.3 M, while the posolyte one was composed of trihydrated  $\text{K}_4\text{Fe}(\text{CN})_6$  0.2 M,  $\text{K}_3\text{Fe}(\text{CN})_6$  0.2 M,  $\text{KNO}_3$  1 M,  $\text{CH}_3\text{COOH}$  0.3 M and  $\text{CH}_3\text{COONa}$  0.3 M. The total negolyte volume was 25 mL (cell + tank not filled) and posolyte one 12 mL (cell). The reservoir was purged with nitrogen to remove oxygen before battery cycling.

Figure 10.2a shows a coronal FLASH<sup>4</sup> image recorded in static conditions, in which not only the negolyte inside the tank was imaged but also the one along tubing. A double potential step chronoamperometry (DPSCA) was conducted under dynamic conditions first at -1.2 V (reduction) and then at 0 V (oxidation) inside the magnet, with the aim of achieving a complete

<sup>4</sup> $\theta = 30^\circ$ , TE = 4 ms, TR = 200 ms, NS = 1, TET = 26 s, FOV = 65 × 65 mm, IS = 128 × 128, BW = 50 kHz



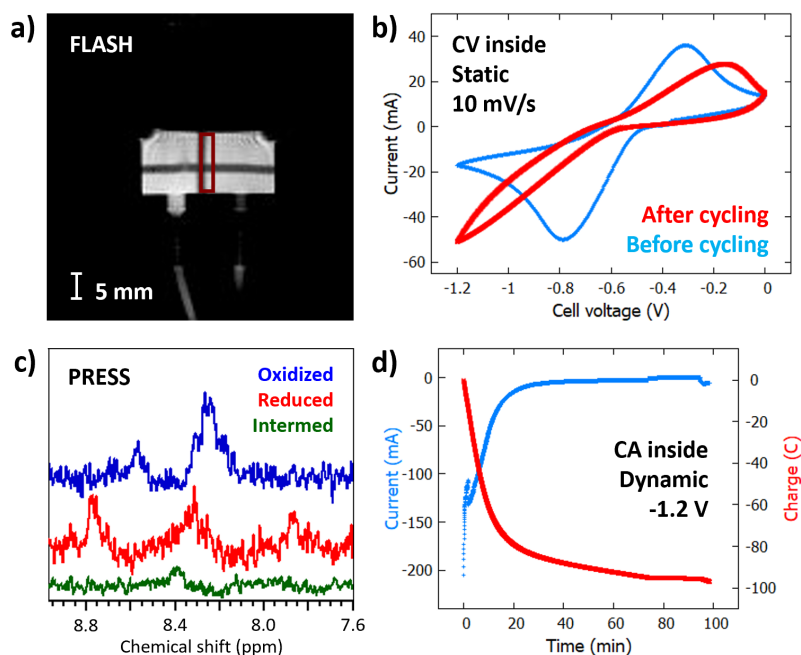


**Figure 10.2:** In situ analysis of a single tank RFB. (a) Coronal FLASH image of the tank and voxel placement for (c); (b) Cyclic voltammograms before and after performing a DPSCA; (c) Localized aromatic region of the PRESS voxel selected in (a) before (oxidized) and after (reduced) the reduction step, as well as after the reoxydation one (intermediate); (d) Chronoamperogram of the potentiostatic reduction depicting current and charge as a function of time.

redox cycle. PRESS<sup>5</sup> sequences were performed at different points of the first potentiostatic reduction step (depicted in Figure 10.2d). The localized spectra were obtained stopping the flow after each reduction/oxidation in order to improve spatial homogeneity. While the water peak intensity was constant, no peaks in the aromatic region were observed. Nonetheless, NMR signal corresponding to the reduced quinone form (see Fig. 10.2c) was recovered at the end of the electrolysis ( $\frac{Q_{\text{exp}}}{Q_{\text{th}}} 100 = \frac{96C}{121C} 100 = 79\%$  with 20% of impurities). From now on, the imaging and localized spectroscopy methods displayed have been conducted in static mode, unless otherwise stated.

Furthermore, the oxidation step of the DPSCA suddenly stopped after 10 minutes (40 coulombs), leading to the intermediate state presented in Figure 10.2c. Moreover, a completely different CV was obtained with respect to the initial one (after which a CA at 0 V was conducted to regain a battery SoC = 0%), both of them performed inside the magnet in static mode. Figure 10.2b shows that the oxidation peak shifted to more positive values and the reduction one seems to have disappeared, although probably shifted to much more negative values leading to a practically irreversible process. At this point, the battery was taken out from the imager and visible precipitates were observed all along the negolyte circuit. Taking into account the high potassium nitrate concentration together with the high potassium atom size, it was concluded that the large number of big ions limited the solubility of the quinone ob-

<sup>5</sup>Voxel = 2.5 × 2.5 × 12 mm, TE = 20 ms, TR = 1336 ms, NS = 128, TET = 2 min 51 s, BW = 6061 Hz, 4096 points, WS = 320 Hz at 4.7 ppm

structuring tubing and luer lock connectors. Therefore, a new model incorporating a second tank was designed with the purpose of operating with larger posolyte volume, allowing to minimize  $K_4Fe(CN)_6/K_3Fe(CN)_6$  concentrations and thereby the  $KNO_3$  one in the negolyte. Likewise,  $NaNO_3$  was again considered as supporting electrolyte since the sodium atom size is smaller than the potassium one.

## 10.2 Double Tank RFB and Conversion Cell Types

As proposed in the previous section, a second tank containing the posolyte (ID = 5 mm, height = 21 mm;  $V = 28$  mL) was incorporated surrounding the negolyte one ( $15 \times 42.5 \times 21$  mm;  $V = 13$  mL), and the solution was put into circulation by an identical bubble pump system. As shown in Figure 10.3a, the negolyte was housed in the inner compartment with the aim of minimizing magnetic susceptibility artifacts (*e.g.* air interface) if big voxels are selected when performing localized spectroscopy. In the beginning, two different types of conversion cell have been conceived and fully adapted to the double tank: the 3D-printed toric cell and the full graphite-based cell.

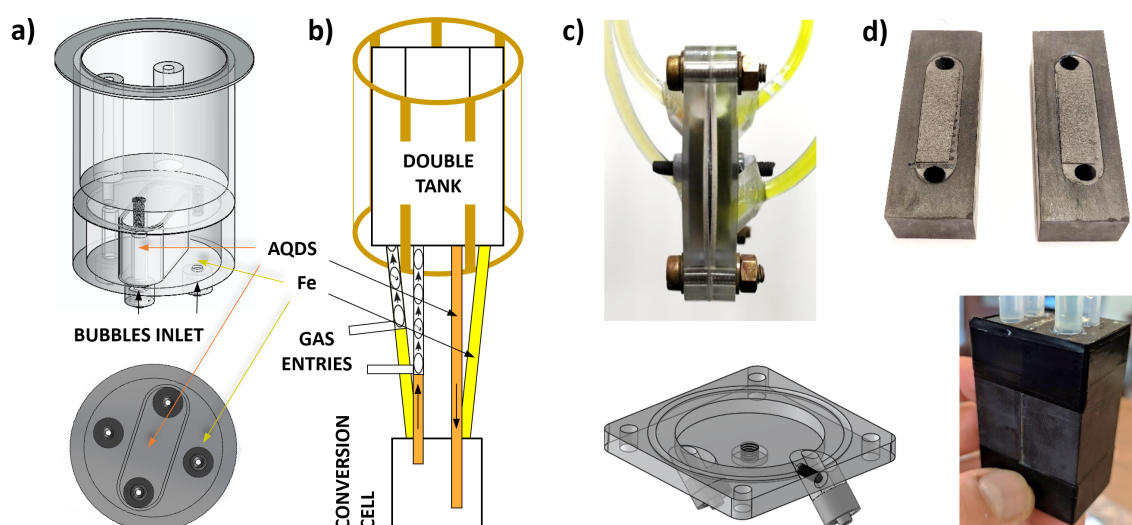


**Figure 10.3:** Complete RFB and conversion cell types. (a) 3D rendering of the double tank indicating its different components; (b) Relative size of the tank inside the probehead coil; (c) Picture and 3D rendering of the toric cell; (d) Pictures of the full graphite-based cell disassembled (upper panel) and assembled (lower panel).

The toric model, depicted in Figure 10.3c, was devised as an evolution of the square one. A circular-shaped membrane ( $\varnothing = 47$  mm) was placed between two 3D-printed pieces ( $60 \times 60 \times 5$  mm) and fastened with a silicone gasket cut to size (outer diameter = 44 mm, inner diameter = 50 mm, thickness = 1 mm) in one of the sides. The cell incorporated a Viton O-ring ( $\varnothing = 55$  mm) that minimizes fluid leaks and was assembled with the help of brass washers, nuts and screws ( $\varnothing = 4$  mm). Each compartment (ID = 42 mm, height = 4 mm) had one threaded

hole at the top ( $\varnothing = 3$  mm) to introduce the electrolyte (5.5 mL). A graphite current collector was driven through a stack of carbon felt electrodes ( $\varnothing = 40$  mm) and a hole in the central area of the compartment ( $\varnothing = 4$  mm), together with a dash of inert vacuum grease to ensure watertightness. Additional brass nuts facilitated the contact between the graphite screw and insulated copper wires outside the cell, which in turn were connected to the potentiostat. The distance between the electrodes was minimized to limit the ohmic drop ( $iR$ ), reaching values of uncompensated resistance about 10-40  $\Omega$ . Nonetheless, when several carbon felt electrodes are stacked raising the total active surface area, and therefore the current density, the ohmic drop also increases.

On the other hand, the graphite model shown in Figure 10.3d was handcrafted from two graphite blocks ( $65 \times 24 \times 18$  mm). Each one had an inlet channel ( $\varnothing = 5$  mm, length = 48-53 mm) and an outlet channel ( $\varnothing = 5$  mm, length = 15-18 mm) that communicated to the bottom and the upper part of the compartments ( $44 \times 12 \times 0.5$  mm), respectively. Two carbon felt rectangles ( $34 \times 10$  mm) were placed inside each compartment increasing the electrode active surface area. The total volume inside each block (channels + compartment) stands at about 1 mL. A rectangular-shaped membrane ( $65 \times 24 \times 0.1$  mm) was placed between the compartments with a dash of inert vacuum grease at the edges, and all the parts were held together by means of insulating tape. Two aluminum magnesium braided meshes ( $50 \times 5$  mm) were put in contact with the graphite block surface acting as current collectors. Additional brass screws, nuts and washers facilitated the contact between the meshes and insulated copper wires with nonmagnetic brass washers welded at the end. The latter were in turn connected to the potentiostat. The distance between the electrodes is minimal and the uncompensated resistance seldom exceeds 1  $\Omega$  (*i.e.* overpotentials < 100 mV for 100 mA currents).

## 10.3 Complete RFB Operation

### 10.3.1 3D-printed Toric Model

A complete redox flow battery with a toric conversion cell (see Fig. 10.4a) was prepared with the negolyte compartment containing AQDS 25 mM 80%,  $\text{NaNO}_3$  0.5 M,  $\text{KNO}_3$  0.7 M,  $\text{CH}_3\text{COOH}$  0.3 M and  $\text{CH}_3\text{COONa}$  0.3 M, while the posolyte was composed of trihydrated  $\text{K}_4\text{Fe}(\text{CN})_6$  0.1 M,  $\text{K}_3\text{Fe}(\text{CN})_6$  0.1 M,  $\text{NaNO}_3$  0.5 M,  $\text{CH}_3\text{COOH}$  0.3 M and  $\text{CH}_3\text{COONa}$  0.3 M. The total negolyte volume was 15 mL and the posolyte one 20 mL. Each compartment comprised two carbon felt electrodes in order to raise the current density accelerating reaction kinetics.

Figures 10.4b and 10.4c show axial and coronal FLASH<sup>6</sup> images of the double tank where the contrast between both compartments was caused by their difference of longitudinal relaxation times. CV were performed inside the magnet in static and dynamic conditions at 20 mV/s

---

<sup>6</sup> $\theta = 30^\circ$ , TE = 4 ms, TR = 200 ms, NS = 1, TET = 26 s, FOV =  $65 \times 65$  mm, IS =  $128 \times 128$ , BW = 50 kHz

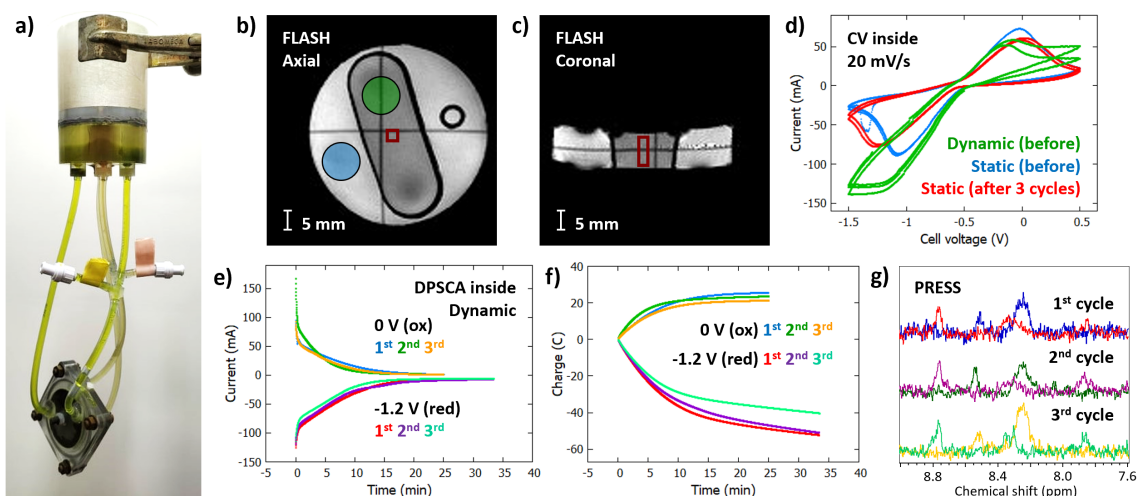


**Figure 10.4:** In situ analysis of a double tank RFB with a 3D-printed toric cell. (a) Picture; (b) Axial and (c) coronal FLASH images of the tank with voxel placement for (g) and blue/green circles corresponding to the spot of RAREVTR measurements; (d) Cyclic voltammograms before and after performing the three consecutive redox cycles; (e-f) Chronoamperogram of the DPSCA, depicting (e) current and (f) charge as a function of time; (g) Localized aromatic region of the PRESS voxel selected in (b-c) as a function of the number of cycles.

(see Figure 10.4d). It can be observed that the cathodic current intensity was higher when the bubble pump was in operation. This may be explained by the fact that more starting (oxidized) AQDS molecules made contact with the same electrode area per second. Once reduced, they left its surface arriving new predominantly oxidized molecules to it and enhancing the reduction reaction rate. It can be also stated that mass transport is faster than electron-transfer as no diffusion region was observed (Nernst equation not applicable). Conversely, weaker anodic currents are found, which implies slower kinetics of the oxidation reaction and therefore a chemically disfavored process on behalf of the reduction one ( $i_{Pa}/i_{Pc} < 1$ ). The difference of peak voltage in both segments ( $\Delta E_P$ ) barely changed depending on the pump operation. Once the CV study completed, a CA at 0 V was conducted to regain a battery state-of-charge value equal to 0%.

Subsequently, consecutive DPSCA were performed in the same conditions as in the previous potentiostatic experiments (-1.2 V and 0 V) together with PRESS<sup>7</sup> sequences. Figure 10.4g confirms that three consecutive redox cycles were accomplished as the oxidized and reduced spectra were obtained at the end of each step. It can be noted that the spectral resolution and the SNR can be enhanced by manually local shimming and increasing the number of scans, respectively. However, minimizing the amount of time the reduced product existed in solution was prioritized as it is an oxygen scavenger. Regarding the chronoamperograms shown in Figures 10.4e and 10.4f, the total charge observed during the first reduction (52 C) was lower with respect to the theoretical calculated value (72 C) for the reasons previously stated (impurities). However, the difference of coulombs is much bigger in the case of the first reoxidation step (25 C), suggesting a dimerization mechanism where only one AQDS electron

<sup>7</sup>Voxel =  $3 \times 3 \times 8$  mm, TE = 20 ms, TR = 1336 ms, NS = 128, TET = 2 min 51 s, BW = 6061 Hz, 4096 points, WS = 310 Hz at 4.7 ppm

over the two was accessible. This phenomenon was also observed during the second cycle in a reproducible manner, dramatically decreasing the current intensity during the third one. This current drop was also observed in a CV conducted after the third reoxidation (see Fig. 10.4d).

It is well known that an electrochemically active dimer was formed in acetate buffer, which produces the observed solution color changing from yellow to green.[206] In principle, it is considered a charge-transfer complex of the anthraquinone and hydroxyanthraquinone, rather than a dimer of a semiquinone radical that could lead to the previously suggested degradation pathways (see Chapter 9.11). With the aim to rule out the formation of the latter, RAREVTR<sup>8</sup> (Rapid Imaging with Refocused Echoes with Variable Repetition Time) sequences measured  $T_1$  and  $T_2$  at different state-of-charge (SoC) of the battery in a similar experiment to the one showed in Figure 10.4. Regarding the negolyte (green circle in Fig. 10.4b),  $T_1$  values oscillated between 2400 and 2800 ms depending on the circle position inside the tank, while  $T_2$  values were found about 850-1050 ms. As for the posolyte,  $T_1 = 900-1100$  ms and  $T_2 = 180-200$  ms. The results showed that no variation of the transversal nor longitudinal relaxation times was produced in none of the compartments, which means that the capacity fade observed during the third reduction is not associated with dimers arising from semiquinones but potentially from other type of dimers. Despite this, it remained impossible to obtain NMR signal coming from AQDS in SoC different from those of the fully oxidized (< 5%) and fully reduced (> 95%) forms within reasonable experimental times (< 1 h).

## Magnetohydrodynamic Effect

A similar mini-battery to that of the previous experiment was built except that this time a thermocouple was taped to the surface of the conversion cell negolyte side and it was connected to the Autolab PGSTAT101 potentiostat. Cyclic voltammetry experiments were performed at 20 mV/s with the battery (and the rest of the setup) out of the fringe field of the NMR magnet and inside it with the battery oriented parallel to the static magnetic field. Between each experiment, the bubble pump was operated for thirty seconds in order to renew the solution in contact with the carbon felt electrodes.

The monitored temperature of the compartment of interest surface did not change during experiments (21 °C) and therefore the phenomenon described below did not arise from temperature evolution. The voltammograms displayed in Figure 10.5a show that  $\Delta E_P$  was higher after having subjected the system to the magnetic field, both inside ( $t = t_1$ ) and outside the magnet ( $t = t_2$ ). This higher overall battery polarization once outside the magnet could be related to changes in the potential difference between the electrode and the solution or in the reaction mechanism. In addition, the cathodic current was stronger and the peak voltage shifted in the case of the CV inside the magnet compared to the one outside, as already noted earlier (*cf.* Chapter 9.4.1). This effect may be explained by the action of Lorentz force ( $F_L$ ) on mass transport, which leads to faster ions migration between the electrodes enhancing the

---

<sup>8</sup>TE = 60 ms (8 phase encoding echoes with 20 ms of spacing), TR = 609-4000 ms (5 different experiments), NS = 4, TET = 8 min 50 s, FOV = 65 × 65 mm, IS = 128 × 128, BW = 50 kHz

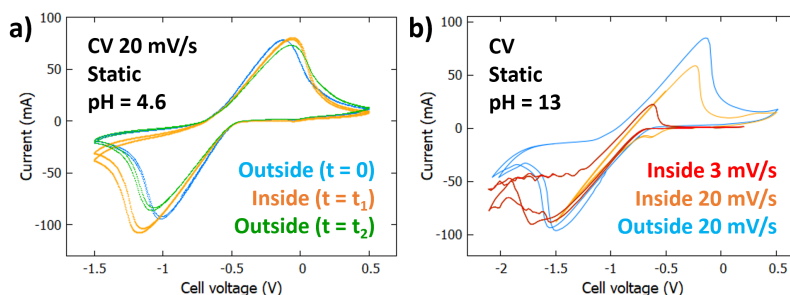


**Figure 10.5:** Analysis of the MHD effect in a double tank RFB with a 3D-printed toric cell at different pH. (a) Cyclic voltammograms inside and outside the magnet at 20 mV/s in acetate buffer solutions (pH = 4.6); (b) Cyclic voltammograms inside and outside the magnet at different scan rates in alkaline solutions (pH = 13).

reaction rate. The same experiments were conducted axially rotating the conversion cell by 90° inside the magnet with similar results. In the present case, the magnitude of the effect is not minimized when the charge transport is parallel to the  $B_0$  direction as suggested in the literature.

On the other hand, an analogous system was prepared by replacing the sodium acetate buffer ( $\text{CH}_3\text{COOH}$  0.3 M +  $\text{CH}_3\text{COONa}$  0.3 M) with  $\text{KOH}$  0.1 M in both compartments. The  $\text{KOH}$  concentration was chosen according to a compromise solution between maintaining an alkaline environment and ensuring the integrity of the battery materials susceptible to alkali attacks (*e.g.* PMMA). Cyclic voltammetry experiments were performed at 20 mV/s outside the magnet and at 3 and 20 mV/s inside parallel to  $B_0$ . The bubble pump was operated as previously described between each experiment. Figure 10.5b shows that at 20 mV/s the anodic current was weaker inside the magnet and the voltage peak barely shifted, while the cathodic one exceeded the acceptable current limits of the potentiostat (100 mA). At 3 mV/s the cathodic current inside the magnetic field was of the same order of magnitude as that at 20 mV/s outside the magnet, and the peak voltage shifted to slightly more negative values. Besides, the anodic current was far less intense and the peak voltage shifted to much more negative values and thereby also the cell OCP value. The huge increase of the cathodic current observed in Figure 10.5b (pH = 13) contrasts strongly with the slight noticed in Figure 10.5a (pH = 4.6), which suggests the dependence of the MHD effect with the pH of the solution. This phenomenon may be related to the deprotonation of the reduced form of the anthraquinone under alkaline conditions (dianions), which gives rise to induced giant magnetocurrent in electrochemical cells.<sup>[207]</sup>

### 10.3.2 Full Graphite-based Model

A complete redox flow battery with a graphite-based conversion cell (see Fig. 10.6a) was built with the same electrolyte compositions and concentrations as in the experiment represented in Figure 10.4. The total negolyte volume was 14 mL and the posolyte one 20 mL. The sagittal

FLASH<sup>9</sup> image shown in Figure 10.6b was selected as pilot image for PRESS<sup>10</sup> sequences. Cyclic voltammetry experiments were performed at 20 mV/s outside and inside the magnet, and in each case with and without operating the bubble pump (see Figure 10.6c). With regard to the fluid flow circuit operation, the same conclusions as in Section 10.2 can be drawn, except for the fact that using the graphite model both anodic and cathodic reactions were diffusion-limited (Nernst equation can be applied). The high area-to-volume ratio of the graphite cell may explain the faster electron-transfer reaction with respect to mass transport, together with the fact that bubbling induced less turbulence in its nearly planar compartments (0.5 mm thick) in opposition to the bigger parallelepiped-shaped ones of the toric cell. On the other hand, the voltammograms did not evolve depending on the magnetic field and the curves can be virtually overlapped, suggesting that no MHD effect was observed in such systems. This may be explained by the fact that the pathways for the charge transport between electrodes are so short that the induced Hall effect (*i.e.* the potential difference across the conducting) is minimal. Once the CV study completed, a CA at 0 V was conducted to regain a battery state-of-charge value equal to 0%.

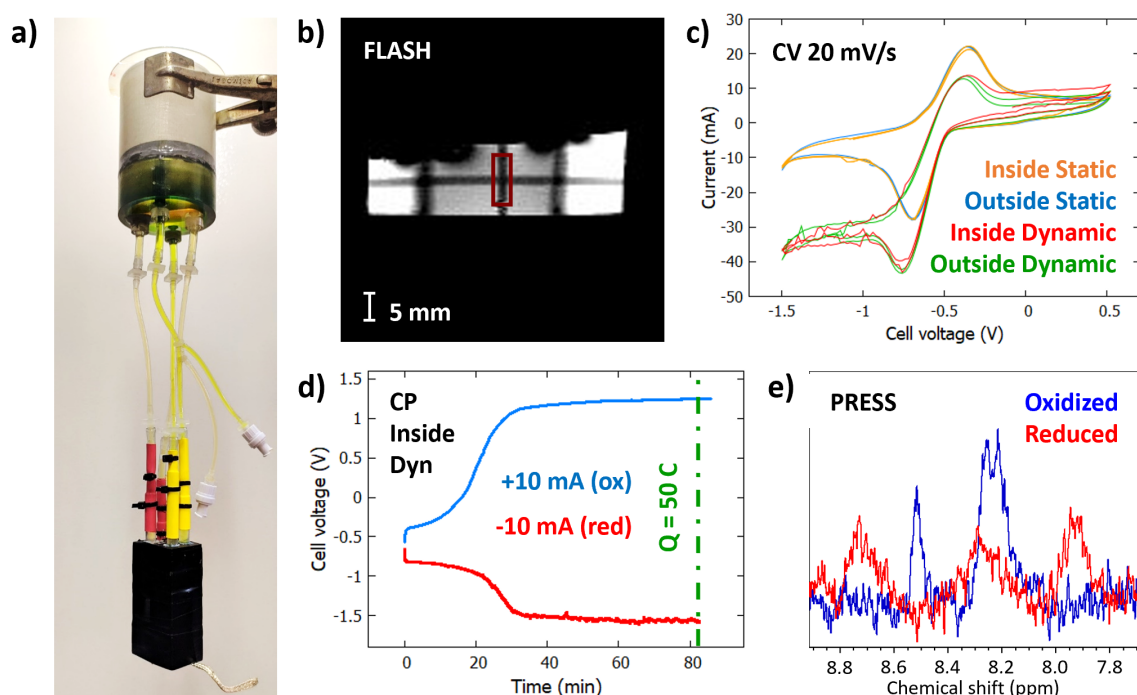


**Figure 10.6:** In situ analysis of a double tank redox flow battery with a full graphite-based cell. (a) Picture; (b) Sagittal FLASH image of the tank with voxel placement for (e); (c) Cyclic voltammograms at 20 mV/s inside and outside the magnet, both in static and dynamic conditions; (d) Chronopotentiogram of the galvanostatic reduction and oxidation performed inside the magnet at -10 mA and +10 mA, respectively; (e) Localized aromatic region of the PRESS voxel selected in (b) before (oxidized) and after (reduced) the galvanostatic reduction.

Furthermore, two consecutive CP (Chronopotentiometry) were performed in dynamic con-

<sup>9</sup> $\theta = 30^\circ$ , TE = 4 ms, TR = 100 ms, NS = 1, TET = 13 s, FOV = 65 × 65 mm, IS = 128 × 128, BW = 100 kHz

<sup>10</sup>Voxel = 3.5 × 3.5 × 10 mm, TE = 15 ms, TR = 2039 ms, NS = 128, TET = 4 min 22 s, BW = 6061 Hz, 8192 points, WS = 400 Hz at 4.7 ppm

ditions inside the magnet at -10 mA and +10 mA (starting from the OCP value) in order to conduct the quinone reduction and oxidation, respectively. Relatively high current values were chosen with the aim of avoiding high states of charge that would promote decomposition pathways of AQDS ending with irreversibly dimerization. Both reduction and oxidation reactions were stopped after the passage of 50 C (83 min). Theoretically, the potential evolves once 90% of the product has been electrolyzed and it stabilizes again in the following redox couple [Eq. 7.2]. Figure 10.6d shows that the point of inflection of the cell voltage curve, which corresponds to the AQDS-AQDSH<sub>2</sub> redox couple, was over after 21 C (35 min). With this, the actual number of AQDS molecules that underwent the reduction was significantly smaller than the theoretical one ( $\frac{Q_{\text{exp}}}{Q_{\text{th}}}100 = \frac{21\text{C}}{67\text{C}}100 = 31\%$ ), even taking into account 20% of impurities ( $\frac{21\text{C}}{54\text{C}}100 = 39\%$ ). This suggests that electrochemically inactive molecules were formed (*e.g.* dimers) during the reduction process, probably owing to the relatively low current density that the system can withstand ( $\frac{\text{Current}}{\text{Total electrode surface area}} = \frac{10}{10} = 1 \text{ mA}\cdot\text{cm}^{-2}$  in this particular experiment<sup>11</sup>).

A LSV was performed between both electrolysis with a view to verifying the battery state-of-charge. It was conducted under dynamic conditions at the same scan rate of the previous CV (20 mV/s) and was stopped as soon as possible (from -1.5 to -0.55 V) in order to avoid altering the SoC. The curve (not shown) suggested that the initially oxidized quinone was completely reduced or dimerized as no current (0 mA) flowed at the cathodic reduction peak observed in dynamic conditions in Figure 10.6c (-0.73 V). The localized spectra depicted in Figure 10.6e confirmed that a large proportion of the quinone molecules were reduced at the end of the galvanostatic step at -10 mA, not without an important loss of NMR signal intensity with respect to the starting spectrum.

Besides, the CP at +10 mA shows that a similar percentage of the quinone molecules underwent a reoxydation in comparison to the initial reduction (31.3%). This indicates that, even if less than half of the available AQDS could be initially reduced, no further degradation occurred during this process, contrary to the trend observed in the previous potentiostatic experiments (see Fig. 10.4). Moreover, the values of the stabilized reduction (-1.5 V) and oxidation potentials (1.2 V) seem to correspond to the hydrogen and oxygen evolution reactions respectively, which means that it is advisable not to reach these potential limits to avoid side reactions. Having all included, it can be assumed that a comparable percentage of quinone molecules underwent a complete redox cycling in this galvanostatic experiment ( $\frac{21}{67}100 = 31.3\%$ ) and in the potentiostatic one performed in section 10.2 ( $\frac{25}{72}100 = 35\%$ ). However, the conversion cells and electrochemical methods employed are different in both cases, hence further studies at different potentials (CA) and current densities (CP) should be carried out in order to determine which cycling parameters are the most appropriate for the chosen chemical system.

On another front, a new complete RFB was prepared with the negolyte compartment containing AQDS 25 mM 95%, NaNO<sub>3</sub> 1 M, KNO<sub>3</sub> 1.05 M, CH<sub>3</sub>COOH 1 M and CH<sub>3</sub>COONa 1 M, while the posolyte was composed of trihydrated K<sub>4</sub>Fe(CN)<sub>6</sub> 0.15 M, K<sub>3</sub>Fe(CN)<sub>6</sub> 0.15 M,

<sup>11</sup>Total electrode surface area = graphite compartment surface + inlet channel + outlet channel + carbon felt surface = 5.3 + 3.4 + 1 + 0.3 = 10 cm<sup>-2</sup>



NaNO<sub>3</sub> 1 M, CH<sub>3</sub>COOH 1 M and CH<sub>3</sub>COONa 1 M. The quinone was of greater purity compared to the previous experiment and from now on in order to improve electrochemical performance. The total negolyte volume was 14 mL and the posolyte one 23 mL. The concentration of sodium nitrate (minimize overpotentials), potassium ferro/ferricyanide (ensure negolyte as capacity limiting side), potassium nitrate (compensate osmotic pressure) and sodium buffer were also increased. The latter was modified as it was supposed that the capacity fade observed during the third potentiostatic reduction in Figure 10.4 could have been caused by a pH variation.

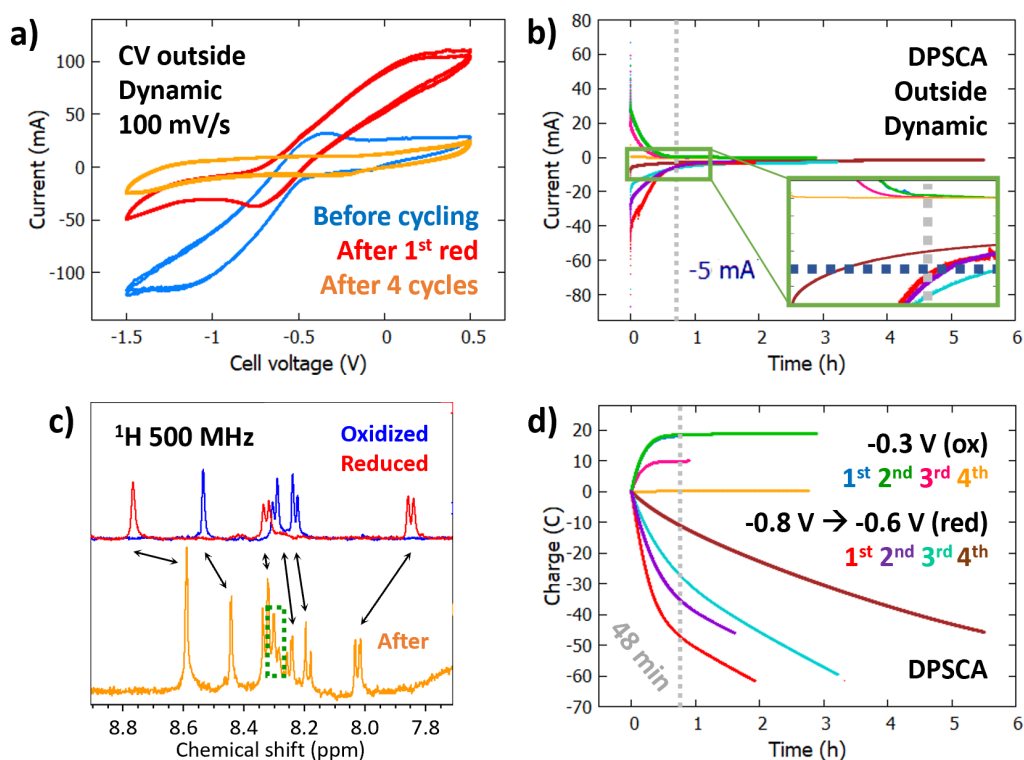


**Figure 10.7:** Ex situ analysis of a double tank redox flow battery with a full graphite-based cell. (a) Cyclic voltammograms before and after performing one and four consecutive redox cycles; (b-d) Chronoamperogram of the DPSCA, depicting (b) current and (d) charge as a function of time; (c) Aromatic region of the 2,7-AQDS proton spectra measured at 500 MHz oxidized, reduced and after performing the four cycles (after).

An ex situ analysis was carried out by means of consecutive CV and DPSCA cycles. A first cyclic voltammetry was performed at 100 mV/s when the bubble pump was in operation, as shown in Figure 10.7a. Similar results as those previously discussed were found having regard to the higher scan rate. Then, a chronoamperometry was conducted at -0.8 V in dynamic conditions. The applied voltage value differed from the one in the toric battery experiment (-1.2 V) as the ohmic and polarization losses were minimized and side reactions were to be avoided. The reduction was conducted until the number of coulombs reached the theoretical expected one (64 C). However, an intensity of -5 mA (see Fig. 10.7c) and a charge of -50 C (see Fig. 10.7d) were reached in approximately 48 min (dotted gray line). From that moment on, the current started to evolve sluggishly, stabilizing at around -3.5 mA, and the slope of the

charge curve barely varied. At this point, a CV taken in the same conditions as the first one showed that the curve shifted to more positive current values, which means that a large part of the quinone molecules were reduced. Later, a potentiostatic reoxydation was carried out at  $-0.3$  V, which is the anodic voltage peak value of the blue curve in Fig. 10.7a. The electrolysis was over after the same time as the quick evolution reduction step (48 min) since a negligible current value was achieved after this time ( $< 10 \mu\text{A}$ ). A charge of 20 C was retrieved, which means that the dimerization process remained of great importance under these experimental conditions.

Subsequently, another three redox cycles were conducted varying the reduction potential to  $-0.7$ ,  $-0.65$  and  $-0.6$ , respectively (the oxidation one was always  $-0.3$  V). The purpose of this potential change was to identify if this parameter minimized the residual current and/or the dimerization process, to the detriment of slower reaction kinetics (the lower is the potential step, the lower current flows through the cell). Figure 10.7b shows that the remaining current intensity did not vary greatly during the first two hours, which suggests that a side reaction occurred regardless the reduction potential. Besides, a current drop was once again observed after the third complete cycle (pink curve) and no current flowed after the fourth one (orange curve). At this stage, a CV confirmed that neither oxidation nor reduction peaks were easily identified in the same potential range of the previous experiments (orange curve in Fig. 10.7a). Finally, an ex situ analysis of the product was carried out in the same way to the experiment shown in Figure 9.12. The spectrum was compared with them in Figure 10.7c, showing a lower signal-to-noise ratio (31) in a much longer experimental time (NS = 256, TET = 8 min vs NS = 8, TET = 23 s) and hinting at low homogeneity of the cycled sample. Most of the peaks could be assigned either to the oxidized or the reduced form of the quinone, with the exception of two present at 8.35 ppm (dotted green square).

Recent papers suggested a negolyte capacity fade mechanism where 2,7-AQDS decomposes to anthranol-2,7-disulfonic acid (ADS) over cycling, both in alkaline and acidic conditions.[208, 209] In addition, they stated that ADS can be electrochemically regenerated to AQDS by means of a GCPL (Galvanostatic Cycling with Potential Limitations) hold at a negolyte potential 1.8 V higher than that of the posolyte, and with a relatively high current cutoff that prevents OER (*e.g.*  $1 \text{ mA}\cdot\text{cm}^{-2}$ ). Thus, the CV observed after cycling looked quite similar to the ADS one, and the non-assigned peaks may fit with the presence of ADS in the cycled AQDS.[209] At this stage, a galvanostatic cycling at a rather high current density hold at  $+1.2$  V vs  $\text{K}_4\text{Fe}(\text{CN})_6/\text{K}_3\text{Fe}(\text{CN})_6$  would have been recommended to regenerate AQDS from ADS existing in the negolyte and reduce the overall fade rate. Nevertheless, a preliminary measure to avoid this degradation pathway can be to identify the threshold current value at which AQDS is not reduced anymore to  $\text{AQDSH}_2$ , and consequently ADS is being generated. In the system under study, this reduction current value was found at around  $-5$  mA (dotted blue line in Fig. 10.7b), which has to be taken into consideration for potential future experiments.

### 10.3.3 3D-printed Double Sense Model

Lastly, a 3D-printed double sense cell was designed as shown in Figure 10.8. Taking advantage of the inherent flow properties of the complete battery, two in situ techniques can be applied to study this system depending on its arrangement: online and operando NMR.

- In an online experiment the electrolyte solutions are flown for detection in the double tank located in the NMR detection zone, while the conversion cell is either inside the probe (as described earlier) or outside it. The latter setup requires longer tubing and more powerful pumping to offset the pressure drop. Its main goal is to avoid the MHD effect described in Figure 10.5 through positioning the battery either (i) at the foot of the magnet and shielded with mu-metal, or (ii) out of the fringe field of the NMR magnet.
- In an operando experiment the conversion cell is positioned within the NMR detection region (see Chapter 9) and the double tank moved upwards or downwards out of it. In order to enable optimal real-time monitoring of the electrolytes, the battery has to be aligned with respect to the static magnetic field ( $B_0$ ) and to the applied radio-frequency one ( $B_1$ ).

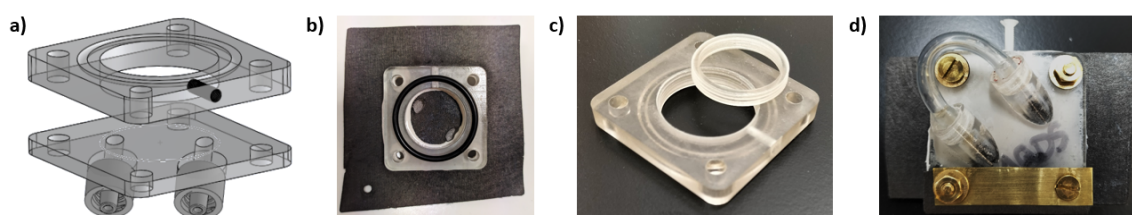


**Figure 10.8:** Pictures and 3D rendering of the double sense cell.

With regard to the conversion cell, the toric model was modified with the purpose of removing the graphite current collectors that partially obstructed the passage of the  $B_1$  field (see Chapter 9.4.1). For this, the former 3D-printed cell was reduced in size ( $45 \times 45$  mm) for easy handling and avoid interruptions in the closed-loop flow circuit encountered before. Each side was also splitted into two pieces (see Fig. 10.8a) that enabled an easy placement of square-shaped carbon felts (side = 80 mm), which in turn were glued to both pieces with silicone sealant. The electrodes size exceeded the cell limits (see Fig. 10.8b) since there was no current collector and the electrical connection had to be done directly in touch with them. As regards the compartments (ID = 27 mm, height = 6 mm), each one had a threaded hole at the top ( $\varnothing = 3$  mm) to introduce the electrolyte (3.5 mL). A circular-shaped membrane ( $\varnothing = 30$  mm) was placed between the compartments and fastened with a silicone gasket cut to size (OD = 32 mm, ID = 28 mm, thickness = 1 mm) in one of the sides. The cell incorporated a Viton O-ring ( $\varnothing = 35$  mm) that minimizes fluid leaks and was assembled with the help of brass washers, nuts and screws ( $\varnothing = 4$  mm). The 3D printing of a screw thread in both compartments allowed to receive the cylindrical piece (OD = 27 mm, ID = 23 mm, height = 4 mm) which aimed to stack carbon felt electrodes ( $\varnothing = 26$  mm), raising the total active

surface area and therefore the current density (see Fig. 10.8c). Additional brass plates ( $44 \times 8 \times 1$  mm) and nuts facilitated the contact between the folded carbon felt and insulated copper wires outside the cell (see Fig. 10.8d), which in turn were connected to the potentiostat.

An in situ and operando analysis of the conversion cell in the NMR detection zone was carried out in order to test the implementability of the most challenging setup. A mini-battery was built with two pieces of silicone tubing (ID = 2 mm, length = 40 mm) blocking the inner and outer channels of each side, as shown in Figure 10.8d. The negolyte compartment contained AQDS 25 mM 95%,  $\text{NaNO}_3$  0.5 M,  $\text{KNO}_3$  1.05 M,  $\text{CH}_3\text{COOH}$  0.3 M and  $\text{CH}_3\text{COONa}$  0.3 M, while the posolyte was composed of trihydrated  $\text{K}_4\text{Fe}(\text{CN})_6$  0.15 M,  $\text{K}_3\text{Fe}(\text{CN})_6$  0.15 M,  $\text{NaNO}_3$  0.5 M,  $\text{CH}_3\text{COOH}$  0.3 M and  $\text{CH}_3\text{COONa}$  0.3 M. The negolyte volume was 4 mL and the posolyte one 3 mL. The concentration of sodium nitrate and sodium buffer were decreased with respect to the previous experiment to avoid precipitate formation (see section 10.1) and once demonstrated that the capacity fade was not caused by a pH variation. Each compartment comprised three extra carbon felt electrodes (aside from the one glued to the 3D-printed pieces) with the purpose of raising the current density accelerating reaction kinetics.

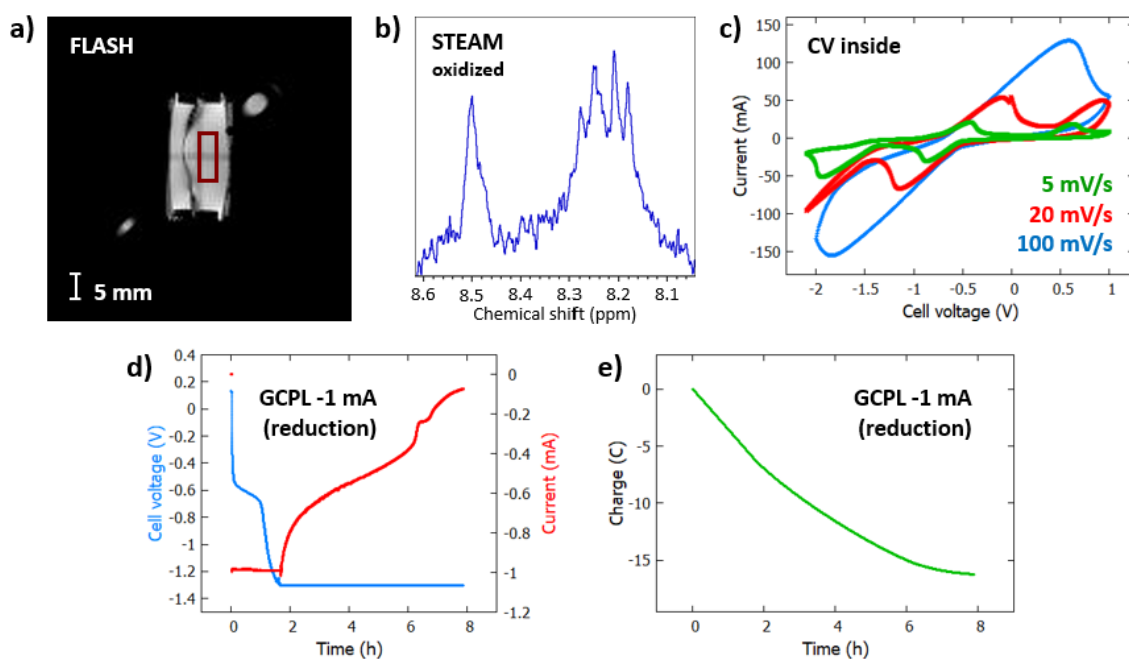


**Figure 10.9:** In situ and operando analysis of a 3D-printed double sense conversion cell. (a) Sagittal FLASH image of the cell with voxel placement for (b); Localized aromatic region of the STEAM voxel selected in (a) before the reduction; (c) Cyclic voltammograms at different scan rates inside the magnet; (d-e) Chronoamperogram of the GCPL conducted inside the magnet at -1 mA and limited at -1.2 V, representing (d) potential and (e) charge as a function of time.

Figure 10.9a shows a sagittal FLASH<sup>12</sup> image where the electrolytes in both the cell and

<sup>12</sup> $\theta = 30^\circ$ , TE = 4 ms, TR = 1000 ms, NS = 1, TET = 2 min 8 s, FOV =  $65 \times 65$  mm, IS =  $128 \times 128$ , BW = 100 kHz

tubing are identified. This can be considered a proton density-weighted image as the contribution of both  $T_1$  and  $T_2$  contrast was minimized as a result of the long repetition time (1000 ms). It was selected as pilot image for the STEAM<sup>13</sup> sequence in Fig.10.9b. Despite the existing RF perturbation between the electrodes, accentuated by the stack of 3+1 carbon felts, a well-resolved localized spectrum could be obtained using small flip angles (*i.e.* STEAM). Cyclic voltammeteries were performed at 5, 20 and 100 mV/s, as depicted in Figure 10.9c. It can be noted that, even without external induced mass transport (*e.g.* dynamic conditions or MHD effect), the current intensities were the maximum obtained so far. This had however a negative impact in the peak-to-peak separation, given that the ohmic drop increased accordingly. In addition, it could be considered a chemically reversible process, as the ratio of anodic and cathodic peak current was close to one ( $i_{Pa}/i_{Pc} = 1$ ) at each scan rate. Last, additional redox peaks were observed at low scan rates (5 mV/s). They might be attributed to HER/OER, although the potential seems low for oxygen generation (see Fig. 10.6d), or to physical phenomena such as inefficient soaking of the electrodes or molecules adsorbed at their surface (higher resistance, higher ohmic drop). Once the CV study completed, a CA at 0 V was conducted to regain a battery SoC = 0%.

Subsequently, a GCPL was carried out at -1 mA from the OCP value to -1.3 V, with a current limitation of -70  $\mu$ A. A higher reduction potential limit was chosen for the galvanostatic step with respect to the previous potentiostatic experiments in order to accelerate reaction kinetics (given the higher ohmic drop of this model), while avoiding the aforementioned additional redox peak (< -1.5 V). A relatively high current limit for the potentiostatic step was selected in order to avoid the AQDS decomposition discussed in the above section. Previous (not shown) experiments found that the threshold current at which ADS is generated for this particular system was at around -50  $\mu$ A, so a slight greater value was chosen accordingly (*cf.* Chapter 10.3.2). Figure 10.9d shows the electrolysis performed for about 8 hours or, more precisely, up to the current limit. A total charge of 16 coulombs passed through the battery (see Fig. 10.9e), which did not differ in excess from the theoretical calculated value (19 C with impurities, 18 C without). Nevertheless, it was impossible to obtain well-resolved NMR signal coming from AQDS after 2 h 20 min (NS = 4096). The signal-to-noise ratio (4) corresponded to that of the found for the starting state after 4 minutes 22 s (NS = 128). This suggests that the battery SoC was different from that of fully reduced form, in light of the already experienced difficulties measuring the intermediate electrochemically active dimers.

Once the conversion cell is coupled with the double tank, a real-time monitoring of the electrolytes is possible in what constitutes one of the first operando redox flow battery setups ever conceived. If some improvements are introduced such as the selection of a simpler chemical system (*i.e.* no dimers) together with stopped-flow NMR techniques triggering the bubble pump operation (already tested), this system can represent a breakthrough with respect to the already developed setups that entail magnetic field inhomogeneities and limited spectral resolution.[204]

---

<sup>13</sup>Voxel = 3.5 × 3.5 × 10 mm, TE = 15 ms, TM = 10 ms, TR = 2058 ms, NS = 2048, TET = 1 h 10 min, BW = 6061 Hz, 8192 points, WS = 400 Hz at 4.7 ppm



## **Part V**

# **Conception of a Fluidic NMR Micro-Detection Device**

# 11 - Miniaturization in a Microimaging Probe

## 11.1 Specifications

In view of the sensitivity and homogeneity problems encountered when analyzing the battery through a 7 T vertical NMR imager (see Chapters 9 and 10), a 3D-printed insert pluggable on the basis of a micro-imaging probehead inserted into a 11.7 T NMR spectrometer has been conceived. The challenging transition from a Super Wide Bore (65 mm) to a Narrow Bore (18 mm) magnet was justified by higher sensitivity linked to the magnetic field, higher spectral resolution due to a more sophisticated shim system, higher spatial resolution related to a gradient strength up to 200 G/cm instead of 67 G/cm, an optimal filling factor (adaptable antenna) and shorter cycling times (smaller volumes). But the most important advantage was the passage to a software (TopSpin) more user-friendly for the creation of new pulse sequences compared with that of the imager (ParaVision), since the latter contains a black-box feature given its common medical use.

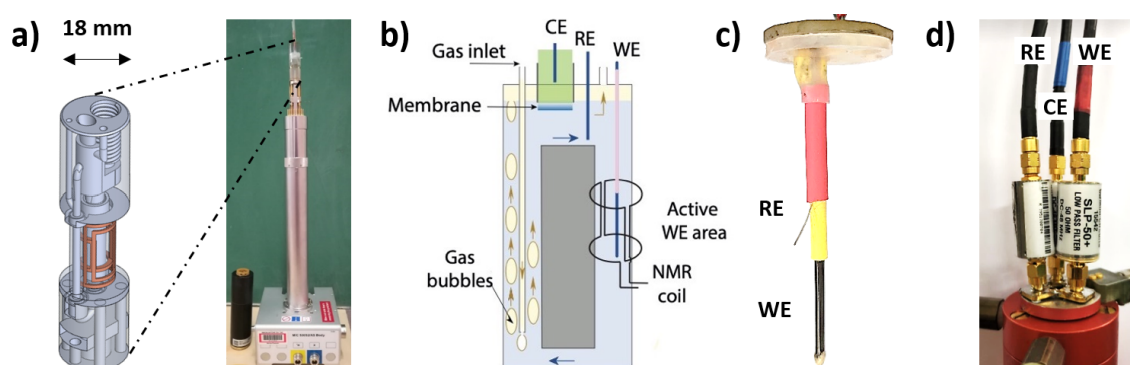


**Figure 11.1:** Miniaturized redox flow battery. (a) 3D rendering of the insert plugged onto the basis of a Bruker Micro-5 imaging probe; (b) Schematic diagram including the three-electrode system and the solution circuit loop; (c) Printed circuit board acting as the interface between the working and the reference electrodes and the potentiostat connectors (a cut-to-size silicone sheet renders the 3D-printed insert where it fits gas proof); (d) Low-pass filters and shielded cables for each electrode at the exit of the probe body.

The miniaturized device depicted in Figure 11.1 is described in depth in Chapter 12, as it is central to a manuscript submitted to *Analytical Chemistry*. The current version of the miniaturized device is thus quite accomplished, but before reaching the current stage it was necessary to take into account many parameters:

- Saddle is the chosen geometry for the transmission/detection antennae, since it provides a uniform static magnetic field in the central part of the sample. Moreover, its geometric configuration enables the inclusion of two independently tunable coils in quadrature. In this particular case,  $^1\text{H}$  and  $^{13}\text{C}$  are the chosen NMR active nuclei given the organic



nature of the molecule of interest. The coils were initially conceived as 2 mm tracks on a flexible printed circuit board<sup>1</sup> (PCB). Nevertheless, the best homogeneity results were obtained by means of handmade coils with copper wire, such as the ones shown in Figure 11.1a.

- The miniaturized electrochemical system may be regarded as a hybrid flow battery where only the negolyte solution is put into circulation with the aid of an inert carrier gas (similarly to the bubble-pump based system described in Chapter 10.1. A closed-loop fluid flow circuit from the top to the bottom of the NMR detection region is established, as illustrated in Figure 11.1b. A cylindrical receptacle bordered by a screw thread allows to receive a Nafion 212 membrane ( $\varnothing = 6$  mm) that can be replaced after each use, as well as an external 3D-printed tank containing the posolyte.
- A three-electrode setup was the chosen electrochemical system, with the working electrode (WE) and the reference electrode (RE) positioned inside the negolyte solution and the counter electrode (CE) in the external compartment described above (see Fig. 11.1b). The WE goes through the entire insert and is insulated by a heat-shrinkable sheath everywhere but in the NMR active region as shown in Figure 11.1c, enabling simultaneous generation and detection of the electrochemical products. The current loop linking the WE and CE is largely vertical minimizing not only lineshape effects but also the MHD effect, as the net ionic flow is parallel to the static magnetic field direction.
- In order to control the potential at the WE, the correct choice of a RE is of paramount importance. Different treatment methods of silver wire ( $\varnothing = 0.2$  mm) were performed without the expected results, including pretreatment with diluted HCl or AgNO<sub>3</sub>, electroplating at constant current with HCl, and bleaching with a dilute solution of NaClO. Eventually, the RE was made by pouring the Ag wire in Ag/AgCl ink (ALS) and subsequently drying with hot air (121 °C during 15 min). Then the electrode was coated with a Nafion D2020 solution (Ion Power) in order to obtain a stable RE even under extreme pH conditions.
- With regard to the chemical system, the negolyte solution is analogous to that used in Chapters 9 and 10, whereas the posolyte solution only contains the supporting electrolyte used in the negolyte (*i.e.* conducting salts and/or pH buffer). Thus, when the starting oxidized anthraquinone (AQ) is reduced at the WE surface, a complementing oxidation reaction occurs at the CE site ( $O_2 + 4H^+ + 4e^- \rightleftharpoons 2H_2O$  at pH < 7), and vice versa when oxidizing back the AQ ( $2H^+ + 2e^- \rightleftharpoons 2H_2$ ). As such, the CE is chosen as inert as possible (*e.g.* Pt,  $\varnothing = 1.55$  mm) but, nevertheless, byproducts can be generated at its surface. The aforementioned membrane also prevents electrolyte convection near the CE from influencing the electrochemical reaction at the WE.

---

<sup>1</sup>Conceived following the next steps: (a) UV insulation for 3 min 30 s; (b) Development by soaking in K<sub>2</sub>CO<sub>3</sub> 10 g/L for 5 min; (c) Etching by soaking in (NH<sub>4</sub>)S<sub>2</sub>O<sub>8</sub> 250 g/L at 40 °C for 30 min; (d) Stripping by soaking again in K<sub>2</sub>CO<sub>3</sub> 10 g/L for 5 min.

- The axial symmetry of the insert allows to minimize local field inhomogeneities coming from the different permeability of the materials placed inside the magnet. This, together with the insertion of aluminium foils that enable RF shielding of the unwanted insert parts, provides considerably lower proton spectra full width at half maximum (FWHM) values than those obtained before the RF insulators integration.
- The potentiostat generates unwanted frequencies and associated noise that might be minimized by means of the integration of low-pass filters (SLP-50 DC to 48 MHz pass-band) and shielded cables. The incorporation of one filter per terminal of the three-electrode system was considered as illustrated in Figure 11.1d, leading to similar NMR results with and without them in terms of signal-to-noise ratio and spectral resolution. Therefore, their integration was further discarded with the aim of simplifying the setup.

NMR velocimetry experiments using PGSTE (Pulsed Gradient STimulated Echo) sequences<sup>2</sup> measured liquid speed as a function of the setpoint nitrogen flowrate, as shown in Figure 11.2a. This simple and fast experiment periodically ensures the net solution displacement, of vital importance when monitoring the electrochemical reaction. A projection of the 3D FLASH image<sup>3</sup> (Figure 11.2b) illustrates different velocity profiles at different positions inside the NMR tank (orange and green arrows). In addition, diffusion coefficient measurements of the molecular species in solution were performed using PGDSTE (Pulsed Gradient Double STimulated Echo) sequences at two different AQDS concentrations (25 mM<sup>4</sup> and 0.5 M<sup>5</sup>), both in the presence and absence of a supporting electrolyte (NaNO<sub>3</sub>) and an acetate buffer (CH<sub>3</sub>COOH 0.1 M + CH<sub>3</sub>COONa 0.1 M). The results indicated that the AQDS self-diffusion coefficient decreases with increasing concentrations (6.48·10<sup>-10</sup> m<sup>2</sup>·s<sup>-1</sup> at 25 mM vs 2.18·10<sup>-10</sup> m<sup>2</sup>·s<sup>-1</sup> at 0.5 M without salts) as well as in the presence of the supporting electrolyte and the buffer (4.30·10<sup>-10</sup> m<sup>2</sup>·s<sup>-1</sup> vs 1.67·10<sup>-10</sup> m<sup>2</sup>·s<sup>-1</sup>).

## 11.2 Choice of the Working Electrode

In order to exert almost no deleterious effect on the homogeneity of the magnetic field, the WE choice held out as the main challenge to be addressed once the previously handled parameters were optimized. The main obstacles to overcome were line broadening caused by magnetic susceptibility mismatches, as well as SNR degradation caused by RF field inhomogeneities and power dissipation in the electrodes. Glassy carbon was the selected WE material because of its relative low cost, good electrical conductivity, chemical stability and electrochemical inertness in a wide potential window. On the one hand, a commercial glassy carbon type II ( $\varnothing = 1$  mm, Alfa Aesar) was cut into 25 mm pieces and polished before each experiment. Polishing was

<sup>2</sup>Gradient duration  $\delta = 1$  ms, inter-gradient delay  $\Delta = 100$  ms, TET ca. 1 min

<sup>3</sup> $\theta < 90^\circ$ , TE = 0.2 ms, TR = 150 ms, NS = 32, TET = 96 min, FOV = 11 × 11 × 17 mm, image size = 256 × 32 × 32

<sup>4</sup> $\delta = 1$  ms,  $\Delta = 100$  ms, TET = 28 min

<sup>5</sup> $\delta = 1$  ms,  $\Delta = 200$  ms, TET = 94 min

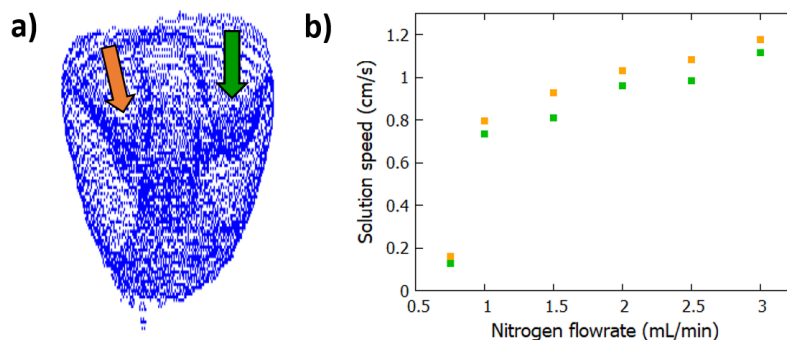


**Figure 11.2:** NMR velocimetry experiments while operating the bubble pump using a non-commercial glassy carbon rod ( $\varnothing = 1.55$  mm) as working electrode. (a) Three-dimensional FLASH image; (b) Solution speed as a function of the nitrogen flowrate. The orange and green squares indicate two different region of the reservoir.

conducted on a cloth pad in a water-alumina slurry  $0.05 \mu\text{m}$  (Sigma-Aldrich) with figure-eight motions. On the other hand, non-commercial glassy carbon was generated from polyimide tubing (ID = 1.8 mm, OD = 1.9 mm, Cole-Parmer) following the instructions below:

1. Cut pieces of 28-43 mm and place them inside quartz tubes (ID = 3 mm) to avoid twisting during the next steps. The future electrodes were oversized bearing in mind a retraction of about 30% during debinding (final length = 20-30 mm).
2. Position samples inside a sintering furnace and perform in an inert atmosphere (a) an initial heating along a uniform temperature rise ramp of  $1 \text{ }^\circ\text{C}/\text{min}$  until  $300 \text{ }^\circ\text{C}$ , followed by (b) a step at  $0.1 \text{ }^\circ\text{C}/\text{min}$  until  $950 \text{ }^\circ\text{C}$  and (c) a natural cooling to room temperature that takes around 5 days.
  - A carbonaceous backbone/skeleton is formed at initial heating stages ( $< 550 \text{ }^\circ\text{C}$ ), where hydrocarbon radicals are generated with highest concentration at  $600 \text{ }^\circ\text{C}$ .
  - A pyrolytic carbon containing dangling bonds is constituted between  $550$  and  $700 \text{ }^\circ\text{C}$ , while carbon-carbon bond formation starts at the latter temperature.
  - A network of graphene fragments containing defects and impurities starts forming at  $800 \text{ }^\circ\text{C}$ , and further graphitization ( $> 900 \text{ }^\circ\text{C}$ ) anneals these defects and increases mechanical strength and crystallite diameter.
3. Fill the hollow tubes ( $\text{OD}_{\text{final}} = 1.65$  mm) with epoxy bi-components glue with the aid of a fine needle in order to harden them, control the reaction active surface and minimize magnetic susceptibility effects arising from potential air inside them.

Initial tests were carried out with both electrodes axially offset, with the dual purpose of leaving room for a bigger voxel and avoiding the rod to get stuck in the narrow interface between the bottom and middle parts of the insert (assembling of the different parts explained in depth in Chapter 12). However, this arrangement led to a very marked field lines distortion mainly around the end of the commercial electrode. This can be explained by the fact that, even if

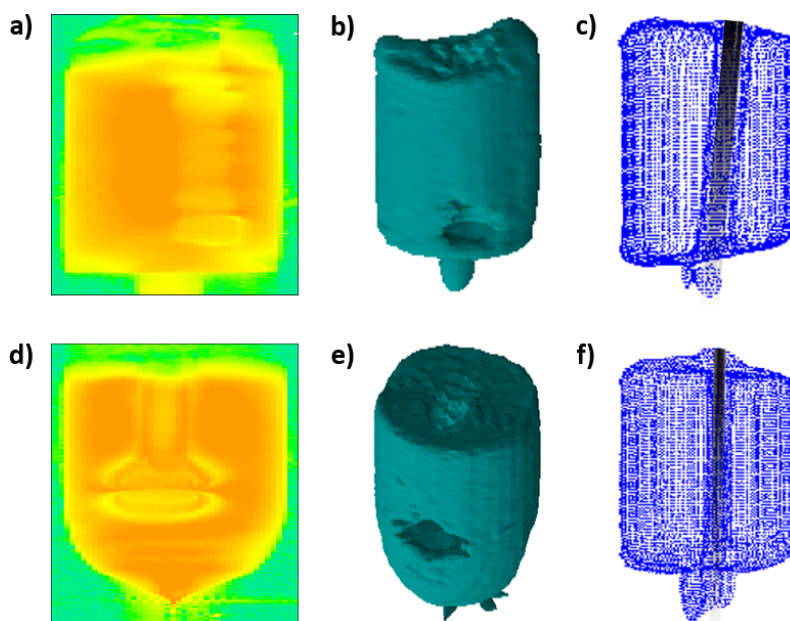


**Figure 11.3:** Effects of glassy carbon electrodes on the  $^1\text{H}$  image of the detection region: (a-c) non-commercial vs (d-f) commercial rods. (a, d) Sagittal FLASH images before positioning optimization; (b-c, e-f) Projection of the three-dimensional FLASH image (b, e) before and (c, f) after positioning optimization.

the commercial electrode diameter was smaller (1 mm vs 1.65 mm), its massiveness caused major field inhomogeneities as can be drawn from the comparison of the sagittal FLASH<sup>6</sup> images (Figures 11.3a and 11.3d) and the 3D FLASH<sup>7</sup> projections (Figures 11.3b and 11.3e). However, this homogeneity issue entailed line broadening in both cases, so we proceeded to place the end of each electrode out of the detection region and attempted to get the greatest axial symmetry possible. Figures 11.3c and 11.3f (3D FLASH projection, same acquisition parameters) show less local field inhomogeneities with respect to the previous arrangement in both cases, leading to (Still significant) water peak FWHM values of 22 Hz for the non-commercial glassy carbon electrode and 60 Hz for the commercial rod. Thus, the non-commercial model was initially chosen to perform in situ and operando analysis of the miniaturized ORFB.

### 11.2.1 Real-Time Monitoring with a Non-Commercial WE

As the working electrode was directly occupying the NMR detection region, the entire assembly was not 'transparent' to both magnetic field and RF radiation, which has a direct impact on the system resolution and sensitivity. It seemed therefore necessary to perform spatially localized experiments to obtain an optimal spectral resolution. The NMR reservoir contained 1.6 mL of a 25 mM solution of 2,7-AQDS (negolyte). Figure 11.4a illustrates sagittal

<sup>6</sup> $\theta < 90^\circ$ , TE = 0.4 ms, TR = 256 ms, NS = 1, TET = 18 s, FOV = 11 × 17 mm, image size = 64 × 128

<sup>7</sup>Phase-encoding gradients along  $x$  and  $y$  axis, readout frequency-encoding gradient along  $z$  axis:  $\theta < 90^\circ$ , TE = 0.2 ms, TR = 150 ms, NS = 4, TET = 12 min, FOV = 11 × 11 × 17 mm, image size = 256 × 32 × 32

FLASH images without<sup>8</sup> (blue) and with slice selection<sup>9</sup> in order to bypass the electrode (red). High-resolution homonuclear 1D<sup>10</sup> (Fig. 11.4b) and 2D<sup>11</sup> (Fig. 11.4c) spectra were obtained when selecting a *xy* pixel, allowing to discriminate a <sup>1</sup>H-<sup>1</sup>H J-coupling of about 5 Hz. It should be noted that there is no need to select a *xyz* voxel given the RF shielding provided by the aluminium foils in the *z* direction.

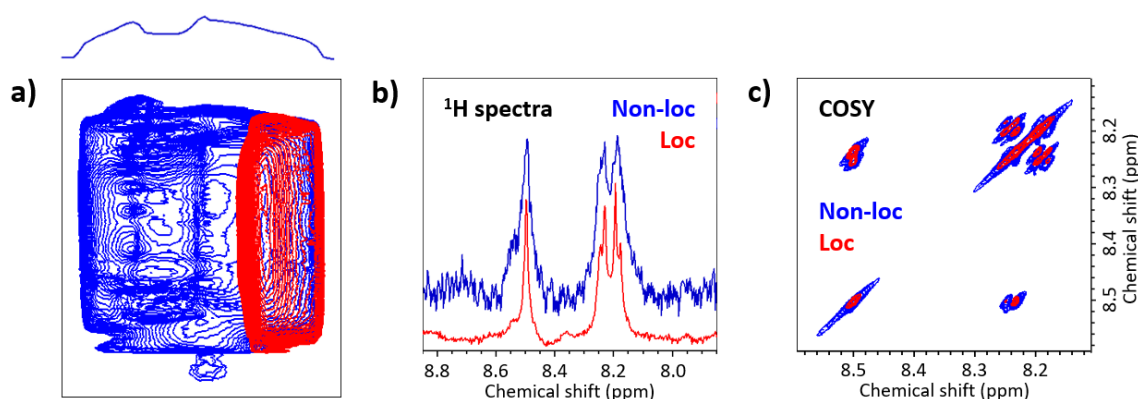


**Figure 11.4:** Comparison between spatially localized (red) and non-localized (blue) experiments. (a) Sagittal FLASH images; (b-c) Aromatic region of the 2,7-AQDS (b) proton spectra and (c) COSY (CORrelated SpectroscopY) experiment.

A new miniaturized ORFB was built, the negolyte containing 1.6 mL of AQDS 25 mM 95%, NaNO<sub>3</sub> 1 M, CH<sub>3</sub>COOH 0.3 M and CH<sub>3</sub>COONa 0.3 M, and the posolyte 0.3 mL of the same concentrations of supporting electrolyte and acetate buffer. The three-electrode system was connected to the Biologic SP-150 potentiostat, which was placed out of the fringe field of the NMR magnet. The device was coupled to the laboratory nitrogen line and the bubbling rate was set at 1 mL/min with a flowmeter (calculated through Fig. 11.2b). Cyclic voltammetry (CV) experiments were performed inside and outside the magnet at 20 mV/s in the absence of NMR radio-frequency emission under static and dynamic conditions. The results depicted in Figure 11.5a indicate the correct operation of the electrochemical setup, albeit subject to uncompensated resistances of about 40 Ω. A minor magnetohydrodynamic (MHD) effect was observed both in static and dynamic conditions, being of less important when the solution circulates. This may be explained by the fact that the Lorentz force favored more the AQDS reduction reaction (initially oxidized molecules) under static conditions than the bubble pump action at the above-mentioned rate.

At this stage, the micro-detection device enabled the operando monitoring of the quinone oxidation state via spatially localized well-resolved spectra. A chronoamperometry (CA) was therefore conducted inside the magnet at -0.8 V under dynamic conditions, simultaneously with the acquisition of spatially localized proton spectra (NS = 256, TET = 324 s) each 8 minutes.

<sup>8</sup> $\theta < 90^\circ$ , TE = 0.4 ms, TR = 256 ms, NS = 1, TET = 18 s, FOV = 11 × 17 mm, image size = 64 × 128

<sup>9</sup>Same parameters except for the use of a sinc-pulse and TET = X s

<sup>10</sup>Non-localized: NS = 1, TET = 1 s / Localized: NS = 128, TET = 162 s

<sup>11</sup>Non-localized: NS = 4, TET = 23 min / Localized: NS = 128, TET = 13 h

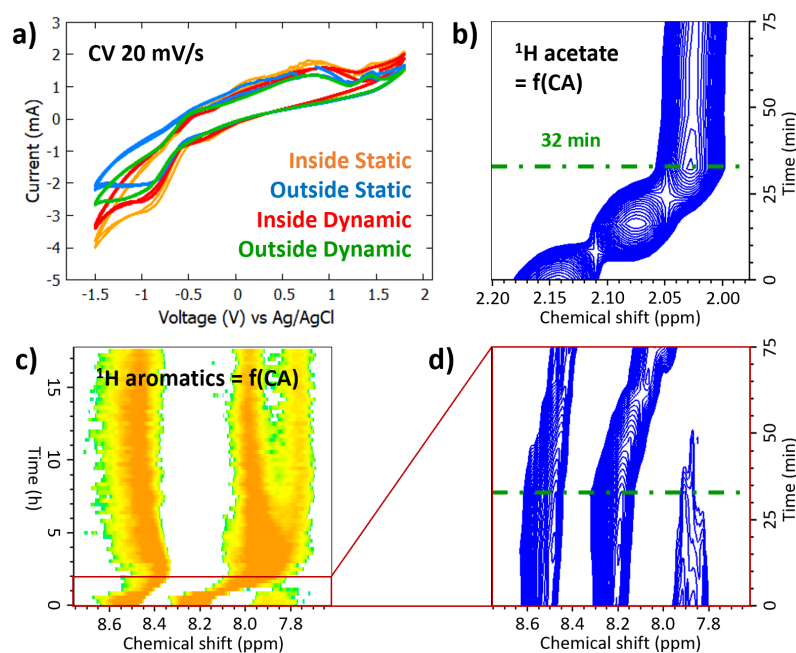


**Figure 11.5:** Operando analysis of a miniaturized ORFB using a non-commercial glassy carbon as a WE, sodium nitrate 1 M as supporting electrolyte, and acetic acid 0.3 M and sodium acetate 0.3 M as a pH buffer. (a) Cyclic voltammograms at 20 mV/s inside and outside the magnet, both in static and dynamic conditions; (b) Contour plot of the acetate region spectra evolution according to time; (c-d) Contour plot of the aromatic region spectra evolution according to time.

Figure 11.5b shows the evolution of the  $^1\text{H}$  NMR spectrum of 2,7-AQDS during the reduction step (charge of the mini-battery) according to time: from the starting oxidized state ( $t = 0$ ) to the final reduced one ( $t = 18$  h). It can be observed that the acetate peak signal shifted to higher fields during the early stages of the reaction (see Fig. 11.5b). This means that there was a progressive increase of pH as AQDS was being reduced, until being stabilized after 32 minutes (dotted blue line) at  $\text{pH} = 7-8$  (pH-indicator paper). Quinone dianion ( $\text{AQ}^{2-}$ ) and protonated monoanion ( $\text{AQH}^-$ ) species consumed solvent protons to form the hydroanthraquinone ( $\text{AQH}_2$ ), and the pH increased as a consequence of a low buffer capacity. Therefore, even if the pH returned to its original value upon oxidation (not shown), AQDS did not cycle reversibly as protons are needed to structurally stabilize the  $\text{AQH}_2$ -AQ dimer.

Buffering capacity increases as the concentrations of the conjugate acid and base increase. Thus, a similar miniaturized battery was prepared except for a higher buffer concentration in both negolyte and posolyte solutions, *i.e.* acetic acid 1 M and sodium acetate 1 M. A double potential step chronoamperometry (DPSCA) was conducted inside the magnet under dynamic conditions, first at  $-0.8$  V (reduction) and later on at  $0.5$  V (oxidation), simultaneously with the acquisition of spatially localized proton spectra (same acquisition parameters). A slightly higher reduction potential value was chosen in order to accelerate reaction kinetics under the risk of favouring side reactions such as hydrogen evolution reaction. Figure 11.6 illustrates the achievement of a complete redox cycle. The acetate peak signal stabilized from

the beginning at 2.04 ppm (not displayed), meaning no significant changes in the pH. Regarding the chronoamperograms shown in Figures 11.6a and 11.6b, the total charge observed during the first reduction (8.4 C) exceeded the theoretical calculated value (7.7 C) at the time of the emergence of the fully reduced spectrum (three signals at 8.6, 8.1 and 7.8 ppm after 15 hours, see Figure 11.6c), which may be explained by the occurrence of the foreseeable side reactions. So, from now on, lower reduction potential values (in absolute terms) were chosen to the detriment of slower reaction kinetics. With regard to the reoxidation reaction, the small total charge value (3.0 C) observed once the fully oxidized spectrum was obtained suggested the already evoked dimerization mechanism (*cf.* Chapter 10.3.1), where only one AQDS electron over the two are accessible. The quick transition between the reduced and a partially oxidized state observed in Figure 11.6c (dotted red line) indicates a potential oxygen intake, since reduced AQDS is an oxygen scavenger extremely sensitive to its content.[205]

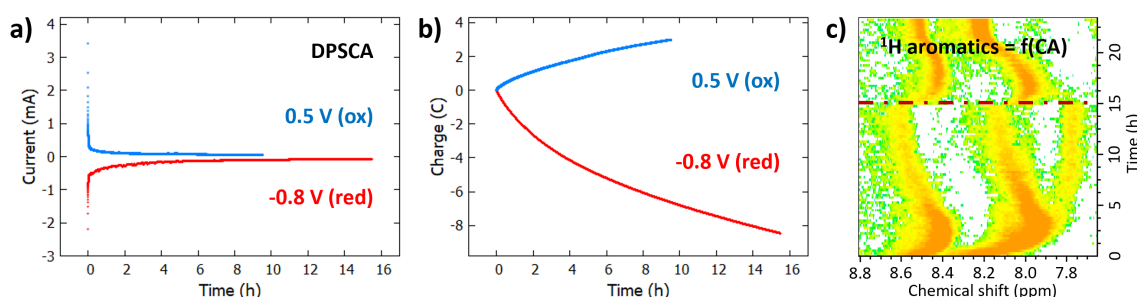


**Figure 11.6:** Operando analysis of a miniaturized ORFB using a non-commercial glassy carbon as a WE, sodium nitrate 1 M as supporting electrolyte, and acetic acid 1 M and sodium acetate 1 M as a pH buffer. (a-b) Chronoamperogram of the DPSCA, depicting (a) current and (b) charge as a function of time; (c) Contour plot of the aromatics region spectra evolution according to time.

## 11.2.2 Operando Monitoring with a Commercial WE

Although it was initially discarded, the commercial rod was preferred over the non-commercial electrode at a second stage as it offers enhanced electrochemical performances and longer lifespan. The surface of the latter is brittle and abrades after few cycles, especially when high current densities pass through it. When performing spatially localized experiments where the electrode is bypassed, local field inhomogeneities caused by the commercial electrode are avoided. Notwithstanding, field homogeneity was optimized at this stage thanks to a  $B_0$  mapping and the spectral resolution of the non-localized experiments greatly improved. Lastly, operating in excess acid condition was preferred over the buffered solution due to the faster reaction kinetics obtained, while taking into account the limited potential stability window of glassy carbon under acidic and alkaline conditions.[210]

Figure 11.7 depicts the analysis in real time of a miniaturized bubble pump-based ORFB with the above described modifications under acidic conditions, the negolyte containing 1.6 mL of AQDS 50 mM 95% and  $H_2SO_4$  0.2 M and the posolyte 0.3 mL of  $H_2SO_4$  0.2 M. The

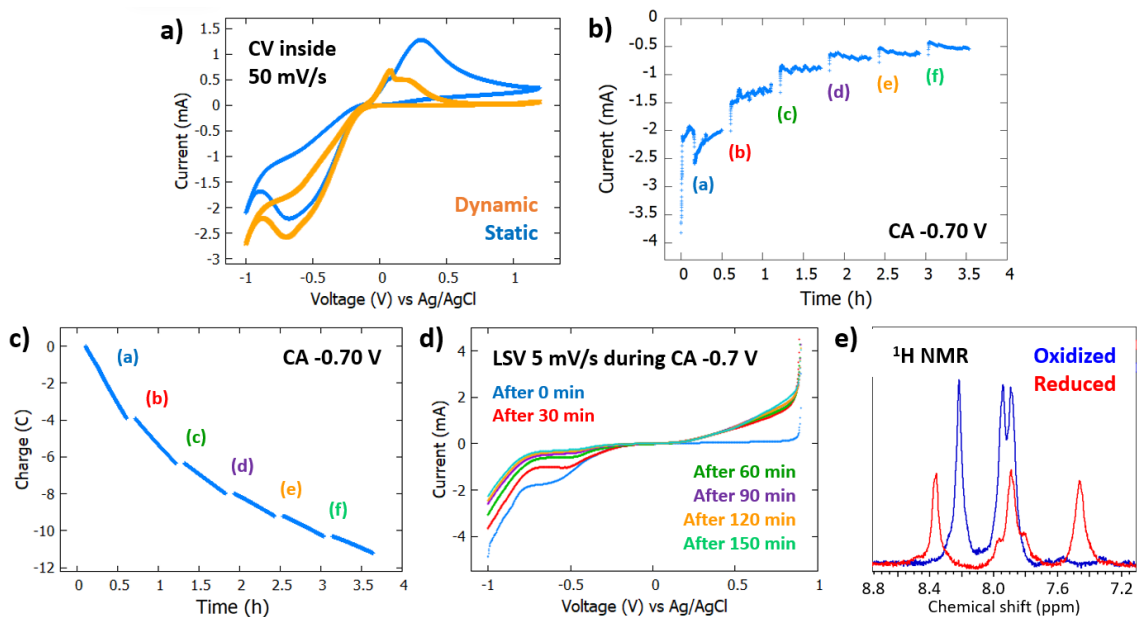


**Figure 11.7:** Operando analysis of a miniaturized ORFB using a commercial glassy carbon as a WE and sulfuric acid 0.2 M as supporting electrolyte (pH = 0.4). (a) Cyclic voltammograms at 50 mV/s inside the magnet, both in static and dynamic conditions; (b-c) Chronoamperogram of the reduction at -0.7 V, depicting (b) current and (c) charge as a function of time; (d) Linear sweep voltammogram at 5 mV/s taken every half an hour; (e) Aromatic region of the 2,7-AQDS non-localized proton spectra before the CA (oxidized) and after 150 minutes (reduced).

battery state-of-charge was monitored during the quinone reduction (Figures 11.7b and 11.7c) through both linear sweep voltammetry (Fig. 11.7d) and non-localized proton (Fig. 11.7e) experiments every half an hour. The potential of the reduction step (-0.7 V) is low enough to avoid side reactions (*e.g.* HER) but high enough to offer high reaction rates, enabling the complete reduction of the quinone in less than 4 hours (four times faster at twice the previous concentration). The present results reveal system model allowing straightforward monitoring of the redox reaction (fast non-localized spectra<sup>12</sup>, Fig. 11.7e) with excellent electrochemical stability (reproducible CV over cycles, Fig. 11.7a). In the next chapter, the optimization of this promising high-sensitivity device is being handled in more details.

<sup>12</sup>NS = 64, TET = 1 min



## 12 - A 3D-printed Device for In Situ Monitoring of an ORFB via NMR/MRI

Manuscript accepted in *Analytical Chemistry*

# A 3D-printed device for in situ monitoring of an organic redox-flow battery via NMR/MRI

Borja Caja-Munoz,<sup>‡</sup> Kévin Chighine,<sup>‡</sup> Jean-Pierre Dognon,<sup>‡</sup> Lionel Dubois,<sup>§</sup> and Patrick Berthault\*,<sup>‡</sup>

<sup>‡</sup> NIMBE, CEA, CNRS, Université de Paris Saclay, CEA Saclay, 91191 Gif-sur-Yvette, France

<sup>§</sup> Univ. Grenoble Alpes, CEA, CNRS, IRIG-SyMMES UMR 5819, 38000 Grenoble, France

**KEYWORDS:** Battery, Redox-flow, NMR, MRI, Operando, 3D printing, Anthraquinone

**ABSTRACT:** A mini organic redox-flow battery pluggable on the basis of a high-resolution NMR probehead has been conceived and built mainly by 3D printing. This device allows the realization of all modern spectroscopy experiments as well as imaging experiments. It has been tested for the real-time monitoring of redox cycling of 9,10-Anthraquinone-2,7-disulfonic acid disodium salt (2,7-AQDS) in acidic conditions, which has revealed the preponderant role of dimerization in the processes of oxidation and reduction. Determination of the thermodynamic properties of homo- and heterodimer formation through quantum chemical, multilevel modeling workflows confirm our hypotheses about the molecular processes occurring during charge and discharge.

Large-scale development of renewable intermittent energy has led to a strong increase in storage capacity needs. As it allows dissociating quantity of store energy and power, redox-flow batteries (RFB) are specifically suited and developed for the large-scale stationary energy storage. In this technology, two electrolytes, able to exchange electrical charges at low (negolyte) or high (posolyte) potential, are pumped from the tank where they are stored through a conversion cell where the electrochemical process takes place. Nowadays, vanadium redox-flow battery (V-RFB) is the most developed and used RFB technology. Due to the cost and scarcity of vanadium, new chemistries based on organic redox molecules (O-RFB) are in development, mainly based on quinone chemistry. However, the high molecular concentration in solution (up to 2 or 3 M) giving rise to a lot of side reactions, associated or not to electron transfer during cycling, can result in a rapid loss of performances. For example, dimerization / polymerization or chemical modification can lead to a complete degradation of the electrolyte properties.<sup>1,2</sup>

As a consequence, there is strong need to develop operando analysis tools to understand degradation processes occurring during O-RFB cycling. Strongly linked to the electrochemical process, self-diffusion of the species near the electrodes is also a very important parameter to study in order to understand O-RFB performance degradations. In such a field, NMR is a powerful tool, as this non-destructive modality enables a detailed analysis at the atomic scale allowing studies of both chemical structure of organic molecule and diffusion process associated to each species in solution. The usual method would consist in manually sample the electrolyte solution during battery operation and fill NMR tubes for high resolution analysis. The problem with such an approach is that it requires opening the electrolyte reservoir, which can introduce air in the circuit, leading to unwanted oxidation of the

generated chemical species. Since the first in situ spectroscopic study of an electrochemical cell in 1964<sup>3</sup> until recently,<sup>4</sup> several approaches have been developed in order to identifying species electrochemically generated in solution. In the case of electrochemistry-NMR coupling some studies<sup>5,6,7</sup> utilized a flow cell arrangement in which the electrochemical reaction takes place outside of the radio frequency coils of the probe and the product was subsequently flowed into the detection area. These setups provide suitable conditions for the NMR measurements (enhanced field homogeneity) and allow the coupling with other spectroscopic methods such as EPR.<sup>8</sup> Nevertheless, they require large solution volumes and, above all, there is an inherent time delay between formation and detection of products and intermediates (leading to an indirect, non-real-time, monitoring method). As some products are not stable over time, other research groups decided to perform EC-NMR studies in a three-electrode mode with the working electrode positioned inside the NMR-active region (“probe-in”), simultaneously generating and detecting the electrochemical products (for a recent review on the analysis tools of electrochemical processes, see ref. 9).

Here we present a device for the operando NMR monitoring of a mini-organic redox-flow battery that exhibits several advantages. First, being in large part built by 3D-printing, it is of reduced size and can fit inside a narrow-bore magnet of a high-resolution NMR spectrometer. Its size is also an advantage for the quantity of organic redox derivatives that one might want to test but which price could be elevated. Second, it is designed to be electrically plugged onto the basis of a Bruker Micro-5 imaging probe, for the radiofrequency tuning/matching. This imposes a maximum diameter of 18 mm, but in this way, both magnetic resonance imaging and localized spectroscopy experiments can be achieved with the commercial hardware and software. For the circulation of the electrolyte we capitalize on the principle of the mini bubble pump that we developed a few years ago, for applications ranging from dissolution of hyperpolarized species,<sup>10</sup> to study of slowly relaxing nuclei.<sup>11,12</sup> A flow of inert gas drives the motion of the electrolyte solution in the circuit shown in Figure 1, so that the molecules at the working electrode surface are constantly renewed. This operando device is tested on 9,10-anthraquinone-2,7-disulfonic acid disodium salt (2,7-AQDS) in acidic conditions, which behaviour in redox-flow devices is well documented.<sup>13,14</sup>

For the purpose of the study of the evolution of the 2,7-AQDS molecules during charge and discharge cycles, the compartment of the counter-electrode contains only the solvent in the same concentration as in the main reservoir. The design of the mini-organic redox-flow battery (see Figure 1, and the full-size version in Figure S1 of the Supporting Information) is optimized according to the following specifications: i) a large volume is devoted to the NMR detection area which is centred with respect to the magnet bore (region of highest static field homogeneity) and is flanked by saddle coils in order to exhibit a high filling factor; ii) the bubbles that create the solution flow must not reach either the NMR detection area or the membrane region; iii) the working electrode – counter electrode distance is optimized in order to minimize the ohmic drop of the cell; iv) the geometry of the cell is such that the diffusion of the ions is as much as possible parallel to the static magnetic field, which minimizes the magneto-hydrodynamic effect.<sup>15,16</sup> It is still present, but low enough that it does not significantly modify the behaviour of the battery (see below).

The CAD of the battery was made in three parts fitted together. This not only facilitates the cleaning of crevices after Polyjet 3D printing, but also allows the insertion of aluminium foils horizontally on either side of the middle piece to act as rf insulators. The material chosen for printing is PMMA, not

solely to provide transparent parts, but also because its magnetic susceptibility is close to that of water, thus of the study medium. The bottom part (1) is devoted to the connection to the NMR probe basis; it contains the inductors and capacitors. The channel constituting the loop of the solution circuit is also in this part. The middle part (2) contains the rising and falling parts of the solution channels, the latter being surrounded by saddle coils while the former is isolated by winding of an aluminium foil. We denote this region as the NMR area. Two other aluminium foils are placed horizontally between parts (1) and (2) and (2) and (3). Without this rf isolation the entire solution circuit loop, including the rising portion of the solution channel and the upper tank, is detected, as displayed in Figure S2.

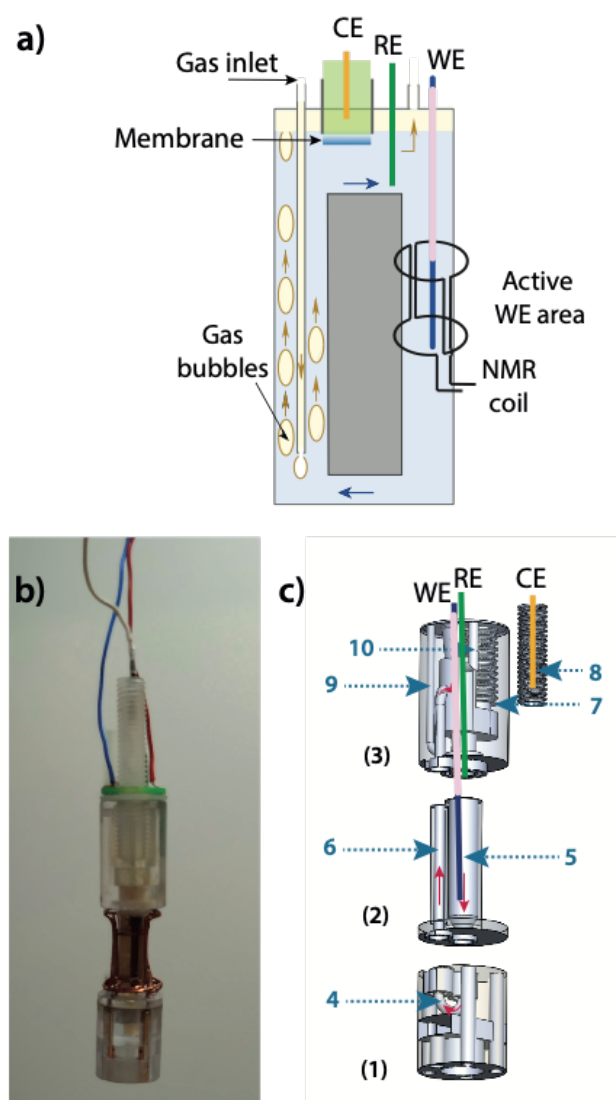


**Figure 1.** The mini redox-flow battery. a) Schematic diagram. WE: working electrode; RE: reference electrode; CE: counter-electrode. b) Picture; c) 3D rendering of the bottom (1), middle (2) and top (3) parts of the device. (4) Solution circuit loop, (5) NMR area, (6) back channel, rf-isolated with aluminum foil, (7) proton-exchange membrane, (8) counter-electrode compartment, (9) nitrogen inlet, (10) nitrogen exhaust, WE: working electrode (glassy carbon), RE: reference electrode (Ag/AgCl), CE: counter-electrode (Pt). For the sake of clarity, neither the rf coils nor the copper connectors at the bottom of the part (1) for the electric connection to the NMR probehead are drawn.

The top part (3) is the most complex. i) The 3D printing of a cylindrical receptacle bordered by a screw thread allows to receive the Nafion membrane and the tank containing the counter-electrode. This part is axially offset to leave room for the working and reference electrodes. The upper part of the working electrode, outside the NMR detection area, is insulated by a heat-shrinkable sheath. ii) The gas inlet is high enough in the part to avoid the formation of bubbles at the membrane surface. iii) The gas outlet is far enough from the inlet enabling high-speed bubbling to put into circulation the electrolyte solution, while avoiding it from pouring out of the insert. On top of this part a PCB (print card board) on which the reference electrode and the working electrode are welded achieves the interface with the potentiostat connectors. Between the PCB and the 3D printed piece, a cut sized silicon foil renders the latter gas proof, in order to avoid any unwanted oxidation. The fully dimensioned drawings of the cell are provided in the Supporting Information (Figs. S3-S6).

The proof of concept of the performances of this device have been made on a spectrometer working at 11.7 T ( $^1\text{H}$  Larmor frequency 500 MHz). Several versions of this disposable insert have been printed and equipped with either a single  $^1\text{H}$  saddle coil or two  $^1\text{H}$  and  $^{13}\text{C}$  saddle coils in quadrature, in direct (inner coil  $^{13}\text{C}$ ) or inverse mode (inner coil  $^1\text{H}$ ). The experiments which are now described have been performed in this configuration. In a first time, field homogeneity has been optimized, in particular thanks to  $B_0$  mapping.  $^1\text{H}$  and  $^{13}\text{C}$  pulses have been calibrated. Then 2D  $^1\text{H}$  gradient echo imaging experiments have been performed to set up the localized spectroscopy experiments inside the NMR reservoir. Figure 2a displays such longitudinal and axial images recorded with the electrode in place. The donut shape of the axial image is due to the presence of the electrode. The images reveal that the aluminium foils act as expected: only the area of interest (5) in Figure 1c gives an NMR signal. Such images enable us to select a pixel of interest outside the electrode region for a  $^1\text{H}$  spectrum with high resolution through PRESS or STEAM approaches (Figure 2b). On the spectrum localized in the 2.4 mm x 2.4 mm region delimited by the red dashed line, a resolution better than 4 Hz is achieved, and the  $J_{\text{HH}}$  scalar couplings are well observed. The water signal also is not too broad, and the anthraquinone signals can be observed without pre-saturation. It is possible to improve this spectral resolution, by taking a smaller voxel, but obviously at the cost of a lower signal-to-noise ratio per time unit. A compromise allowing to obtain a spectral resolution not too degraded while keeping enough signal to monitor the battery in action is here chosen. The  $^{13}\text{C}$  spectrum (recorded without spatial localization) shows as expected the signals of the oxidized form of the anthraquinone, see Fig. 2c. Note that the  $^1\text{H}$ -decoupling is efficient.

The identification of the redox state of the 2,7-AQDS is thus possible at any state of charge of the battery. The only limitation is linked to the case where too many free radicals are generated, which would drastically broaden the signals. The identification of potential intermediate molecular species and degradation products requires a more sophisticated tool than 1D NMR. This is why we turned to localized 2D homo- and heteronuclear experiments. Several authors have already developed localized heteronuclear correlation experiments, and even applied them *in vivo* on clinical imagers.<sup>17,18,19,20</sup> Here, given the cylindrical geometry of the NMR area and the rf shielding provided by the aluminium foils, it is sufficient to select a xy pixel instead of an xyz voxel. We have thus modified in accordance the original HSQC pulse sequence with sensitivity improvement<sup>21</sup> implemented on the spectrometer, principally in replacing the first two  $^1\text{H}$   $90^\circ$  hard pulses by frequency-selective ones simultaneous to

magnetic field gradients (see Figure 3a). Note that the HSQC scheme was preferred to the HMQC one as the presence of multi-quantum coherences which relaxation is accelerated is detrimental to the sensitivity of the experiment. Due to a possible spatial spreading of  $B_1$  field linked to the presence of the electrode, we have preferred to render the  $90^\circ$  pulses spatially-selective instead of the  $180^\circ$  refocusing pulses. Thus the first  $^1\text{H}$   $90^\circ$  pulse excites the protons placed inside a slice along  $x$ . The INEPT scheme occurs there. In order to ensure that the final amount of magnetization flipped along  $z$  by the second  $90^\circ$  pulse only depends on the C-H coupling constant, and not on the spatial position of the spins along the gradient direction, a second gradient of the same sign and amplitude as the slice gradient but of half duration (the tilting of the magnetization in the transverse plane by the soft pulse is considered to occur in the middle of the pulse) is applied after the  $180^\circ$   $^1\text{H}$  pulse. Note that the carbon  $90^\circ$  pulse is shifted just after the gradient of the second slice selection so that it is not spatially selective.

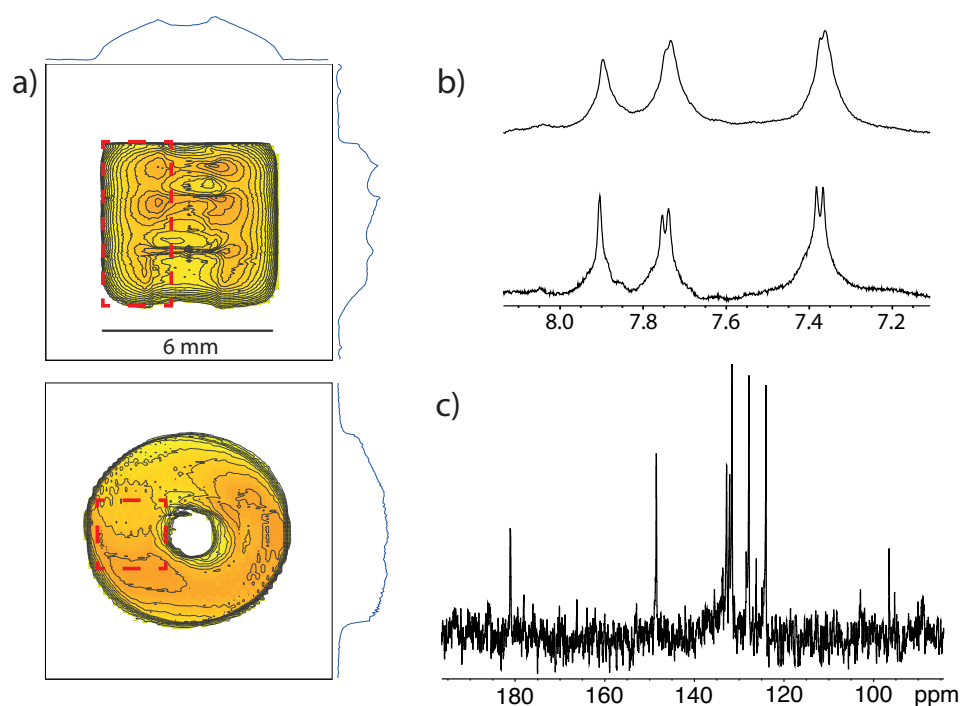


**Figure 2.** a) 2D  $^1\text{H}$  gradient echo images of the NMR reservoir. The presence of the electrode is clearly visible. b) Comparison between normal (4 scans, up) and localized (8 scans, down)  $^1\text{H}$  spectra of 2,7-AQDS (0.5 M). The selected area corresponds to the region delimited by the red dashed lines in a). c)  $^1\text{H}$ -decoupled  $^{13}\text{C}$  spectrum of 2,7-AQDS (0.5 M; 128 scans).

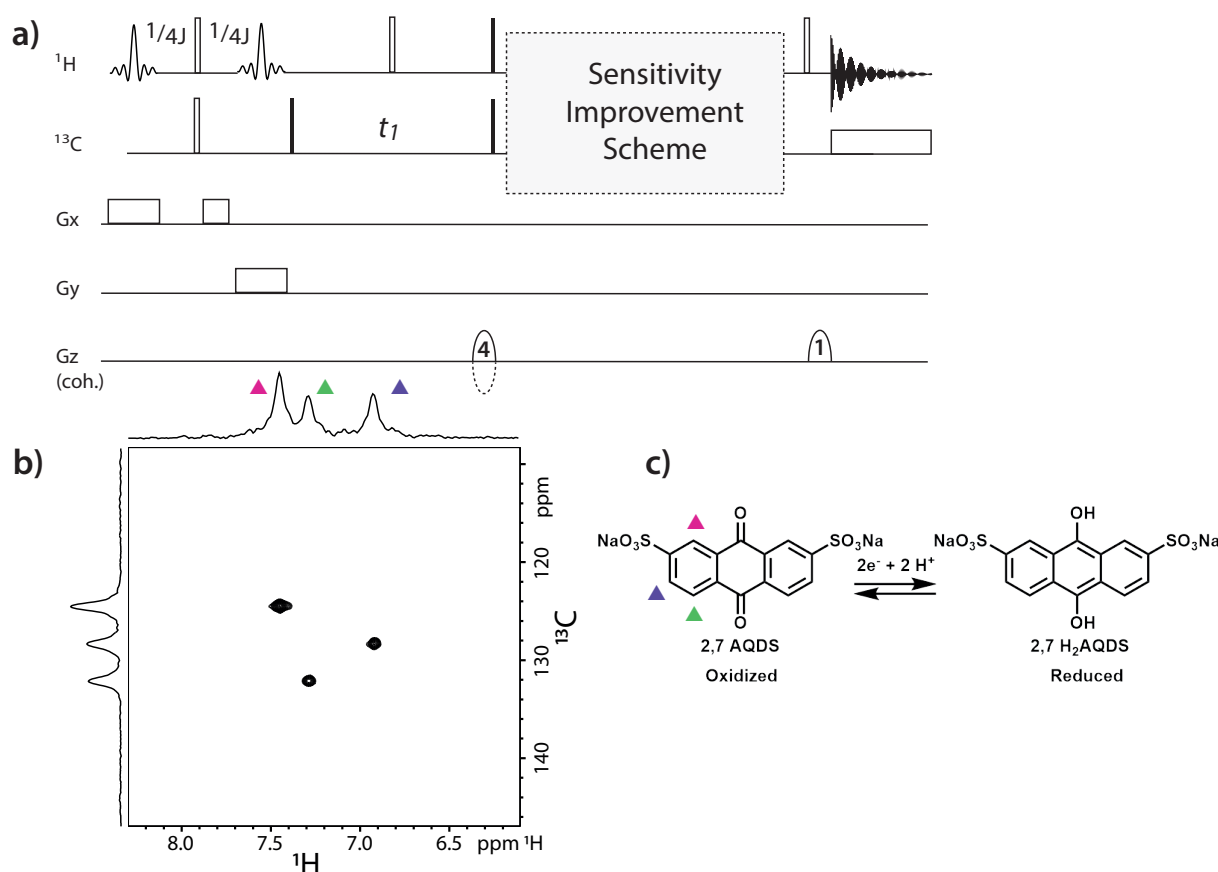


**Figure 3.** a) Pulse sequence of the localized 2D HSQC experiment. The black and white rectangles indicate  $90^\circ$  and  $180^\circ$  hard pulses respectively, the  $90^\circ$  soft pulses being represented by a sinc shape. For the z gradients, their relative value is indicated inside the shape. The dashed negative shape indicates the echo-antiecho scheme for quadrature in the indirect dimension. b)  $^1\text{H}$ - $^{13}\text{C}$  HSQC performed on the oxidized form of 2,7-AQDS at 0.5 M (experiment time: 1h) inside the  $2.4 \times 2.4$  mm pixel of the NMR reservoir drawn in previous Figure. c) Structure of 2,7-AQDS, under its oxidized and reduced forms.

While x and y gradients serve for spatial localization, the z gradients are used for coherence selection. The factor 4 between the two gradients allows to select only  $^{13}\text{C}$  coherences that have evolved during  $t_1$  and transferred to the protons for detection.

Figure 3b displays the contour plot of the localized HSQC recorded in one hour on a 0.5 M solution of 2,7-AQDS. The one-bond  $^1\text{H}$ - $^{13}\text{C}$  correlations are quite clean. This contour plot can be compared with the one recorded on the same sample without localization. On Fig. S7 of the Supp. Info., the improvement in spectral resolution is obvious in the  $^1\text{H}$  dimension.

In addition to the identification of the molecular structure of compounds in solution, this device allows the measurement of two other important parameters: i- measurement of the diffusion coefficient of the molecular species in solution, according to the pH, concentration and temperature conditions 2,7-AQDS can be subjected to multimerization<sup>22</sup> which can be detected through self-diffusion experiments. ii- solution flow monitoring, the operation of a redox flow battery requires electrolytes circulation, so as to renew the molecular species at the electrodes surface. In our battery, where this

flow is driven by an inert gas, this monitoring is essential. The solution flux can be characterized by NMR velocimetry experiments, as shown in Figure 4.

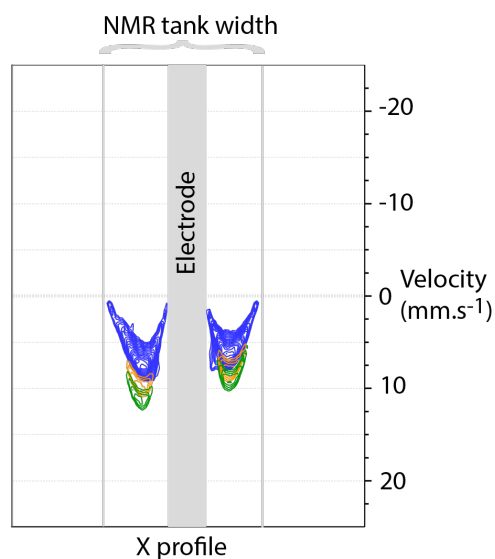


**Figure 4.** Velocity profiles of the solution inside the NMR tank, with a nitrogen flow of 1 mL/min (blue), 2 mL/min (orange) and 3 mL/min (green).

This point is important, since an insufficient level of liquid in the upper part of the insert prevents the proper functioning of the bubble pump and thus the circulation of the electrolyte solution. In this case, the solution ‘oscillates’ without a net solution displacement (see Fig. S8 of the Supp. Info.). Thus, this simple and fast experiment (less than 1 min) is sufficient to periodically ensure that the solution is flowing.

As an application, we have monitored the evolution of 2,7-AQDS during cycles of charge (reduction) and discharge (oxidation). The first step has been to perform a cyclic voltammetry to define the oxidation and reduction voltage peaks. Figure S9 of the Supp. Info. shows that these peaks appear at +0.3 V and -0.6 V. Obviously a magnetic field has an effect on mass transport of charged species, proportional to the cross product between magnetic field intensity and current density.<sup>15</sup> This can lead to complex flow pattern, but, as already stated, due to the design of the cell this so-called magneto-hydrodynamic effect is reduced. This can be checked on Figure S10 of the Supporting Information, which compares the cyclic voltammograms recorded with and without magnetic field.

Figure 5 displays the <sup>1</sup>H spectra of 2,7-AQDS 50 mM in H<sub>2</sub>SO<sub>4</sub> 0.5 M at three different steps after a voltage of -0.5 V has been applied (see the corresponding chronoamperometry in Fig. S11). The medium in which the counter-electrode immersed is also H<sub>2</sub>SO<sub>4</sub> 0.5 M. A -0.5 V voltage is chosen instead of -0.6 V, in order to avoid the formation of hydrogen bubbles at the surface of the WE electrode that reduces the spectral homogeneity.



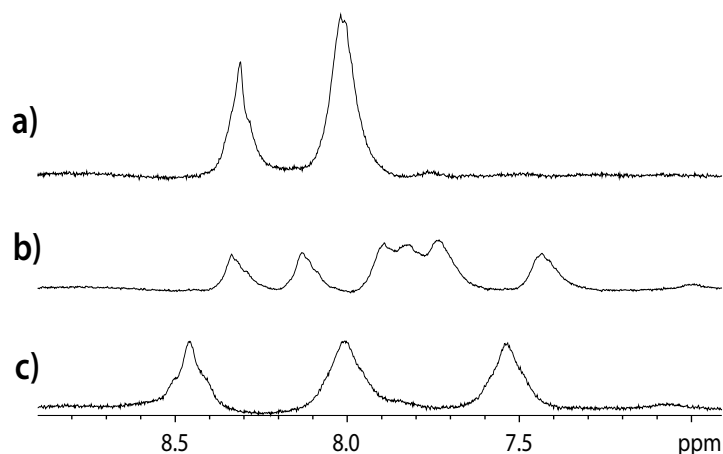


**Figure 5.** Three  $^1\text{H}$  spectra of 2,7-AQDS during a reduction process. a) Oxidized form; b) Intermediate form; c) Reduced form.

A more complete representation is a contour plot of the successive spectra recorded each 5 minutes during the reduction steps (Figure 6a). More meaningful, Figure 6b displays the spectra as a function of the number of Coulombs that are exchanged. Figure 6c shows the 3D profile of the time evolution of the spectra, and Figure 6d the sum of the peak area as a function of the number of Coulombs exchanged. Figs 6e-h follow the same principle for an oxidation step, in which a voltage of +0.45 V is applied. The corresponding chronoamperometry is displayed in Figure S12.

From Figure 6b it is immediate to see that the first and last spectra correspond to the oxidized and reduced forms of 2,7-AQDS, respectively. Given the equation  $Q = c.V.n.F$ , where  $Q$  stands for the number of Coulombs for a complete electrochemical reaction,  $c$  the 2,7-AQDS concentration (50 mM),  $V$  the solution volume (here 1.8 mL),  $n$  the number of exchanged electrons (2 for 2,7-AQDS) and  $F$  the Faraday constant, 17 Coulombs are expected for a full redox conversion. This is approximately what is observed in Figs 6b and 6d (for the return to the oxidized state, the NMR acquisition started well after the electrochemical reaction).

From these graphs, several observations can be made. i) At the beginning of both the reduction step and the oxidation step, the three aromatic proton signals experience a high field shift, with an almost identical slope variation. ii) A progressive loss of global intensity occurs, before the appearance of the other form. iii) The protons of the new form are then subjected to a downfield shift and the global intensity re-increases.

The change in the global line intensities (Fig. 6d and h) indicates that some intermediates of the reaction are radical species, as already observed by Wiberg et al.<sup>22</sup> Note that their predominance occurs at ca. 11 Coulombs, i. e. 60% of the oxidation.

Also the initial high field chemical shift variation for the three aromatic protons and in the second part the subsequent low field variation suggest that heterodimers associating 2,7-AQDS and  $\text{H}_2$ 2,7-AQDS are more stable than 2,7-AQDS-2,7-AQDS and  $\text{H}_2(2,7\text{-AQDS})\text{-H}_2(2,7\text{-AQDS})$  homodimers,

probably favoured by hydrogen bonds. This can be explained by the following reasoning, leaving aside the monomer/homodimer equilibrium.

For both the oxidized and the reduced species, each proton chemical shift experiencing fast exchange between the monomeric form and the heterodimeric form can be expressed as:

$$\delta = x \delta_M + (1-x) \delta_D$$

where  $\delta_M$  and  $\delta_D$  stand for the chemical shift of the monomer and of the dimer, respectively,

and  $x = [\text{Monomer}]/([\text{Monomer}]+[\text{Dimer}])$  is the molar fraction of monomer. For the following, we will refer to the oxidized, reduced, and heterodimeric forms as O, R and O-R, respectively.

In accordance with Carney et al.<sup>23</sup> it is known that the passage from the oxidized monomeric form to the (homo)dimeric form due to concentration increase leads to an upfield shift of the three proton signals (from 8.4, 8.15, 8.0 to 7.7, 7.05, 7.55 ppm in H<sub>2</sub>SO<sub>4</sub> 0.5 M). Here there is no reason to imagine that the concentration increases during the redox cycle, but rather that the high field shift is due to hetero-dimers between the oxidized and reduced forms.

At about half the charge (or discharge) the second monomeric form becomes predominant, and as the homodimers are less probable the chemical shifts start to re-increase. At this step, 6 distinct <sup>1</sup>H peaks are clearly visible (Fig. 5b), corresponding to the six protons of the heterodimer. To confirm our hypothesis, the same 2D self-diffusion NMR experiment (DOSY) has been performed on the oxidized state and at this step where 6 peaks appear (Fig. S13), both experiments being performed in the absence of solution flow and electric current. While it has been checked that the water diffusion coefficient remains constant at 2.2 10<sup>-9</sup> m<sup>2</sup>s<sup>-1</sup>, the diffusion coefficient of the aromatic protons decreases from 0.48 10<sup>-9</sup> m<sup>2</sup>s<sup>-1</sup> to 0.40 10<sup>-9</sup> m<sup>2</sup>s<sup>-1</sup>. Passing from a fast mixture of monomer/homodimer to the heterodimer is not expected to divide by 2 the diffusion coefficient, as the  $\pi$ -stacking arrangement is not prone to significantly modify the hydrodynamic radius of the molecule.<sup>24</sup> Thus although the self-diffusion experiment is only qualitative, it comforts our assertions. To confirm or deny our hypotheses we have undertaken theoretical chemistry calculations.

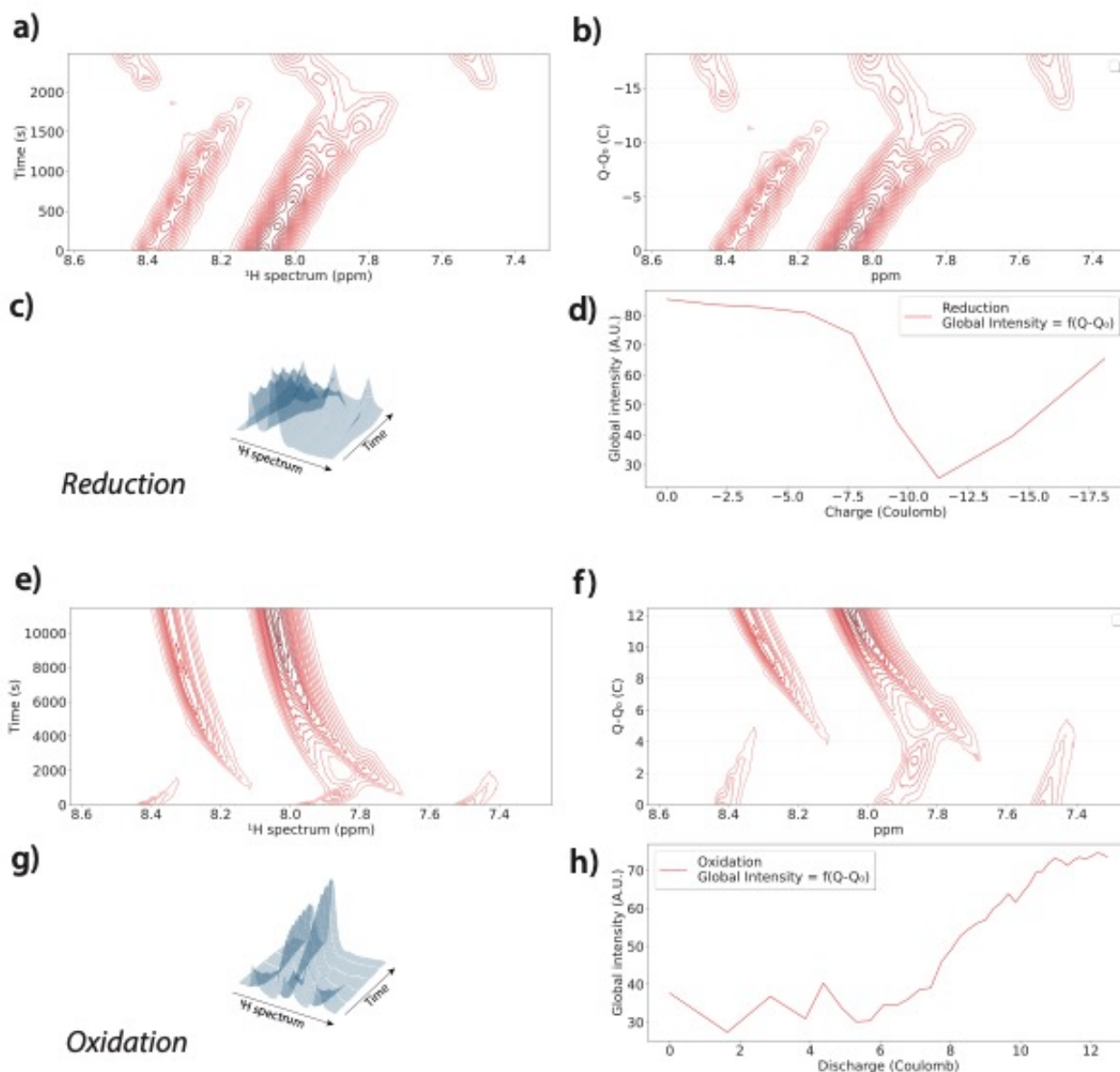


**Figure 6.** a-d) Evolution of the  $^1\text{H}$  NMR spectrum of 2,7-AQDS (50 mM in  $\text{H}_2\text{SO}_4$  0.5 M) during the reduction step (charge of the mini-battery). a) Contour plot of the spectra according to time; b) Spectra according to the number of Coulombs exchanged; c) 3D view of these spectra; d) Sum of the peak intensities as a function of the number of Coulombs exchanged. e-f) Evolution of the  $^1\text{H}$  NMR spectrum of 2,7-AQDS during the oxidation step (discharge of the mini-battery). e) Contour plot of the spectra according to time; f) Spectra according to the number of Coulombs exchanged; g) 3D view of these spectra; h) Sum of the peak intensities as a function of the number of Coulombs exchanged.

For the dimers, various  $\pi$ - $\pi$  stacking and hydrogen bonding motifs are possible. We implemented quantum chemical, multilevel modelling workflows for the determination of the 2,7-AQDS dimerization preferences. This is accomplished by a conformer search based on the CREST sampling software.<sup>25</sup> The main goal of the conformer search is to find the energetically most favourable conformers.

For the final geometry optimization (and the final free energy calculation) of the most stable conformers, we used the composite DFT method r2SCAN-3c<sup>26</sup> with the ORCA 5.0.3 program.<sup>27</sup>

The binding free energies ( $\Delta G$ ) for the formation of an A-B dimer (used for the cases of the O-O, R-R and O-R dimers) are defined as  $\Delta G_{\text{bind}} = G_{\text{AB}} - G_{\text{A}} - G_{\text{B}}$ . The most stable dimer geometries and binding free energies are shown in Figure 7.

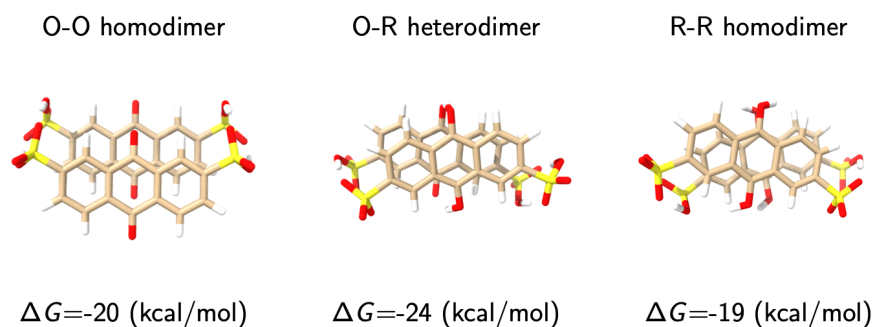


**Figure 7.** Most stable geometries and binding free energies of the dimers appearing during the redox cycle.

These quantum chemistry results indicate that the oxidized 2,7-AQDS and the reduced 2,7-AQDS ligands can form together a stable heterodimer in preference to homodimers. This is in good accordance with literature studies who demonstrate that at the low concentration used for our 2,7-AQDS electrolyte, the 2,7-AQDS dimer is not the main species.<sup>22</sup> The stabilization of the heterodimer is mainly due to H-bonds and van der Waals attractive interaction as graphically revealed in Figure 8 from the Interaction Region Indicator (IRI)<sup>28</sup> calculated with the Multiwfn program.<sup>29</sup> Note that Tong et al.,<sup>30</sup> using UV-Vis spectroscopy, also evidenced an heterodimer stabilized via hydrogen bonding between oxidized and reduced quinone forms in solution. Thus, in the scenario that we envision (depicted in Figure 9), in our experimental conditions four main species are in fast equilibrium at the NMR time scale during cycling: the 2,7-AQDS and H<sub>2</sub>(2,7-AQDS) monomers, the 2,7-AQDS/H<sub>2</sub>(2,7-AQDS) heterodimer and the H(2,7-AQDS)<sup>•</sup> radicals. The relative concentration of each species evolves with the state of charge. As expected, the concentrations of the heterodimer and of the H(2,7-AQDS)<sup>•</sup> radicals are maximum when half the theoretical number of electrons is transferred both in charge and in discharge. This mechanism is in accordance with previous works performed by Wiberg et al.<sup>22</sup>

Our experimental setup obviously does not allow yet direct detection of the free radical states, which would require an in situ system including both NMR and EPR.<sup>7,8</sup> But this low-cost, custom-made, disposable device has some interesting potentialities. First of all, the low volumes of solution required will enable the study of expensive organic electrolytes, and will induce short cycling times. Second, the observation of other nuclei such as lithium or sodium will only require a change of the tuning capacitor at the base of the insert, which can be done at low cost. It gives this device a high versatility. Third, the device as designed is based on a micro-imaging probe, which allows us to use localized spectroscopy, and to obtain reasonable spectral homogeneity, even in the most electrochemically interesting region, which is that surrounding the working electrode. Last, the availability of pulsed field

gradients also opens the way to characterization techniques of the flow or of the molecular species, such as velocimetry, self-diffusion experiments.

The perspectives are now to replace our polymer inserts, which however resist well to acidic environments, by inserts still 3D printed, but in more inert ceramic or glass, using the low-cost processes proposed among others by Kotz et al.<sup>31</sup> based on the initial use of organic inks loaded in SiO<sub>2</sub>, Al<sub>2</sub>O<sub>3</sub> or ZrO<sub>2</sub> particles.

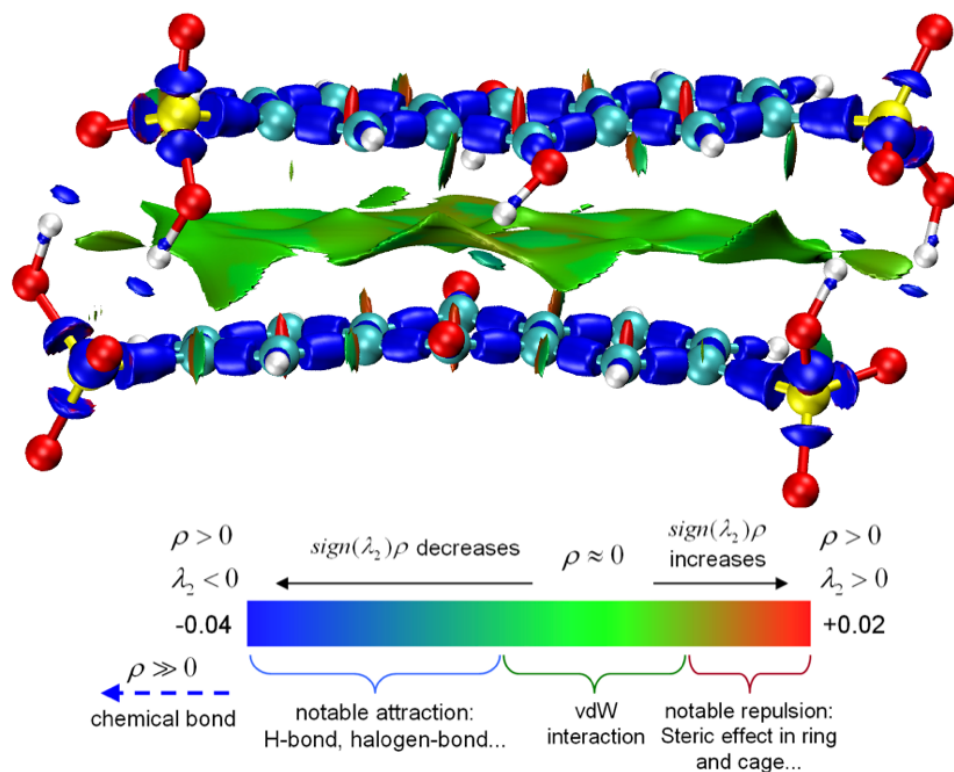


**Figure 8.** Weak interaction and chemical bond regions from IRI map for the 2,7-AQDS / 2,7-H2AQDS heterodimer.

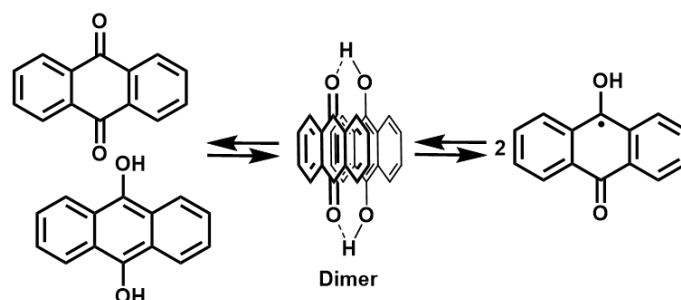


**Figure 9.** a) Scheme of the hypothetical processes occurring during the charge/discharge cycles for 2,7-AQDS. The sulfonate groups are not displayed for sake of clarity.

## EXPERIMENTAL SECTION

### Building of the ORFB

The CAD of the battery body was made with SolidWorks (Dassault System) and the piece bodies were built by additive manufacturing using a PolyJet Objet30 printer (Stratasys) equipped with PMMA-based VeroClear resin. The saddle coils were made with 0.7 mm diameter copper wire with two loops for the outer 13C coil and one loop for the 1H inner coil. The tuning capacitors were MLCC KEMET ceramics. The rf shielding of the back channel was made with a 0.02 mm width aluminium foil. The working and reference electrodes were welded on 0.8 mm copper wire insulated by heat-shrink tube itself welded on a print card board (designed on KiCad electronics CAD software) for interface with the potentiostat connectors. The shape of the PCB was mechanically adapted to interface with a silicon joint cut to size for the gas proof of the receptacle limiting any oxidation reaction with air.

### Electrochemistry

Electrochemical measurements were performed with a SP 150 potentiometer (Biologic). The working electrode (WE) was a 1 mm-diameter glassy carbon rod type 2 (Alfa Aesar) polished with a water-alumina slurry 0.05  $\mu\text{m}$  (Sigma-Aldrich) before each experiment. The reference electrode (RE) was a 0.2 mm-diameter silver wire poured in Ag/AgCl Ink (ALS) and dried with hot air (121°C during 15 min); a homogeneous coating with a cation-exchange Nafion D2020 solution (Ion Power) was applied to provide protection and guarantee a stable potential in acidic conditions. The counter electrode was a 1.55 mm-diameter 99.9% platinum wire cleaned with 10% nitric acid before each experiment.

### NMR

NMR experiments were performed at room temperature on a narrow-bore 11.7 T Bruker Avance II spectrometer equipped with 3-axes field gradients of max. amplitude 200  $\text{G}\cdot\text{cm}^{-1}$ . The NMR probe body on which the 3D-printed insert was plugged was a dual-channel Bruker Micro-5. Self-diffusion experiments used stimulated echo and longitudinal eddy current delay (LED32), with a gradient duration  $\delta$  of 1 ms and inter-gradient delay  $\Delta$  of 150 ms. The gradients had a sine shape and the indirect dimension of the experiments contained 16 points linearly spaced from 4 to 90  $\text{G}/\text{cm}$ .

### Processing of the operando NMR data

The evolution of the anthraquinone derivatives during reduction or oxidation was monitored by one-dimensional  $^1\text{H}$  spectra performed with or without spatial localization, and then assembled in a 2D

map, with the time as ordinate (Figs 6a and 6e). A Python program then established a temporal correlation between chronoamperometry and NMR, in order to transform the time ordinate axis into a number of exchanged Coulombs, more useful for analysis (Figs 6b and 6f). In the same program, the 3D view of the spectra is computed (Figs 6c and 6g), as well as the curve giving the sum of the aromatic peak intensities as a number of Coulombs (Figs 6d and 6h). This program is available upon request to the authors.

## ASSOCIATED CONTENT

### Supporting Information

Full-size reproduction of Fig. 1c;  $^1\text{H}$  image of the cell without the aluminum shields; CAD drawings of the mini-battery; 2D maps of the localized and non-localized  $^1\text{H}$ - $^{13}\text{C}$  HSQC experiments performed on 2,7-AQDS;  $^1\text{H}$  NMR velocimetry experiment in the presence of an insufficient solution level; Cyclic Voltammetry; Chronoamperometry curves; DOSY experiments at the oxidized and intermediate states (PDF).

## AUTHOR INFORMATION

### Corresponding Author

\* [patrick.berthault@cea.fr](mailto:patrick.berthault@cea.fr)

### Author Contributions

The manuscript was written through contributions of all authors. All authors have given approval to the final version of the manuscript.

## ACKNOWLEDGMENT

Supports from the French Ministry of Research (project 17-LCV2-0002-01 LabCom DESIR) and from CEA (Programmes Transverses de Compétences; project ROBO3D) are acknowledged.

## REFERENCES

- (1) Kwabi, D. G.; Ji, Y.; Aziz, M. J. Electrolyte Lifetime in Aqueous Organic Redox Flow Batteries: A Critical Review. *Chem. Rev.* 2020, 120 (14), 6467–6489. <https://doi.org/10.1021/acs.chemrev.9b00599>.
- (2) Goulet, M.-A.; Tong, L.; Pollack, D. A.; Tabor, D. P.; Odom, S. A.; Aspuru-Guzik, A.; Kwan, E. E.; Gordon, R. G.; Aziz, M. J. Extending the Lifetime of Organic Flow Batteries via Redox State Management. *J. Am. Chem. Soc.* 2020, 141 (20), 8014–8019. <https://doi.org/10.1021/jacs.8b13295>.
- (3) Kuwana, Theodore.; Darlington, R. K.; Leedy, D. W. Electrochemical Studies Using Conducting Glass Indicator Electrodes. *Anal. Chem.* 1964, 36 (10), 2023–2025. <https://doi.org/10.1021/ac60216a003>.
- (4) Jones, A. E.; Ejigu, A.; Wang, B.; Adams, R. W.; Bissett, M. A.; Dryfe, R. A. W. Quinone Voltammetry for Redox-Flow Battery Applications. *J. Electroanal. Chem.* 2022, 920, 116572. <https://doi.org/10.1016/j.jelechem.2022.116572>.
- (5) Richards, J. A.; Evans, D. H. Flow Cell for Electrolysis within the Probe of a Nuclear Magnetic Resonance Spectrometer. *Anal. Chem.* 1975, 47 (6), 964–966. <https://doi.org/10.1021/ac60356a016>.
- (6) Albert, K.; Dreher, E.-L.; Straub, H.; Rieker, A. Monitoring Electrochemical Reactions by <sup>13</sup>C NMR Spectroscopy. *Magn. Reson. Chem.* 1987, 25 (10), 919–922. <https://doi.org/10.1002/mrc.1260251017>.
- (7) Jing, Y.; Zhao, E. W.; Goulet, M.-A.; Bahari, M.; Fell, E. M.; Jin, S.; Davoodi, A.; Jónsson, E.; Wu, M.; Grey, C. P.; Gordon, R. G.; Aziz, M. J. In Situ Electrochemical Recomposition of Decomposed Redox-Active Species in Aqueous Organic Flow Batteries. *Nat. Chem.* 2022, 14 (10), 1103–1109. <https://doi.org/10.1038/s41557-022-00967-4>.
- (8) Zhao, E. W.; Jónsson, E.; Jethwa, R. B.; Hey, D.; Lyu, D.; Brookfield, A.; Klusener, P. A. A.; Collison, D.; Grey, C. P. Coupled In Situ NMR and EPR Studies Reveal the Electron Transfer Rate and Electrolyte Decomposition in Redox Flow Batteries. *J. Am. Chem. Soc.* 2021, 143 (4), 1885–1895. <https://doi.org/10.1021/jacs.0c10650>.
- (9) McKenzie, E. C. R.; Hosseini, S.; Petro, A. G. C.; Rudman, K. K.; Gerroll, B. H. R.; Mubarak, M. S.; Baker, L. A.; Little, R. D. Versatile Tools for Understanding Electrosynthetic Mechanisms. *Chem. Rev.* 2022, 122 (3), 3292–3335. <https://doi.org/10.1021/acs.chemrev.1c00471>.
- (10) Causier, A.; Carret, G.; Boutin, C.; Berthelot, T.; Berthault, P. 3D-Printed System Optimizing Dissolution of Hyperpolarized Gaseous Species for Micro-Sized NMR. *Lab. Chip* 2015, 15 (9), 2049–2054. <https://doi.org/10.1039/C5LC00193E>.

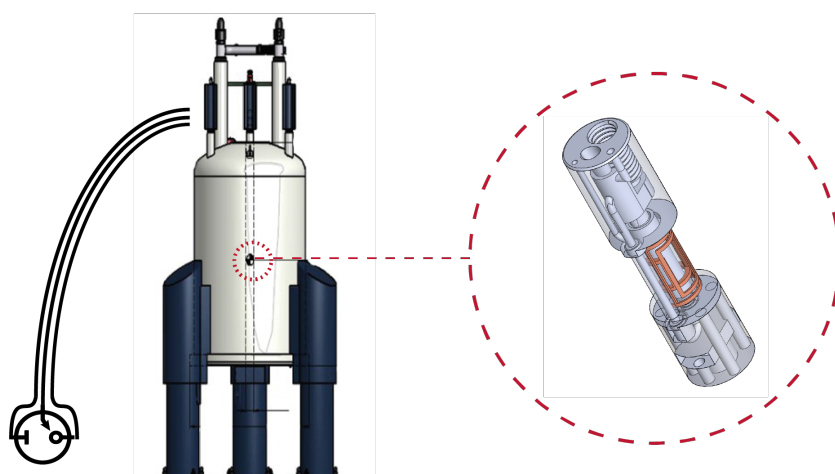


- (11) Carret, G.; Berthelot, T.; Berthault, P. Enhancing NMR of Nonrelaxing Species Using a Controlled Flow Motion and a Miniaturized Circuit. *Anal. Chem.* 2017, 89 (5), 2995–3000. <https://doi.org/10.1021/acs.analchem.6b04488>.
- (12) Carret, G.; Berthelot, T.; Berthault, P. Inductive Coupling and Flow for Increased NMR Sensitivity. *Anal. Chem.* 2018, 90 (19), 11169–11173. <https://doi.org/10.1021/acs.analchem.8b01775>.
- (13) Huskinson, B.; Marshak, M. P.; Suh, C.; Er, S.; Gerhardt, M. R.; Galvin, C. J.; Chen, X.; Aspuru-Guzik, A.; Gordon, R. G.; Aziz, M. J. A Metal-Free Organic–Inorganic Aqueous Flow Battery. *Nature* 2014, 505 (7482), 195–198. <https://doi.org/10.1038/nature12909>.
- (14) Gerhardt, M. R.; Tong, L.; Gómez-Bombarelli, R.; Chen, Q.; Marshak, M. P.; Galvin, C. J.; Aspuru-Guzik, A.; Gordon, R. G.; Aziz, M. J. Anthraquinone Derivatives in Aqueous Flow Batteries. *Adv. Energy Mater.* 2017, 7 (8), 1601488. <https://doi.org/10.1002/aenm.201601488>.
- (15) Ferreira Gomes, B.; Ferreira da Silva, P.; Silva Lobo, C. M.; da Silva Santos, M.; Colnago, L. A. Strong Magneto-electrolysis Effect during Electrochemical Reaction Monitored in Situ by High-Resolution NMR Spectroscopy. *Anal. Chim. Acta* 2017, 983, 91–95. <https://doi.org/10.1016/j.aca.2017.06.008>.
- (16) Benders, S.; Gomes, B. F.; Carmo, M.; Colnago, L. A.; Blümich, B. In-Situ MRI Velocimetry of the Magnetohydrodynamic Effect in Electrochemical Cells. *J. Magn. Reson.* 2020, 312, 106692. <https://doi.org/10.1016/j.jmr.2020.106692>.
- (17) Watanabe, H.; Ishihara, Y.; Okamoto, K.; Oshio, K.; Kanamatsu, T.; Tsukada, Y. 3D Localized <sup>1</sup>H-<sup>13</sup>C Heteronuclear Single-Quantum Coherence Correlation Spectroscopy in Vivo. *Magn. Reson. Med.* 2000, 43 (2), 200–210. [https://doi.org/10.1002/\(SICI\)1522-2594\(200002\)43:2<200::AID-MRM6>3.0.CO;2-H](https://doi.org/10.1002/(SICI)1522-2594(200002)43:2<200::AID-MRM6>3.0.CO;2-H).
- (18) De Feyter, H. M.; Herzog, R. I.; Steensma, B. R.; Klomp, D. W. J.; Brown, P. B.; Mason, G. F.; Rothman, D. L.; de Graaf, R. A. Selective Proton-Observed, Carbon-Edited (SelPOCE) MRS Method for Measurement of Glutamate and Glutamine <sup>13</sup>C-Labeling in the Human Frontal Cortex. *Magn. Reson. Med.* 2018, 80 (1), 11–20. <https://doi.org/10.1002/mrm.27003>.
- (19) Kanamori, K.; Ross, B. D. In Vivo Detection of <sup>15</sup>N-Coupled Protons in Rat Brain by ISIS Localization and Multiple-Quantum Editing. *J. Magn. Reson.* 1999, 139 (2), 240–249. <https://doi.org/10.1006/jmre.1999.1764>.
- (20) Méric, P.; Autret, G.; Doan, B. T.; Gillet, B.; Sébrié, C.; Beloeil, J.-C. In Vivo 2D Magnetic Resonance Spectroscopy of Small Animals. *Magn. Reson. Mater. Phys. Biol. Med.* 2004, 17 (3), 317–338. <https://doi.org/10.1007/s10334-004-0084-2>.

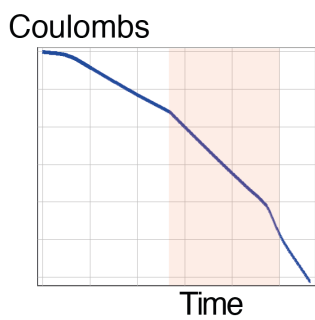
- (21) Schleucher, J.; Schwendinger, M.; Sattler, M.; Schmidt, P.; Schedletsky, O.; Glaser, S. J.; Sørensen, O. W.; Griesinger, C. A General Enhancement Scheme in Heteronuclear Multidimensional NMR Employing Pulsed Field Gradients. *J. Biomol. NMR* 1994, 4 (2), 301–306. <https://doi.org/10.1007/BF00175254>.
- (22) Wiberg, C.; Carney, T. J.; Brushett, F.; Ahlberg, E.; Wang, E. Dimerization of 9,10-Anthraquinone-2,7-Disulfonic Acid (AQDS). *Electrochimica Acta* 2019, 317, 478–485. <https://doi.org/10.1016/j.electacta.2019.05.134>.
- (23) Carney, T. J.; Collins, S. J.; Moore, J. S.; Brushett, F. R. Concentration-Dependent Dimerization of Anthraquinone Disulfonic Acid and Its Impact on Charge Storage. *Chem. Mater.* 2017, 29 (11), 4801–4810. <https://doi.org/10.1021/acs.chemmater.7b00616>.
- (24) Hamelin, B.; Jullien, L.; Derouet, C.; Hervé du Penhoat, C.; Berthault, P. Self-Assembly of a Molecular Capsule Driven by Electrostatic Interaction in Aqueous Solution. *J. Am. Chem. Soc.* 1998, 120 (33), 8438–8447. <https://doi.org/10.1021/ja980046g>.
- (25) Pracht, P.; Bohle, F.; Grimme, S. Automated Exploration of the Low-Energy Chemical Space with Fast Quantum Chemical Methods. *Phys. Chem. Chem. Phys.* 2020, 22 (14), 7169–7192. <https://doi.org/10.1039/C9CP06869D>.
- (26) Grimme, S.; Hansen, A.; Ehlert, S.; Mewes, J.-M. R2SCAN-3c: A “Swiss Army Knife” Composite Electronic-Structure Method. *J. Chem. Phys.* 2021, 154 (6), 064103. <https://doi.org/10.1063/5.0040021>.
- (27) Neese, F. Software Update: The ORCA Program System—Version 5.0. *WIREs Comput. Mol. Sci.* 2022, 12 (5). <https://doi.org/10.1002/wcms.1606>.
- (28) Lu, T.; Chen, Q. Interaction Region Indicator: A Simple Real Space Function Clearly Revealing Both Chemical Bonds and Weak Interactions. *Chemistry—Methods* 2021, 1 (5), 231–239. <https://doi.org/10.1002/cmtd.202100007>.
- (29) Lu, T.; Chen, F. Multiwfn: A Multifunctional Wavefunction Analyzer. *J. Comput. Chem.* 2012, 33 (5), 580–592. <https://doi.org/10.1002/jcc.22885>.
- (30) Tong, L.; Chen, Q.; Wong, A. A.; Gómez-Bombarelli, R.; Aspuru-Guzik, A.; Gordon, R. G.; Aziz, M. J. UV-Vis Spectrophotometry of Quinone Flow Battery Electrolyte for in Situ Monitoring and Improved Electrochemical Modeling of Potential and Quinhydrone Formation. *Phys. Chem. Chem. Phys.* 2017, 19 (47), 31684–31691. <https://doi.org/10.1039/C7CP05881K>.
- (31) Kotz, F.; Arnold, K.; Bauer, W.; Schild, D.; Keller, N.; Sachsenheimer, K.; Nargang, T. M.; Richter, C.; Helmer, D.; Rapp, B. E. Three-Dimensional Printing of Transparent Fused Silica Glass. *Nature* 2017, 544 (7650), 337–339. <https://doi.org/10.1038/nature22061>.

- (32) Altieri, A. S.; Hinton, D. P.; Byrd, R. A. Association of Biomolecular Systems via Pulsed Field Gradient NMR Self-Diffusion Measurements. *J. Am. Chem. Soc.* 1995, 117 (28), 7566–7567. <https://doi.org/10.1021/ja00133a039>.

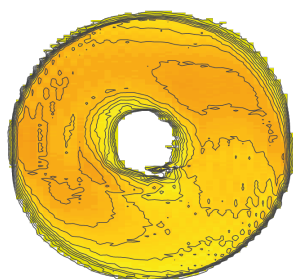
### TABLE OF CONTENT



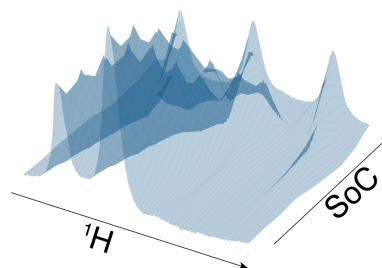
#### Electrochemistry



#### MRI



#### Operando NMR



# Supporting Information

## Table of Contents

<b>Figure S1:</b> 3D rendering of the mini-battery. Full-size reproduction of Fig. 1c	20
<b>Figure S2:</b> $^1\text{H}$ image of the cell without the aluminum shields	21
<b>Figure S3:</b> Drawing of the lower part of the mini redox-flow battery	22
<b>Figure S4:</b> Drawing of the middle part of the mini redox-flow battery	23
<b>Figure S5:</b> Drawing of the top part of the mini redox-flow battery	24
<b>Figure S6:</b> Drawing of the counter-electrode reservoir	25
<b>Figure S7:</b> Comparison between classical $^1\text{H}$ - $^{13}\text{C}$ HSQC and spatially-localized $^1\text{H}$ - $^{13}\text{C}$ HSQC performed on 2,7-AQDS	26
<b>Figure S8:</b> NMR velocimetry experiment performed with insufficient solution level in the cell	27
<b>Figure S9:</b> Cyclic Voltammetry recorded on the cell filled with oxidized 2,7-AQDS 50 mM in $\text{H}_2\text{SO}_4$ 0.5 M	28
<b>Figure S10:</b> Influence of the magneto-hydrodynamic effect on the cyclic voltammetry	29
<b>Figure S11:</b> Chronoamperometry performed on the cell filled with oxidized 2,7-AQDS 50 mM in $\text{H}_2\text{SO}_4$ 0.5 M	30
<b>Figure S12:</b> Chronoamperometry performed on the cell filled with reduced 2,7- $\text{H}_2\text{AQDS}$ 50 mM in $\text{H}_2\text{SO}_4$ 0.5 M	30
<b>Figure S13:</b> DOSY experiments performed on a) the oxidized state of AQDS, b) the intermediate state where 6 $^1\text{H}$ signals appear	31

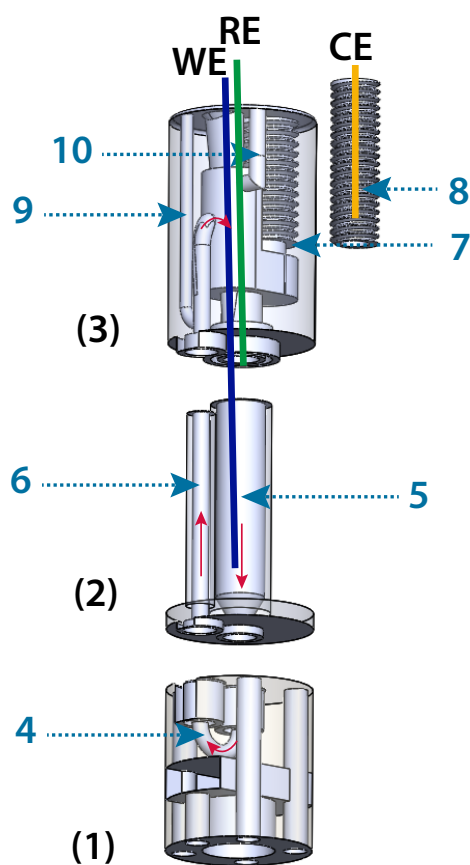


**Figure S1.** Full-size reproduction of Fig. 1c. 3D rendering of the bottom (1), middle (2) and top (3) parts of the device. (4) Solution circuit loop, (5) NMR area, (6) back channel, rf-isolated with aluminum foil, (7) proton-exchange membrane, (8) counter-electrode compartment, (9) nitrogen inlet, (10) nitrogen exhaust, WE: working electrode (glassy carbon), RE: reference electrode (Ag/AgCl), CE: counter-electrode (Pt). For the sake of clarity, neither the rf coils nor the copper connectors at the bottom of the part (1) for the electric connection to the NMR probehead are drawn.

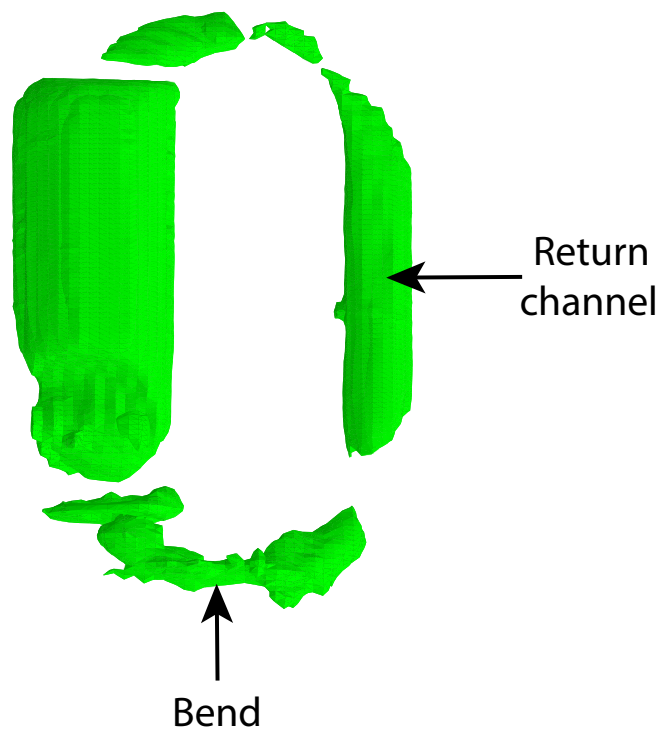


**Figure S2.**  $^1\text{H}$  image of the cell without the aluminum shields. The water in the return channel and in the bend of the lower part is clearly visible. This leads to magnetic field heterogeneity (numerous air-liquid interfaces), which prevents a good spectral resolution.

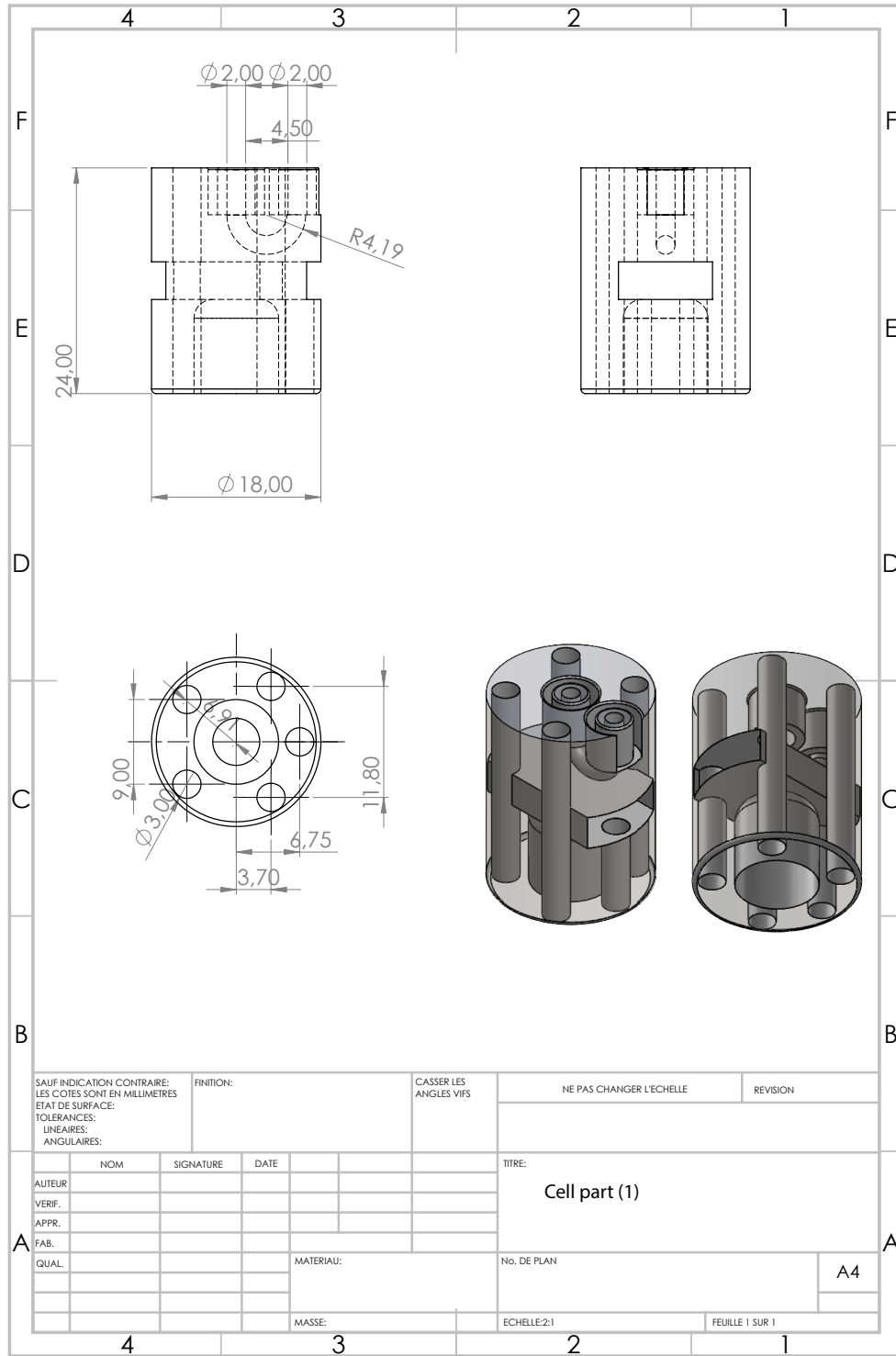


**Figure S3.** Drawing of the lower part of the mini redox-flow battery, to be plugged on a Bruker Micro-5 probe basis. The dimensions are in millimeters.

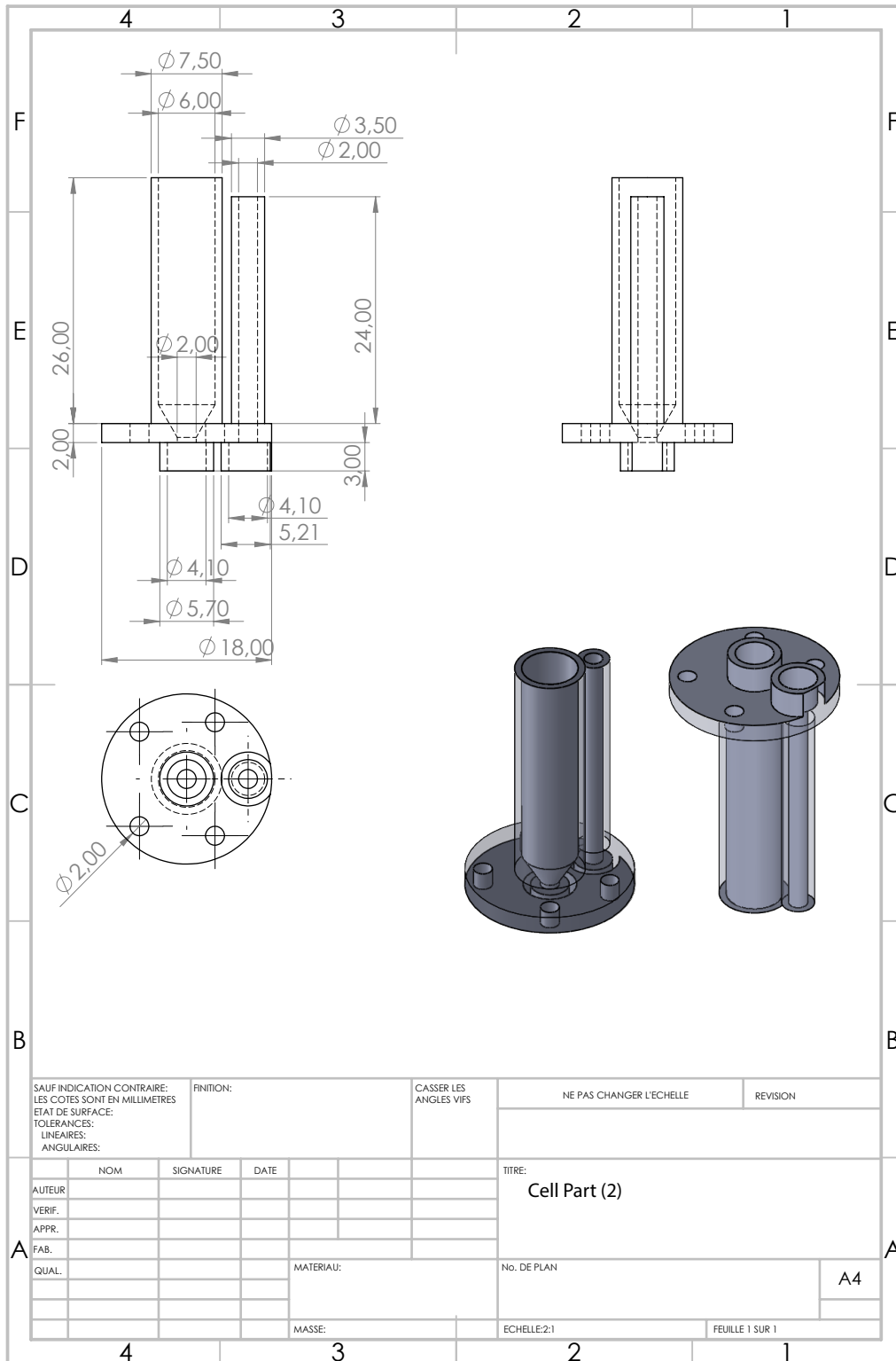


**Figure S4.** Drawing of the middle part of the mini redox-flow battery. The dimensions are in millimeters.



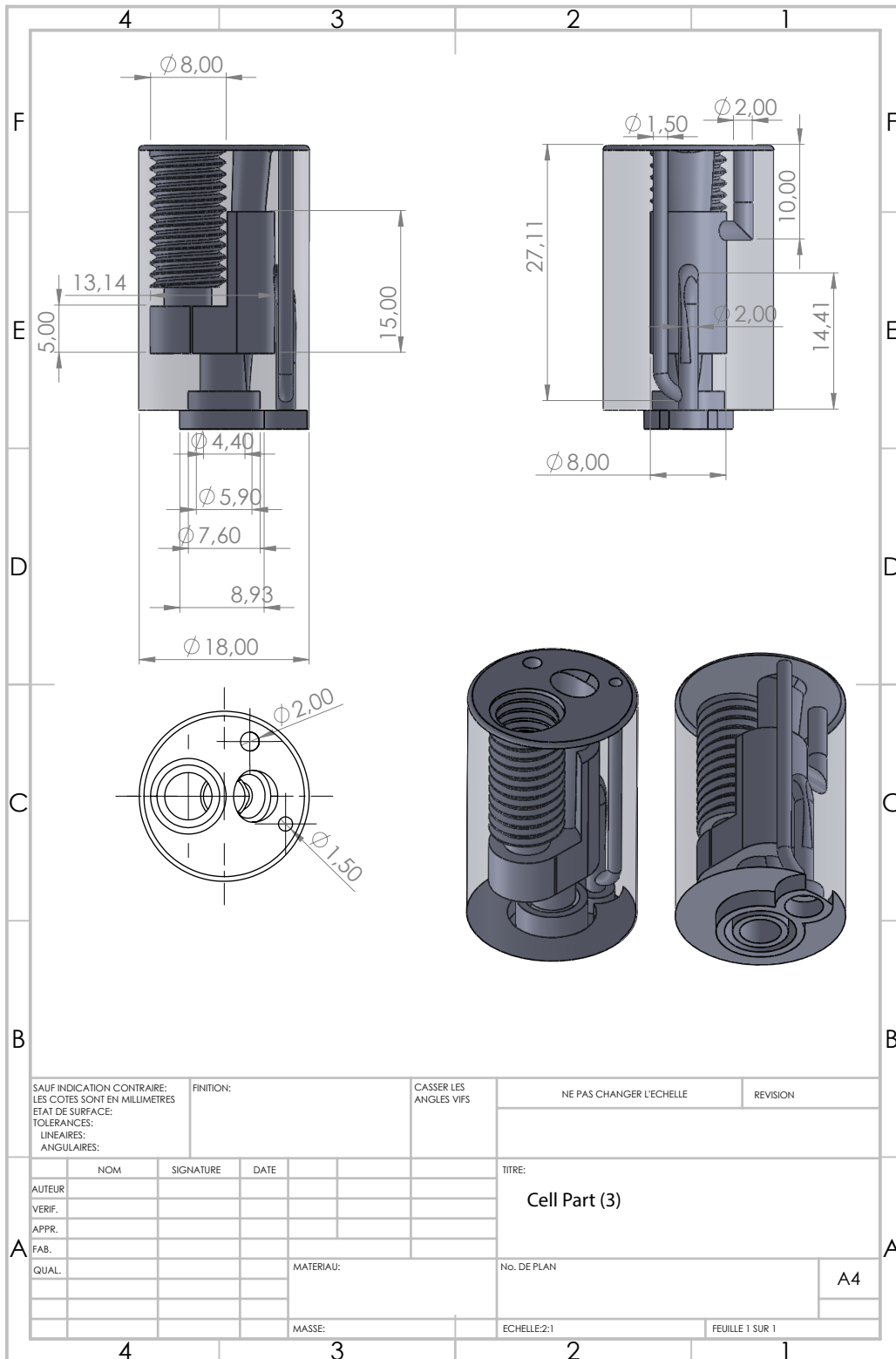


**Figure S5.** Drawing of the top part of the mini redox-flow battery. The dimensions are in millimeters.

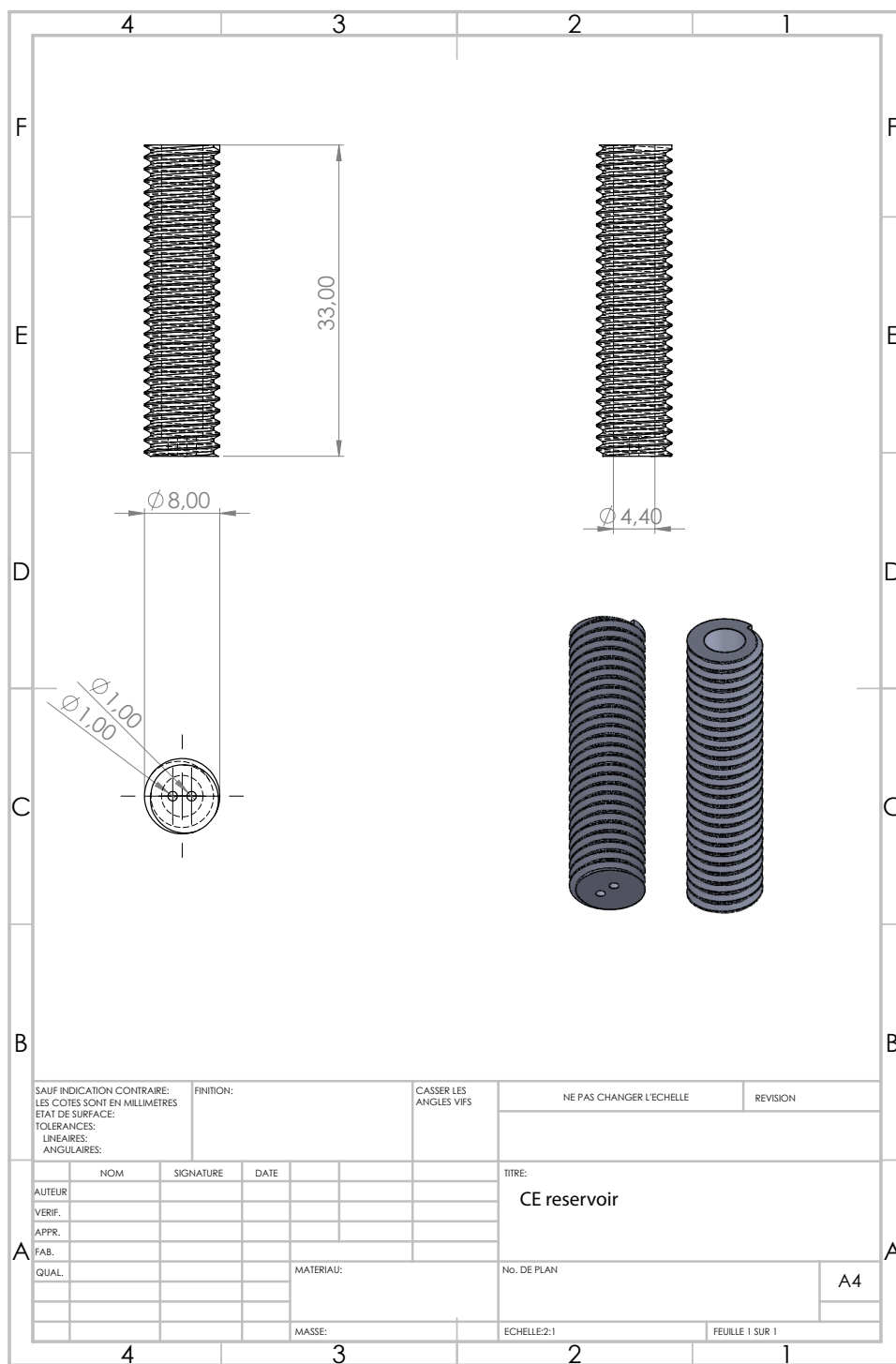


**Figure S6.** Drawing of the counter-electrode reservoir, to be inserted to the top part of the mini redox-flow battery. The Nafion membrane is stuck between these two pieces. The dimensions are in millimeters.

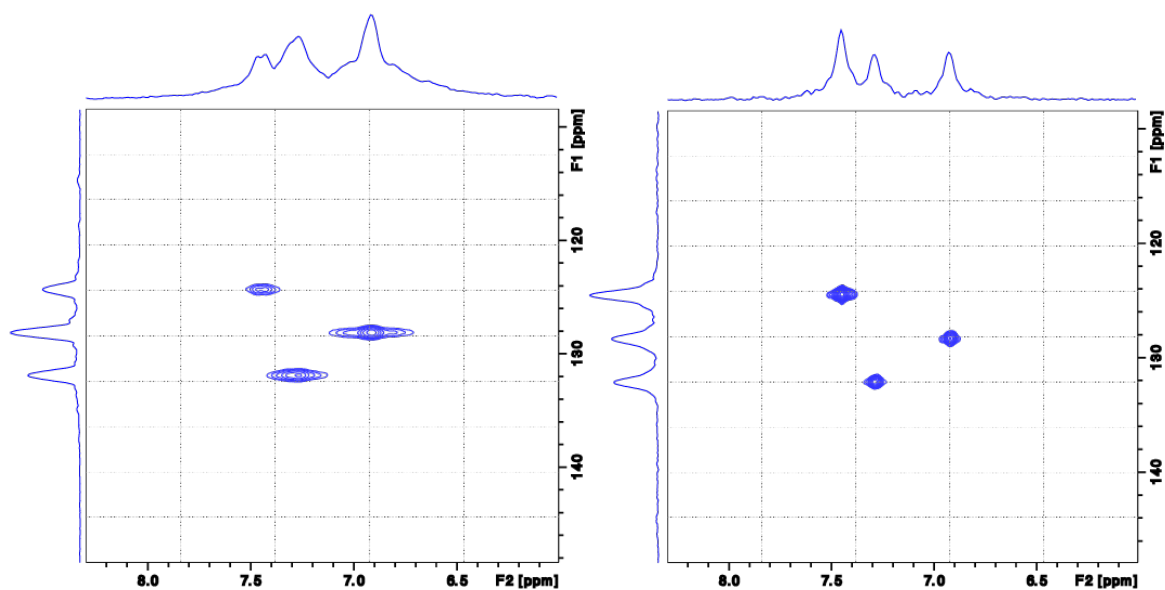


**Figure S7.** Comparison between classical  $^1\text{H}$ - $^{13}\text{C}$  HSQC (left) and spatially-localized  $^1\text{H}$ - $^{13}\text{C}$  HSQC (right) performed on 2,7-AQDS. 0.5 M. Both experiments have been performed with the same experimental conditions (10 ppm, 1024 complex points in the  $^1\text{H}$  dimension; 40 ppm, 128 points in the  $^{13}\text{C}$  dimension; 32 scans, for 1h17 experiment time). Also the processing is the same: apodization by a sine bell shifted by  $\pi/2.5$  in both dimensions and zero-filling to 512 points in the  $^{13}\text{C}$  dimension.

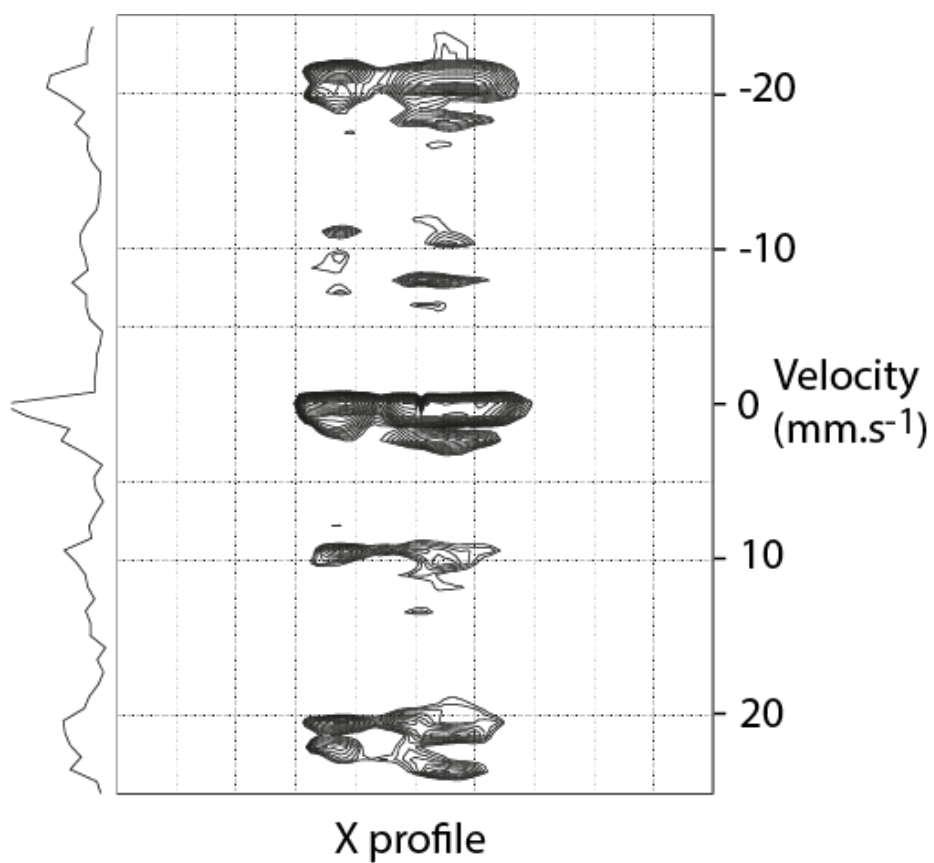


**Figure S8.** NMR velocimetry experiment performed with insufficient solution level inside the upper part of the insert. Signals on both sides of the zero frequency in the indirect dimension indicate that the solution oscillates but does not experience a net displacement.

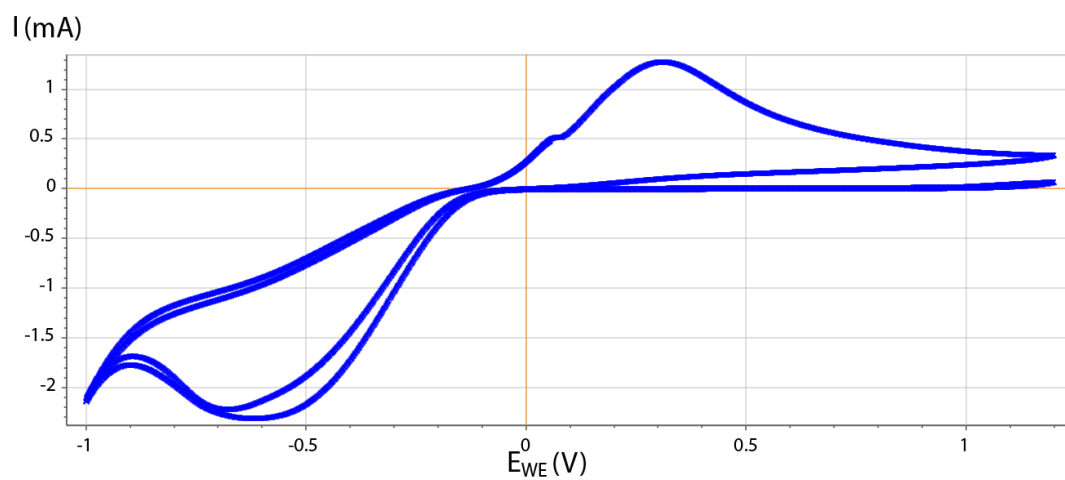
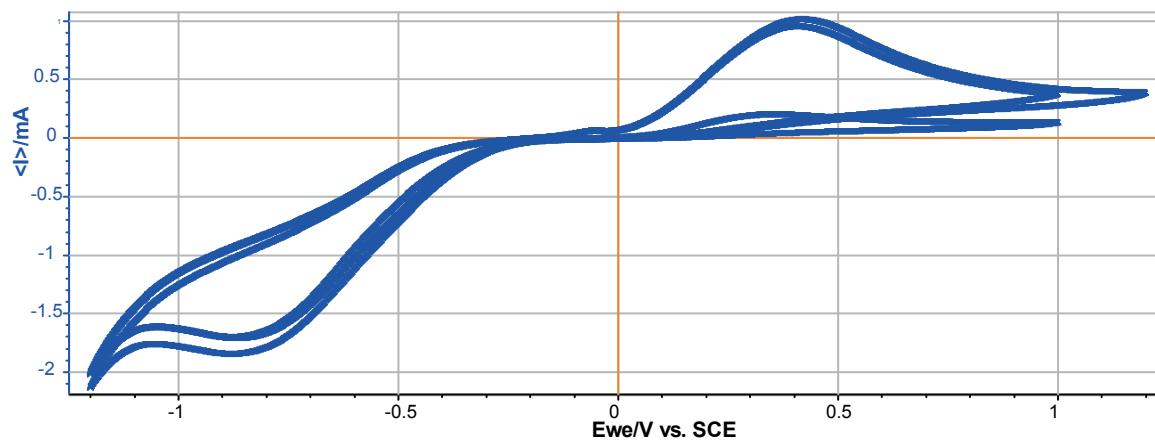


**Figure S9.** Cyclic Voltammetry recorded on the cell filled with oxidized 2,7-AQDS 50 mM in H<sub>2</sub>SO<sub>4</sub> 0.2 M (without solution flow). Scan rate 50 mV/s from +1.2 V to -1 V with 2 loops.

a)



b)

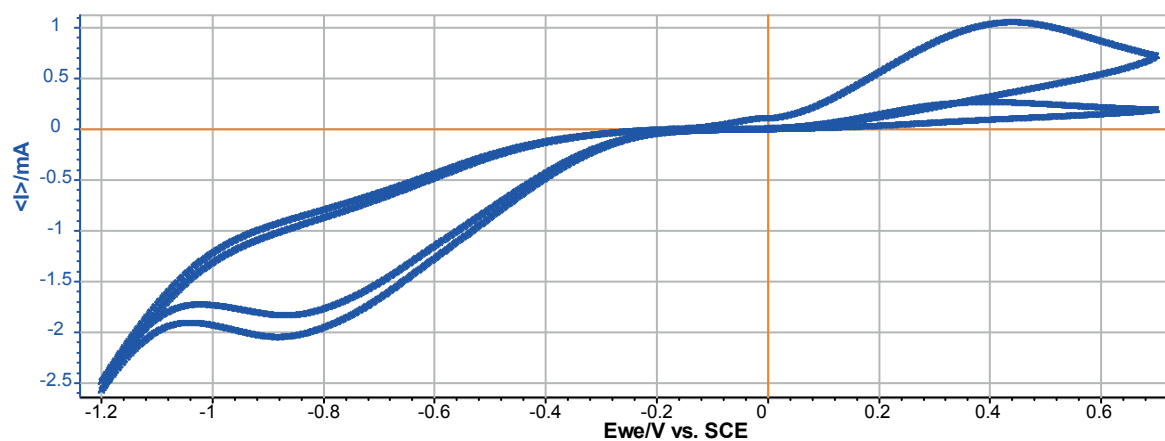


**Figure S10.** Influence of the magneto-hydrodynamic effect on the cyclic voltammetry. a) cell in a magnetic field lower than 5 gauss; b) cell placed inside the 11.7 T magnet. 2,7-AQDS 50 mM in  $\text{H}_2\text{SO}_4$  0.2 M without solution flow, scan rate 50 mV/s.

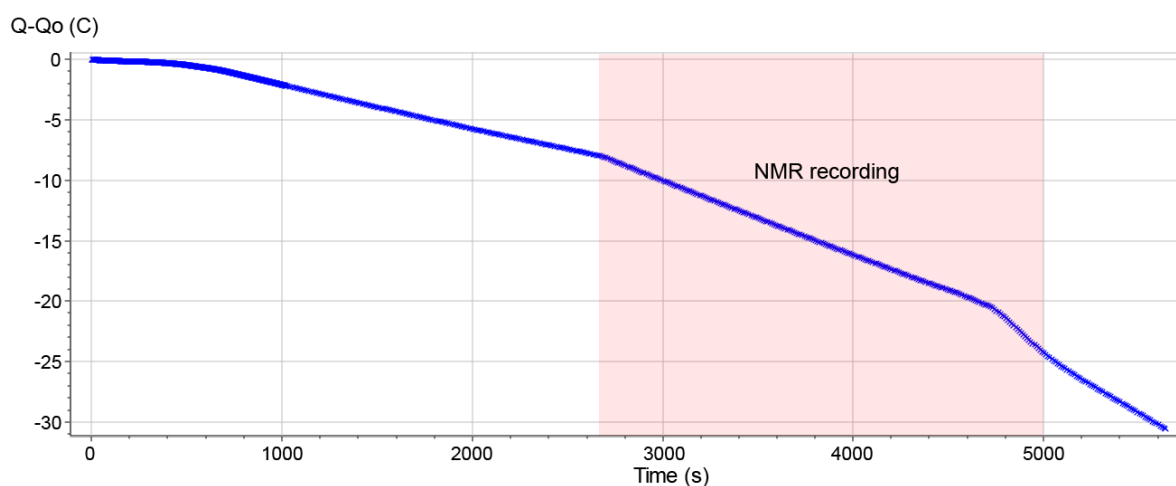


**Figure S11.** Chronoamperometry performed on the cell filled with oxidized 2,7-AQDS 50 mM in  $\text{H}_2\text{SO}_4$  0.5 M (with solution flow). The time period in which the  $^1\text{H}$  spectra have been recorded is represented by a pink area. The respective voltages applied are -0.3 V until the NMR starts (without effect on the anthraquinone; the first  $^1\text{H}$  NMR spectra still show the oxidized form) and -0.5 V after.

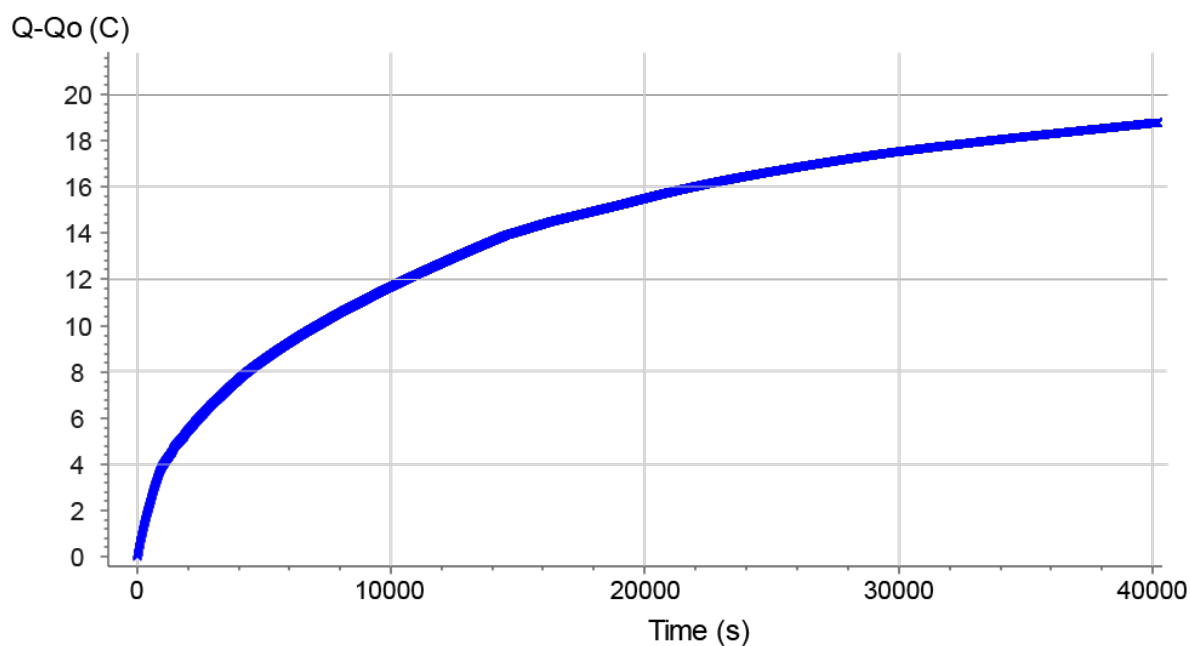


**Figure S12.** Chronoamperometry performed on the cell filled with reduced 2,7-AQDS 50 mM in  $\text{H}_2\text{SO}_4$  0.5 M (with solution flow). A voltage of +0.45 V is applied.

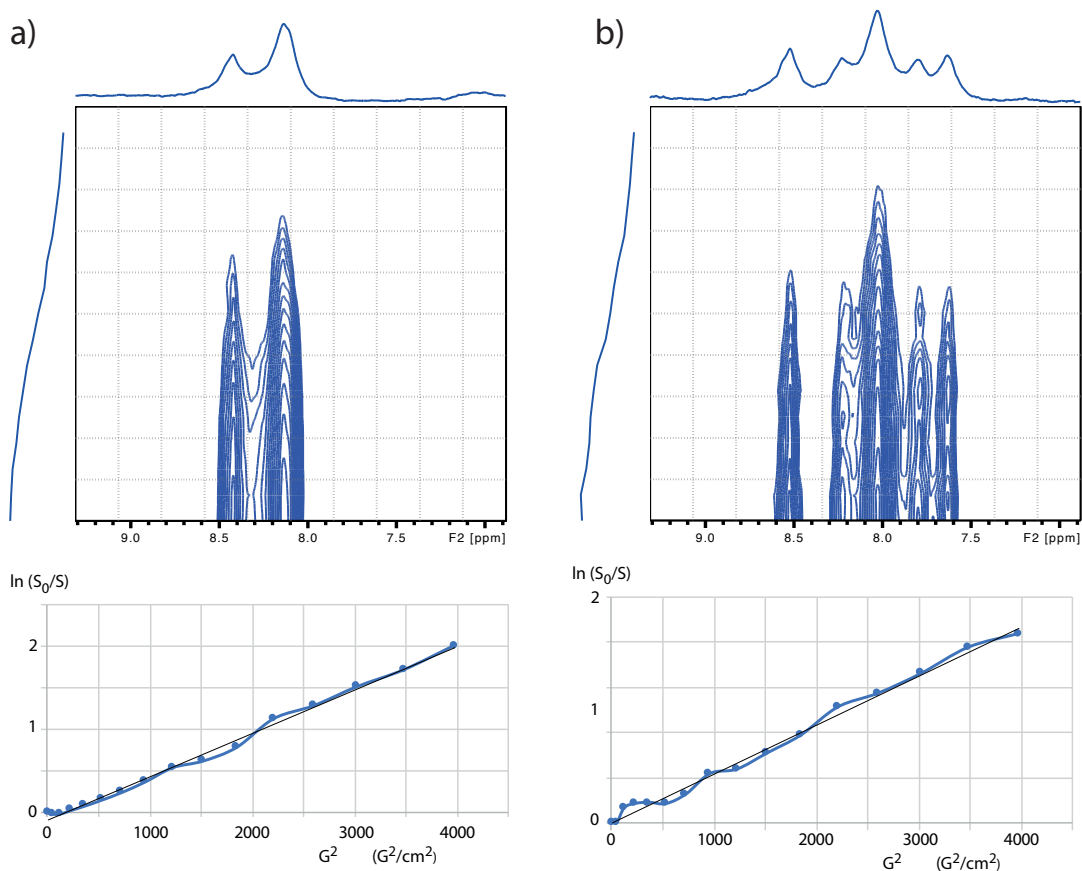


**Figure S13.** 2D DOSY experiments performed on a) the oxidized state of AQDS, b) the intermediate state where six  $^1\text{H}$  signals appear. At the bottom the curves  $\ln(S_0/S) = f(G^2)$  that have enabled extraction of the diffusion coefficients ( $S_0$  is the signal recorded with the lowest gradient value of 2.8 G/cm) are displayed. Note that the sum of all the aromatic proton signals has been used.





# **Part VI**

## **Conclusions and Outlooks**

## 13 - Concluding Remarks

### 13.1 Key Findings

Aiming at testing the capabilities of NMR/MRI for the operando monitoring of a redox-flow battery, two main electrochemical setups have been utilized and studied with a model chemical system throughout the project. Firstly, a 3D-printed organic redox flow battery was studied in a SuperWide Bore magnet, secondly an also 3D-printed miniaturized redox-flow battery entirely inserted in a narrow-bore magnet could be analyzed in operation.

Dealing with the first issue, a thorough understanding of the concerns associated with the coupling of electrochemical and NMR techniques has been achieved, including magnetic susceptibility effects or field perturbations through the cell, voxel position and size definition, and magneto-hydrodynamic effect among others. The chemical model and the electrochemical setup have been optimized according to the magnetic field constraints. This comprises a correct choice of the conversion cell components (electrodes and current collectors) that minimizes  $B_1$  shielding and allows current to flow inside the magnet, a careful setup of the mini-battery orientation that maximizes radio-frequency penetration, or a well-buffered media that limits the formation of paramagnetic free radical intermediates. Having all included, an in situ analysis of a complete bubble pump-based RFB has been accomplished by means of localized spectroscopy measurements in the organic-based negolyte tank (9,10-Anthraquinone-2,7-disulfonic acid disodium salt) through consecutive redox cycles.

In regard to the study conducted in the narrow-bore magnet, a high-sensitivity device based on a micro-imaging probe has been developed. It enables real-time monitoring of liquid electrolytes via  $^1\text{H}$  and  $^{13}\text{C}$  NMR, by studying the displacement mechanisms (self-diffusion and velocimetry measurements) and structure of molecular species (high-resolution homonuclear and heteronuclear spatially localized 1D and 2D spectra) generated during redox cycles of an organic RFB. The small required volumes, on the order of few mL, allow the study of expensive compounds with a low-cost, custom-made, disposable tool. The emergence of heterodimers in the selected system (2,7-AQDS 50 mM in  $\text{H}_2\text{SO}_4$  0.5 M) has been predicted by diffusion coefficient measurements and subsequently confirmed by first principals calculations (DFT and ab initio).

## 13.2 Perspectives and Future Developments

The 3D-printed double sense cell coupled with the double tank can be optimized to constitute the first high-resolution operando NMR setup for the study of complete redox flow batteries. This ambitious goal can be accomplished by carrying out straightforward modifications, such as choosing a simpler chemical system and triggering the bubble pump operation. Other potential improvements include the placement of a surface coil over the object of study (*i.e.* conversion cell or double tank) in order to minimize  $B_1$  inhomogeneities, as well as the incorporation of carbon fibers as current collectors when strictly necessary (*e.g.* optimal electric contact) as they have 0% ferromagnetic content.

On the other hand, the miniaturization of the device based on a microimaging probe makes it possible to be very economical with the amount of electrolyte. Now it is not unthinkable to install a second low cost flow circuit for the polysolite, thanks to 3D printing techniques in perpetual improvement, or even use it for operando analysis of other electrochemical processes such as fuel cells via liquid-state NMR. Its versatility renders also easy the observation of other nuclei of great interest (Li, Na) by tailoring the tuning capacitors connected to the saddle coils. The incorporation of temperature microsensors is under study in order to improve electrochemical performances, given that the optimal operating temperature of most electrochemical systems differs from the ambient temperature.

The current limitations in the choice of the chemical system and experimental conditions are linked to the resistance of the 3D-printed insert material to harsh environments. The PMMA polymer used for the construction of our devices, for example, is not resistant to basic media, which limits the redox couples that can be studied. The laboratory staff are keeping the research alive to produce pieces in ceramics or even glass by additive manufacturing. To this end, we are using recent works which start from polymer resins charged with  $Al_2O_3$ ,  $ZrO_2$  or  $SiO_2$  particles.[211, 212] Then, in a first chemical or thermal debinding step (or both), all the organic matter is removed, giving rise to a very fragile porous piece. A last step is a high-temperature sintering, under inert atmosphere or under vacuum to recover a very compact piece after a matter shrink as homothetic as possible. Obviously the difficulty here is to reproduce all the details of the initially designed object after all these steps, but it is worth the effort.

Finally, one analytical tool was very much missing in our studies. EPR, allowing to observe radical species directly, would have been very complementary to NMR. A large number of projects aim at miniaturizing EPR (see for instance [Development of a miniaturised EPR spectrometer](#)). Here, it would be clever to incorporate into the solution circuitry, a micro-EPR device using the same static magnetic field. Nothing seems impossible; such a device would give magnetic resonance its letters of nobility.



## References

- <sup>1</sup>H. Ritchie, M. Roser, and P. Rosado, "Energy", *Our World in Data* (2020).
- <sup>2</sup>H. Ritchie, M. Roser, and P. Rosado, "CO<sub>2</sub> and Greenhouse Gas Emissions", *Our World in Data* (2020).
- <sup>3</sup>P. Denholm, J. C. King, C. F. Kutcher, and P. P. H. Wilson, "Decarbonizing the electric sector: Combining renewable and nuclear energy using thermal storage", *Energy Policy* **44**, 301–311 (2012).
- <sup>4</sup>Z. Zhang, T. Ding, Q. Zhou, Y. Sun, M. Qu, Z. Zeng, Y. Ju, L. Li, K. Wang, and F. Chi, "A review of technologies and applications on versatile energy storage systems", *Renewable and Sustainable Energy Reviews* **148**, 111263 (2021).
- <sup>5</sup>R. Shan, J. Reagan, S. Castellanos, S. Kurtz, and N. Kittner, "Evaluating emerging long-duration energy storage technologies", *Renewable and Sustainable Energy Reviews* **159**, 112240 (2022).
- <sup>6</sup>M. M. Rahman, A. O. Oni, E. Gemechu, and A. Kumar, "Assessment of energy storage technologies: A review", *Energy Conversion and Management* **223**, 113295 (2020).
- <sup>7</sup>Grid-Scale U.S. Storage Capacity Could Grow Five-Fold by 2050, <https://www.nrel.gov/news/program/2021/grid-scale-storage-us-storage-capacity-could-grow-five-fold-by-2050.html> (visited on 02/13/2023).
- <sup>8</sup>K. T. Møller, T. R. Jensen, E. Akiba, and H.-w. Li, "Hydrogen - A sustainable energy carrier", *Progress in Natural Science: Materials International, SI-HYDROGEN STORAGE MATERIALS* **27**, 34–40 (2017).
- <sup>9</sup>K. Sekai and T. Endo, "Nonaqueous electrolyte secondary battery", European pat. 0511632A1 (Sony Corp, Nov. 4, 1992).
- <sup>10</sup>A. Kebede, T. Kalogiannis, J. Van Mierlo, and M. Berecibar, "A comprehensive review of stationary energy storage devices for large scale renewable energy sources grid integration", *Renewable and Sustainable Energy Reviews* **159**, 10.1016/j.rser.2022.112213 (2022).
- <sup>11</sup>T. Palmer, A. Beamer, T. Pitt, I. Popov, C. Cammack, H. Pratt III, T. Anderson, E. Batista, P. Yang, and B. Davis, "A Comparative Review of Metal-Based Charge Carriers in Nonaqueous Flow Batteries", *ChemSusChem* **14**, 1214–1228 (2021).
- <sup>12</sup>P. Poizot, J. Gaubicher, S. Renault, L. Dubois, Y. Liang, and Y. Yao, "Opportunities and Challenges for Organic Electrodes in Electrochemical Energy Storage", *Chemical Reviews* **120**, 6490–6557 (2020).
- <sup>13</sup>L. H. Thaller, "Electrically rechargeable redox flow cells", in (Jan. 1, 1974).
- <sup>14</sup>M. Dieterle, P. Fischer, M.-N. Pons, N. Blume, C. Minke, and A. Bischi, "Life cycle assessment (LCA) for flow batteries: A review of methodological decisions", *Sustainable Energy Technologies and Assessments* **53**, 102457 (2022).
- <sup>15</sup>J. Winsberg, T. Hagemann, T. Janoschka, M. Hager, and U. Schubert, "Redox-Flow Batteries: From Metals to Organic Redox-Active Materials", *Angewandte Chemie - International Edition* **56**, 686–711 (2017).

- <sup>16</sup>A. D. Bain, "Coherence levels and coherence pathways in NMR. A simple way to design phase cycling procedures", *Journal of Magnetic Resonance* (1969) **56**, 418–427 (1984).
- <sup>17</sup>E. L. Hahn, "Spin Echoes", *Physical Review* **80**, 580–594 (1950).
- <sup>18</sup>K. G. R. Pachler and P. L. Wessels, "Selective Population Inversion (SPI). A pulsed double resonance method in FT NMR spectroscopy equivalent to INDOR", *Journal of Magnetic Resonance* (1969) **12**, 337–339 (1973).
- <sup>19</sup>A. A. Maudsley and R. R. Ernst, "Indirect detection of magnetic resonance by heteronuclear two-dimensional spectroscopy", *Chemical Physics Letters* **50**, 368–372 (1977).
- <sup>20</sup>D. M. Doddrell, D. T. Pegg, and M. R. Bendall, "Distortionless enhancement of NMR signals by polarization transfer", *Journal of Magnetic Resonance* (1969) **48**, 323–327 (1982).
- <sup>21</sup>R. Freeman and G. A. Morris, "Experimental chemical shift correlation maps in nuclear magnetic resonance spectroscopy", *Journal of the Chemical Society, Chemical Communications* **0**, 684–686 (1978).
- <sup>22</sup>H. Kessler, C. Griesinger, J. Zarbock, and H. R. Loosli, "Assignment of carbonyl carbons and sequence analysis in peptides by heteronuclear shift correlation via small coupling constants with broadband decoupling in t1 (COLOC)", *Journal of Magnetic Resonance* (1969) **57**, 331–336 (1984).
- <sup>23</sup>L. Mueller, "Sensitivity enhanced detection of weak nuclei using heteronuclear multiple quantum coherence", *Journal of the American Chemical Society* **101**, 4481–4484 (1979).
- <sup>24</sup>A. Bax and M. F. Summers, "Proton and carbon-13 assignments from sensitivity-enhanced detection of heteronuclear multiple-bond connectivity by 2D multiple quantum NMR", *Journal of the American Chemical Society* **108**, 2093–2094 (1986).
- <sup>25</sup>G. Bodenhausen and D. J. Ruben, "Natural abundance nitrogen-15 NMR by enhanced heteronuclear spectroscopy", *Chemical Physics Letters* **69**, 185–189 (1980).
- <sup>26</sup>W. P. Aue, E. Bartholdi, and R. R. Ernst, "Two-dimensional spectroscopy. Application to nuclear magnetic resonance", *The Journal of Chemical Physics* **64**, 2229–2246 (1976).
- <sup>27</sup>S. Vega, T. W. Shattuck, and A. Pines, "Fourier-Transform Double-Quantum NMR in Solids", *Physical Review Letters* **37**, 43–46 (1976).
- <sup>28</sup>W. P. Aue, J. Karhan, and R. R. Ernst, "Homomuclear broad band decoupling and two-dimensional J-resolved NMR spectroscopy", *The Journal of Chemical Physics* **64**, 4226–4227 (1976).
- <sup>29</sup>L. Braunschweiler and R. R. Ernst, "Coherence transfer by isotropic mixing: Application to proton correlation spectroscopy", *Journal of Magnetic Resonance* (1969) **53**, 521–528 (1983).
- <sup>30</sup>S. Macura and R. Ernst, "Elucidation of cross relaxation in liquids by two-dimensional N.M.R. spectroscopy", *Molecular Physics* **41**, 95–117 (1980).
- <sup>31</sup>A. A. Bothner-By, R. L. Stephens, J. Lee, C. D. Warren, and R. W. Jeanloz, "Structure determination of a tetrasaccharide: transient nuclear Overhauser effects in the rotating frame", *Journal of the American Chemical Society* **106**, 811–813 (1984).

- <sup>32</sup>J. Jeener, B. H. Meier, P. Bachmann, and R. R. Ernst, "Investigation of exchange processes by two-dimensional NMR spectroscopy", *The Journal of Chemical Physics* **71**, 4546–4553 (1979).
- <sup>33</sup>H. J. V. Tyrrell and K. R. Harris, "Chapter 6 - Theoretical interpretations of diffusion coefficients", in *Diffusion in Liquids*, edited by H. J. V. Tyrrell and K. R. Harris (Butterworth-Heinemann, Jan. 1, 1984), pp. 258–310.
- <sup>34</sup>E. O. Stejskal and J. E. Tanner, "Spin Diffusion Measurements: Spin Echoes in the Presence of a Time-Dependent Field Gradient", *The Journal of Chemical Physics* **42**, 288–292 (1965).
- <sup>35</sup>J. E. Tanner, "Use of the Stimulated Echo in NMR Diffusion Studies", *The Journal of Chemical Physics* **52**, 2523–2526 (1970).
- <sup>36</sup>Y. Qiao, P. Galvosas, and P. T. Callaghan, "Diffusion correlation NMR spectroscopic study of anisotropic diffusion of water in plant tissues", *Biophysical Journal* **89**, 2899–2905 (2005).
- <sup>37</sup>K. F. Morris and C. S. J. Johnson, "Diffusion-ordered two-dimensional nuclear magnetic resonance spectroscopy", *Journal of the American Chemical Society* **114**, 3139–3141 (1992).
- <sup>38</sup>M. L. Wood, M. Silver, and V. M. Runge, "Optimization of spoiler gradients in flash MRI", *Magnetic Resonance Imaging* **5**, 455–463 (1987).
- <sup>39</sup>R. M. Cotts, M. J. R. Hoch, T. Sun, and J. T. Markert, "Pulsed field gradient stimulated echo methods for improved NMR diffusion measurements in heterogeneous systems", *Journal of Magnetic Resonance* (1969) **83**, 252–266 (1989).
- <sup>40</sup>A. Jerschow and N. Müller, "3D Diffusion-Ordered TOCSY for Slowly Diffusing Molecules", *Journal of Magnetic Resonance, Series A* **123**, 222–225 (1996).
- <sup>41</sup>P. C. Lauterbur, "Image Formation by Induced Local Interactions: Examples Employing Nuclear Magnetic Resonance", *Nature* **242**, 190–191 (1973).
- <sup>42</sup>A. Haase, J. Frahm, D. Matthaei, W. Hanicke, and K. -. Merboldt, "FLASH imaging. Rapid NMR imaging using low flip-angle pulses", *Journal of Magnetic Resonance* (1969) **67**, 258–266 (1986).
- <sup>43</sup>W. A. Edelstein, J. M. S. Hutchison, G. Johnson, and T. Redpath, "Spin warp NMR imaging and applications to human whole-body imaging", *Physics in Medicine & Biology* **25**, 751 (1980).
- <sup>44</sup>J. Hennig, A. Nauerth, and H. Friedburg, "RARE imaging: a fast imaging method for clinical MR", *Magnetic Resonance in Medicine* **3**, 823–833 (1986).
- <sup>45</sup>L. Reese, T. Carr, and R. L. Nicholson, "MRI experience with multiple sclerosis - Comparison to CT and clinical status", *J. Nucl. Med.; (United States)* **26:5** (1985).
- <sup>46</sup>M. D. Robson, P. D. Gatehouse, M. Bydder, and G. M. Bydder, "Magnetic Resonance: An Introduction to Ultrashort TE (UTE) Imaging", *Journal of Computer Assisted Tomography* **27**, 825 (2003).
- <sup>47</sup>M. Weiger and K. P. Pruessmann, "MRI with Zero Echo Time", in *eMagRes* (John Wiley & Sons, Ltd, 2012).



- <sup>48</sup>M. Weiger and K. P. Pruessmann, "MRI with Zero Echo Time", en, in [Encyclopedia of Magnetic Resonance](#), edited by R. K. Harris (John Wiley & Sons, Ltd, Chichester, UK, June 2012), emrstm1292.
- <sup>49</sup>S. Meiboom and D. Gill, "Modified Spin-Echo Method for Measuring Nuclear Relaxation Times", [Review of Scientific Instruments](#) **29**, 688–691 (1958).
- <sup>50</sup>R. J. Ordidge, A. Connelly, and J. A. B. Lohman, "Image-selected in Vivo spectroscopy (ISIS). A new technique for spatially selective nmr spectroscopy", [Journal of Magnetic Resonance](#) (1969) **66**, 283–294 (1986).
- <sup>51</sup>A. Connelly, C. Counsell, J. A. B. Lohman, and R. J. Ordidge, "Outer volume suppressed image related in vivo spectroscopy (OSIRIS), a high-sensitivity localization technique", [Journal of Magnetic Resonance](#) (1969) **78**, 519–525 (1988).
- <sup>52</sup>P. A. Bottomley, "Selective volume method for performing localized NMR spectroscopy", U.S. pat. 4480228A (General Electric Co, Oct. 30, 1984).
- <sup>53</sup>J. Star-Lack, S. J. Nelson, J. Kurhanewicz, L. R. Huang, and D. B. Vigneron, "Improved water and lipid suppression for 3D PRESS CSI using RF band selective inversion with gradient dephasing (BASING)", [Magnetic Resonance in Medicine](#) **38**, 311–321 (1997).
- <sup>54</sup>J. Frahm, K.-D. Merboldt, and W. Hänicke, "Localized proton spectroscopy using stimulated echoes", [Journal of Magnetic Resonance](#) (1969) **72**, 502–508 (1987).
- <sup>55</sup>C. T. Moonen, M. von Kienlin, P. C. van Zijl, J. Cohen, J. Gillen, P. Daly, and G. Wolf, "Comparison of single-shot localization methods (STEAM and PRESS) for in vivo proton NMR spectroscopy", [NMR in biomedicine](#) **2**, 201–208 (1989).
- <sup>56</sup>J. Frahm, T. Michaelis, K. D. Merboldt, H. Bruhn, M. L. Gyngell, and W. Hänicke, "Improvements in localized proton NMR spectroscopy of human brain. Water suppression, short echo times, and 1 ml resolution", [Journal of Magnetic Resonance](#) (1969) **90**, 464–473 (1990).
- <sup>57</sup>R. B. Thompson and P. S. Allen, "Response of metabolites with coupled spins to the STEAM sequence", [Magnetic Resonance in Medicine](#) **45**, 955–965 (2001).
- <sup>58</sup>T. R. Brown, B. M. Kincaid, and K. Ugurbil, "NMR chemical shift imaging in three dimensions", [Proceedings of the National Academy of Sciences of the United States of America](#) **79**, 3523–3526 (1982).
- <sup>59</sup>L. Brateman, "Chemical shift imaging: a review", [American Journal of Roentgenology](#) **146**, 971–980 (1986).
- <sup>60</sup>H. Zhu and P. B. Barker, "MR Spectroscopy and Spectroscopic Imaging of the Brain", [Methods in molecular biology](#) (Clifton, N.J.) **711**, 203–226 (2011).
- <sup>61</sup>A. Groß, "Structure of Electrode-Electrolyte Interfaces, Modeling of Double Layer and Electrode Potential", in [Handbook of Materials Modeling: Applications: Current and Emerging Materials](#), edited by W. Andreoni and S. Yip (Springer International Publishing, Cham, 2020), pp. 1439–1472.
- <sup>62</sup>A. J. Bard, L. R. Faulkner, and H. S. White, [Electrochemical Methods: Fundamentals and Applications](#) (John Wiley & Sons, May 31, 2022), 1112 pp.

- <sup>63</sup>R. Rousseau, M.-L. Délia, and A. Bergel, "A theoretical model of transient cyclic voltammetry for electroactive biofilms", *Energy Environ. Sci.* **7**, 1079 (2014).
- <sup>64</sup>X. Yang and A. L. Rogach, "Electrochemical Techniques in Battery Research: A Tutorial for Nonelectrochemists", *Adv. Energy Mater.* **9**, 1900747 (2019).
- <sup>65</sup>H. Matsuda and Y. Ayabe, "Zur Theorie der Randles-Sevcik'schen Kathodenstrahl-Polarographie", *Zeitschrift für Elektrochemie, Berichte der Bunsengesellschaft für physikalische Chemie* **59**, 494–503 (1955).
- <sup>66</sup>E. M. Espinoza, J. A. Clark, J. Soliman, J. B. Derr, M. Morales, and V. I. Vullev, "Practical Aspects of Cyclic Voltammetry: How to Estimate Reduction Potentials When Irreversibility Prevails", *J. Electrochem. Soc.* **166**, H3175–H3187 (2019).
- <sup>67</sup>J. Luo, B. Hu, M. Hu, Y. Zhao, and T. L. Liu, "Status and Prospects of Organic Redox Flow Batteries toward Sustainable Energy Storage", *ACS Energy Letters* **4**, 2220–2240 (2019).
- <sup>68</sup>L. Tang, P. Leung, Q. Xu, M. R. Mohamed, S. Dai, X. Zhu, C. Flox, and A. A. Shah, "Future perspective on redox flow batteries: aqueous versus nonaqueous electrolytes", *Current Opinion in Chemical Engineering* **37**, 100833 (2022).
- <sup>69</sup>S. Ha and K. G. Gallagher, "Estimating the system price of redox flow batteries for grid storage", *Journal of Power Sources* **296**, 122–132 (2015).
- <sup>70</sup>H. Prifti, A. Parasuraman, S. Winardi, T. Lim, and M. Skyllas-Kazacos, "Membranes for redox flow battery applications", *Membranes* **2**, 275–306 (2012).
- <sup>71</sup>P. Xiong, L. Zhang, Y. Chen, S. Peng, and G. Yu, "A Chemistry and Microstructure Perspective on Ion-Conducting Membranes for Redox Flow Batteries", *Angewandte Chemie International Edition* **60**, 24770–24798 (2021).
- <sup>72</sup>B. Jiang, L. Wu, L. Yu, X. Qiu, and J. Xi, "A comparative study of Nafion series membranes for vanadium redox flow batteries", *Journal of Membrane Science* **510**, 18–26 (2016).
- <sup>73</sup>Z. Yuan, Y. Duan, H. Zhang, X. Li, H. Zhang, and I. Vankelecom, "Advanced porous membranes with ultra-high selectivity and stability for vanadium flow batteries", *Energy & Environmental Science* **9**, 441–447 (2016).
- <sup>74</sup>P. Xing, G. Robertson, M. Guiver, S. Mikhailenko, K. Wang, and S. Kaliaguine, "Synthesis and characterization of sulfonated poly(ether ether ketone) for proton exchange membranes", *Journal of Membrane Science* **229**, 95–106 (2004).
- <sup>75</sup>C. Fujimoto, S. Kim, R. Stains, X. Wei, L. Li, and Z. Yang, "Vanadium redox flow battery efficiency and durability studies of sulfonated Diels Alder poly(phenylene)s", *Electrochemistry Communications* **20**, 48–51 (2012).
- <sup>76</sup>I. S. Chae, T. Luo, G. H. Moon, W. Ogieglo, Y. S. Kang, and M. Wessling, "Ultra-High Proton/Vanadium Selectivity for Hydrophobic Polymer Membranes with Intrinsic Nanopores for Redox Flow Battery", *Advanced Energy Materials* **6**, 1600517 (2016).
- <sup>77</sup>R. Tan, A. Wang, R. Malpass-Evans, R. Williams, E. W. Zhao, T. Liu, C. Ye, X. Zhou, B. P. Darwich, Z. Fan, L. Turcani, E. Jackson, L. Chen, S. Y. Chong, T. Li, K. E. Jelfs, A. I. Cooper, N. P. Brandon, C. P. Grey, N. B. McKeown, and Q. Song, "Hydrophilic microporous membranes for selective ion separation and flow-battery energy storage", *Nature Materials* **19**, 195–202 (2020).

- <sup>78</sup>C. Li, A. L. Ward, S. E. Doris, T. A. Pascal, D. Prendergast, and B. A. Helms, "Polysulfide-Blocking Microporous Polymer Membrane Tailored for Hybrid Li-Sulfur Flow Batteries", *Nano Letters* **15**, 5724–5729 (2015).
- <sup>79</sup>D. Chen, C. Kang, W. Duan, Z. Yuan, and X. Li, "A non-ionic membrane with high performance for alkaline zinc-iron flow battery", *Journal of Membrane Science* **618**, 118585 (2021).
- <sup>80</sup>P. Navalpotro, J. Palma, M. Anderson, and R. Marcilla, "A Membrane-Free Redox Flow Battery with Two Immiscible Redox Electrolytes", *Angewandte Chemie International Edition* **56**, 12460–12465 (2017).
- <sup>81</sup>M. O. Bamgbopa, Y. Shao-Horn, R. Hashaikeh, and S. Almheiri, "Cyclable membraneless redox flow batteries based on immiscible liquid electrolytes: Demonstration with all-iron redox chemistry", *Electrochimica Acta* **267**, 41–50 (2018).
- <sup>82</sup>P. Navalpotro, C. M. S. S. Neves, J. Palma, M. G. Freire, J. A. P. Coutinho, and R. Marcilla, "Pioneering Use of Ionic Liquid-Based Aqueous Biphasic Systems as Membrane-Free Batteries", *Advanced Science* **5**, 1800576 (2018).
- <sup>83</sup>P. Navalpotro, C. Trujillo, I. Montes, C. M. S. S. Neves, J. Palma, M. G. Freire, J. A. P. Coutinho, and R. Marcilla, "Critical aspects of membrane-free aqueous battery based on two immiscible neutral electrolytes", *Energy Storage Materials* **26**, 400–407 (2020).
- <sup>84</sup>L. Castañeda, F. Walsh, J. Nava, and C. Ponce de León, "Graphite felt as a versatile electrode material: Properties, reaction environment, performance and applications", *Electrochimica Acta* **258**, 1115–1139 (2017).
- <sup>85</sup>L. Eifert, R. Banerjee, Z. Jusys, and R. Zeis, "Characterization of carbon felt electrodes for vanadium redox flow batteries: Impact of treatment methods", *Journal of the Electrochemical Society* **165**, A2577–A2586 (2018).
- <sup>86</sup>Y. Zhang, J. Sun, Y. Hu, S. Li, and Q. Xu, "Bio-cathode materials evaluation in microbial fuel cells: A comparison of graphite felt, carbon paper and stainless steel mesh materials", *International Journal of Hydrogen Energy* **37**, 16935–16942 (2012).
- <sup>87</sup>J.-H. Kim, K. J. Kim, M.-S. Park, N. J. Lee, U. Hwang, H. Kim, and Y.-J. Kim, "Development of metal-based electrodes for non-aqueous redox flow batteries", *Electrochemistry Communications* **13**, 997–1000 (2011).
- <sup>88</sup>P. K. Leung, C. Ponce-de-León, C. T. J. Low, A. A. Shah, and F. C. Walsh, "Characterization of a zinc–cerium flow battery", *Journal of Power Sources* **196**, 5174–5185 (2011).
- <sup>89</sup>M. Rychcik and M. Skyllas-Kazacos, "Evaluation of electrode materials for vanadium redox cell", *Journal of Power Sources* **19**, 45–54 (1987).
- <sup>90</sup>Y. Long, M. Ding, and C. Jia, "Application of Nanomaterials in Aqueous Redox Flow Batteries", *ChemNanoMat* **7**, 699–712 (2021).
- <sup>91</sup>A. Permatasari, J. Shin, W. Lee, J. An, and Y. Kwon, "The effect of plasma treated carbon felt on the performance of aqueous quinone-based redox flow batteries", *International Journal of Energy Research* **45**, 17878–17887 (2021).

- <sup>92</sup>J. Sun, M. Wu, H. Jiang, X. Fan, and T. Zhao, "Advances in the design and fabrication of high-performance flow battery electrodes for renewable energy storage", *Advances in Applied Energy* **2**, 100016 (2021).
- <sup>93</sup>W. Lee, K. S. Yoo, and Y. Kwon, "Alkaline aqueous redox flow batteries using 2,5-dihydroxy-1,4-benzoquinone and ferrocyanide adopting bismuth and carboxylic acid functionalized carbon nanotube catalyst", *International Journal of Energy Research* **n/a**, 10.1002/er.8652.
- <sup>94</sup>R. K. Emmett and M. E. Roberts, "Recent developments in alternative aqueous redox flow batteries for grid-scale energy storage", *Journal of Power Sources* **506**, 230087 (2021).
- <sup>95</sup>Z. Li, T. Jiang, M. Ali, C. Wu, and W. Chen, "Recent Progress in Organic Species for Redox Flow Batteries", *Energy Storage Materials* **50**, 105–138 (2022).
- <sup>96</sup>Y. Ding, C. Zhang, L. Zhang, Y. Zhou, and G. Yu, "Molecular engineering of organic electroactive materials for redox flow batteries", *Chemical Society Reviews* **47**, 69–103 (2018).
- <sup>97</sup>K. Gong, Q. Fang, S. Gu, S. Li, and Y. Yan, "Nonaqueous redox-flow batteries: Organic solvents, supporting electrolytes, and redox pairs", *Energy and Environmental Science* **8**, 3515–3530 (2015).
- <sup>98</sup>M. Rychcik and M. Skyllas-Kazacos, "Characteristics of a new all-vanadium redox flow battery", *Journal of Power Sources* **22**, 59–67 (1988).
- <sup>99</sup>K. W. Knehr and E. C. Kumbur, "Open circuit voltage of vanadium redox flow batteries: Discrepancy between models and experiments", *Electrochemistry Communications* **13**, 342–345 (2011).
- <sup>100</sup>S. Roe, C. Menictas, and M. Skyllas-Kazacos, "A High Energy Density Vanadium Redox Flow Battery with 3 M Vanadium Electrolyte", *Journal of The Electrochemical Society* **163**, A5023 (2015).
- <sup>101</sup>H. R. Jiang, J. Sun, L. Wei, M. C. Wu, W. Shyy, and T. S. Zhao, "A high power density and long cycle life vanadium redox flow battery", *Energy Storage Materials* **24**, 529–540 (2020).
- <sup>102</sup>E. Sánchez-Díez, E. Ventosa, M. Guarnieri, A. Trovò, C. Flox, R. Marcilla, F. Soavi, P. Mazur, E. Aranzabe, and R. Ferret, "Redox flow batteries: Status and perspective towards sustainable stationary energy storage", *Journal of Power Sources* **481**, 228804 (2021).
- <sup>103</sup>S. Kim, *Vanadium Redox Flow Batteries: Electrochemical Engineering* (IntechOpen, Apr. 3, 2019).
- <sup>104</sup>F. Walsh, C. Poncedelón, L. Berlouis, G. Nikiforidis, L. Arenas-Martínez, D. Hodgson, and D. Hall, "The development of Zn-Ce hybrid redox flow batteries for energy storage and their continuing challenges", *ChemPlusChem* **80**, 288–311 (2015).
- <sup>105</sup>D. Pletcher and R. Wills, "A novel flow battery: A lead acid battery based on an electrolyte with soluble lead( ii ) Part II. Flow cell studies", *Physical Chemistry Chemical Physics* **6**, 1779–1785 (2004).
- <sup>106</sup>L. W. Hruska and R. F. Savinell, "Investigation of Factors Affecting Performance of the Iron-Redox Battery", *Journal of The Electrochemical Society* **128**, 18 (1981).
- <sup>107</sup>L. Sanz, D. Lloyd, E. Magdalena, J. Palma, and K. Kontturi, "Description and performance of a novel aqueous all-copper redox flow battery", *Journal of Power Sources* **268**, 121–128 (2014).

- <sup>108</sup>H. S. Lim, A. M. Lackner, and R. C. Knechtli, "Zinc-Bromine Secondary Battery", *Journal of The Electrochemical Society* **124**, 1154 (1977).
- <sup>109</sup>G. P. Rajarathnam, "The Zinc/Bromine Flow Battery: Fundamentals and Novel Materials for Technology Advancement", Thesis (July 19, 2016).
- <sup>110</sup>W. Yu, W. Shang, P. Tan, B. Chen, Z. Wu, H. Xu, Z. Shao, M. Liu, and M. Ni, "Toward a new generation of low cost, efficient, and durable metal-air flow batteries", *Journal of Materials Chemistry A* **7**, 26744–26768 (2019).
- <sup>111</sup>J. Rubio-Garcia, A. Kucernak, D. Zhao, D. Li, K. Fahy, V. Yufit, N. Brandon, and M. Gomez-Gonzalez, "Hydrogen/manganese hybrid redox flow battery", *JPhys Energy* **1**, 10.1088/2515-7655/aeee17 (2019).
- <sup>112</sup>J. Rubio-Garcia, A. Kucernak, A. Parra-Puerto, R. Liu, and B. Chakrabarti, "Hydrogen/functionalized benzoquinone for a high-performance regenerative fuel cell as a potential large-scale energy storage platform", *Journal of Materials Chemistry A* **8**, 3933–3941 (2020).
- <sup>113</sup>J. Rubio-Garcia, J. Cui, A. Parra-Puerto, and A. Kucernak, "Hydrogen/Vanadium Hybrid Redox Flow Battery with enhanced electrolyte concentration", *Energy Storage Materials* **31**, 1–10 (2020).
- <sup>114</sup>Y. Yang, G. Zheng, and Y. Cui, "A membrane-free lithium/polysulfide semi-liquid battery for large-scale energy storage", *Energy & Environmental Science* **6**, 1552–1558 (2013).
- <sup>115</sup>Y. Ding, Y. Zhao, and G. Yu, "A Membrane-Free Ferrocene-Based High-Rate Semiliquid Battery", *Nano Letters* **15**, 4108–4113 (2015).
- <sup>116</sup>SET Plan documents, [https://setis.ec.europa.eu/implementing-actions/set-plan-documents\\_en](https://setis.ec.europa.eu/implementing-actions/set-plan-documents_en) (visited on 11/18/2022).
- <sup>117</sup>M. Küttinger, J. K. Włodarczyk, D. Daubner, P. Fischer, and J. Tübke, "High energy density electrolytes for H<sub>2</sub>/Br<sub>2</sub> redox flow batteries, their polybromide composition and influence on battery cycling limits", *RSC Advances* **11**, 5218–5229 (2021).
- <sup>118</sup>H. Zhang and C. Sun, "Cost-effective iron-based aqueous redox flow batteries for large-scale energy storage application: A review", *Journal of Power Sources* **493**, 10.1016/j.jpowsour.2020.229445 (2021).
- <sup>119</sup>C. Menictas and M. Skyllas-Kazacos, "Performance of vanadium-oxygen redox fuel cell", *Journal of Applied Electrochemistry* **41**, 1223 (2011).
- <sup>120</sup>M. Skyllas-Kazacos, "Novel vanadium chloride/polyhalide redox flow battery", *Journal of Power Sources* **124**, 299–302 (2003).
- <sup>121</sup>M. Skyllas-Kazacos, "New Vanadium Bromide Redox Fuel Cell", in (June 28, 2004).
- <sup>122</sup>Y. Liu, J. Zhang, S. Lu, and Y. Xiang, "Polyoxometalate-based electrolyte materials in redox flow batteries: Current trends and emerging opportunities", *Materials Reports: Energy, Celebrating Prof. San Ping Jiang's 65th Birthday* **2**, 100094 (2022).
- <sup>123</sup>E. Ventosa, "Semi-solid flow battery and redox-mediated flow battery: two strategies to implement the use of solid electroactive materials in high-energy redox-flow batteries", *Current Opinion in Chemical Engineering* **37**, 100834 (2022).

- <sup>124</sup>V. Singh, S. Kim, J. Kang, and H. Byon, "Aqueous organic redox flow batteries", *Nano Research* **12**, 1988–2001 (2019).
- <sup>125</sup>P. Singh, "Application of non-aqueous solvents to batteries", *Journal of Power Sources* **11**, 135–142 (1984).
- <sup>126</sup>X. Wei, W. Xu, M. Vijayakumar, L. Cosimbescu, T. Liu, V. Sprenkle, and W. Wang, "TEMPO-Based Catholyte for High-Energy Density Nonaqueous Redox Flow Batteries", *Advanced Materials* **26**, 7649–7653 (2014).
- <sup>127</sup>C. Zhang, H. Chen, Y. Qian, G. Dai, Y. Zhao, and G. Yu, "General Design Methodology for Organic Eutectic Electrolytes toward High-Energy-Density Redox Flow Batteries", *Advanced Materials* **33**, 10.1002/adma.202008560 (2021).
- <sup>128</sup>H. Chen and Y.-C. Lu, "A High-Energy-Density Multiple Redox Semi-Solid-Liquid Flow Battery", *Advanced Energy Materials* **6**, 1502183 (2016).
- <sup>129</sup>G. Cong and Y.-C. Lu, "Strategies to Improve the Energy Density of Non-Aqueous Organic Redox Flow Batteries", *Wuli Huaxue Xuebao/ Acta Physico - Chimica Sinica* **38**, 10.3866/PKU.WHXB202106008 (2022).
- <sup>130</sup>J. Yuan, Z.-Z. Pan, Y. Jin, Q. Qiu, C. Zhang, Y. Zhao, and Y. Li, "Membranes in non-aqueous redox flow battery: A review", *Journal of Power Sources* **500**, 229983 (2021).
- <sup>131</sup>Y. Matsuda, K. Tanaka, M. Okada, Y. Takasu, M. Morita, and T. Matsumura-Inoue, "A rechargeable redox battery utilizing ruthenium complexes with non-aqueous organic electrolyte", *Journal of Applied Electrochemistry* **18**, 909–914 (1988).
- <sup>132</sup>R. W. Hogue and K. E. Toghil, "Metal coordination complexes in nonaqueous redox flow batteries", *Current Opinion in Electrochemistry, Energy Storage - Energy Transformation* **18**, 37–45 (2019).
- <sup>133</sup>Z. Li, S. Li, S. Liu, K. Huang, D. Fang, F. Wang, and S. Peng, "Electrochemical Properties of an All-Organic Redox Flow Battery Using 2,2,6,6-Tetramethyl-1-Piperidinyloxy and N-Methylphthalimide", *Electrochemical and Solid-State Letters* **14**, A171 (2011).
- <sup>134</sup>J. Luo, B. Hu, C. Debruler, and T. L. Liu, "A  $\pi$ -Conjugation Extended Viologen as a Two-Electron Storage Anolyte for Total Organic Aqueous Redox Flow Batteries", *Angewandte Chemie International Edition* **57**, 231–235 (2018).
- <sup>135</sup>J. D. Milshtein, A. P. Kaur, M. D. Casselman, J. A. Kowalski, S. Modekrutti, P. L. Zhang, N. H. Attanayake, C. F. Elliott, S. R. Parkin, C. Risko, F. R. Brushett, and S. A. Odom, "High current density, long duration cycling of soluble organic active species for non-aqueous redox flow batteries", *Energy & Environmental Science* **9**, 3531–3543 (2016).
- <sup>136</sup>J. Chai, A. Lashgari, X. Wang, C. K. Williams, and J. " Jiang, "All-PEGylated redox-active metal-free organic molecules in non-aqueous redox flow battery", *Journal of Materials Chemistry A* **8**, 15715–15724 (2020).
- <sup>137</sup>X. Wei, W. Xu, J. Huang, L. Zhang, E. Walter, C. Lawrence, M. Vijayakumar, W. Henderson, T. Liu, L. Cosimbescu, B. Li, V. Sprenkle, and W. Wang, "Radical Compatibility with Nonaqueous Electrolytes and Its Impact on an All-Organic Redox Flow Battery", *Angewandte Chemie - International Edition* **54**, 8684–8687 (2015).

- <sup>138</sup>E. I. Romadina, I. A. Volodin, K. J. Stevenson, and P. A. Troshin, "New highly soluble triarylamine-based materials as promising catholytes for redox flow batteries", *Journal of Materials Chemistry A* **9**, 8303–8307 (2021).
- <sup>139</sup>E. C. Montoto, G. Nagarjuna, J. S. Moore, and J. Rodríguez-López, "Redox Active Polymers for Non-Aqueous Redox Flow Batteries: Validation of the Size-Exclusion Approach", *Journal of The Electrochemical Society* **164**, A1688 (2017).
- <sup>140</sup>B. Hu and T. L. Liu, "Two electron utilization of methyl viologen anolyte in nonaqueous organic redox flow battery", *Journal of Energy Chemistry* **27**, 1326–1332 (2018).
- <sup>141</sup>W. Duan, J. Huang, J. A. Kowalski, I. A. Shkrob, M. Vijayakumar, E. Walter, B. Pan, Z. Yang, J. D. Milshtein, B. Li, C. Liao, Z. Zhang, W. Wang, J. Liu, J. S. Moore, F. R. Brushett, L. Zhang, and X. Wei, "Wine-Dark Sea" in an Organic Flow Battery: Storing Negative Charge in 2,1,3-Benzothiadiazole Radicals Leads to Improved Cyclability", *ACS Energy Letters* **2**, 1156–1161 (2017).
- <sup>142</sup>C. Sevov, D. Hickey, M. Cook, S. Robinson, S. Barnett, S. Minter, M. Sigman, and M. Sanford, "Physical Organic Approach to Persistent, Cyclable, Low-Potential Electrolytes for Flow Battery Applications", *Journal of the American Chemical Society* **139**, 2924–2927 (2017).
- <sup>143</sup>X. Wei, W. Duan, J. Huang, L. Zhang, B. Li, D. Reed, W. Xu, V. Sprenkle, and W. Wang, "A High-Current, Stable Nonaqueous Organic Redox Flow Battery", *ACS Energy Letters* **1**, 705–711 (2016).
- <sup>144</sup>E. Romadina, D. Komarov, K. Stevenson, and P. Troshin, "New phenazine based anolyte material for high voltage organic redox flow batteries", *Chemical Communications* **57**, 2986–2989 (2021).
- <sup>145</sup>W. Wang, W. Xu, L. Cosimbescu, D. Choi, L. Li, and Z. Yang, "Anthraquinone with tailored structure for a nonaqueous metal-organic redox flow battery", *Chemical Communications* **48**, 6669–6671 (2012).
- <sup>146</sup>Y. Ding, Y. Li, and G. Yu, "Exploring Bio-inspired Quinone-Based Organic Redox Flow Batteries: A Combined Experimental and Computational Study", *Chem* **1**, 790–801 (2016).
- <sup>147</sup>M. Pahlevaninezhad, P. Leung, P. Q. Velasco, M. Pahlevani, F. C. Walsh, E. P. L. Roberts, and C. Ponce de León, "A nonaqueous organic redox flow battery using multi-electron quinone molecules", *Journal of Power Sources* **500**, 229942 (2021).
- <sup>148</sup>R. A. Potash, J. R. McKone, S. Conte, and H. D. Abruña, "On the Benefits of a Symmetric Redox Flow Battery", *Journal of The Electrochemical Society* **163**, A338–A344 (2016).
- <sup>149</sup>J. Huang, Z. Yang, M. Vijayakumar, W. Duan, A. Hollas, B. Pan, W. Wang, X. Wei, and L. Zhang, "A Two-Electron Storage Nonaqueous Organic Redox Flow Battery", *Advanced Sustainable Systems* **2**, 1700131 (2018).
- <sup>150</sup>Y. Zhen, C. Zhang, J. Yuan, and Y. Li, "Anthraquinone-based electroactive ionic species as stable multi-redox anode active materials for high-performance nonaqueous redox flow batteries", *Journal of Materials Chemistry A* **9**, 22056–22063 (2021).

- <sup>151</sup>B. Huskinson, M. Marshak, C. Suh, S. Er, M. Gerhardt, C. Galvin, X. Chen, A. Aspuru-Guzik, R. Gordon, and M. Aziz, "A metal-free organic-inorganic aqueous flow battery", *Nature* **505**, 195–198 (2014).
- <sup>152</sup>M. Gerhardt, L. Tong, R. Gómez-Bombarelli, Q. Chen, M. Marshak, C. Galvin, A. Aspuru-Guzik, R. Gordon, and M. Aziz, "Anthraquinone Derivatives in Aqueous Flow Batteries", *Advanced Energy Materials* **7**, 10.1002/aenm.201601488 (2017).
- <sup>153</sup>D. P. Tabor, R. Gómez-Bombarelli, L. Tong, R. G. Gordon, M. J. Aziz, and A. Aspuru-Guzik, "Mapping the frontiers of quinone stability in aqueous media: implications for organic aqueous redox flow batteries", *Journal of Materials Chemistry A* **7**, 12833–12841 (2019).
- <sup>154</sup>K. Lin, Q. Chen, M. Gerhardt, L. Tong, S. Kim, L. Eisenach, A. Valle, D. Hardee, R. Gordon, M. Aziz, and M. Marshak, "Alkaline quinone flow battery", *Science* **349**, 1529–1532 (2015).
- <sup>155</sup>D. G. Kwabi, K. Lin, Y. Ji, E. F. Kerr, M.-A. Goulet, D. De Porcellinis, D. P. Tabor, D. A. Pollack, A. Aspuru-Guzik, R. G. Gordon, and M. J. Aziz, "Alkaline Quinone Flow Battery with Long Lifetime at pH 12", *Joule* **2**, 1894–1906 (2018).
- <sup>156</sup>Y. Ji, M.-A. Goulet, D. Pollack, D. Kwabi, S. Jin, D. De Porcellinis, E. Kerr, R. Gordon, and M. Aziz, "A Phosphonate-Functionalized Quinone Redox Flow Battery at Near-Neutral pH with Record Capacity Retention Rate", *Advanced Energy Materials* **9**, 10.1002/aenm.201900039 (2019).
- <sup>157</sup>S. Jin, Y. Jing, D. Kwabi, Y. Ji, L. Tong, D. De Porcellinis, M.-A. Goulet, D. Pollack, R. Gordon, and M. Aziz, "A Water-Miscible Quinone Flow Battery with High Volumetric Capacity and Energy Density", *ACS Energy Letters* **4**, 1342–1348 (2019).
- <sup>158</sup>B. Hu, J. Luo, M. Hu, B. Yuan, and T. Liu, "A pH-Neutral, Metal-Free Aqueous Organic Redox Flow Battery Employing an Ammonium Anthraquinone Anolyte", *Angewandte Chemie - International Edition* **58**, 16629–16636 (2019).
- <sup>159</sup>A. Khataee, K. Wedege, E. Dražević, and A. Bentien, "Differential pH as a method for increasing cell potential in organic aqueous flow batteries", *Journal of Materials Chemistry A* **5**, 21875–21882 (2017).
- <sup>160</sup>A. Khataee, E. Dražević, J. Catalano, and A. Bentien, "Performance Optimization of Differential pH Quinone-Bromide Redox Flow Battery", *Journal of The Electrochemical Society* **165**, A3918–A3924 (2018).
- <sup>161</sup>E. S. Beh, D. De Porcellinis, R. L. Gracia, K. T. Xia, R. G. Gordon, and M. J. Aziz, "A Neutral pH Aqueous Organic–Organometallic Redox Flow Battery with Extremely High Capacity Retention", *ACS Energy Letters* **2**, 639–644 (2017).
- <sup>162</sup>Y. Liu, M.-A. Goulet, L. Tong, Y. Liu, Y. Ji, L. Wu, R. Gordon, M. Aziz, Z. Yang, and T. Xu, "A Long-Lifetime All-Organic Aqueous Flow Battery Utilizing TMAP-TEMPO Radical", *Chem* **5**, 1861–1870 (2019).
- <sup>163</sup>K. Lin, R. Gómez-Bombarelli, E. Beh, L. Tong, Q. Chen, A. Valle, A. Aspuru-Guzik, M. Aziz, and R. Gordon, "A redox-flow battery with an alloxazine-based organic electrolyte", *Nature Energy* **1**, 10.1038/nenergy.2016.102 (2016).
- <sup>164</sup>A. Orita, M. G. Verde, M. Sakai, and Y. S. Meng, "A biomimetic redox flow battery based on flavin mononucleotide", *Nature Communications* **7**, 13230 (2016).



- <sup>165</sup>S. Hu, T. Li, M. Huang, J. Huang, W. Li, L. Wang, Z. Chen, Z. Fu, X. Li, and Z. Liang, "Phenylene-Bridged Bispyridinium with High Capacity and Stability for Aqueous Flow Batteries", *Advanced Materials* **33**, 10.1002/adma.202005839 (2021).
- <sup>166</sup>B. Hu, M. Hu, J. Luo, and T. Liu, "A Stable, Low Permeable TEMPO Catholyte for Aqueous Total Organic Redox Flow Batteries", *Advanced Energy Materials* **12**, 10.1002/aenm.202102577 (2022).
- <sup>167</sup>V. Krishnamurti, B. Yang, A. Murali, S. Patil, G. Surya Prakash, and S. Narayan, "Aqueous organic flow batteries for sustainable energy storage", *Current Opinion in Electrochemistry* **35**, 10.1016/j.coelec.2022.101100 (2022).
- <sup>168</sup>M. Tang, R. Fu, M. Deschamps, K. Romanenko, and A. Jerschow, "CHAPTER 2: The Methodology of Electrochemical In Situ NMR and MRI", in *NMR and MRI of Electrochemical Energy Storage Materials and Devices* (June 17, 2021), pp. 71–105.
- <sup>169</sup>T. Kuwana, R. K. Darlington, and D. W. Leedy, "Electrochemical Studies Using Conducting Glass Indicator Electrodes.", *Anal. Chem.* **36**, 2023–2025 (1964).
- <sup>170</sup>E. C. R. McKenzie, S. Hosseini, A. G. C. Petro, K. K. Rudman, B. H. R. Gerroll, M. S. Mubarak, L. A. Baker, and R. D. Little, "Versatile Tools for Understanding Electrosynthetic Mechanisms", *Chem. Rev.* **122**, 3292–3335 (2022).
- <sup>171</sup>E. W. Zhao, E. Jónsson, R. B. Jethwa, D. Hey, D. Lyu, A. Brookfield, P. A. A. Klusener, D. Collison, and C. P. Grey, "Coupled In Situ NMR and EPR Studies Reveal the Electron Transfer Rate and Electrolyte Decomposition in Redox Flow Batteries", *J. Am. Chem. Soc.* **143**, 1885–1895 (2021).
- <sup>172</sup>S. Luo, K. Elouarzaki, and Z. J. Xu, "Electrochemistry in Magnetic Fields", *Angew Chem Int Ed* **61**, 10.1002/anie.202203564 (2022).
- <sup>173</sup>L. M. Monzon and J. Coey, "Magnetic fields in electrochemistry: The Kelvin force. A mini-review", *Electrochemistry Communications* **42**, 42–45 (2014).
- <sup>174</sup>L. M. A. Monzon and J. M. D. Coey, "Magnetic fields in electrochemistry: The Lorentz force. A mini-review", *Electrochemistry Communications* **42**, 38–41 (2014).
- <sup>175</sup>B. Ferreira Gomes, P. Ferreira da Silva, C. M. Silva Lobo, M. da Silva Santos, and L. A. Colnago, "Strong magnetoelectrolysis effect during electrochemical reaction monitored in situ by high-resolution NMR spectroscopy", *Anal Chim Acta* **983**, 91–95 (2017).
- <sup>176</sup>J. A. Koza, S. Mühlhoff, P. Zabinski, P. Nikrityuk, K. Eckert, M. Uhlemann, A. Gebert, T. Weier, L. Schultz, and S. Odenbach, "Hydrogen evolution under the influence of a magnetic field", *Electrochimica Acta* **56**, 2665–2675 (2011).
- <sup>177</sup>C. M. Costa, K. J. Merazzo, R. Gonçalves, C. Amos, and S. Lanceros-Méndez, "Magnetically active lithium-ion batteries towards battery performance improvement", *iScience* **24**, 102691 (2021).
- <sup>178</sup>R. Cheng, P. Sun, H. Su, W. Yang, P. Leung, and Q. Xu, "Effect of exerted magnetic field on the performance of non-aqueous iron-vanadium redox flow battery with deep eutectic solvent (DES) electrolyte", *Electrochimica Acta* **399**, 139404 (2021).

- <sup>179</sup>R. Cheng, J. Xu, X. Wang, Q. Ma, H. Su, W. Yang, and Q. Xu, "Electrochemical Characteristics and Transport Properties of V(II)/V(III) Redox Couple in a Deep Eutectic Solvent: Magnetic Field Effect", *Frontiers in Chemistry* **8**, 10.3389/fchem.2020.00619 (2020).
- <sup>180</sup>M. C. Wapler, J. Leupold, I. Dragonu, D. von Elverfeld, M. Zaitsev, and U. Wallrabe, "Magnetic properties of materials for MR engineering, micro-MR and beyond", *Journal of Magnetic Resonance* **242**, 233–242 (2014).
- <sup>181</sup>G. P. Arrighini, M. Maestro, and R. Moccia, "Magnetic Properties of Polyatomic Molecules. I. Magnetic Susceptibility of H<sub>2</sub>O, NH<sub>3</sub>, CH<sub>4</sub>, H<sub>2</sub>O<sub>2</sub>", *The Journal of Chemical Physics* **49**, 882–889 (1968).
- <sup>182</sup>K. Wedege, J. Azevedo, A. Khataee, A. Bentien, and A. Mendes, "Direct Solar Charging of an Organic–Inorganic, Stable, and Aqueous Alkaline Redox Flow Battery with a Hematite Photoanode", *Angewandte Chemie International Edition* **55**, 7142–7147 (2016).
- <sup>183</sup>W. Lee, A. Permatasari, and Y. Kwon, "Neutral pH aqueous redox flow batteries using an anthraquinone-ferrocyanide redox couple", *Journal of Materials Chemistry C* **8**, 5727–5731 (2020).
- <sup>184</sup>F. Fenini, E. Drazevic, and A. Bentien, "Impact of pH management on utilization and performance of anthraquinone/ferrocyanide flow batteries", *Journal of Power Sources* **540**, 10.1016/j.jpowsour.2022.231641 (2022).
- <sup>185</sup>I. Tkáč, Z. Starcuk, I. Y. Choi, and R. Gruetter, "In vivo <sup>1</sup>H NMR spectroscopy of rat brain at 1 ms echo time", *Magnetic Resonance in Medicine* **41**, 649–656 (1999).
- <sup>186</sup>J. P. Felmlee and R. L. Ehman, "Spatial presaturation: a method for suppressing flow artifacts and improving depiction of vascular anatomy in MR imaging", *Radiology* **164**, 559–564 (1987).
- <sup>187</sup>T. J. Carney, S. J. Collins, J. S. Moore, and F. R. Brushett, "Concentration-Dependent Dimerization of Anthraquinone Disulfonic Acid and Its Impact on Charge Storage", *Chemistry of Materials* **29**, 4801–4810 (2017).
- <sup>188</sup>M. M. Britton, P. M. Bayley, P. C. Howlett, A. J. Davenport, and M. Forsyth, "In situ, real-time visualization of electrochemistry using magnetic resonance imaging", *The Journal of Physical Chemistry Letters* **4**, PMID: 24265861, 3019–3023 (2013).
- <sup>189</sup>A. J. Illott, S. Chandrashekar, A. Klöckner, H. J. Chang, N. M. Trease, C. P. Grey, L. Greengard, and A. Jerschow, "Visualizing skin effects in conductors with MRI: <sup>7</sup>Li MRI experiments and calculations", *Journal of Magnetic Resonance* **245**, 143–149 (2014).
- <sup>190</sup>M. Quan, D. Sanchez, M. F. Wasylkiw, and D. K. Smith, "Voltammetry of Quinones in Unbuffered Aqueous Solution: Reassessing the Roles of Proton Transfer and Hydrogen Bonding in the Aqueous Electrochemistry of Quinones", *Journal of the American Chemical Society* **129**, 12847–12856 (2007).
- <sup>191</sup>P. S. Guin, S. Das, and P. C. Mandal, "Electrochemical Reduction of Quinones in Different Media: A Review", *International Journal of Electrochemistry* **2011**, e816202 (2011).
- <sup>192</sup>R. J. Forster and J. P. O'Kelly, "Protonation reactions of anthraquinone-2,7-disulphonic acid in solution and within monolayers", *Journal of Electroanalytical Chemistry* **498**, 127–135 (2001).

- <sup>193</sup>L. Tong, Q. Chen, A. Wong, R. Gómez-Bombarelli, A. Aspuru-Guzik, R. Gordon, and M. Aziz, "UV-Vis spectrophotometry of quinone flow battery electrolyte for: In situ monitoring and improved electrochemical modeling of potential and quinhydrone formation", *Physical Chemistry Chemical Physics* **19**, 31684–31691 (2017).
- <sup>194</sup>C. Wiberg, T. Carney, F. Brushett, E. Ahlberg, and E. Wang, "Dimerization of 9,10-anthraquinone-2,7-Disulfonic acid (AQDS)", *Electrochimica Acta* **317**, 478–485 (2019).
- <sup>195</sup>M. Wu, M. Bahari, Y. Jing, K. Amini, E. M. Fell, T. Y. George, R. G. Gordon, and M. J. Aziz, "Highly Stable, Low Redox Potential Quinone for Aqueous Flow Batteries\*\*", *Batteries & Supercaps* **5**, e202200009 (2022).
- <sup>196</sup>F. Beck and G. Heydecke, "On the Mechanism of the Cathodic Reduction of Anthraquinone to Anthrone", *Berichte der Bunsengesellschaft für physikalische Chemie* **91**, 37–43 (1987).
- <sup>197</sup>M.-A. Goulet, L. Tong, D. Pollack, D. Tabor, S. Odom, A. Aspuru-Guzik, E. Kwan, R. Gordon, and M. Aziz, "Extending the lifetime of organic flow batteries via redox state management", *Journal of the American Chemical Society* **141**, 8014–8019 (2020).
- <sup>198</sup>I. M. Kolthoff and E. A. Pearson, "Stability of potassium ferrocyanide solutions", *Industrial & Engineering Chemistry Analytical Edition* **3**, 381–382 (1931).
- <sup>199</sup>C. A. P. Arellano and S. S. Martínez, "Effects of pH on the degradation of aqueous ferri-cyanide by photolysis and photocatalysis under solar radiation", *Solar Energy Materials and Solar Cells* **94**, 327–332 (2010).
- <sup>200</sup>S. Ašpergër, "Kinetics of the decomposition of potassium ferrocyanide in ultra-violet light", *Transactions of the Faraday Society* **48**, 617–624 (1952).
- <sup>201</sup>M. Reinhard, T. J. Penfold, F. A. Lima, J. Rittmann, M. H. Rittmann-Frank, R. Abela, I. Tavernelli, U. Rothlisberger, C. J. Milne, and M. Chergui, "Photooxidation and photoaquation of iron hexacyanide in aqueous solution: A picosecond X-ray absorption study", *Structural Dynamics* **1**, 024901 (2014).
- <sup>202</sup>M. Cazot, G. Maranzana, J. Dillet, F. Beille, T. Godet-Bar, and S. Didierjean, "Symmetric-cell characterization of the redox flow battery system: Application to the detection of degradations", *Electrochimica Acta* **321**, 134705 (2019).
- <sup>203</sup>S. Granados, "Long-term stability of ferri-/ferrocyanide as an electroactive component for redox flow battery applications: On the origin of apparent capacity fade",
- <sup>204</sup>E. W. Zhao, T. Liu, E. Jónsson, J. Lee, I. Temprano, R. B. Jethwa, A. Wang, H. Smith, J. Carretero-González, Q. Song, and C. P. Grey, "In situ NMR metrology reveals reaction mechanisms in redox flow batteries", *Nature* **579**, 224–228 (2020).
- <sup>205</sup>B. Wermeckes and F. Beck, "Acid Catalyzed Disproportionation of Anthrahydroquinone to Anthraquinone and Anthrone", *Denki Kagaku oyobi Kogyo Butsuri Kagaku* **62**, 1202–1205 (1994).
- <sup>206</sup>A. D. Broadbent and R. J. Melanson, "The Redox Behavior of 9,10-Anthraquinone-2-sulfonate in Acidic Aqueous Solution", *Canadian Journal of Chemistry* **53**, 3757–3760 (1975).
- <sup>207</sup>H. Pan, Y. Shen, J. Duan, K. Lu, and B. Hu, "Spin-dependent deprotonation induced giant magnetocurrent in electrochemical cells", *Phys. Chem. Chem. Phys.* **18**, 9897–9901 (2016).

- <sup>208</sup>Y. Jing, E. W. Zhao, M.-A. Goulet, M. Bahari, E. Fell, S. Jin, A. Davoodi, E. Jónsson, M. Wu, C. Grey, R. Gordon, and M. Aziz, "Electrochemical Regeneration of Anthraquinones for Lifetime Extension in Flow Batteries", [10.33774/chemrxiv-2021-x05x1](https://doi.org/10.33774/chemrxiv-2021-x05x1) (2021).
- <sup>209</sup>Y. Jing, E. W. Zhao, M.-A. Goulet, M. Bahari, E. M. Fell, S. Jin, A. Davoodi, E. Jónsson, M. Wu, C. P. Grey, R. G. Gordon, and M. J. Aziz, "In situ electrochemical recomposition of decomposed redox-active species in aqueous organic flow batteries", *Nat. Chem.*, 1–7 (2022).
- <sup>210</sup>H. Wendt, "K. Kinoshita: Carbon, Electrochemical and Physical Properties, John Wiley + Sons, Chichester, New York, Brisbane, Toronto 1988. 533 Seiten, Preis: £ 65.–", *Berichte der Bunsengesellschaft für physikalische Chemie* **92**, 1060–1060 (1988).
- <sup>211</sup>F. Kotz, K. Arnold, W. Bauer, D. Schild, N. Keller, K. Sachsenheimer, T. M. Nargang, C. Richter, D. Helmer, and B. E. Rapp, "Three-dimensional printing of transparent fused silica glass", en *Nature* **544**, 337–339 (2017).
- <sup>212</sup>D. T. Nguyen, C. Meyers, T. D. Yee, N. A. Dudukovic, J. F. Destino, C. Zhu, E. B. Duoss, T. F. Baumann, T. Suratwala, J. E. Smay, and R. Dylla-Spears, "3D-Printed Transparent Glass", en *Advanced Materials* **29**, 1701181 (2017).